Nanocrystalline ZnO obtained from pyrolytic decomposition of layered basic zinc acetate: Introducing a novel rapid microwave-assisted hydrothermal technique.

Tarat, Afshin

4/17

Nanocrystalline ZnO obtained from pyrolytic decomposition of layered basic zinc acetate

Introducing a Novel Rapid Microwave-assisted Hydrothermal Technique

Swansea University
Prifysgol Abertawe

Afshin Tarat

Submitted to Swansea University in the fulfillment of the requirements for the Degree of Doctor of Philosophy.

Department of Multidisciplinary Nanotechnology
School of Engineering
Swansea University

September 2014

Declarations

This work has not previously been accepted in substance for any degree and is not currently submitted in candidature for a degree in any University.

Signed (Candidate)

Dated 08.10.2014

This thesis is the result of my own investigation except where otherwise stated. Other sources are acknowledged giving explicit references. A bibliography is appended.

Signed (Candidate)

Dated 08/10/2014

I Herby consent for my thesis, if accepted, to be available for photocopying and for inter-library loan, and for the title and summary to be available to outside organizations.

Signed (Candidate)

Dated 08.10.2014

Certificate of Originality

This thesis is submitted to Swansea University under the supervision of Dr. Thierry Maffeis in the Multidisciplinary Nanotechnology Centre in Swansea University in candidature for the degree of Doctor of Philosophy. The material in this thesis is the original work of the author except where acknowledgment to other authors is expressed.

Signed .....

Dated .....

Afahin Tarat

(Candidate)

Signed .....

Dated .....

Dr. Thierry Maffeis

(Supervisor)

Acknowledgement

There are a lot of people I would like to thank for a huge variety of reasons. Firstly, I would like to thank my supervisor, Dr. Thierry Maffeis. I could not have imagined having a better advisor and mentor for my PhD. Thank you for supervising my thesis work and for encouragement and unconditional support along the way, and for enthusiasm and inspiration which was always there when I needed it. Thank you for your patience in reading and correcting my thesis. Throughout my thesis-writing period, you provided encouragement, sound advice, good teaching, good company, and lots of good ideas. I really do appreciate that very much.

Thank you to everyone in my group: Richard Brown, Christ Bonnet, Dan Jones, Jonathan Evans and Dr. Alex Lord for your help, advice and friendship. Exclusively thank you to Prof. Kenith Meissner and Dr. Ravish Majithia for all the help and support that you have dedicated to PhD work. An especially thank you to Dr. Mark Penny, Dr. Rowan Brown, Dr. Richard Colby, Dr. Chris Wright and Dr. Paul Williams for all your help with my first steps in the research world. Also, an especially big thank you to Irene Turner, I really appreciate you correcting my written English, teaching me new words and giving me English lessons. Many thanks to everyone in the Nanotechnology department: Ruth Baker and Michelle Rees for your help in various situations over last few years.

Finally, I would like to express my heartfelt thankfulness to my wife, Nafiseh and my daughter, Helia for their support and patience, which enabled me to overcome difficulties and hardship encountered in the course of this study.

Abstract

Zinc oxide (ZnO) crystal with a direct wide band gap (3.37 eV) and large excition binding energy (60 meV) is one of the most potential semiconductors in numerous application fields such as room-temperature UV-laser, light-emitting-diode (LED), photocatalyst, gas sensor, solar cell, piezoelectric device, etc. In past decades, different methods have been investigated to produce a variety of different shapes of nano and submicron ZnO nanostructures. Among them, the ZnO nanobelts (NBs) with a rectangular cross section have unique optoelectronic properties due to its unusual shape and structure. It is well demonstrated by recent success in field-effect transistor, nanoresonator, and spintronics applications of the ZnO NBs. Two-dimensional (2D) nanostructures such as nanosheets (NSs) and thin films have also great potential for unique purposes where a large uniform coverage at nanoscale is essential. One of the conventional methods for synthesis of the ZnO nanostructures is vapour transport and condensation process at high temperature, in some cases up to 1400°C. Such an extreme condition for vaporization of precursor could induce many oxygen defects on surface of the ZnO nanobelts. These specific defects hinder progress to the applications of ZnO in optoelectronic and lasing devices. In this respect, mild processing is strongly demanded for the synthesis of the ZnO nanoparticles. In terms of low energy consumption and simplicity, soft-solution process based on hydrothermal reactions at low temperature (under 100°C) is a green chemical procedure. However, there are only few reports on the synthesis of the ZnO NBs and NSs due to their unusual growth habit against typical growth rate of the ZnO crystal. Here we are reporting a developed simple, low cost and high yield hydrothermal technique to synthesis layered basic zinc acetate (LBZA) NBs and also a novel rapid microwave-assisted hydrothermal technique to grow LBZA NSs only in 2 minutes. Growth procedures are followed by pyrolytic decomposition to produce nanocrystalline NBs and NSs. SEM and AFM results revealed that the morphology and quantity of the nanobelts and nanosheets are strongly temperature and pH dependent. In addition, results showed that as-grown LBZA nanostructures could be easily transformed to corresponding ZnO nanostructures through pyrolytic decomposition without

Table of Contents

List of Figures

LIST OF TABLES

1 INTRODUCTION

1.1 Nanotechnology

Nanotechnology is a powerful emerging technology, which is seeking to investigate distinct technological advances of controlling the structure of materials at a reduced dimensional scale approaching individual molecules and atoms and their organized aggregates or supramolecular such as polymers and crystalline state[1]. Basically, the nanometer-length scale is creating possibilities for novel materials that can be used for the construction of devices and systems. So literally the term means any technology on a nanoscale that has applications in the real world. But, nanotechnology must be distinguished from the nanoscience enabling such technology. Fundamentally, nanoscience is the investigation of phenomena and material properties at nanoscale, while nanotechnology is applying the resulting knowledge to create novel materials and structures. Knowledge in nanoscience and nanotechnology is increasing worldwide, leading to numerous scientific developments. In turn, this is expected to lead to fundamental changes in the way those materials, devices, and systems (including biological systems) are understood and created. In addition, applications in life sciences research, predominantly at the cell level sets the stage for an exciting role of nanotechnology in healthcare. Therefore, nanotechnology includes the production and application of chemical, physical, and biological systems at scales ranging from individual atoms or molecules to submicron dimensions, and furthermore, the fabrication of the resulting nanostructures into larger systems or devices[2].

Nanotechnology is likely to have a significant influence and a profound impact on our society and economy in the future similar to that of semiconductor technology, information technology, or cellular and molecular biology. Science and technology research in this field promise breakthroughs in areas such as advanced materials engineering and manufacturing, medicine and healthcare, biotechnology and sensors, tissue engineering, energy and nanogenerators, nanoelectronics, national security and information technology. It is widely felt

that nanotechnology will be the next Industrial Revolution. In addition, the discovery of novel advanced-materials at the nanoscale and the development of new experimental and theoretical methods for research may provide fresh opportunities for the development of sophisticated micro and nanosystems include micro/nano electro-mechanical systems (MEMS/NEMS) and nanostructured materials[3]. Also the potential impact of novel nanomedical applications on disease diagnosis, therapy and prevention is foreseen to change healthcare in a fundamental way. Furthermore, therapeutic selection can increasingly be tailored to each patient's profile. Therefore nanotechnology has advantages such as it can revolutionize a lot of electronic products, procedures, and applications. The areas that benefit from the continued development of nanotechnology when it comes to electronic products include nano transistors, nano diodes, OLED, plasma displays, quantum computers, and many more[4]. It can also benefit the energy sector. The development of more effective energy-producing, energy-absorbing, and energy storage products in smaller and more efficient devices is possible with this technology[5]. Such items like batteries, fuel cells, and solar cells can be built smaller but can be made to be more effective with this technology[6]. Another industry that can benefit from nanotechnology is the manufacturing sector that will need materials like nanotubes, aerogels, nano particles, and other similar items to produce their products with. These materials are often stronger, more durable, and lighter than those that are not produced with the help of nanotechnology[7]. In the medical world, nanotechnology is also seen as a boon since these can help with creating what is called smart drugs[8]. These help cure people faster and without the side effects that other traditional drugs have. You will also find that the research of nanotechnology in medicine is now focusing on areas like tissue regeneration, bone repair, immunity and even cures for such ailments like cancer, diabetes, and other life threatening diseases[9].

1.2 Marketing

With almost every manufactured product, if the same performance can be achieved by using less material, there will be a cost advantage in doing so. It is more significant where the used materials either are of the expensive ones such as platinum and gold, which are widely used in electronics as highly conductive materials or they are of the rare Earth elements such as scandium and yttrium. There is a similar scenario for sensitivity and response time of manufactured devices such as miniaturized electromechanical devices (MEMS/NEMS)[10]. MEMS refers to microscopic devices that have a characteristic length of less than 1mm but more than 100nm and that combine electrical and mechanical components. NEMS refers to nanoscopic devices that have a characteristic length of less than 100nm and that combine electrical and mechanical components. In devices, if the functional components are on the micro- or nanoscale, they may be referred to as MEMS or NEMS, respectively. These are referred to as intelligent miniaturized systems, comprising sensing, processing, and/or actuating functions and combining electrical and mechanical components. The terms MEMS/NEMS are also now used in a broad sense and include electrical, mechanical, fluidic, optical, and/or biological function. MEMS/NEMS and Bio-MEMS/Bio-NEMS are expected to have a major impact on our lives, comparable to that of semiconductor technology, information technology, or cellular and molecular biology [11] MEMS/NEMS and Bio-MEMS/Bio-NEMS are used in electromechanical, electronics, information/communication, chemical, and biological applications. The MEMS industry in 2004 was worth about US$ 4.5 billion, while according to MEMS' Trend magazine, issue 10, April 2012 "the MEMS market will continue to see steady, sustainable double-digit growth for the next six years, with 20% compound average annual growth in units and 13% growth in revenues, leading to a US$21 billion market by 2017"[12].

Growth of Si-based MEMS/NEMS may slow down and that of nonsilicon-based MEMS may pick up during the next decade. It is expected to expand in this decade, for nanomaterials and biomedical applications as well as

nanoelectronics or molecular electronics. For example, miniaturized diagnostics could be implanted for early diagnosis of illness. In addition, targeted drug-delivery devices are under development. Due to the enabling nature of these systems and because of the significant impact they can have on both commercial and defense applications, industry as well as federal governments have taken a special interest in seeing growth in this field nurtured. MEMS/NEMS and Bio-MEMS/Bio-NEMS are the next logical step in the *silicon revolution*[13].

Nanomedicine including drug delivery, biosensors, tissue engineering etc. is already an established market. Unlike some other potential applications of nanotechnology, which are still largely experimental in laboratories and research centers, nanomedicine has already produced a number of novel products in which the nano dimension has made a significant contribution to product efficiency and performance. The global nanomedicine market reached $63.8 billion in 2010 and $72.8 billion in 2011 [14]. The market is expected to grow to $130.9 billion by 2016 at a compound annual growth rate (CAGR) of 12.5% between years 2011 and 2016 [14]. For example, the central nervous system (CNS) products market reached $11.7 billion in 2010 and $14.0 billion in 2011. It is expected to grow to $29.5 billion by 2016, a CAGR of 16.1% between years 2011 and 2016. The anticancer products market reached $25.2 billion in 2010 and $28.0 billion in 2011. It is expected to reach $46.7 billion by 2016, a CAGR of 10.8% between years 2011 and 2016.

However, in terms of nanomaterials definition (nanomaterials as defined in a 2011 Commission Recommendation are materials which often have specific properties due to their small particle size), practically it is not possible to separate medical nanomaterials and applications from others, so according to a report [15], the global market for nanomaterials is estimated at 11 million tones at a market value of 20 billions €. The current direct employment in the nanomaterial sector is estimated at 300 000 to 400 000 in Europe[16]. It is still dominated by materials, which have been in use for decades, such as carbon black (mainly used in tyres) or synthetic amorphous silica (used in a wide variety of applications including tyres, as polymer filler but also in toothpaste or as anticoagulant in food powders)[16].

In the past years, many new nanomaterial-related applications have been developed; those include a number of consumer products such as UV-filters in sun creams and anti-odor textiles. However, many medical and technical applications such as tumor therapies, lithium-ion batteries, which can drive electrical cars, or solar panels as a renewable source of energy, also exist. Those applications have the potential to create major technological breakthroughs, and therefore nanomaterials have been identified as a key enabling technology. Products underpinned by nanotechnology are forecast to grow from a global volume of 200 billions € in 2009 to 2 trillions € by 2015 [17].

Different ZnO nanostructures and morphologies have been competitively developed by a number of methods such as thermal vapour transport-condensation method [94], metal organic chemical vapour deposition (MOCVD) [95], electrochemical reaction [96], hydrothermal reaction [52], etc. Vapour transport and condensation process based on vapour liquid solid (VLS) mechanism is a conventional method to produce ZnO nanobelts at high temperature above 1400°C [97]. One of the most common problems that occur during such an extreme condition for vapourization of precursor is to induce many oxygen defects on surface of the ZnO nanobelts [98], which hinder progress where the applications need a pure ZnO lattice without these specific surface defects such as optoelectronic and lasing devices. Hence, it seems that mild processing and slow-reaction approaching growth system such as hydrothermal reactions at low temperature (under 100°C) is more demanded for the synthesis of the ZnO nanobelts. In addition, such a low temperature process is a green chemical procedure in terms of low energy consumption and simplicity [98]. However, mixed product with the nanowires (~60%) and nanobelts (~40%) was usually obtained from the hydrothermal methods [99] due to unusual growth habit of ZnO nanocrystals against typical growth rate, [0001]>[01-10]>[000 -1], [66,98]. In this respect, the aim of this research is to develop hydrothermal techniques to grow ZnO nanostructures at a low cost and with a high yield. In addition, gas sensors, fabricated with the ZnO nanomaterials developed in this work are tested to demonstrate the potential of the techniques for practical application.

1.3 Thesis layout

The present work includes different chapters:

- Chapter 1 is an introduction to nanotechnology; importance of nanoscale particles and their marketing. In addition, the aim and targets of this research.

- Chapter 2 is about nanostructures, length scale in different materials, semiconductor nanostructures. In addition, ZnO different crystal structures and nanostructures are described focusing on nanobelts and nanosheets.

- Chapter 3 is a literature review about the most relevant papers to this research including different growth techniques to synthesis ZnO nanostructure from very high temperature growth route such as VPD to hydrothermally growth which is possible in atmosphere and low temperature, comparison between them and their advantages and disadvantages. Also some examples of different methods to fabricate metal oxide gas sensing and their sensitivity to CO have been revised.

- Chapter 4 is description of the techniques and different equipment, which were employed in this research. Also the home-assembled sensing apparatus and the details of sensing procedures are explained.

- Chapter 5 presents the investigation results from as-synthesized nanobelts and nanosheets. Also there is a comparison between our developed hydrothermal technique to produce LBZA nanobelts and resulting ZnO nanobelts using pyrolytic decomposition. In this chapter the influence of temperature and pH on the shape and morphology of crystals is discussed. Also our novel rapid technique to produce LBZA nanosheets using a commercial kitchen microwave is explained in details. Nanosheets characterizations are compared with pervious works and

advantages and disadvantages are discussed. Finally, the results from CO sensing using home-assembled sensor apparatus are compared with the previous works and the sensitivity and performance of the new materials are discussed.

- Chapter 6. In this chapter the difference between our developed hydrothermal method and novel rapid microwave technique with previous works are explained. Finally, the advantages and disadvantages are debated and future work is suggested.

2 Semiconductor Nanostructures Background

2.1 Nanoscale materials

The properties of materials at the nanoscale are very different from those at their bulk. Many properties of solids are strongly size-dependent. Macro scale objects are generally studied in traditional field of physics such as electricity, mechanics, magnetism and optics, the size of the materials in this category range from millimeters to kilometers. However, nano length scales can be explained as a regime where the optical and electrical properties of material become size and shape dependent. In terms of semiconductors such as ZnO it is given by the bulk exciton Bohr radius or alternatively by the Broglie wavelength of carriers in the materials [18]. Nano effects occur when the physical dimensions of the system become comparable to or smaller than the natural size of electrons and holes in it. As the physical dimensions become smaller and smaller quantum mechanical confinement effect begin to occur.

It can also be explained as the confinement of electrons in small dimensions may lead to a discretization of energy levels. The associated quantum size effects in turn lead to an out-of-plane conductivity that shows nonanalytic behavior in the approach to the classical limit. For instance, the principal size dependence of the conductivity is $\sim 1/d$ for a film of thickness d; however, there is also a correction term that has an essential singularity in the small parameter l/d, where l is the mean free path in a bulk sample. Surface roughness in the film is introduced by establishing two physical length scales. Variations in d on length scales shorter than l are treated quantum mechanically by a suitable coordinate transformation. On the other hand, large-scale fluctuations which might reflect the presence of grains are incorporated classically by segmenting the film into independent units of length l. Impurity effects have also been included and in fact crossover behavior in the conductivity is found from a surface-dominated to an impurity-dominated regime.

The transport coefficients—conductivity and thermopower—are found to show oscillations as a function of *d* with a period of half the Fermi wavelength [19].

2.2 Length scales in semiconductors

In terms of the binding energy, the most important factor is the Coulomb attraction between oppositely charged electrons and holes. Amount of this energy is proportional to r^{-1}. On the other hand, the confinement energy associated with either electron or hole is proportional to r^{-2}. So confinement grows faster than Coulomb attraction between electrons and holes while the size of the particles become smaller. Consequently, as the Coulomb term is important in bulk material, in nanoscale materials the confinement of individual electrons and holes dominates at small enough sizes. Therefore, there is same scenario where the optical and electrical properties of materials become size and shape dependent and where some of the most fascinating aspects of nano begin. In terms of the confinement of electrons and holes, three regimes have been described, strong, intermediate and week confinement. In a week confinement regime, critical dimension of the nanoparticle is larger than both the individual electron and hole Bohr radii. Consequently, the exciton binding energy is week as in bulk material. In addition, optical and electrical properties of the nanostructure are similar to the bulk system. But in intermediate confinement regime, the critical dimension of the nanostructure is smaller than one carrier's Bohr radius but larger than the other's. As the effective mass of electron is generally smaller than the effective mass of the hole, so it means that the critical dimension of the nanoparticle is smaller than the electron's Bohr radius and larger than hole's one. At this point, quantization effects of the nanostructure become apparent. The strong confinement regime, this type of the confinement occurs in very small nanostructures where both carrier's Bohr radius are smaller than the critical dimension of the material. As a result, the optical and electrical properties of such nanostructure are dominated by confinement effects.

2.3 Length scales in metals

As the length scale in metals is analogous, so it is more complicated to describe it compared to semiconductors. This is because most metal nanostructures exhibit bulk-like properties even at very small sizes, critical dimension is about 2nm. In addition, most of their optical properties can be described as classical bulk models. So, instead of focusing on one type of length scales, which is used for semiconductors, there are at least three different critical sizes to consider, depending on whether one is interested in size effects on the optical or electrical properties of metal nanoparticles. Figure 1 outlines them schematically.

Specifically, there is one length scale associated with carrier confinement, Fermi wavelength λ_F. It is identical to the electron de Broglie wavelength. It is shown in Figure 1. Increasing gradually to the larger sizes, resulting in another critical size, $d_{charging}$, related to the electrical properties of small metal nanostructures. Smaller than this size, the Coulomb charging energy of nanostructures becomes significant compared with kT. And the third length scale is again associated with the optical properties of metals and occurs when the nanostructures possess a size (d_{mean}) smaller than the mean free path of electrons within it[20]. This is the size below it metal's optical properties change due to variations of its dielectric constant.

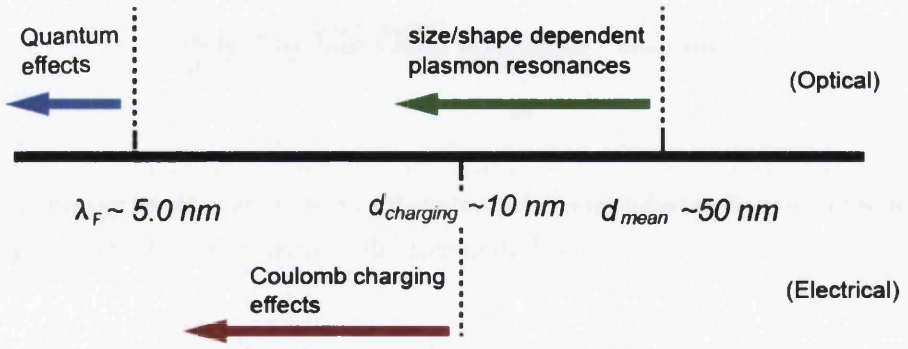

Figure 1. Illustration of the various critical length scales in metals

2.4 Solid-state

In solid-state theory, in terms of energy bands, there are three different kinds of solid, Insulators, Semiconductors and Conductors. When a solid is formed, the energy levels of the atoms broaden and form different energy bands with forbidden gaps between them. The electrons can only have a range of different energy values that exist within one of the bands, so there is no electron that has energy corresponding to values between the bands. Inner atomic levels have lower energy band, they are narrower and all full of electrons, and therefore, lower levels normally do not contribute to the electronic properties of the materials. In terms of crystalline structures, the outer or valence electrons are responsible of bonding crystal together and occupy where is called a valence band. In an insulator, the valence band is full of electrons, which are not able to move as they are relatively fixed in their positions due to strong chemical bonding between them. In other words, there are no delocalized electrons to conduct current, so the material shows insulating behavior. As shown in Figure 2, the conduction band is far above the valence band in energy, so it is not thermally accessible, and fundamentally remains empty, which means the thermal energy of the insulator at room temperature is not efficient to excite sufficient number of the excitons from valence band to conduction band.

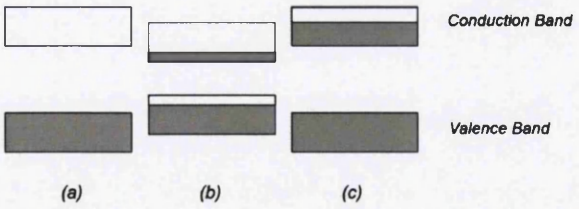

Figure 2: Energy bands of an insulator (a), an intrinsic semiconductor (b) and a conductor (c), the gray area indicates the presence of electrons in the bands.

In the case of semiconductors as shown in Figure 2, generally, the gap between the valence and conduction bands is less than for insulators, so the heat content of the materials at room temperature may be efficient to excite enough electrons from valence band to conduction band and as a consequence, make

the materials capable to carry current. As the density of this kind of excited electrons in conduction band is relatively low, so electrical conductivity does exist but it is small compared to a metal, hence the term "semiconductor" is used to explain their behavior. An intrinsic semiconductor, also called an undoped semiconductor or i-type semiconductor, is a pure semiconductor without any significant dopant species present. The number of charge carriers is therefore determined by the properties of the material itself instead of the amount of impurities. In intrinsic semiconductors the number of excited electrons and the number of holes are equal: n = p. Semiconductors can be doped with donor atoms or molecules, which are able to inject electrons to the conduction band and consequently enhance carrying electrons. In contrast, they may also be doped with acceptor atoms or molecules; in this case, acceptors obtain electrons from valence band and leave behind positive charges named holes, which can also carry current. As illustrated in Figure 3, the energy levels of such donors and acceptors lie in the E_g, the donor produces n-type, which means negative-charge or electron conductivity, and the acceptor makes p-type, that is positive-charge or hole conductivity.

For conductor materials, the valence band is full while the conduction band is partly full with sufficient delocalized electrons to efficiently carry current. The positively charged metal ions at a lattice sites have given up their electrons to the conduction band, and establish a background of positive charge for the delocalized electrons. The energy band for conductors is illustrated in Figure 2(c).

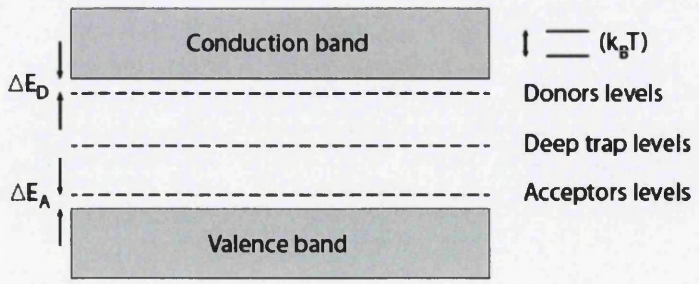

Figure 3: Sketch of the forbidden energy gap showing acceptor levels the typical distance Δ_A above the top of the valence band, donor levels the typical distance Δ_D below the bottom of the conduction band, and deep trap levels nearer to the center of the gap. The value of the thermal energy k_BT is indicated on the right.

2.5 Semiconductor nanostructures

Semiconducting properties are found in both elements and compounds [18], some pure elements found in Group IV of the periodic table have semiconductivity properties; the most commercially important of these elements are silicon and germanium.

Compound semiconductors include Groups III-V binary compounds, such as GaN, GaAs and InAs, Group II-V Zn_3P_2, Cd_3As_2, Zn_3As_2, Zn_3Sb_2, Groups II-VI such as ZnS, ZnO, ZnSe, ZnTe, CdSe and CdTe, which are usually p-type, except ZnTe and ZnO which are n-type, Groups IV-VI such as PbSe, PbS, PbTe, SnS, SnS2 and SnTe, Group V-VI such as Bi_2Te_3 and between different elements of the group IV, e.g. SiC and SiGe. Other semiconductors include ternary compounds and oxides such as PbSnTe, SnO_2 and TiO_2 etc. and also a number of organic compounds such as polymeric organic semiconductors include poly(3-hexylthiophene), poly(p-phenylene vinylene), as well as polyacetylene and its derivatives. From these materials, different semiconductor nanostructures have been successfully synthesized via different techniques including quantum dots, 1D systems such as belts, rods, wires etc. and 2D such as sheets and thin films.

2.6 Si, Ge, GaAs

Silicon Germanium and gallium arsenide are the three most industrially relevant semiconductors so it is worth reviewing briefly their nanostructure applications and growth methods.

2.6.1 Si

Silicon (Si) is the second most abundant element in the universe by mass, making up 25.7% of the crust. Basically, it exists as a compound and its most common form is SiO_2 while as a pure element form in nature is rare. At room temperatures, it exists in two forms, amorphous (brown powder) and

crystalline silicon (shiny metallic or grayish colour). It is one of the most important elements in variety of high electronics.

Molecular electronics is currently one area being studied as a potential replacement to conventional electronics technology [21]. One aspect of molecular electronics is the fabrication of devices whose function is governed by single molecules. Though quite promising, single molecule devices present fundamental new challenges, thereby placing estimates of their mainstream applications around the middle of the 21st century (Figure 4). So one of the greatest potential applications of molecular nanotechnology is the integration of molecular electronic function, but at the present, one of the few possible techniques is through advanced silicon technology. One step in this process is the immobilizing and stabilizing of individual molecules at precise locations on silicon surfaces.

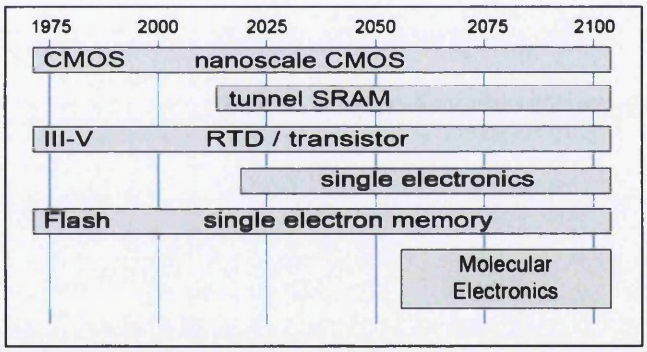

Figure 4. Timeline of anticipated eras for future electronic technologies. This figure is reproduced from the Proceedings of the IEEE [22]

Si has a great potential to make different nanoscale morphologies such as spherical, rods or sheets. G. Belomoin et al [23] reported a successful process to produce spherical silicon nanoparticles of the 1.0, 1.67, 2.15, 2.9 and 3.7 nm. M.R. Scriba et al. [24] reported producing silicon nanoparticles using the hot wire chemical vapour deposition (HWCVD) process. The material is a highly porous agglomeration of nanoparticles of primary size in the order of 40 nm, with a narrow size distribution. The nanoparticles produced are mostly amorphous, hydrogenated and have a partially oxidised surface, Figure 5.

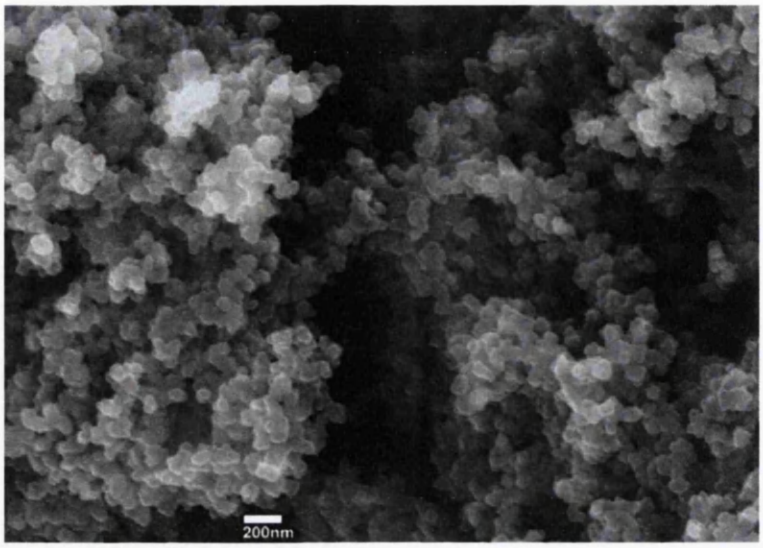

Figure 5 a-Si:H nanoparticles produced at 48 mbar and 40% H_2 dilution.

R. Ko¨rmer et al [25] processed nearly mono-dispersed silicon nanoparticles via pyrolysis of monosilane in a hot wall reactor is presented, Figure 6. Also more different morphology have been reported such as cubic Si nanoparticles [26], amorphous silicon oxide Nanowires [27], silicon nanowires [28], ultrathin silicon nanosheets [29], very thin single-crystal silicon nitride nanobelts [30].

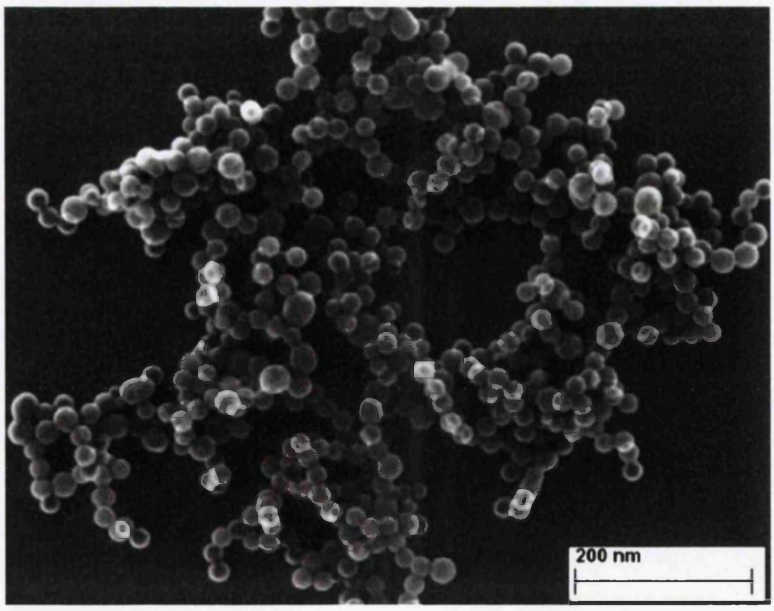

Figure 6 SEM picture of monodispersed SiNP from the production mode.

2.6.2 Ge

The history of the science and technology of the chemical element germanium is at the same time the story of the transition from the "Physics of Dirt" to the birth of modern semiconductor physics and the story of the beginning of solid state electronics. The demonstration of the germanium point contact transistor on Christmas Eve 1947 by J. Bardeen and W. Brattain followed shortly by the invention of the germanium junction transistor by W. Shockley represents the beginning of the "Semiconductor Age," the successor to the Stone, Bronze and Iron Ages. The possibility of quantum confinement causing the intense visible luminescence seen in porous Si, first mentioned by Canham [31], led to enormous interest in that material. The large blue-shift in the band gap and increase in luminescent efficiency attributed to quantum confinement in porous Si, while still controversial, continues to fuel research on colloidal Si nanoparticles prepared by sonicating porous Si [32], and by solution chemistry [33]. This interest continues, and has led naturally to an interest in colloidal Ge nanoparticles, since the elements are both indirect gap semiconductors, and the exciton of Ge has a larger Bohr radius [34]. Germanium has a great potential to make different nanostructures such as nanoporous thin film [35], Ge nanoparticles encapsulated in oxide layers [36], nanowires [37], or Ge nanoparticles doped with different elements such as Mn [38].

2.6.3 GaAs

Gallium Arsenide (GaAs) is a mixture of Gallium and Arsenic through a covalent bond. Gallium is very rare (rarer than gold) but arsenic is fairly common. GaAs is synthetic and is not a natural compound. It also has the potential to make nanostructures such as nanowires [39], quantum dots [40], quantum well structures [41]. GaAs substrate with different dopants was one of the first substrates have been used as the starting material to study the effect of doping on the growth and photoluminescence properties of β-Ga_2O_3 nanostructures [42]. GaAs nanowires also has been successfully used to fabricate a new type of hybrid

solar cell based on a heterojunction between the vertically aligned GaAs nanowires and poly(3,4-ethylenedioxythiophene): poly (styrenesulfonate) (PEDOT:PSS) with incorporating poly(3-hexylthiophene) (P3HT) electron blocking layer [43].

2.7 Zinc oxide (ZnO)

Over the last two decades zinc oxide has attracted a large amount of research as one of the most interesting compound metal oxide semiconductors of the II-VI semiconductor group due to its remarkable properties, including good transparency, high electron mobility, wide band gap, piezoelectric and strong room-temperature luminescence[44,45]. ZnO has a wide direct bandgap of 3.37 eV at room temperature and a large exciton binding energy (~60 meV) These properties make it capable to be an extraordinary candidate to be used in emerging many scientific and industrials applications such as optical waveguides, energy-saving or heat-protecting windows [46], piezoelectric transducers [47], acousto-optic media [48], nanoscale energy generator [49], electronics as thin-film transistors and light-emitting diodes [50,51]. It also has great potential applications in such as, resistive gas sensors [52], transparent conductive electrodes in liquid crystal displays and varistors [53]. Recently it has received more attention and recognized as a promising candidate for its potential in applications related to optoelectronic possibilities in the UV range [54,55]. Its piezoelectric properties could also allow developing surface acoustic wave (SAW) filters to be integrated in future analog circuits for portable electronic, which is challenging to achieve and there is a strong need for [56,57]. Furthermore, ZnO transparent thin-film transistors (TTFTs) are a recent and important development in the emerging field of transparent electronics. This great variety of the potential applications has boosted research related to the growth of high quality ZnO nanostructures and thin films through different techniques [58,59].

Fabricating nanoparticles with different structures and geometries has been extensively studied during last decades [60]. Among these nanoparticles, metal

compound semiconductors have attracted more attention due to their particular electrical, optical and physical properties and wide range of possible applications such as room temperature UV-laser [61,62], light emitting diode (LED) [63-65], photocatalyst [66], gas sensor [52,67,68], solar cell [69,70], piezoelectric device [71,72], and so on. Therefore, control of their shape and structure has been the key issue in the nanomaterials engineering field. ZnO is one of the most interesting metal compound semiconductors not only because its intrinsic properties but because it can exist in a variety of different shapes and morphologies such as nanorod [73], nanobelt [74], nanoplate [75], nanoring [76], nanohelix [77], multipod [78,79], hierarchical nanostructure [80], single-crystal tubular ZnO whiskers [81], mesoporous structured polyhedral drum and spherical cages and shells [82] and tower-like, flower-like and tube-like ZnO arrays [83] and more several different morphologies. In addition, interestingly, according to a series of experiments performed during past decades, ZnO is not toxic and showed biocompatible behavior. The study of the interaction of ZnO wires with horse blood serum shows that the ZnO wires can survive in the fluid for hours, after which they degrade into mineral ions. The biodegradability and biocompatibility of ZnO nanostructures could potentially allow their applications in in situ biosensing and biodetection [84]. A mixture of ZnO with 0.5% Fe_2O_3 is known as Calamine and is used in manufacturing Calamine lotions. Fine ZnO particles are used for packaging purposes due to their anti microbial and deodorizing qualities [85]. These properties along with its ability of neutralizing acids makes it ideal for use in antiseptic creams, healing creams etc. Due to its ability to absorb ultraviolet light, ZnO is also used in sunscreens and sunblocks to prevent sunburns. ZnO is also used in the making of cigarette filters as it helps in removing harmful substances like H_2S and HCN without affecting the flavor. They are also an important component of toothpastes and dental prosthetics [86]. Also a well-known mixture of ZnO powder and eugenol (zinc-oxide eugenol-based) has been used for more than century by dentists as a root canal sealer [87], antibacterial agent [88] and thermal and galvanic insulator for big amalgam fillings [89]. Therefore, along with variety of applications, it has also potential to be used in bionanotechnology purposes such as drug delivery, biosensors or

tissue engineering [90].

2D ZnO nanoparticles, nanosheets or thin films may have a great potential to use for very specific applications duo to having capability to cover a large area as well as having reasonably uniform nanoscale thickness which is reported about 10 to 50 nm [52,91,92]. Also One-dimensional nanostructures, such as nanowires and nanotubes, represent the smallest dimension for efficient transport of electrons and excitons and thus are ideal building blocks for hierarchical assembly of functional nanoscale electronic and photonic structures [93]. In addition, presence of either porosity or polycrystalline nanocrystal pattern could significantly increase the surface area to volume ratio, which is critically important at the nanoscale, in some cases such as gas sensors more surface area means more sensitivity and more faster response.

2.7.1 ZnO Crystal Structure

ZnO belongs to the group II-VI binary compound semiconductors, which like other members of this group, can crystallize in either cubic zinc blende or hexagonal Wurtzite lattice structure. In both structures each anion is surrounded by four cations, which are located at the corners of an imaginary tetrahedron, Figure 7. Ionic crystals that consist of alternating layers of oppositely charged ions, stacked parallel to the polar surfaces, producing an accumulating normal dipole moment, resulting in divergence in surface energy. The stability of the polar surfaces is one of the most interesting topics of modern surface science [100]. Crystals with polar surfaces generally have facets or exhibit massive surface reconstructions to compensate the electrostatic charge on the surface, but ZnO ±(0001) is an exception, which is stable and without reconstruction [101–103]. Structurally, the Wurtzite structured ZnO crystal is described schematically as a number of alternating planes composed of fourfold tetrahedral-coordinated O^{2-} and Zn^{2+} ions, stacked alternatively along the c axis. The oppositely charged ions produce positively charged (0001)-Zn and negatively charged (000$\bar{1}$)-O polar surfaces. Extensive theoretical and experimental studies have been carried out very recently to investigate the

superior stability of the ZnO ±(0001) polar surfaces, and several mechanisms have been proposed: the decrease of the surface Zn concentration on (0001)-Zn [104]; an electronic mechanism involving the transfer of charge from oxygen to Zn [105]; and surface adsorbed atoms [106].

Although the structures shared by ZnO are zinc blende, rocksalt (or Rochelle salt), and Wurtzite, under ambient conditions, the thermodynamically stable phase is that of Wurtzite symmetry. In contrast, the zinc blende ZnO lattice can only be stabilized when it grows on cubic substrates such as GaAs [107], while the Rochelle salt (NaCl) structure may be produced at relatively high pressure, as it is known for GaN [108].

Ionic crystals that consist of alternating layers of oppositely charged ions, stacked parallel to the polar surfaces; produce an accumulating normal dipole moment, resulting in divergence in surface energy. The stability of the polar surfaces is one of the most interesting topics of modern surface science [100]. Crystals with polar surfaces generally have facets or exhibit massive surface reconstructions to compensate for the electrostatic charge on the surface, but ZnO ±(0001) is an exception, which is stable and without reconstruction [101-103]. Structurally, the Wurtzite structured ZnO crystal is described schematically as a number of alternating planes composed of fourfold tetrahedral-coordinated O^{2-} and Zn^{2+} ions, stacked alternatively along the c axis. The oppositely charged ions produce positively charged (0001)-Zn and negatively charged (000$\bar{1}$)-O polar surfaces. Extensive theoretical and experimental studies have been carried out very recently to investigate the superior stability of the ZnO ±(0001) polar surfaces, and several mechanisms have been proposed: the decrease of the surface Zn concentration on (0001)-Zn [104]; an electronic mechanism involving the transfer of charge from oxygen to Zn [105]; and surface adsorbed atoms [106].

Like other II–VI semiconductors, Wurtzite ZnO can be transformed to the rocksalt (NaCl) structure at relatively modest external hydrostatic pressures. The reason for this is that the reduction of the lattice dimensions causes the interionic Coulomb interaction to favor the ionicity more over the covalent nature. In ZnO, the pressure-induced phase transition from the Wurtzite to the rocksalt phase occurs in the range of 10 GPa associated with a large decrease in

volume of about 17% [109,110]. High-pressure cubic phase has been found to be metastable for long periods of time even at ambient pressure and above 100°C [111]. Energy-dispersive X-ray diffraction (EDXD) measurements using synchrotron radiation have shown that the hexagonal Wurtzite structure of ZnO undergoes a structural phase transformation with a transition pressure pT 1/4 10 GPa and completed at about 15 GPa [76,112].

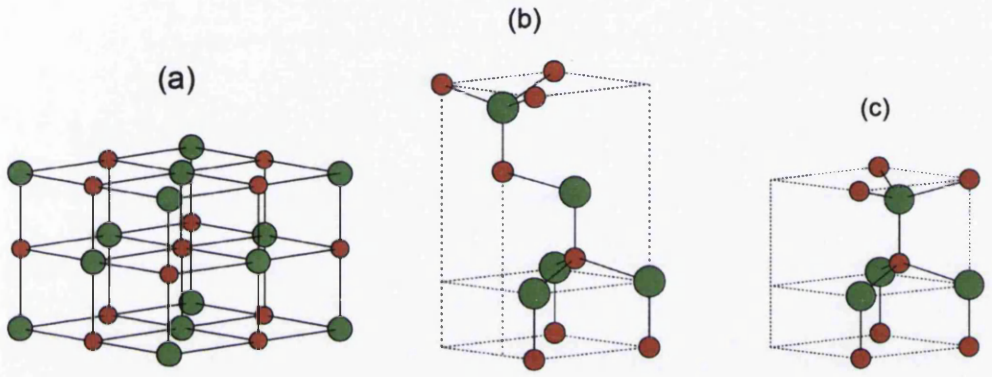

Figure 7. The structures shared by ZnO are zinc blende (a), hexagonal Wurtzite (b) and rocksalt (or Rochelle salt)(c)

2.7.2 Lattice Parameter

Due to importance of ZnO properties, its lattice parameters have broadly been investigated over many decades [113-122]. In a semiconductor, lattice parameters usually depend on the following factors:

- Concentration of foreign atoms and defects and the difference between their ionic radii and the substituted matrix ion.
- Free electron concentration acting via deformation potential of a conduction band minimum occupied by these electrons.
- External strains (e.g., those induced by substrate).
- Temperature.

The lattice parameters of any crystalline material are commonly and most accurately measured by high-resolution X-ray diffraction (HRXRD) using the Bond method [123] a set of symmetrical and asymmetrical reactions. Table 1 shows measured lattice parameters, 'c/a' ratio, and 'u' parameter reported using XRD for ZnO crystallized in Wurtzite. The lattice constants are a = ~ 3.25 A°) and c = ~ 5.2 A°); their ratio c/a ~1.60 is close to the ideal value for hexagonal cell c/a = 1.633 [124].

Wurtzite			
a (A°)	c (A°)	c/a	u
3.2496	5.2042	1.6018	0.3819

Table 1. The lattice parameters of Wurtzite ZnO crystal measured by XRD

The data in Table 1 are also consistent with the values obtained by data processing in earlier investigations, reviewed by Reeber [117], which shows the 'c/a' ratio and 'u' parameter in a slightly wider range. They range from 1.593 to 1.6035 and 0.383 to 0.3856 respectively. This difference in an ideal Wurtzite zinc oxide crystal is probably due to lattice ionicity and stability. It has been reported that free charge is the dominant factor responsible for expanding the lattice proportional to the deformation potential of the conduction band minimum and inversely proportional to the carrier density and bulk modulus. The point defects such as zinc antisites, oxygen vacancies, and extended defects, such as threading dislocations, also increase the lattice constant, albeit to a lesser extent in the heteroepitaxial layers [125].

3 LITERATURE REVIEW

3.1 ZnO Nanostructures Growth Techniques

Structurally, ZnO has potential to grow in three different directions (Figure 8):

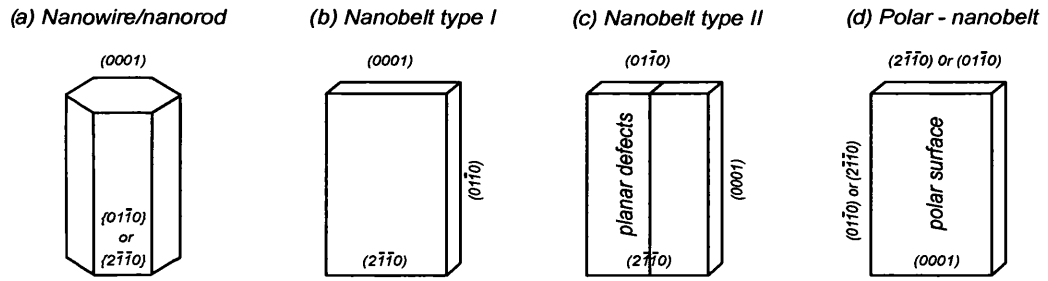

Figure 8. Typical growth morphologies of one-dimensional ZnO nanostructures and the corresponding facets

Therefore, in terms of ZnO nanocrystal growth, it is of critical importance to consider that the relative surface activity of different growth facets under specified conditions. It is one of the most vital factors to control the shape of the as-synthesized ZnO crystals. Simultaneously, ZnO may have polar surfaces due to atomic terminations. This phenomenon may enhance ZnO capability to exhibit a wide range of novel structures, which are tunable by controlling the growth rates along these directions.

Growth of crystal ranges from small inexpensive techniques to the complex and sophisticated expensive procedures, and also crystallization time ranges from few minutes to, in some cases, months. Crystals may be synthesized by the transport of crystal constituents in the solid, liquid or vapour phase. On the basis of this, crystal growth can be classified into three main categories, shown in Table 2.

Technique	Description
Solid Growth	Solid-to-Solid phase transformation
Liquid Growth	Liquid to Solid phase transformation
Vapour Growth	Vapour to Solid phase transformation

Table 2. Three main categories of the crystal growth

Based on the phase transformation process, crystal growth techniques are classified as solid growth, vapour growth, melt growth and solution growth [126]. It is obvious that finding new techniques through which nanostructures can be grown faster, easier, as uniform as possible and with high yield is of importance, however, these techniques must be reproducible due to size-dependant properties of nanoparticles. So an efficient process is the one that produces crystals adequately for their use at minimum cost. Choosing the best method to grow a given material depends on material characteristics. Over the last decades, various methods have been extensively studied to produce ZnO nanostructures such as vapour transport process or physical vapour deposition (PVD) [127-129]. Metal-organic chemical vapour deposition (MOCVD) [130], different hydrothermal synthesis techniques [131,132], electrochemical deposition [133,134], and microwave plasma deposition [135] have also been employed. In this chapter, the most common techniques used to grow ZnO nanostructures are briefly described, then the methods used to specifically produce 1D and 2D ZnO nanostructures are reviewed in more details.

3.1.1 Physical vapour deposition (PVD) or vapour transport process (VTP)

PVD is a vapourization transferring procedure through which materials are transferred on an atomic level. It can be used in a tube furnace at high temperature to grow nanostructures but it also can be employed as an alternative process to electroplating such as sputter coating and pulsed laser deposition (PLD) coating. In PVD process, the raw materials or precursors that are going to be deposited start out in solid form. Figure 9 shows a typical tube furnace system. This process is carried out under controlled atmosphere and pressure and involves four steps: evapouration, transportation, reaction and deposition. During the evapouration phase for crystal growth, high temperature is generated (about 1000°C or even higher, depending on experiment needs) by the furnace, resulting in evapouration of the source materials. In the transport step, vapourized materials are transferred toward the target (substrate). This is

carried out via controlled flow of a gas or a mixture of different gases (as needed), which are run through the tube within the furnace in only one direction. In case of metal oxide crystals such as ZnO, the source consists of metallic Zn or powder ZnO and these atoms then react with the appropriate gas during the transport phase. For the above example, the reactive gases may be oxygen, and the carrier gas nitrogen or Argon. The deposition step is when the source material, whether reacted or not reacted in the transportation step, takes part in crystal synthesis and builds up a particular crystalline structure depending on crystallographic properties of the source on the substrate surface.

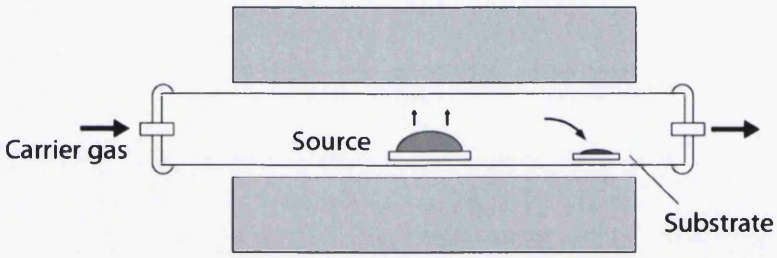

Figure 9. Furnace setup for synthesis of ZnO nanoneedles via PVD

Like any other techniques PVD has some advantages and disadvantages. Some advantages are materials can be deposited with improved properties compared to the source materials. Also almost all inorganic materials can be used as well as some types of organic materials. For coatings, as very small amount of materials is used and there is no aqueous media and chemical, the process is more environmentally friendly than processes such as electroplating. While disadvantages of the PVD Process for crystal synthesis are, firstly and most importantly, PVD is performed at high temperature and vacuum condition. Also transportation system is via a flow of a gas, so as-synthesized crystals are critically dependent on these conditions. As a result it is not easily repeatable. Secondly, in case of coating is a line of sight technique meaning that it is extremely difficult to coat undercuts and similar surface features. Finally, High capital cost is another disadvantage and also some processes are requiring skilled operators. Furthermore, the rate of crystal synthesis and coating deposition is usually quite slow.

Although all these techniques have been successfully performed, despite the disadvantages, PVD route remains a widely accepted technique for the production of wide range of different morphologies of ZnO nanostructures such as nanowires [127], nanobelts [128], nanohelixes and nanorings [11] (Figure 10), more samples are shown in Figure 13.

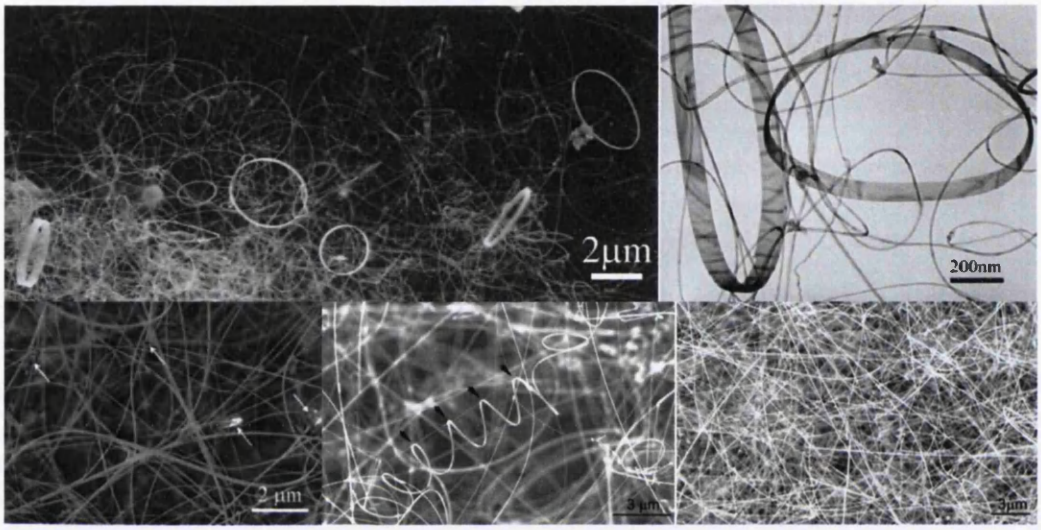

Figure 10. SEM images of different ZnO nanostructures nanobelts, nanorings, nanowires and nanohelix fabricated by PVD.

PVD can be performed either via a direct condensation of the vapours to nanostructures by a catalyst free vapour–solid growth (VS) mechanism [76] or a catalyst assisted vapour–liquid–solid (VLS) growth mechanism [136]. A. George et al. performed an experiment using a vapour–liquid–solid (VLS) mechanism driven process (Figure 9) where the formation of a eutectic alloy droplet occurred at each catalyst site and crystals grow at the liquid-solid interface by precipitation of supersaturated ZnO. They showed that, different sizes of the catalytic nanoparticle could control the structure and the diameter of as-grown nanoneedles. In addition, the results revealed that the location and alignment control can be achievable using patterning techniques and optimal epitaxial lattice matched substrates [137], Figure 11.

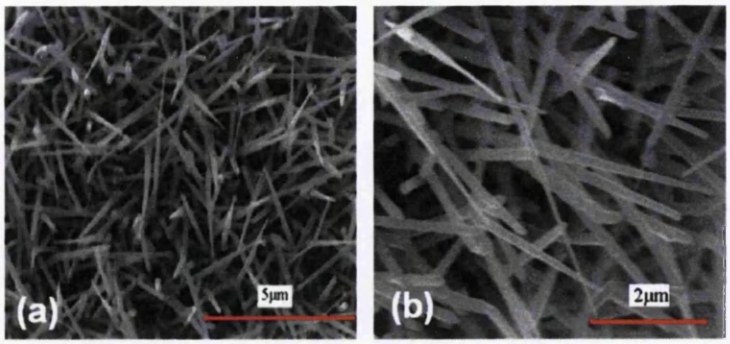

Figure 11. SEM images (a-c) of the ZnO nanoneedles grown on Au(10nm) film deposited on Si(100) substrate at 980°C. (c) HRTEM image of lattice fringes of ZnO nanoneedles. The interplanar distance is 0.25 nm showing the growth direction ⟨0 1 1 0⟩.

Also Z. Zhang et al. designed an experiment in which the effect of catalysts on ZnO nanowire growth was investigated by comparing the performances of Au, Pt, and Ag nanoparticles. Additional control of growth was achieved by implementing a substrate temperature of either 800 °C with a ZnO/graphite powder source or 500 °C with a Zn powder source. Results showed that at 800 °C, the vapour- liquid-solid mechanism plays a very important role when the Au and Pt nanoparticles are in the liquid phase. On the other hand, nanowires can also be grown on solid nanoparticles, that is, oxidized Ag at 800 °C and nanoscale cracks, that is, Pt at 500 °C, where, the vapour-solid is the only possible mechanism. At 500 °C, the vapour-liquid mechanism still dominates even though Au and Ag appear to be liquid, which is a result of high Zn vapour pressure [76].

In an experiment designed by L. Wang et al. in which well-aligned ZnO nanowires were synthesized through simple physical vapour deposition. They used *c*-oriented ZnO thin films as substrates without catalysts or additives. Results revealed that the synthesized ZnO nanowires had two typical average diameters: 60 nm in majority and 120 nm in minority. They are about 4 μm in length and well aligned along the normal direction of the substrate. Most of the synthesized ZnO nanowires were single crystalline in a hexagonal structure and were grown along the [001] direction. The *c*-oriented ZnO thin films control the growth direction, Figure 12.

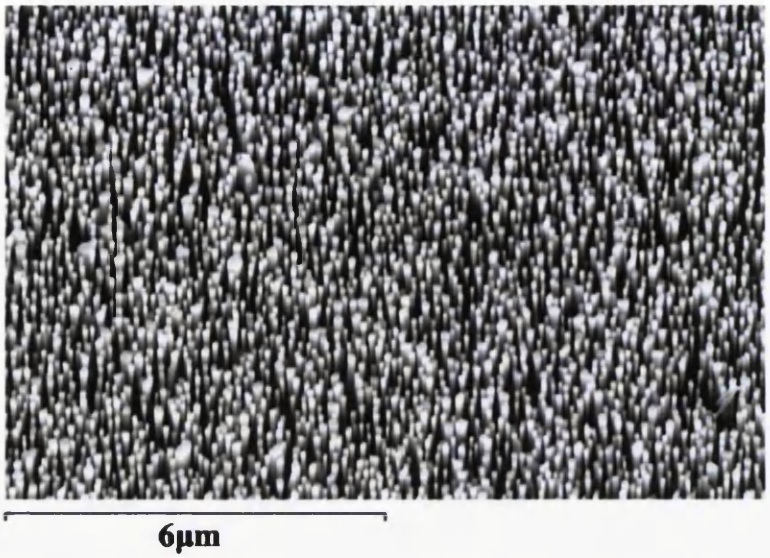

Figure 12. Low magnification SEM image of the typical morphologies of ZnO nanowires

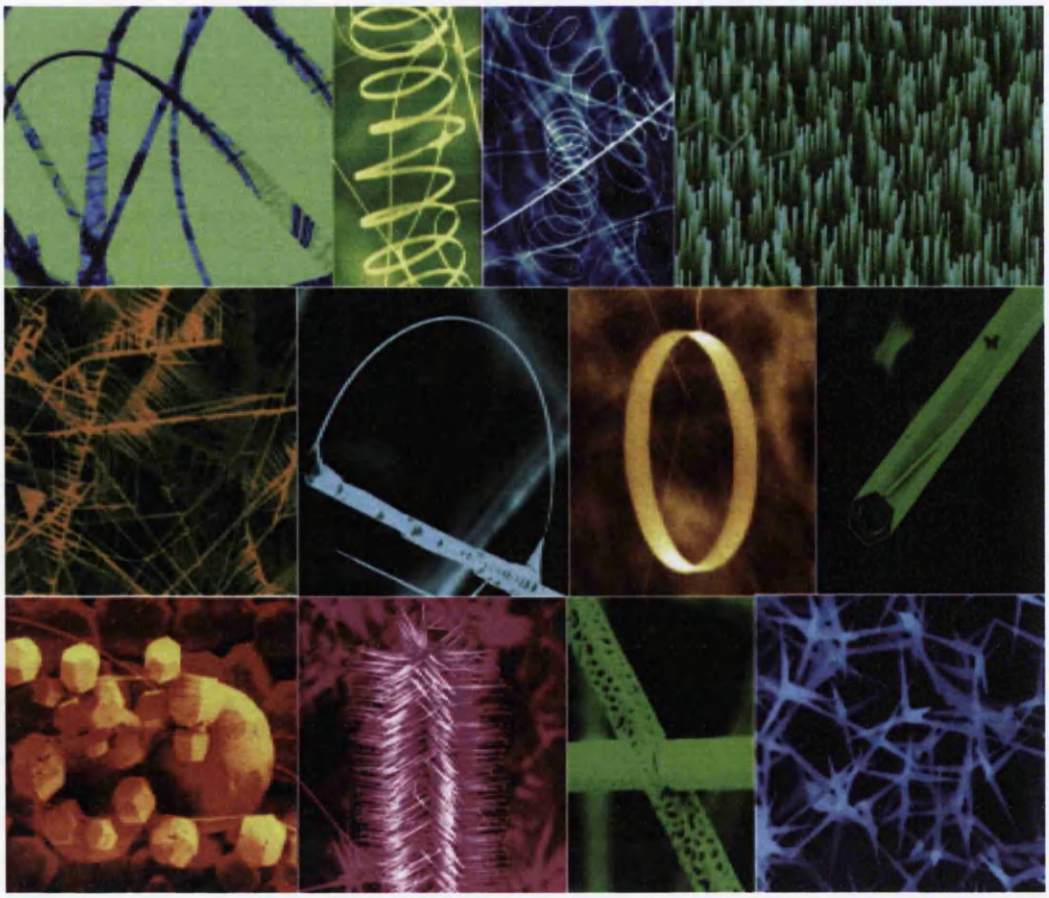

Figure 13. A collection of nanostructures of ZnO synthesized under controlled conditions by thermal evapouration of solid powders. Most of the structures presented can be produced with 100% purity [11].

Electrochemical methods depend on the synthesis of positively charged metallic ions in aqueous solutions, which are attracted towards the negatively biased electrode. Electrons reduce the metallic ions at cathode to their native metal state on an Au (111) coated Si substrate. Electrochemical methods in an aqueous medium have some advantages for ZnO nanostructures production such as high yield, low cost and easy fabrication with significant controls of the morphology and composition. In addition, it is a highly reproducible technique at remarkably lower temperatures compared to the PVD technique. However, as-synthesized ZnO nanocrystals in aqueous media may suffer from poor crystallinity and polydispersity. Electrochemical methods are also possible in non-aqueous medium. Generally, the nanostructures synthesized under non-aqueous conditions at slightly higher temperatures show much better crystal quality and monodispersity [137-140]. Choosing is the right deposition technique strongly depends on the application as well as the substrate requirements. Obviously, the PVD method can be chosen where the substrate can resist high temperatures in excess of 1000°C, while electrochemical deposition can be applied to grow and deposit a variety of different nanostructures at far lower temperatures.

Y. L. Wang et al [141] reported on the synthesis of ZnO nanowires via templated electrochemical deposition (TECD). The deposition was performed in a classical three electrodes electrochemical cell and the samples were mounted as a working electrode. A polycarbonate membrane with random distribution of nanometric pores was used as the working electrode (M90) Figures 14, 15.

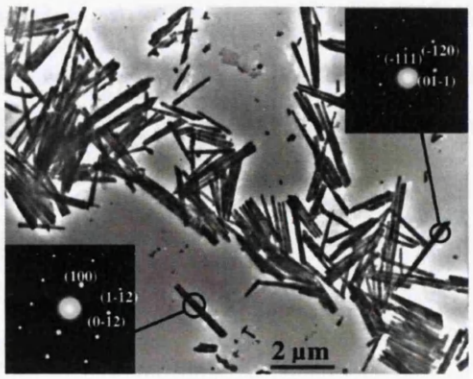

Figure 14. TEM images showing a general morphology of the electrodeposited ZnO nanowires from M90 type membranes.

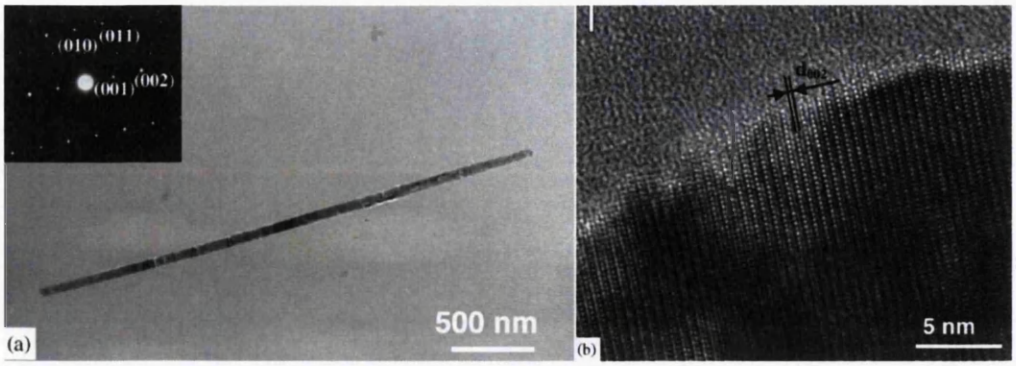

Figure 15. Both TEM observation (a) and HRTEM image (b) showing a M30 type individual nanowire with near [1 0 0] growth direction.

3.1.2 Chemical vapour deposition

CVD is a general name for a group of processes, which involve depositing a solid material from a gaseous phase and is similar in some respects to PVD, but the raw materials or precursors in CVD are introduced to the reaction chamber in the gaseous state. CVD process covers different methods such as atmospheric pressure chemical vapour deposition (APCVD), low-pressure chemical vapour deposition (LPCVD), chemical beam epitaxy (CBE), laser chemical vapour deposition (LCVD), metal-organic chemical vapour deposition (MOCVD), plasma-assisted chemical vapour deposition (PACVD) or plasma-enhanced chemical vapour deposition (PECVD), chemical vapour infiltration (CVI) and photochemical vapour deposition (PCVD). As CVD includes chemical reactions there is a need for an external energy source to provide the energy or heat, which is required to get the precursors to react or decompose. There are several suitable sources of heat for CVD processes including resistive heating such as tube furnaces, radiant heating such as halogen lamps, radio frequency heating (induction heating) and lasers. This variety of techniques and energy sources provides a great potential in different applications across a wide range of industries including coatings for wear resistance, high temperature protection, corrosion resistance, erosion protection and combinations thereof. It can also be employed to fabricate semiconductors and related devices such as integrated circuits, sensors or even optoelectronic devices and optical fibers for telecommunications and MEMS and NEMS.

Z. Zhang et al in 2012 demonstrated high-density heteroepitaxial growth of sub-10 nm diameter gallium phosphide (GaP) nanowire (NW) arrays on silicon (Si), using chemical beam epitaxy (CBE) as shown in Figure 16. The vertical alignment of GaP NW arrays was achieved by an initial phase transition from zinc blende (ZB) to Wurtzite (WZ). Based on the analysis of the crystal structures at the base of the GaP NW and the metal catalyst tip, they concluded that, in the sub-10 nm diameter range, the growth direction of the initial ZB phase depends on the non-equilibrium multilayer ledge-flow mechanism, and WZ formation is favored by high Ga supersaturation. The combination of small radius and high supersaturation leads to formation of the relatively large nucleus of the ZB phase. Optical characterization revealed that a band-to-band recombination occurred with energy similar to the indirect band gap energy of bulk GaP with a short lifetime around 100 ps. This technique might be extended to other functionalized III–V materials integrated on Si nanostructures, and may play an important role in photoelectronic device design and the corresponding fabrication. A calculation of the WZ band gap predicts a direct band gap slightly smaller than the direct band gap of ZB. The character changes from indirect for ZB to direct for WZ [142].

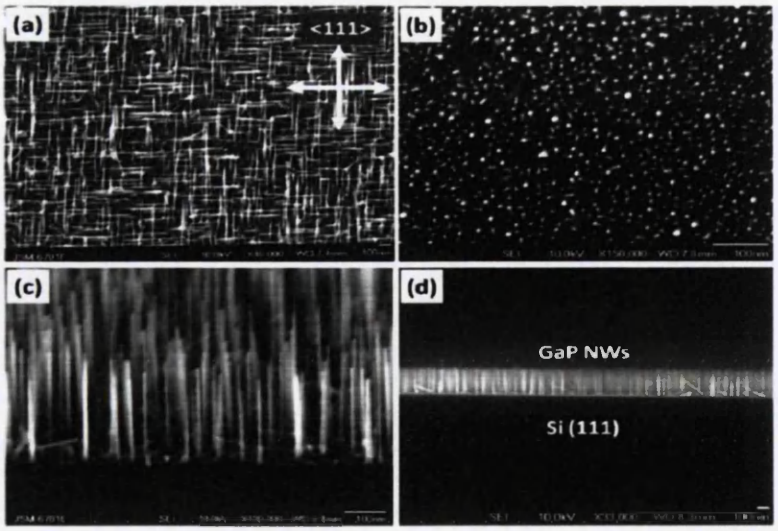

Figure 16. (a) Top-view SEM image of GaP NW arrays grown on Si(100), where the GaP NWs are mostly ,111. oriented. (b) Top-view SEM image of GaP NW arrays vertically grown on Si(111). (c) 10u Tilted side-view and (d) side-view SEM image of GaP NW arrays on Si(111), with the [112^{-}] viewing direction perpendicular to the cleaving surface, the diameter of the GaP NWs is in the sub-10 nm range with a homogeneous length.

J. Hui et al [143] reported a High-density ZnO nanowire arrays with low defect concentrations, which were directly grown on transparent conducting oxide glass substrates under catalyst-free and low temperature conditions by CVD. Their experiments revealed that correct levels of supersaturation and evapouration temperature are beneficial to the growth of ZnO nanowires, Figure 17.

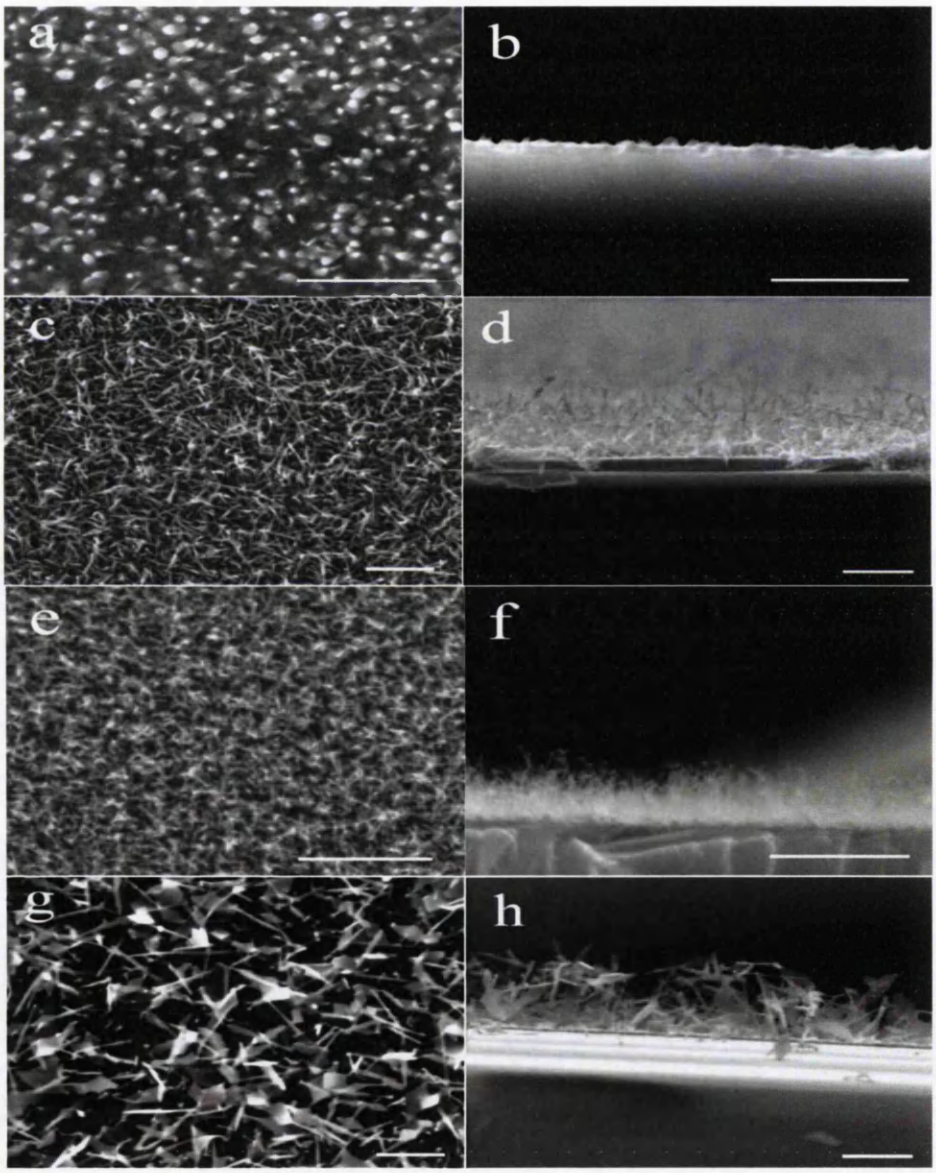

Figure 17. Top and cross-section SEM images of ZnO nanostructures grown at different evapouration temperatures: (a and b) 400 °C, (c and d) 450 °C, (e and f) 500°C and (g and h) 550°C. The scale bar is 2lm.

H. Kou et al. performed an experiment in which ZnO nanoparticles have been synthesized on a silver-modified carbon nanotube/polyimide (Ag-CNT/PI) membrane by electrochemical deposition. The flower-like ZnO nanoparticles was formed by the aggregation of nanosheets, Figure 18. The results demonstrated that the photoelectric activity and photocatalytic performance of ZnO were improved by the deposition [144].

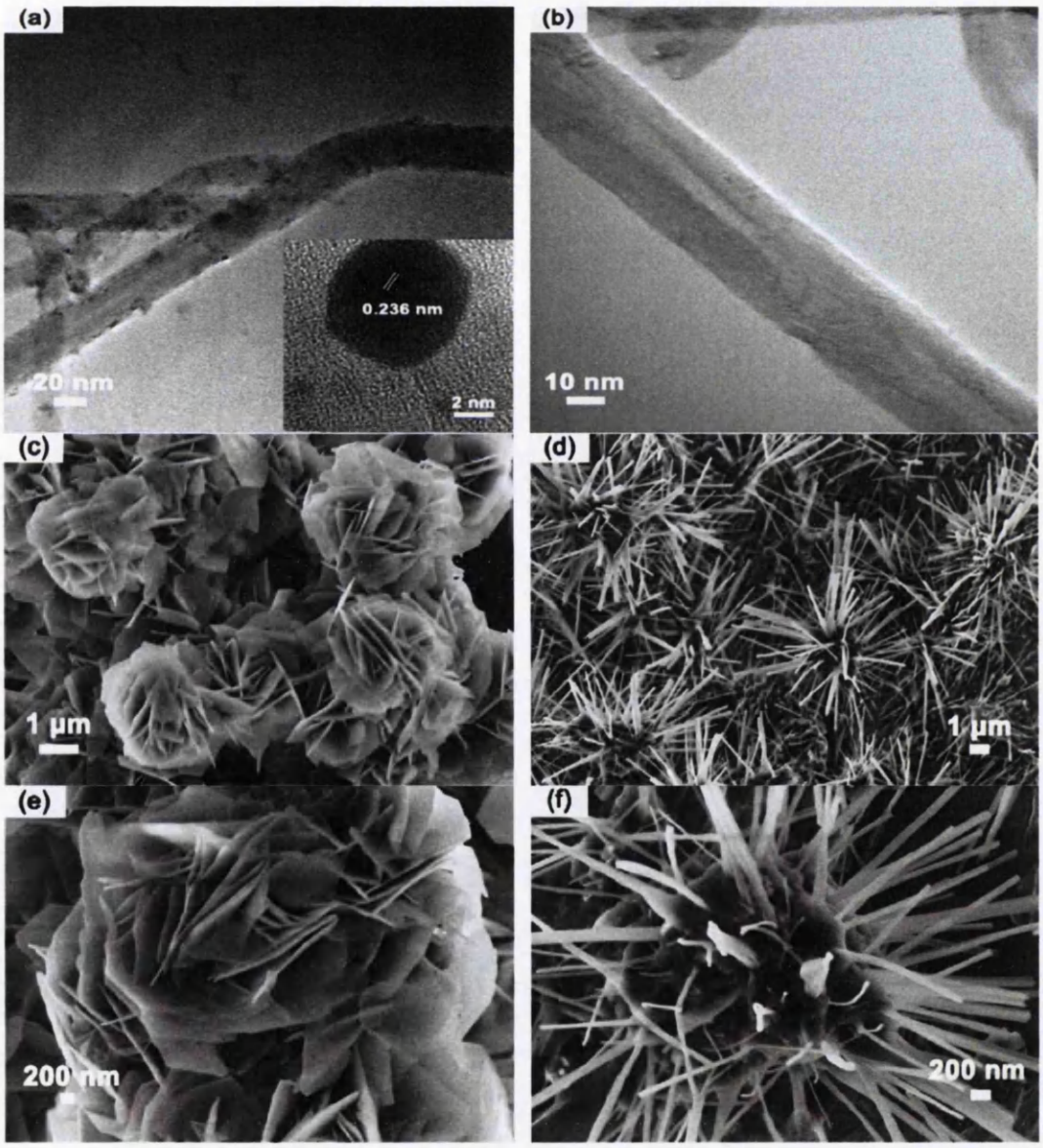

Figure 18. TEM images of (a) Ag-CNT and (b) CNT. Inset of (a) is the HRTEM of Ag. (e) and (f) are the high magnification images of (c) and (4) respectively.

3.1.3 Hydrothermal Techniques

In the last two decades, hydrothermal methods have been very popular, garnering interest from scientists and technologists of different disciplines. However, the term ***hydrothermal*** is purely of geological origin. A British geologist, Sir Roderick Murchison (1792–1871) used this term for the first time to describe the action of water at elevated temperature and pressure in bringing about changes in the earth's crust leading to the formation of various rocks and minerals [145]. The first successful commercial application of hydrothermal technology began with mineral extraction or ore beneficiation in the previous century. The use of sodium hydroxide to leach bauxite was invented in 1892 by Karl Josef Bayer (1871–1908) as a process for obtaining pure aluminum hydroxide which can be converted to pure Al_2O_3 suitable for processing to metal [146]. Hydrothermal techniques have been extensively investigated to synthesize a variety of nanocrystals. Hydrothermal methods for the growth of nanoparticles can be divided into water bath deposition, autoclave growth, and microwave assisted growth.

Hydrothermal techniques have been employed by numerous groups to synthesise many different ZnO nanostructures using a wide range of parameters. Table 3 shows a few examples from the literature of the kind of techniques employed and the resulting nanostructures. It is in by means complete but it gives an idea of the immense range of methods and structures investigated. In this chapter the main hydrothermal techniques are presented.

Table 3. reported morphologies for ZnO nano and submicron structures synthesized through various techniques using different precursor solutions at different temperature.

Synthesis route	Precursor chemicals	Synthesis temperature ° C	Product morphology	Description	Ref.
Hydrothermal	Zinc acetate dihydrate and Urea	90-180	2D petal-like ZnO nanoparticles	Ethylene glycol used as an organic capping reagent	[147]
Hydrothermal	Zinc nitrate hexahydrate, Sodium hydroxide and ethylenediamine	180	Nanorods	Mixture of deionized water or pure alcohol as the solvent	[148]
Hydrothermal	Zinc nitrate hexahydrate	70	Tubular ZnO	TiO2 films on Silicon wafer was	[149]

	and Hexamethylenetetramine			prepared by dip-coating technique	
Hydrothermal	Zinc nitrate hexahydrate and Hexamethylenetetramine	90	Nanorod and nanotube	1D ZnO nanostructures were grown on Si wafer using pulse laser deposition	150
Hydrothermal	Zinc nitrate hexahydrate and Hexamethylenetetramine	92	Nanowire and nanosphere	ZnO seed layer on the FTO glass was formed by thermal decomposition zinc acetate at 350°C	151
Hydrothermal	Zinc acetate dihydrate and Sodium hydroxide	20-65	Bunch-shaped ZnO Nanowires	Seed layer of ZnO on FTO substrate using spin-coating	152
Hydrothermal	Zinc nitrate hexahydrate and Hexamethylenetetramine	100	Nanorods	ZnO seed layer was deposited by RF-reactive magnetron sputtering at 100°C	153
Hydrothermal	Zinc nitrate hexahydrate and Hexamethylenetetramine	90	Vertically aligned nanorod arrays	ZnO seed layer was deposited on Si (100) substrates using diethylzinc as precursor by atomic layer deposition	154
Hydrothermal	Zinc nitrate hexahydrate and Hexamethylenetetramine	90	Vertically well-aligned ZnO nanorods	Seed ZnO layer was directly grown on Au electrode of quartz crystal microbalance via wet chemical route	155
Sonochemical assisted Hydrothermal	Zinc nitrate hexahydrate and Hexamethylenetetramine	85	Pin-cushion cactus, nanopencil and hexagonal nanodisc	Zinc foil as substrate	156
Hydrothermal	Zinc acetate dihydrate	130-150	Nanobullets and nanoflakes	Mixture of water/ethylene glycol as the solvent	157
Chemical bath deposition	Zinc nitrate hexahydrate and Hexamethylenetetramine	95	Well-defined branched ZnO nanorods	Zinc substrate was used for deposition	158
Chemical bath deposition	Zinc acetate dihydrate, ammonia and triethanolamine	80	Nanorods and nanospines	ZnO seed layer was deposited by SILAR using aqueous zinc-ammonia complex as cation precursor and deionized water kept at 85°C as anionic precursor	159
Chemical bath deposition	Zinc nitrate hexahydrate, aqueous ammonia and hydrogen peroxide	75	Vertically aligned ZnO nanorods	The crystallite orientation was controlled by varying content H_2O_2 in the bath solution	160
Chemical bath deposition	Zinc sulphate, Urea and H_2SO_4	80	Mesoporous ZnO	Direct band gap with energy 3.24 eV	161
Chemical bath deposition	Zinc nitrate hexahydrate and aqueous ammonia	30-90	2D flakes and 1D rods	Deposition on glass substrates and annealed at 400°C for 2h	162
Wet chemical route	Metallic zinc powder and Sodium hydroxide	200	Urchin-like multidimensional ZnO nanowhisker	ZnO nanowhisker clusters formed on Zn microspheres via oxidize metallic Zn powder in concentrated NaOH solution	163
Chemical solution route	Zinc nitrate hexahydrate, PVA and diethylenetriamine	95	Dendrite-like ZnO nanostructures	Synthesis of ZnO seed by drop casting at 60°C	164
Wet chemical	Zinc nitrate hexahydrate and aqueous ammonia	120	Nanorods	Zinc foil used as substrates	165
Soft chemical deposition route	Zinc sulphate and Sodium hydroxide	Room temperature	Interconnected flakes	Deposition time was 30-120 h and annealed at 400°C	166
Simple chemical solution route	Zinc nitrate hexahydrate and Sodium hydroxide	50	Flower-like ZnO nanostructures	The flower-like ZnO nanostructures were directly coated on the outer surface of an alumina tube	167
Chemical etching using 0.1 M alkaline solution (KOH)	Zinc nitrate hexahydrate and Hexamethylenetetramine	85	Nanotubes	Electrodeposited ZnO seed layer at 95°C	168
Simple aqueous	Zinc chloride and Sodium	85	Needle and flower-like	Anionic surfactant sodium	169

solution route	hydroxide		ZnO microstructures	dodecyl sulfate was used	
Simple solution route (powder form)	Zinc Chloride and Sodium hydroxide	85	Rod, needle, rugby and flower-like ZnO	Anionic surfactant sodium dodecyl sulfate was used	[170]
Electrodepositio n	Zinc nitrate hexahydrate and Potassium Chloride	70	Nanospikes and nanopillars	ITO coated glass substrates	[171]
Electrochemical deposition	Zinc chloride and Potassium Chloride	85	Vertically oriented ZnO nanowires	ITO coated glass substrates	[172]
Plasma assisted reactive pulsed laser deposition	A metallic zinc target (99.999% in purity)	80	c-axis oriented nanocrystals	Polished n-type single crystalline Si (100) wafer	[173]
DC plasma reactor	Pure Zn powder	-	Tetrapod-like ZnO nanopowder	Screen-printing of ZnO film by mixing tetrapod-like ZnO powder, Ethyl cellulose and terpineol	[174]
Reactive RF sputtering	High-purity Zn metal	Room temperature	Nanostructure grains	n-type Si with a coated thin layer of silicon dioxide of about 1 μm thickness	[175]
Sol-gel route	Zinc acetate dihydrate and Oleic acid	40°C under ultrasonic stirring	Hexagonal faceted ZnO quantum dots	Lithium hydroxide ethanolic solution with addition of ethyl acetate or heptane	[172]
Pyrolysis	Zinc (II) oleate, oleic acid and n-octadecene solvent	317	2D ZnO nanopellets	Zinc (II) oleate precursor was prepared by ion exchange reaction between Zn chloride hexahydrate and potassium oleate	[176]
Chemical route	Zinc nitrate hexahydrate, hexamethylenetetramine, sodium hydroxide and absolute ethanol	85	Hexagonal and spherical shaped zincoxide nanostructures	Morphology could be controlled by changing the concentration of the chemicals	[177]
Facile solution method under mild conditions (Refluxing)	Zinc acetate dihydrate and hexamethylenetetramine	90	Dumbbell-like ZnO microstructures	The paste of dumbbell-like ZnO microcrystals was coated on a ceramic tube	[178]
Ultrasonic spray pyrolysis technique	Zinc acetate dihydrate	300	Islands wit different sizes	Microscope glass substrate	[44]

3.1.3.1 Water Bath Hydrothermal Technique

In this technique, a resistive heater is used as the energy source to raise the water temperature. The time and temperature are adjustable and the water bath can keep conditions constant for long period of time; in terms of growing nanocrystals, this ability is of critical importance. Accuracy, reliability and simplicity of this technique have made it one of the most attracting approaches to hydrothermally synthesis of nanostructures. All reactions proceed in beakers, which are floated in the water bath. So the water bath provides an exact reaction temperature for a needed time. Figure 19 shows a typical dual water bath with adjustable temperature and time.

Figure 19 . Water bath model GRANT 98°C MAX, with adjustable temperature and time

3.1.3.2 Autoclave technique

In this hydrothermal technique, conditions of high pressure as well as high temperature are employed. For instance, this synthesis method may use for materials such as calcite and quartz, which are well known to be insoluble in water but at high temperature and high pressure, these substances are soluble. Temperatures are typically in the range of 400° C to 600° C and the employed pressure compared to other hydrothermal techniques is significantly larger and ranges from hundreds to thousands of atmospheres. Growth is usually carried out in steel autoclaves with gold or silver linings. Depending on the applied pressure, they are grouped into low, medium and high-pressure autoclaves. The concentration gradient required to produce growth is provided by a temperature difference between the nutrient and growth areas. For the growth of large single crystals, a disadvantage of the technique is the requirement of high pressure causes practical difficulties and there are only a few crystals of good quality and large dimensions that can be grown by this technique. Another serious disadvantage of this technique is the frequent incorporation of OH- ions into the crystal, which makes them unsuitable for many applications. However, different shape of nanocrystals have been successfully synthesized using autoclave such as nanorods and nanowires ZnO [179]. Figure 20 shows typical laboratory autoclaves.

Figure 20. Shows a typical desktop lab autoclave (left), high-pressure upright autoclave (right).

M. Law et al performed an experiment using autoclave to fabricate arrays of ZnO nanowires were synthesized on FTO substrates. Synthesized crystals have been used to fabricate DSSC. The arrays were then rinsed with deionized water and baked in air at 400 °C for 30 minutes to remove any residual organics and to optimize cell performance [179], Figure 21.

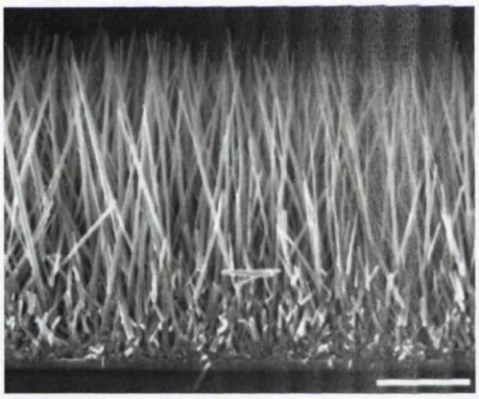

Figure 21. Typical scanning electron microscopy cross-section of a cleaved nanowire array on FTO. The wires are in direct contact with the substrate, with no intervening particle layer. Scale bar, 5 μm.

J. X. Wang et al. successfully fabricated the *C*-axis vertically aligned ZnO nanorod on a ZnO thin film through a simple hydrothermal route using autoclave. SEM images revealed that the nanorods had a diameter of 30–100 nm and a length of about several hundred nm. A gas sensor has also been fabricated using grown ZnO nanorod arrays and showed a high sensitivity to H_2 from room temperature to a maximum sensitivity at 250°C and a detection limit of 20 ppm, Figure 22.

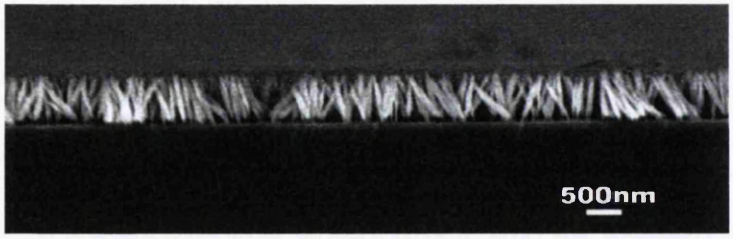

Figure 22. Typical SEM image of ZnO nanorod arrays

3.1.3.3 Microwave-assisted hydrothermal technique (MAHT)

Microwaves have been broadly investigated for rapid heating of materials such as carbon nanotubes functionalization [180] and annealing of organic photovoltaic devices [181]. In this technique electromagnetic waves generated by microwave equipment are used as a source of energy to progress the hydrothermal reactions. Some microwave devices have been especially designed for lab purposes where the user is able to adjust the power and wavelength of the electromagnetic waves from low frequencies to medium or high. But in this study, a commercial microwave oven (kitchen microwave oven) is employed; with a mid range frequency of 2.45 GHz while a turntable is providing uniformity of wave exposure on the sample. Power is also adjustable to low, medium and high, which are 400, 600, and 800w respectively. Different levels of power in this microwave are provided by changing in exposure time, it means to decrease the power, microwave oven uses the longer interval between exposure times and vice versa. In maximum power (used in this research) exposure mode was constantly over the required time. Like other hydrothermal techniques, in the case of using a commercial microwave, it has advantages and disadvantages. Advantages include simplicity, low cost, low temperature and more importantly, fast. Disadvantages include reaction must be performed in aqueous system due to using frequency of 2.45 GHz which is designed to be mostly absorbed by H_2O molecules. Consequently, (in standard atmosphere = 101,325 Pa), the temperature of experiment is always about or under 100°C unless using a lab microwave which is able to increase pressure and temperature. As the maximum penetration of microwave in sample is about less than 10cm so there is a limitation in volume and size of the sample. In addition, microwaves (in

particular 2.45 GHz) are also absorbed by glass containers (such as beakers or testing tubes) and in some cases; increase in glass temperature is faster and higher than the sample. As a result, an unexpected growth results may obtain within the area very near to the inner glass surface due to higher temperature [45]. H. E. Unalan et al reported on the rapid synthesis of ZnO nanowires on various substrates, poly(ethylene terephthalate) (PET), silicon and glass, using a commercially available microwave oven (2.45 GHz) at different power settings (120, 385 and 700 W) at atmospheric pressure, Figure 23(a-c). The maximum growth rate of the nanowires was measured about 100 nm/min at the maximum microwave power. Transmission electron microscopy analysis revealed a defect-free single-crystalline lattice of the nanowires, Figure 23(d).

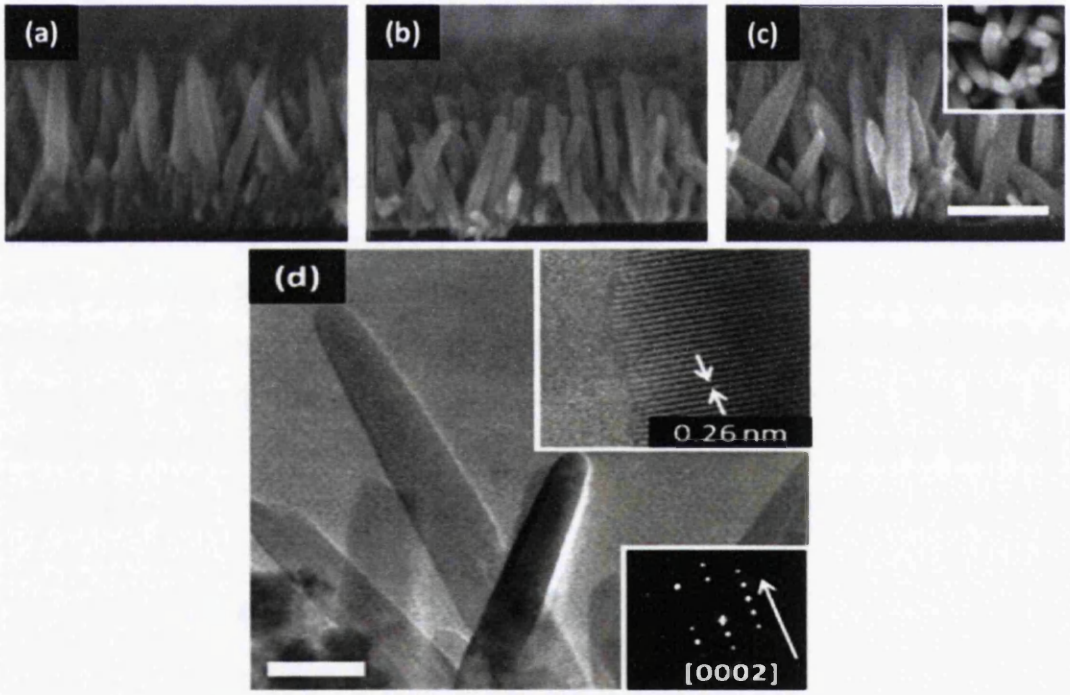

Figure 23. SEM image of ZnO nanowire arrays grown on (a) Si, (b) glass and (c) PET substrates. Inset shows top view of the array. Scale mark 200 nm. (d) TEM image of the nanowire array on Si. Scale mark 50 nm. Inset shows HRTEM image and corresponding electron diffraction pattern. (e) XRD patterns of ZnO nanowires grown on different substrates. Peaks from the substrates were marked with an asterisk.

A detailed analysis of the growth characteristics of ZnO nanowires as functions of growth time and microwave power is reported. Our work demonstrates the possibility of a fast synthesis route using microwave heating for nanomaterials

synthesis. For comparison purposes, several samples were grown at 90°C using a furnace for 90 min; also Microwave heating was performed for 1–30 min. Figure 24 shows results from different techniques and conditions. The results revealed that the high quality and less defective ZnO nanowires were successfully synthesized in few minutes depending on the microwave power level and reaction times.

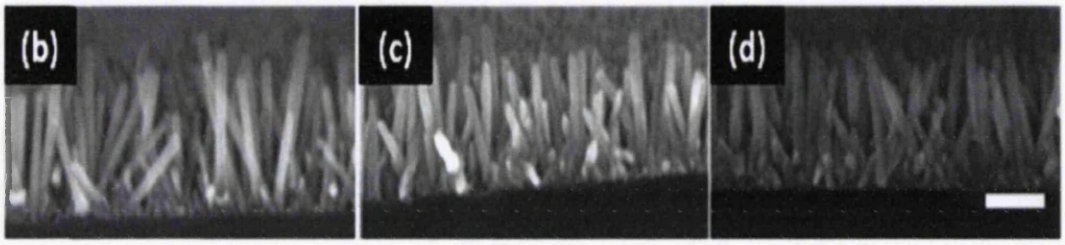

Figure 24. SEM images of ZnO nanowire arrays grown in (a) furnace for 90 min, (b) microwave at 120 W for 30 min and (c) microwave at 700 W for 6 min. Scale mark 200 nm.

Thousands of research articles have been published about the growth of ZnO nanostructures over the last 15 years. In this chapter the most relevant papers to the present research are presented in more details, first, articles related to the growth of nanobelts and nanosheets, particularly via wet chemistry are discussed. Second, the growth of LBZA and the decomposition into ZnO is reviewed. Finally articles reporting on the gas sensing properties of ZnO are discussed.

3.2 ZnO nanobelts

Zinc oxide (ZnO) nanostructures are widely studied nanomaterial, in part because of many properties promising new applications in a variety of nanodevices. Nanorods and nanowires represent a class of one-dimensional nanostructures in which the carrier motion is restricted in two directions. Nanoparticles which are classified in one-dimension category, usually present interesting properties that significantly differ from those of the bulk or even other shapes of nanoparticles such as spherical or sheets (thin films) of the

same chemical composition [182,183]. These nanostructures have potential applications as important components and interconnects in nanodevices [184,185]. One-dimensional structures have already been used in Schottky contacts [186] and logic circuits [187], but ZnO nanoproducts may be synthesized in many different morphologies and structures [188]. In addition, there are different shapes of one-dimension nanoparticles such as nanorods [189], nanowires, nanocombs and nanobelts [190,191] as well as more interesting branched structures such as tetrapods [192,193] and multipods [194]. ZnO nanostructures may be grown using templates [195], physical vapour deposition [196], electrodeposition [197] thermal evapouration [198], solvothermal [199] or and hydrothermal [52,200] methods.

To produce one-dimensional ZnO nanoparticles via some of those techniques mentioned in part 2.1, different complicated equipment and processes are required as well as several organic and inorganic materials. Among these particles, ZnO nanobelts have received more attention not only because of ZnO unique properties but also due to their specific geometry. Having only a few tens of nanometers (10 to 50 nm) thickness, lead to a large surface to volume ratio that is obviously one of the most important factors for a nanoparticle. Having lengths up to hundreds of micrometers makes them a potential candidate to be used in optical and electrical micro/nano devices. Most of the techniques to produce nanobelts are expensive and time consuming. In addition they not only need sophisticated equipment but also standards of proficiency to run the experiments. For instance, PVD technique, as described in part 2.1 [76], is one of the most commonly method to grow 1D nanostructures including nanobelts in which high temperature (about 1000°C) is employed to vapourize ZnO at the hot end and use them to build belts at the cooler end, K. Bando et al [201] used thermal evapouration of ZnO powder, which is similar to the method reported in Z.W. Pan et al [202] in which ZnO nanobelts were simply grown by heating ZnO powder without catalysts on ceramic boats in a furnace at 1450°C for 3h in flowing Ar gas at 50 sccm. The result was an aggregate of ZnO nanobelts, which is a white wool-like product, adhering onto the ceramic tube. In order to separate the aggregate into single nanobelts, it was mixed in ethanol,

treated by sonication and dispersed onto copper substrates by drop casting the ethanol containing the nanobelts. The result is shown in Figure 25.

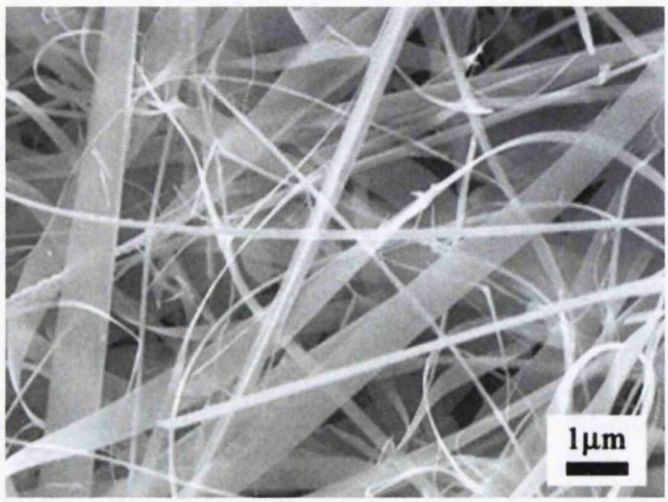

Figure 25. Shows the SEM image of the aggregate of the ZnO nanobelts on the copper substrate.

B. Alema´n *et al.* (2009) [203] performed an experiment in which ZnS and In_2O_3 powders with purities of 99.999% and 99.997%, respectively, were used as precursors. Figure 26 shows the obtained nanostructures, there are different shapes of ZnO nanostructures including nanobelts.

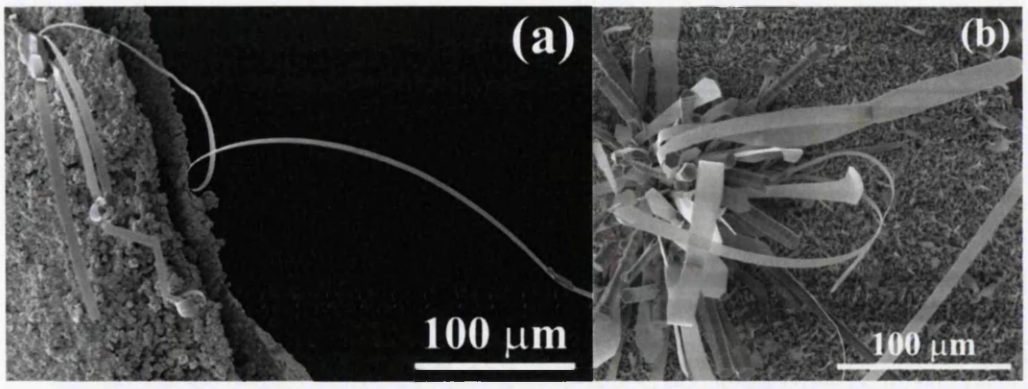

Figure 26. a and b are SEM images of curved ribbons (nanobelts) ZnO nanoparticles . The nanobelts are accompanied by other shapes of ZnO nanostructures.

In another experiment performed by Y.F. Chen *et al* [204], ZnO nanobelts were successfully synthesized via a vapour phase growth, the synthesis was carried

out in an horizontal quartz tube furnace in which one alumina boat with pure Zn powder as the source was placed at 500°C zone. Another boat with pure Se powder was placed adjacent to the Zn source. After evacuation of the quartz tube to (and maintained at) 0.003– 0.007 MPa, a carrier gas of argon was kept flowing through the tube with a flow rate of 145 sccm. Also, small amount of oxygen was introduced into the system throughout the whole reaction. The evaporated material was carried down the tube by the gas mixture and deposited on an oriented silicon substrate (111) washed by hydrochloric acid. Typical growth process lasted for 30 min. SEM imaging of the product revealed that it was a mixture of nanobelts and nanowire with different lengths and widths (Figure 27).

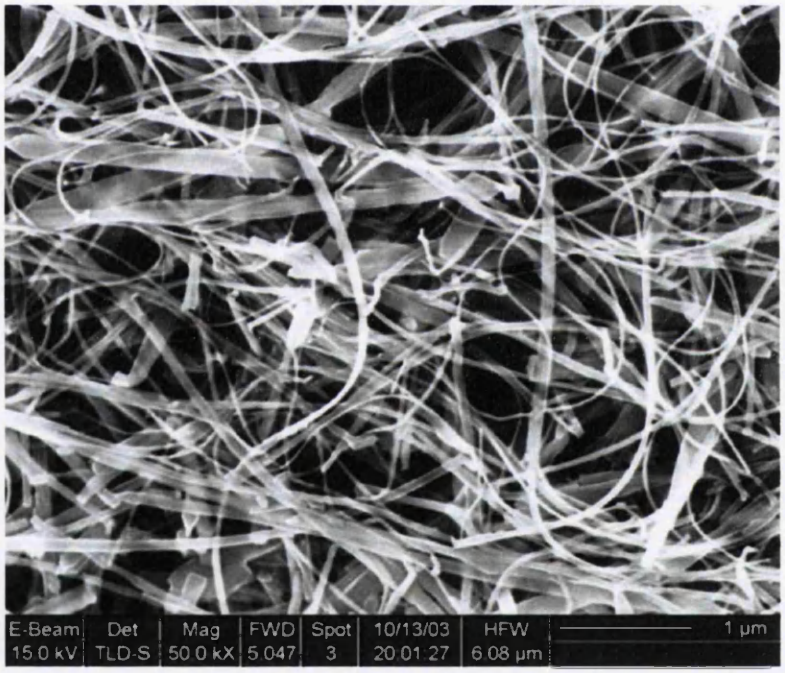

Figure 27. SEM image of the grown ZnO sample; nanobelts are the dominant morphology.

Y.X. Chen and S.W. Guo [205] employed a thermal evapouration method to fabricate ZnO bicrystalline nanobelts in which a small alumina boat containing a mixture of commercial ZnO and graphite powders (weight ratio 1:1) was placed in the closed end of a small quartz tube. Then it was loaded into a big quartz tube and the source materials were placed 7 cm upstream of the furnace center

with the open end of the small tube facing Ar gas flow. After the double-tube system was evacuated to 2 × 10− 2 Torr, synthesis was conducted at 1020°C for 20 min with vacuum pressure 300 Torr, Ar gas flow rate 100 sccm (standard cubic centimeters per minute) and compressed air flow rate 50 sccm. ZnO bicrystalline nanobelts were formed at about 950°C. Figure xx shows the SEM and TEM imaging of ZnO bicrystalline nanobelts. As it can be seen in the Figure 28 as-prepared ZnO nanobelts are accompanied by another type of ZnO crystal.

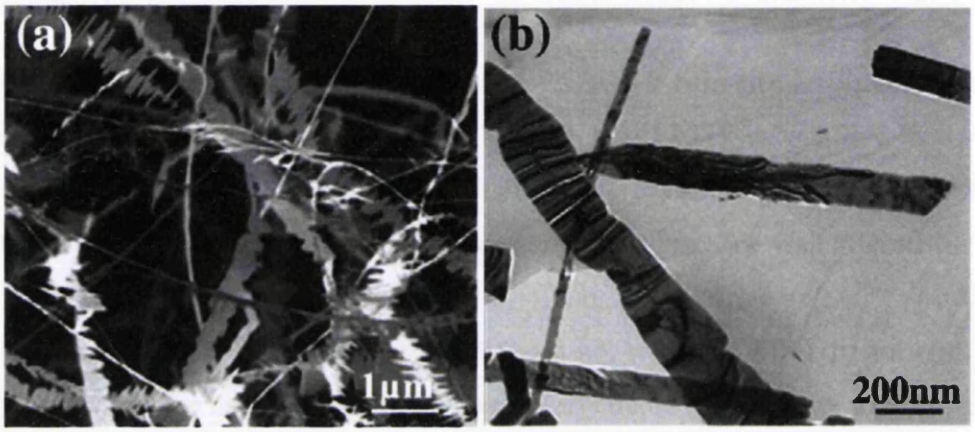

Figure 28. (a) SEM image of ZnO nanobelts mixed with some necklace-like nanostructures; (b) TEM images of ZnO nanobelts

Also, there is variety of reports about producing ZnO nanobelts using different sputtering methods; Supab Choopun *et al* [206] reported an experiment in which radio frequency magnetron sputtering (RF sputtering) was employed to produce single crystalline ZnO nanobelts. In this case, ZnO products were deposited on the copper substrate using a radio frequency magnetron sputtering with no metal catalyst. Initially, the sputtering chamber was evacuated to a pressure lower than $1x10^{-5}$ Torr. Deposition of ZnO products was then carried out at a pressure of 40 mTorr on copper substrates. The deposition time was 60 min using an RF power of 300 W. The ZnO target was prepared by conventional solid- state methods from 99.9% ZnO powder. During the deposition of ZnO, the substrates have no intentional heating. The SEM imaging results are in Figure 29.

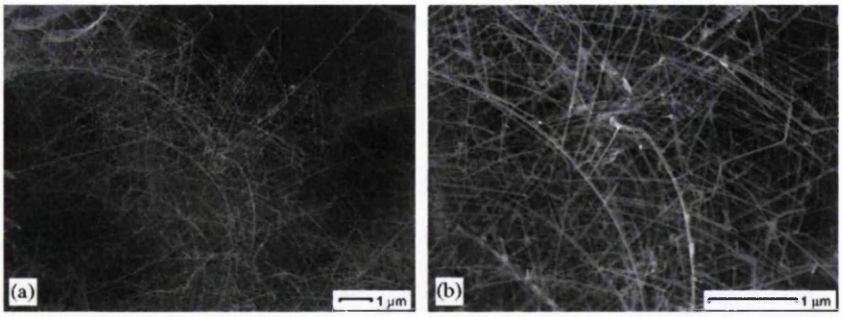

Figure 29. FE-SEM images of deposited ZnO products on copper substrate at magnification of (a) 10,000 and (b) 25,000.

H. Hu et al. [99] planed an hydrothermal technique to synthesize ZnO nanobelts in which 0.2 g $ZnCl_2$, 1.5 g SDSN and 20 g Na_2CO_3 (~4.72 M) were added into a 45 ml of distilled water then mixture transferred to a Telfon-lined stainless steel autoclave container (50ml). The obtained reaction mixture was stirred for an additional 30 min. The autoclave was sealed and maintained at 140°C for 12 h resulting a white product, which was filtered off, washed with ethanol and hot distilled water for several times, and then finally dried in a vacuum at 60°C for 4 hours. Figure 30 shows the result indicating the coexistence of wire-like and belt-like nanostructure.

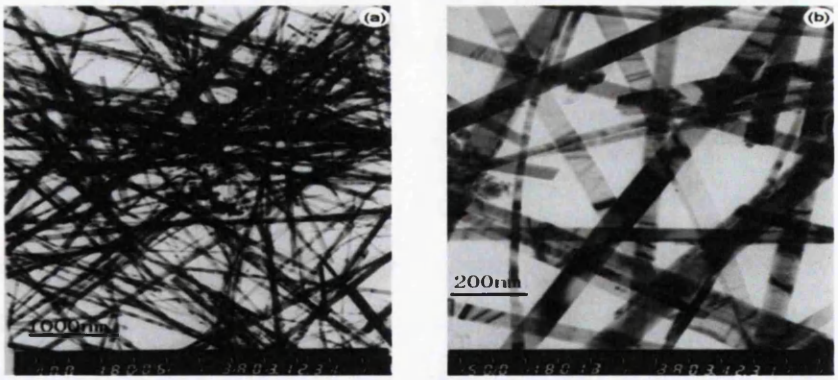

Figure 30. (a and b) TEM images of the ZnO products, indicating the coexistence of wire-like and belt-like nanostructure.

In another experiment performed by E. S. Jang et al [98] 0.1 M zinc acetate dihydrate and 0.1 M HMTA aqueous solutions were prepared in Teflon lined autoclave, which was maintained at 95°C for various reaction time from 6 to 60

hours in conventional furnace. The resulting products were collected by centrifuging, and then washed with deionized water to remove any residual organic salts. The porous ZnO nanobelts were produced from the Zn based hydroxide double salts (Zn-HDS), which was obtained from the above hydrothermal reaction of 60 hours, by calcinations at 400°C for 3 hours. For the synthesis of the nonporous ZnO nanobelts, Teflon lined autoclave including the Zn-HDS (0.5 g) and 0.5 M Na_2CO_3 aqueous solution was heated at 95°C for 24 h. In addition, a flower-like ZnO crystal was obtained from the Zn-HDS product of hydrothermal reaction for 60 hours by using of 0.01 M NaOH as dehydration agent under hydrothermal reaction at 150°C for 3 hours. On the other hand, hierarchical structures (30%) and multipod ZnO crystal (70%) were achieved by increasing hydrothermal temperature up to 230°C. results are shown in Figure 31.

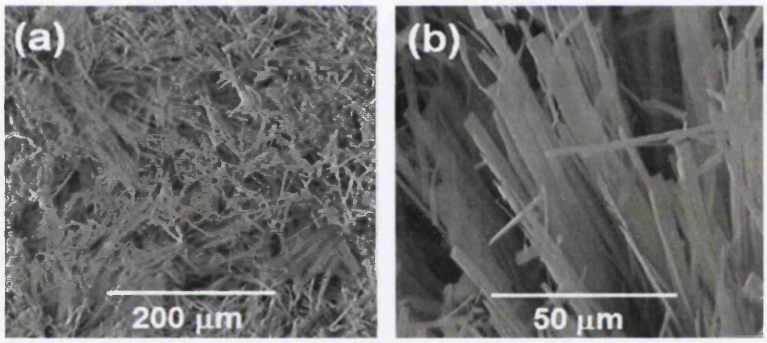

Figure 31. FE-SEM images of the Zn-HDS generated by dissolving the dumbbell-like ZnO twin crystal

Direct melt oxidation (DMO) is another method, which is used to synthesise nanostructures. G. H. Lee, J. H. Song [207] designed an experiment based on DMO in which they successfully produced ZnO nanobelts and nanowires. They used Al alloy with a small amount of Mg as an Al source material. The critical role of Mg in Al–Zn mixture in the formation of ZnO nanoparticles by DMO process was reported previously [207]. The source material was prepared by mixing well the Al alloy and pure Zn powder of 3 wt%. The source material was placed in an alumina crucible and then inserted into an oxidation furnace. The source material was oxidized for 1 h at 1000°C in air at atmospheric pressure. It is well

known that if the oxidation time is over 2 h, only tetrapod- shaped ZnO nanoparticles are synthesized [207,208]. Therefore, the furnace was heated with a rate of 10°C/min. After the oxidation, the furnace was turned off and cooled quickly down to room temperature. White coloured powder was found on the surface of the oxidized source material. The results are in Figure 32.

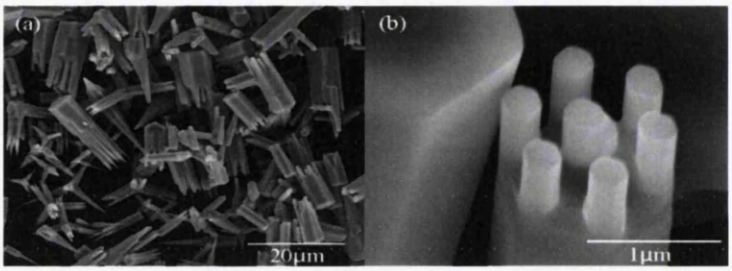

Figure 32. (a) Low magnification and (b) High magnification SEM images of the ZnO particles synthesized by the direct melt oxidation for 1 h at 1000°C in air.

3.3 ZnO nanosheets (ZnO NSs)

There are some investigations in which fabrication and synthesis of the thin films and nanosheets were successfully reported. In 2009, L. Liu et al. designed an experiment in which approximately 0.05 mol/L Zinc acetate dehydrate and HMTA (C6 H12 N4) were put into lined stainless steel autoclave with 30 mL capacity, and then the autoclave was filled with 10 ml of distilled water and 0.30g sodium dodecyl sulfate as well as 10 mL n-butanol. The autoclave was maintained at 150°C for 24h without shaking or stirring during the heating period and allowed to cool to room temperature. A white precipitate was collected and then washed with distilled water and absolute ethanol [209]. Figure 33 shows the results.

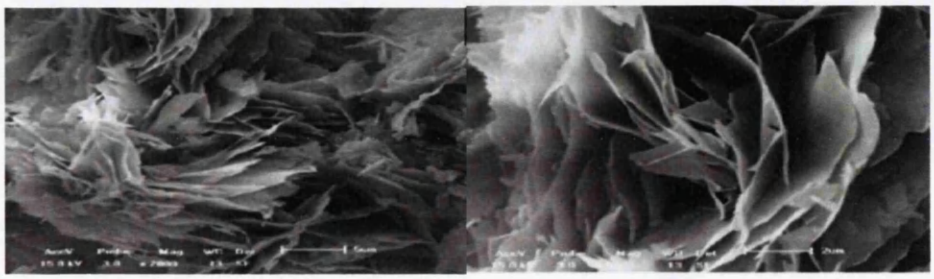

Figure 33 shows SEM images of samples synthesized at150°C for 24 hours using autoclave

In another experiment performed by R. Al-Gaashania et al [210], 0.066 M (100 ml) of ZnCl2 and 1.75 M (20 ml) of NaOH aqueous solutions were prepared in deionized water (DI) (resistivity 18.2 MΩ·cm) under magnetic stirring at room temperature. After stirring the ZnCl2 aqueous solution (pH_i = 7.5 at 22.9 ◦ C) for 5 min, the NaOH aqueous solution was gradually added in the form of drops under constant magnetic stirring until a milky solution of pH_f =13.75 at 24.5◦C resulted. After 1.5h stirring, the final mixture solution was transferred into a 500ml flat-bottom flask. Then, the flask was loaded into the turntable of the microwave oven to irradiate the mixture solution under air for 10 min duration with the power set at 1000 W. The hot solution with a white precipitate was left to cool at room temperature naturally. Then the white precipitate was separated by centrifugation at 4000 rpm for 10 min, washed with DI water and absolute ethyl alcohol several times to remove the remaining of NaCl, and finally dried in air at 60°C for 24 h. The result is shown in Figure 34.

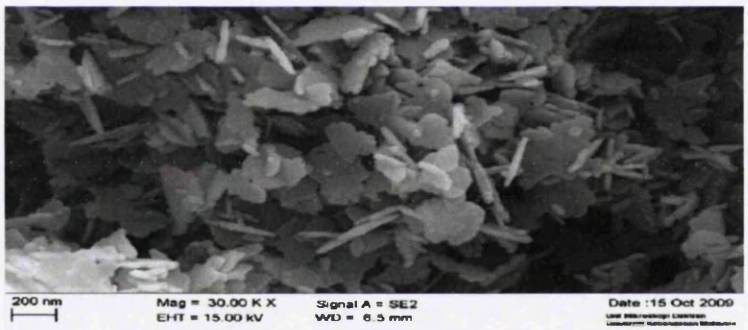

Figure 34 shows SEM image of the morphology of the ZnO nanosheets produced within 10 min under 1000W power microwave irradiation. The images show clearly the effect of microwave power on the morphology and size of the ZnO nanostructures.

H. Kou et al. [211] in an electrochemically synthesis experiment successfully produced ZnO nanoflowers and nanosheets on porous Si as photoelectric materials, in which well aligned ZnO nanoflowers and nanosheets were synthesized on porous Si (100) at different applied potentials by electrodeposition approach. Scanning electronic microscopy (SEM) observation showed the deposits consist of nanoflowers with uniform grain size of about 100nm in diameter and nanosheets. The results are shown in Figure 35.

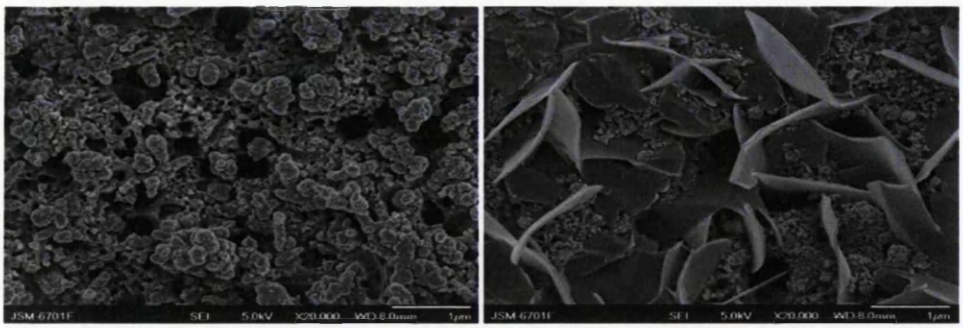

Figure 35. SEM of the surface of ZnO grown on PS vs. non-aqueous Ag/Ag+ reference electrode at (left) E=−0.9 V, (right) E = −0.75 V.

L. L. Xing and X. Y. Xue [212] in another experiment managed to design a highly oriented ZnO-surfactant multilamellar nanostructures were fabricated by electrochemistry-assisted self-assembly on silicon substrates from the solution containing zinc nitrate and dilute surfactant hexadecylamine at 60°C. The co-absorption of inorganic ions with surfactant on the electrode surface implied that the unique growth mechanism depended strongly on the environmental change of cathodic electrode area under the electric field. The ZnO nanosheets (w2.3 nm) were produced. Comparing with pure ZnO film by electrodeposition, the multilamellar nanostructures consisting of the dielectric organic barriers and the semiconducting inorganic well layers give rise to 2-dimensional quantum confinement (Figure 36).

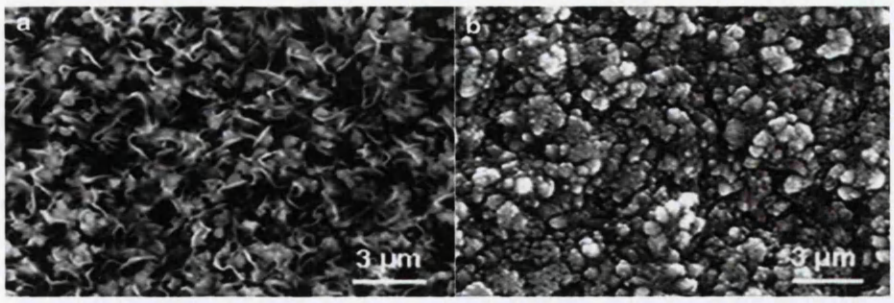

Figure 36. The surface SEM images of (a) the ZnO-HDA nanostructure and (b) the ZnO film

J. Qiu et al. [213] designed an experiment in which a two-step electrochemical deposition process was used to synthesize hierarchical zinc oxide (ZnO) nanorod-nanosheet complex structure on indium tin oxide (ITO) substrate, which involves electrodeposition of ZnO nanosheet arrays on the conductive

glass substrate, followed by electrochemical growth of secondary ZnO nanorods on the backbone of the primary ZnO nanosheets (Figures 37, 38).

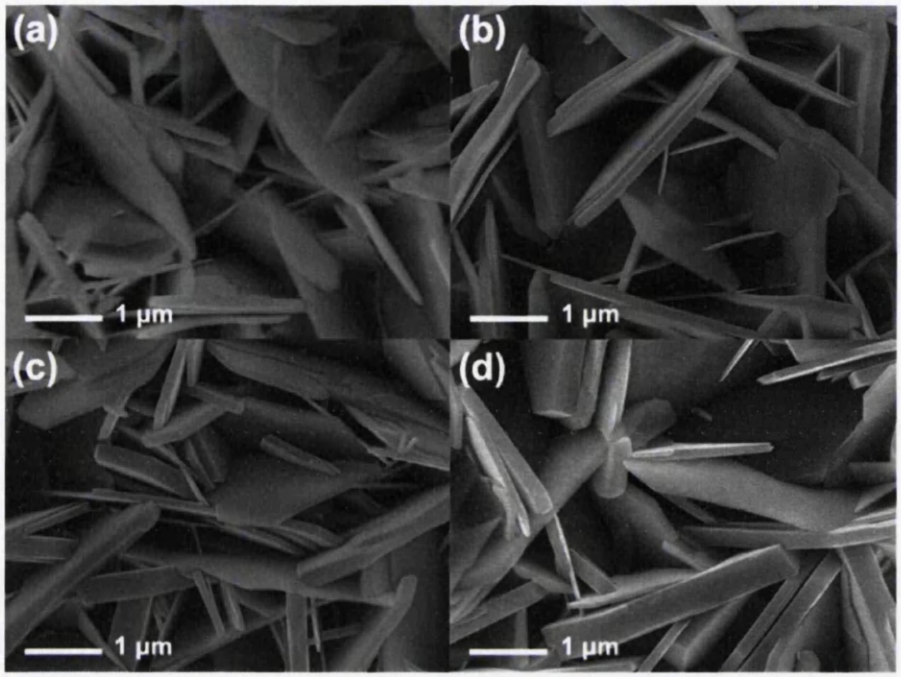

Figure 37. SEM images of $ZnO/Zn_5(OH)_8Cl_2H_2O$ nanosheet arrays electrodeposited at different temperatures (T): (a) 50, (b) 60, (c) 70, and (d) 80°C. Other electrodeposition conditions: CZn^{2+} = 0.05 M (Zn(NO3)2), E =1.0 V, t = 1 h.

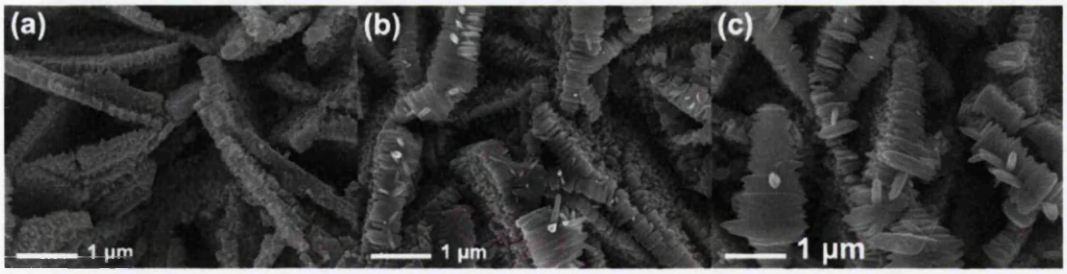

Figure 38. SEM images of ZnO nanorod-nanosheet structures synthesized by two-step deposition process with different second-step deposition times (t_2): (a) 0.5, (b) 1, and (c) 2 h. Other electrodeposition conditions, first-step deposition: T_1 = 70°C, $C_{Zn^{2+}}$ = 0.05 M ($Zn(NO_3)_2$), E_1 = -1.0 V, t_1 = 1 h; second-step deposition: T_2 = 80°C, $C_{Zn^{2+}}$ = 1 mM ($ZnCl_2$), E_2 = -1.0 V.

X. Luo et al. [214] performed and experiment in which a hybrid film of ZnO and tetrasulfonated copper phthalocyanine (TSPcCu) was grown on an indium tin oxide (ITO) glass by one-step cathodic electrodeposition from aqueous mixtures of $Zn(NO_3)_2$, TSPcCu and KCl. Increasing of TSPcCu strongly influences the

morphology and crystallographic orientation of the ZnO. The nanosheets stack of ZnO leads to a porous surface structure, which is advantageous to further adsorb organic dyes. The photovoltaic properties were investigated by assembling the DSSC device based on both the only ZnO film and the ZnO/TSPcCu hybrid films. Photoelectrochemical analysis revealed that the optimized DSSC device with TSPcCu represented a more than three-fold improvement in power conversion efficiency than the device without TSPcCu. The DSSC based on ZnO/TSPcCu hybrid films demonstrates an open circuit voltage of 0.308 V, a short circuit current of 90 μA cm^{-2}, a fill factor of 0.26, and a power conversion efficiency of 0.14% (Figure 39).

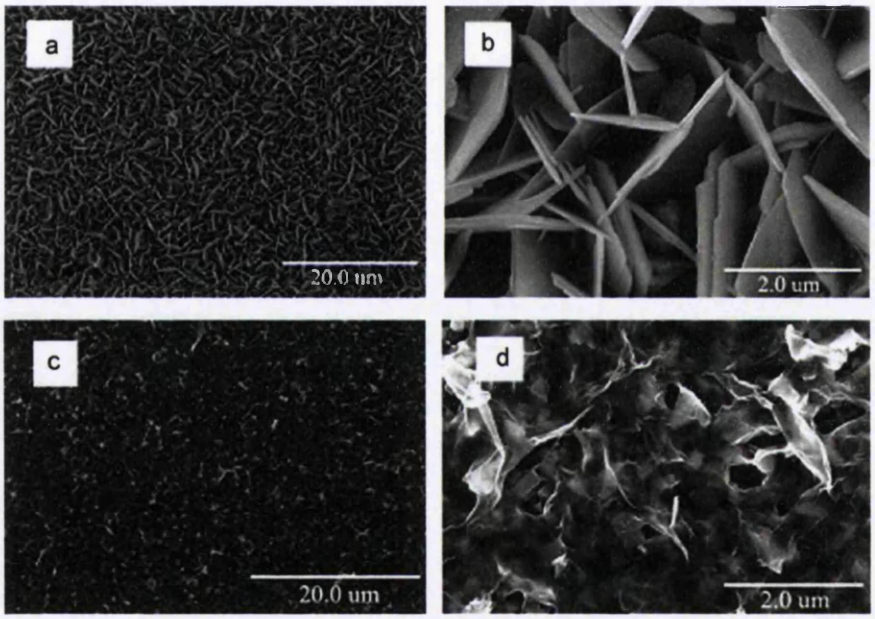

Figure 39. (a, b) Low and high magnification SEM images, respectively, of a ZnO thin film; (c, d) low and high magnification SEM images, respectively, of a ZnO/TSPcCu hybrid film. The films are electrodeposited at 0.5 mA cm^{-2}.

C. Xie et al. [215] designed an experiment to improved ZnO nanostructured morphology obtained by screen-printing on a substrate via solution growth process. Nanostructured ZnO with different MnO_2 additive concentrations was fabricated by a combination of screen-printing technology and solution growth process. The results showed that ZnO nanostructures were induced on the surface of the substrate arrays through the solution growth process. The

nanostructures were composed of nanowalls and nanosheets with the thickness of about 50–200 nm and length of about 1–2 μm. The investigations revealed that the solution growth process could effectively control the morphologies, change the aspect ratio of ZnO nanostructures. Figure 40 shows screen-printing of the ZnO nanostructures fabricated on the substrate. The final results are shown in Figure 41, SEM images show the difference between the morphologies of the ZnO nanostructures in different concentrations of the MnO_2 (0.5 wt%, 1.0 wt% and 5.0% MnO_2).

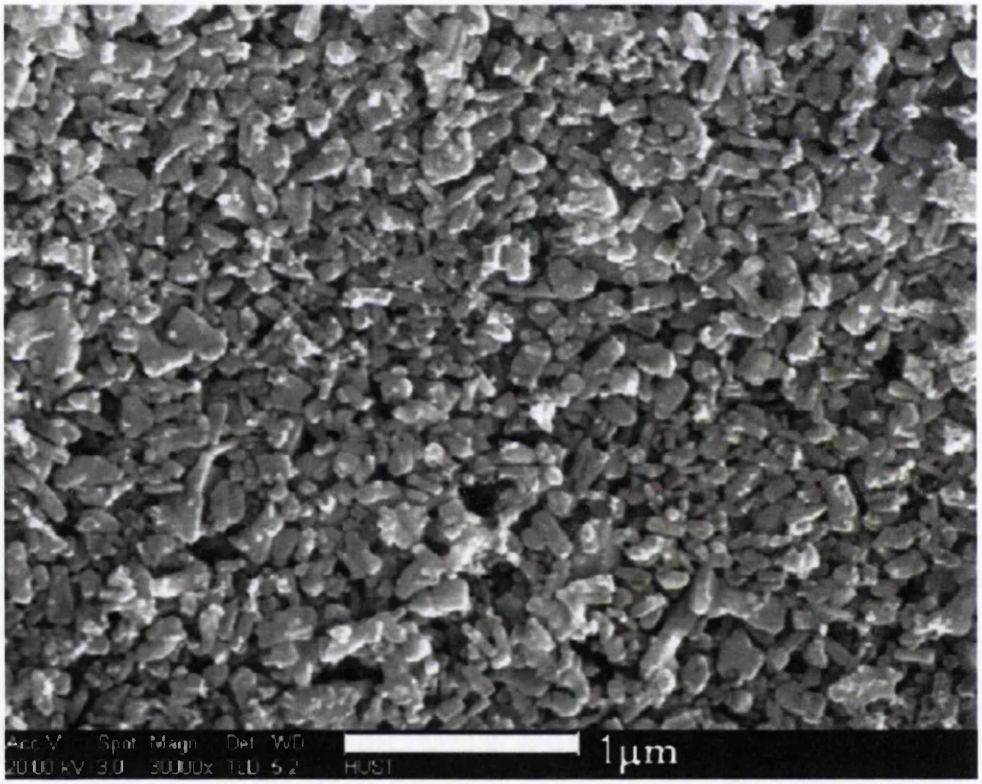

Figure 40. SEM image of the ZnO nanostructures fabricated by screen-printing technique

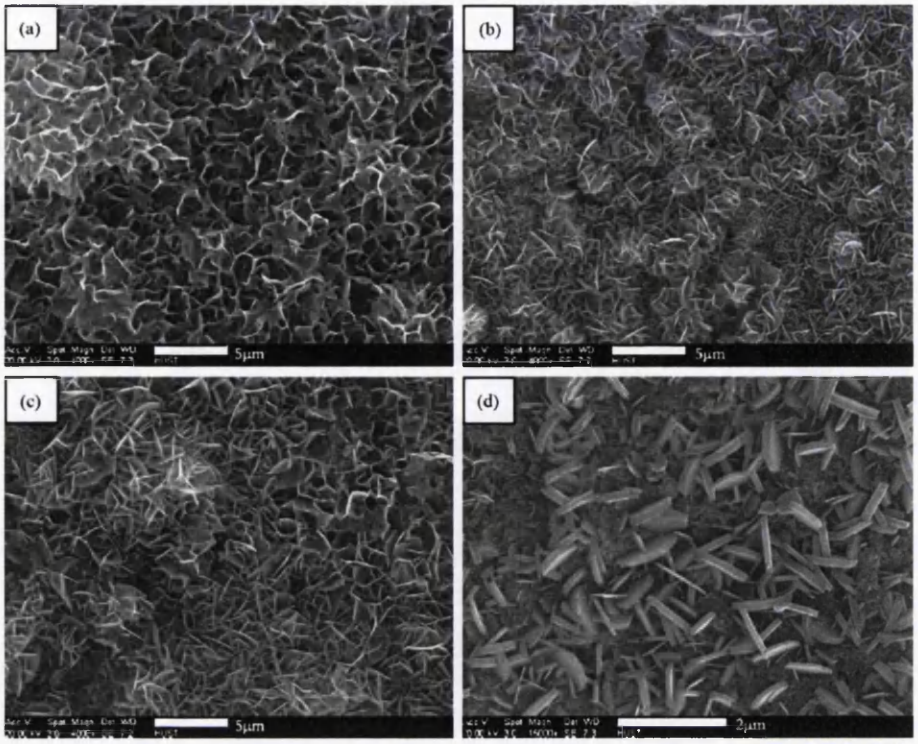

Figure 41. SEM micrographs of the sensor array treated by the solution growth process: (a) pure ZnO, (b) 0.5 wt% MnO_2–ZnO, (c) 1.0 wt% MnO_2–ZnO, and (d) 5.0 wt% MnO_2–ZnO.

In an experiment performed by J. Huanga [216], hierarchically three-dimensional (3D) porous ZnO architectures were synthesized through a template-free, economical aqueous solution method followed by calcination. To synthesize the precursors of interlaced basic zinc nitrate (BZN) nanosheets, zinc nitrate hexahydrate (1.45g) was dissolved into 50 ml of deionized water. Then, the solution was stirred, and the pH value of the resulting solution was adjusted to 6.0 using ammonia (NH3 ·H2 O, 25 wt%) solution. After that the mixture solution was standing for 4 h at room temperature. Finally, the white precipitates were centrifuged and washed with deionized water and absolute ethanol 6 times, then dried at 30°C for 24 h. The final products of hierarchically porous ZnO architectures were obtained by annealing the BZN precursors at 300°C in a muffle furnace for 2 h. results before and after thermal decomposition are shown in Figures 42, 43.

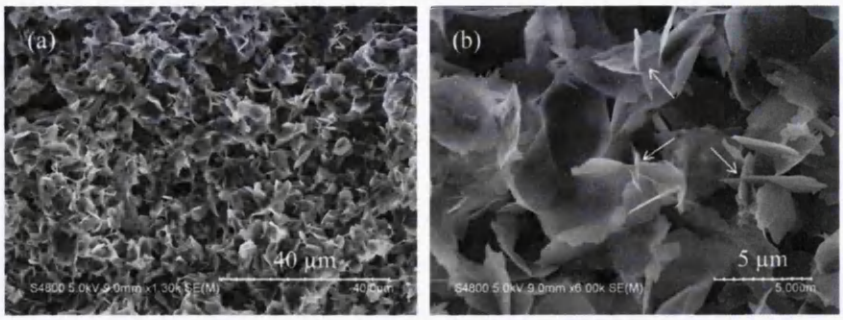

Figure 42. SEM images of (a and b) basic zinc nitrate interlaced nanosheets

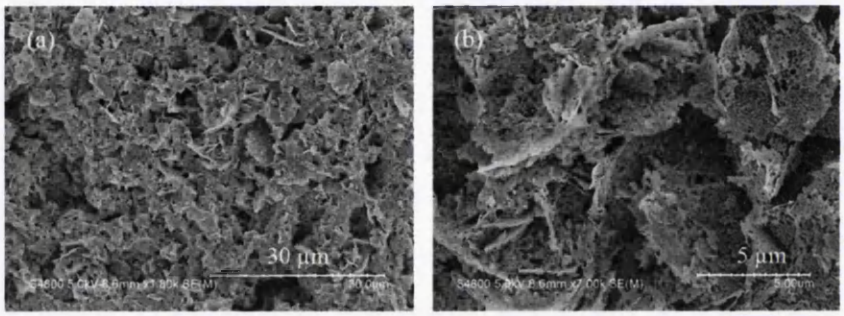

Figure 43. SEM images of (a and b) porous ZnO nanosheets calcined basic zinc nitrate interlaced nanosheets precursor annealed at 300°C for 2 hours.

K. Kakiuchi et al. [217] have successfully designed a simple chemical deposition route to fabricate nanocrystalline and mesoporous ZnO films approximately 4 μm in thickness in an aqueous solution of zinc nitrate and urea and subsequent pyrolytic decomposition at a low temperature of 300°C. Microscopic observation of the films revealed that they were composed of mesoporous nanosheets accumulating with submicrometer-order spacing between them on conducting glass substrates. Results are shown in Figure 44.

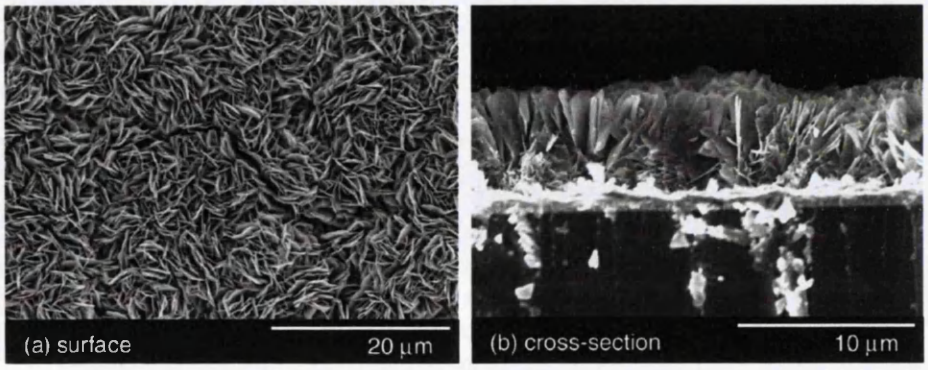

Figure 44 (a) Surface and (b) cross-section FESEM images of the ZnO film heat-treated at 300 °C

A. Lei et al. [218] performed and experiment in which hierarchical porous ZnO microspheres were successfully synthesized by calcining the microspheric zinc hydroxide carbonate (ZHC) precursor, which were the precipitate products of a hydrothermal reaction by zinc nitrate hexahydrate and urea in the presence of trisodium citrate. The as-prepared ZnO microspheres with diameters of 4–5 μm were assembled by numerous porous nanosheets, which had the uniform thickness of about 10 nm. In a typical experiment, 1.5 mmol zinc nitrate hexahydrate, 3 mmol urea ($CO(NH_2)_2$) and 0.15 mmol trisodium citrate were dissolved in 30 mL deionized water to form a clear solution, the mixed solution was transferred into a 50 mL Teflon-lined stainless steel autoclave and heated at 120°C for 6 h. The precipitate was centrifuged and washed several times with deionized water and absolute ethanol, and then dried at 60°C for 12 h. Finally, hierarchical porous ZnO microspheres were obtained by calcining the ZHC precursor at 300°C for 2 h in air. Results are shown in Figure 45.

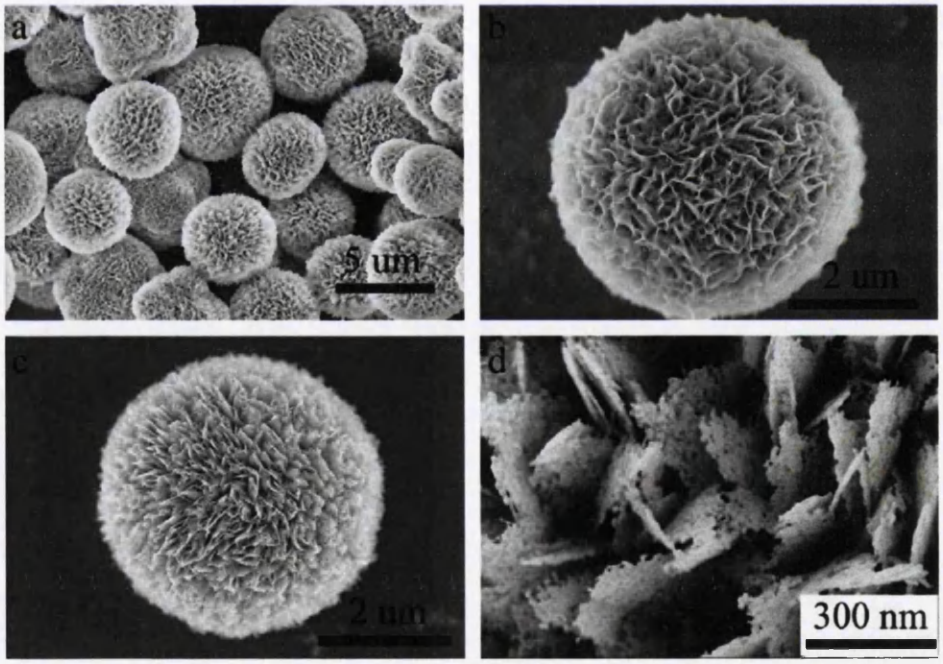

Figure 45. (a-b) SEM images of the ZHC precursor, (c-d) SEM images of samples calcined at 300 °C

3.4 ZnO nanostructures from Layered Basic Zinc Acetate (LBZA)

One-dimensional nanoparticles have a great potential to play a significant role in designing and assembling novel micro/nano devices due to their unique structure, so finding new techniques through which these nanoparticles can be produced cheaper and in a large scale, are always challenging. Most importantly, nanoparticles must be reproducible and as easy and simple as possible to apply, to be promising for future commercial applications. In this research we are reporting an extremely simple and low-cost alternative way to produce ZnO nanocrystalline nanobelts and nanosheets via a hydrothermal technique.

Metal hydroxide salts (MHSs) with layered structures have been widely studied and they have been used for applications such as biosensors, drug delivery agents, catalysts and ion exchangers, [219-224]. But MHSs have more potential applications; one of the most important one is to be used as a precursor to metal oxides by thermal decomposition [224]. In some cases, pyrolytic decomposition proceeds with a topotactic process, which involves structural changes to a crystalline solid, which may include loss or gain of material, so that the final lattice is related to that of the original material by one or more crystallographically equivalent and orientational relationships, as in the case of Ni/Al2O3 and Ni/NiAl2O4 composites obtained from Ni/Al layered double hydroxides [225], and of the formation of cobalt oxide [226] and magnesium oxide [227]. Therefore, thermal transformation of varied MHSs compounds is an effective method to yield corresponding oxides with controlled morphologies. Among ZHSs, in this study, we are particularly focusing on pyrolytic decomposition of layered basic zinc acetate salts (LBZA Ss), this transformation from zinc hydroxide salts (ZHSs) to zinc oxide (ZnO) by the thermal decomposition has got attention, because ZnO is of particular interest in view of its low toxicity and a wide range of possible applications, including transparent conductive electrode, catalyst and photocatalyst, dye sensitized solar cells technology, and fluorescent substance [228-230].

It is really important to know that the pyrolytic decomposition behavior and properties of the corresponding ZnO nanostructures from LBZA Ss are critically

dependent on the precursors of LBZA Ss. Morioka et al. [231] successfully designed and performed an experiment in which ZnO powders with film-like morphology via pyrolytic decomposition of $Zn_5(OH)_8(CH3COO)_2 .2H_2O$ was produced, also Hosono et al. [116] prepared porous ZnO films in the very similar approach. Biswick et al. [232,233] have investigated the thermal decomposition behavior of $Zn_5(OH)_8$ $(CH3COO)_2 .4H_2O$ and $Zn_5(OH)_8(CH3COO)_2 .2H_2O$. Audebrand et al. [234] designed a very detailed study of the early growth stages of the ZnO nanocrystallites generated via pyrolytic decomposition of four different precursors, zinc acetate, hydroxide nitrate, hydroxide carbonate, and oxalate in which ZnO hexagonal sheets were synthesized by calcination of the hexagonal plate-like crystals of the zinc hydroxide chloride, $Zn_5(OH)_8Cl_2. H_2O$, through the hydrothermal slow-cooling method [235].

In a very interesting experiment, Arii and Kishi [236] have conducted the thermal decomposition of $Zn_5(OH)_8(CH3COO)_2 .2H_2O$ in some humidity controlled atmospheres by using a novel thermal analyses, which are sample-controlled thermogravimetry (SCTG), which is thermogravimetry combined with evolved gas analysis using mass spectrometry (TG-MS), and simultaneous measurement of X-ray diffractometry and differential scanning calorimetry (XRD–DSC). In addition, they revealed that, the pyrolytic decomposition behavior of anhydrous zinc acetate was significantly influenced by the partial pressure of water vapour in the atmosphere [236], and anhydrous zinc acetate was directly decomposed to ZnO crystalline by reacting with the water vapour in a high humidity atmosphere. Also, Garcia-Martinez et al. [237] reported the thermal decomposition behaivor of the zinc hydroxide chloride. They investigated the thermal decomposition process of ZHC as a function of a heating rate, which is in good agreement with Arii and Kishi [236]. Therefore, the presence of water vapour in the atmosphere may also affect the thermal decomposition process of ZHC. Also Q. Cui et al [238] reported an experiment in which porous ZnO nanobelts were synthesized by heating layered basic zinc acetate (LBZA) nanobelts in the air. The precursor of LBZA nanobelts consisted of a lamellar structure with two interlayer distances of 1.325 and 0.99 nm were prepared using a low-temperature, solution-based method. The porous ZnO nanobelts have been

grown via two-steps process. First, 1.0 g $Zn(CH_3COO)_2.2H_2O$ (analytical grade) was dissolved in deionized water (20 mL). Ammonia (25 wt.%) was slowly added under magnetic stirring to keep the pH at ~7.2. Then the milky solution was sealed in beaker (50 mL), heated to 40C for 10 h. When it cooled down, the colloid liquid was filtrated. After that, the precipitate was dried at 60 8C in air for 6 h. A white, thin membrane subsequently was found on the filter paper. Second, by heating the membrane in ambient circumstance at 700 8C for 2 h in a crucible, the yellowy samples were observed. The typical length of the ZnO is over 20 mm on average, consisting of abundant nanoparticles with a size of ~80 nm, Figures 46-47.

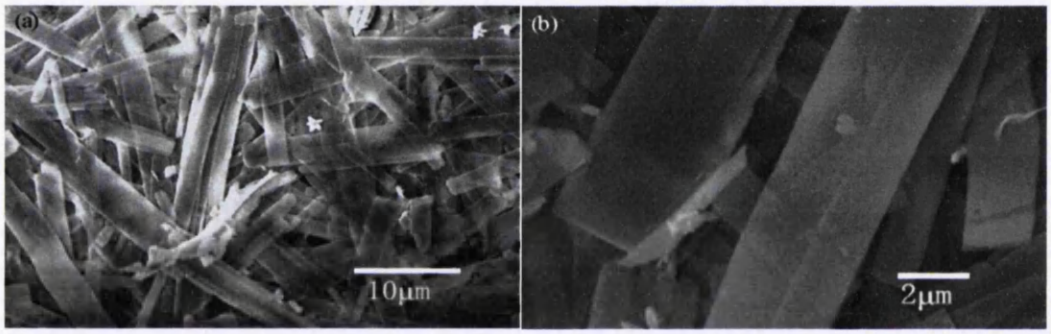

Figure 46. (a, b) SEM images of self-assembly LBZA nanobelts obtained at 40°C.

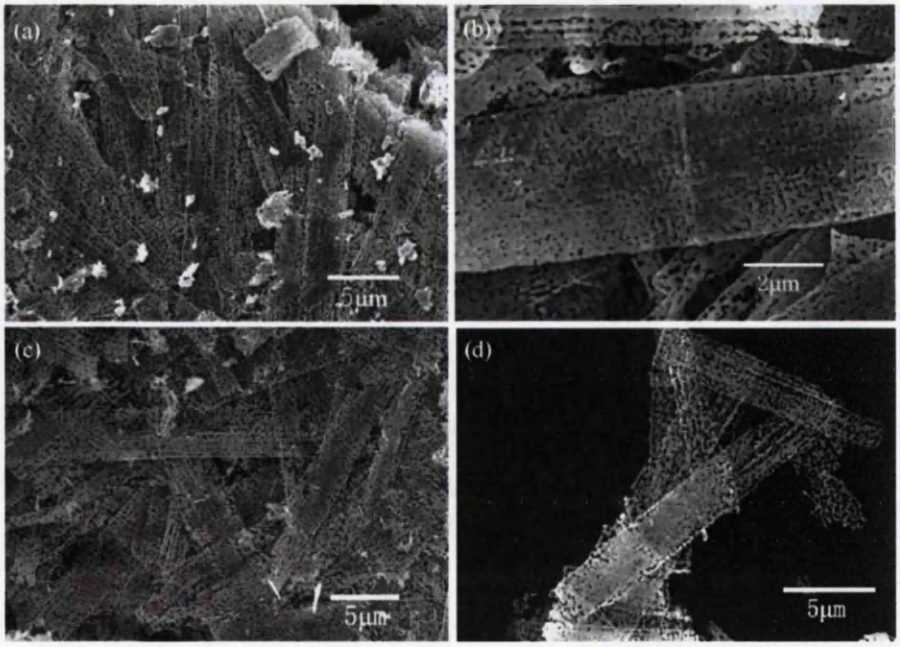

Figure 47. SEM images of porous ZnO at different temperatures (a, b) 500°C, (c, d) 700°C.

Q. Hou et al. performed an experiment in which ultra-thin porous ZnO nanosheets with high regularity were obtained by electrodeposition followed by annealing. The nanosheets were first electrodeposited by controlling the concentration of potassium acetate (KAc) in nitrate electrolyte. In this work, the influence of KAc concentrations on the electrochemical behavior, the composition and morphology of samples were investigated. The results indicated that the as-deposited nanosheets were a mixture of ZnO and zinc acetate hydroxide hydrate (ZAHH), Figure 47.

After annealing at 450°C for 30 min, ZnO/ZAHH nanosheets with smooth surfaces were converted to pure ZnO nanosheets with porous structure, which were oblong in shape, ultra-thin (about 20 nm in thickness) and constructed with well-distributed single-layer ZnO nanoparticles with the size of 30–60 nm, Figure 49 [239].

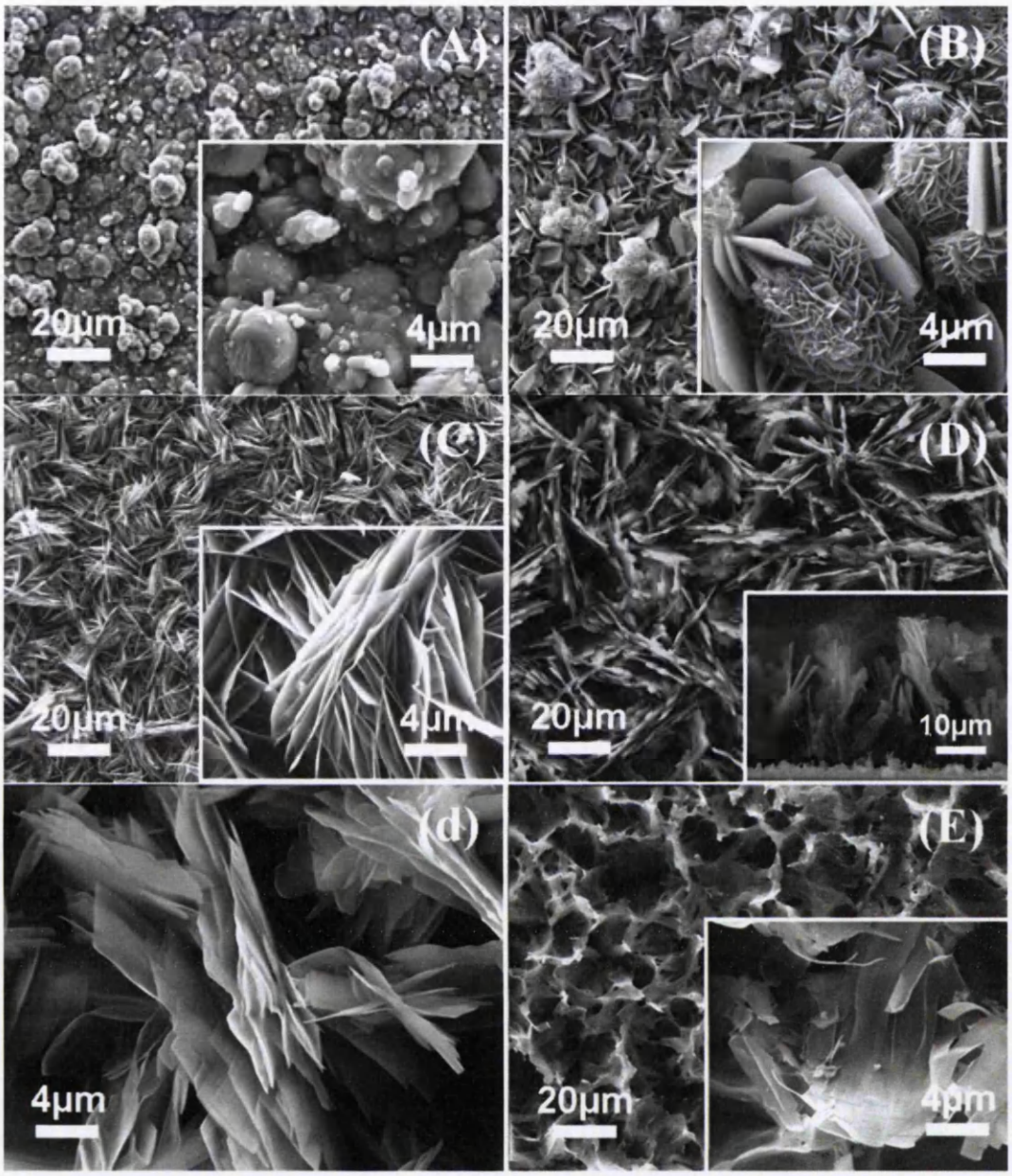

Figure 48. SEM images of the as-deposited films obtained in the electrolytes containing different concentrations of KAc: (A) 0M, (B) 0.01M, (C) 0.05M, (D, d) 0.1 M and (E) 0.5M. The insets in (A), (B), (C), (d) and (E) are the corresponding high magnification images, and the inset in (D) is the corresponding cross-section view of (D).

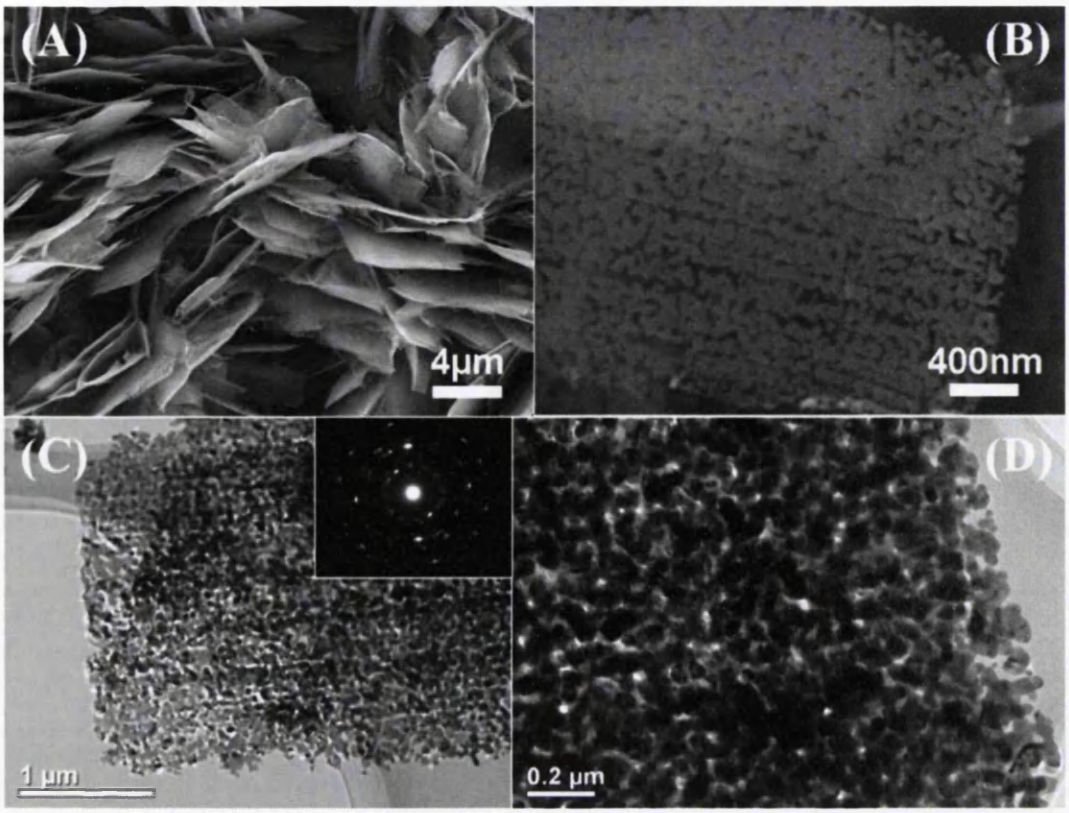

Figure 49. (A and B) SEM images and (C and D) TEM images of annealed ZnO nanosheets after annealing at 450 ° C. Inset in (C) is the corresponding electron diffraction pattern.

3.5 Sensing

In the field of the properties of materials, metal oxides represent a class of compounds, which properties cover the entire range from metals to semiconductors and insulators and also majority aspects of material science and physics including magnetism and specially superconductivity. In terms of chemical sensing and surface study, it has been revealed for more than half a century that the electrical conductivity of a semiconductor varies with the composition of the gas atmosphere surrounding it [240], and basically, gas sensing is based on these changes.

Gas sensors have a great potential in so many areas such as domestic safety, automotive applications, environmental monitoring, air conditioning in airplanes and spaceships, public security, and houses, in fact it has a great influence in modern life. So, because of this huge application range, the need of

low cost, low energy consuming, capability to detect specific gases and reliable gas sensing system has grown over the decades and caused a huge research worldwide to overcome metal oxide sensors fabrication difficulties, which is summed up in improving the well known 3S: Sensitivity, Selectivity and Stability [241].

In terms of the sensing behavior and properties, semiconductor metal oxide (SMO) such as SnO2, TiO2, WO3, ZnO, Fe2 O3 and In2 O3 either in form of thin or thick films, have been extensively investigated as well as the influence and advantages of using noble metals: Pd, Pt, Au, Ag, in improving selectivity and stability. N. Yamazoe showed that the crystallite size is of critical importance in sensor performance. Reducing of crystallite size caused a huge improvement in sensor sensitivity [241]. In nanoscale grain size SMOs, most of the carriers are trapped in surface states and only a few thermal activated carriers are available for conduction. So generally SMOs have low conductivity in room temperature and in this configuration the transition from either activated to strongly not activated or from activated to stronger activated carrier density, produced by target gases species, has a significant effect on sensor conductivity. On the other hand, increasing the temperature can increase thermal activated carriers, so the challenge became to prepare materials with the smallest possible crystallize size, which were stable when operated at high temperature for long periods. In terms of sensing layer preparation, early generation devices were fabricated by a relatively thick film deposition technology using powder form of SMOs. As the performance of the as-prepared sensor strongly depends on percolation path of electrons within intercrystalline regions, any small variations or mistakes during preparation process resulting in slight to remarkable difference between sensors characteristics and consequently sensors sensitivity and performance.

Because of this, the sensing material deposition processes have been improved towards thin film deposition technology and a more automated production and self-assembly methods through which higher reproducibility and compatibility with silicon technology could be more promising such as physical and chemical vapour deposition. However, the technological improvements went along with a decrease of sensing performance caused by lower porosity of the fabricated

devices. Both thin and thick films electrical properties drift due to grain coalescence and merging, decreasing in porosity and grain-boundary alteration. Furthermore, these effects become more significant in higher temperature because the metal oxide layers must be kept at a relatively high temperature in order to guarantee the reversibility of chemical reactions at surface. On the basis of these, several solutions have been put forward to stabilize the nanostructure such as adding of a foreign element [242] or phase [243]. Inventions of the synthesis processes to produce stable single crystal quasi-one-dimensional semiconducting oxides nanostructures, which are also called nanobelts, nanowires or nanoribbons depending on their morphology and cross sections, was a successful step forward, by simply evapourating the desired commercial metal oxide powders at high temperatures [244,245]. Their high quality of the crystallinity guarantees improved stability while the nanoscale lateral dimensions increase their sensing properties.

Among the investigations on 1D nanoparticles and 2D nanostructures such as nanosheets and thin films, several studies have been devoted to SnO (stannous oxide), SnO_2 (stannic oxide), and ZnO nanostructures and different approaches to their synthesis and fabrications [244,246–249].

3.5.1 Metal oxide gas sensors (MOGSs) mechanism

Conductometric MOGSs rely on changes of electrical conductivity due to the interaction with the surrounding atmosphere gases. The normal operation temperature of MOGSs is in general within the range between 200 and 500°C where conduction is electronic and oxygen vacancies are doubly ionized. At higher temperatures, oxygen vacancies mobility become appreciable and the mechanism of conduction become mixed ionic-electronic. MOGSs, to avoid long term changes, should be operated at temperatures low enough so that appreciable bulk variation never occurs and high enough so that gas reactions occur in a time on the order of the desired response time. Clearly when dealing with single crystals synthesized at temperatures higher than the operating

temperatures of the sensors there should not be instability problems caused by structural changes or coalescence.

When a metal oxide is operated in the semiconducting temperature range, the charge transfer process induced by surface reactions determines its resistance. In single crystal-based gas sensors the current flows parallel to the surface and is modulated by the surface reactions like the channel of a Field Effect Transistor by the gate voltage. When the channel is fully depleted, carriers thermally activated from surface states are responsible for conduction.

At the interface between metal and metal oxide, which is inevitable to connect the nanostructures to the electric circuit, metal-semiconductor junction will appear. The role that the junction plays is of critical importance in the sensing mechanism. In the case of single crystalline layers the contact resistance is more important since it is in series to the semiconductor resistance while for polycrystalline material it is connected to a large number of resistances. Density of carriers is thermally activated from surface states into the conduction band. In the case of reaction between surface of the sensing materials with chemisorbed oxygen, the density of charge decreases resulting in producing large variations of carrier concentrations, and consequently of conductivity. This can also be described as the transition from strongly activated to not activated carrier density [250].

The sensing mechanism in metal oxide gas sensors is related to chemosorption of species over their surfaces. The most important chemisorbed species when operating in ambient air are oxygen and water. At temperature range from 100 to 500°C oxygen chemisorbs over metal oxide, for instance, in a molecular O^{2-} and atomic form O^{-}, as O^{2-} has a lower activation energy it dominates up to about 200°C, while at higher temperature the O^{-} form dominates. However, reaction of reducing gases with sensing materials is different. In this case, gas detection system is based on the reactions between the species to be detected and chemisorbed surface oxygen. When a reducing gas like CO comes into contact with the surface, the following reactions may take place, Equations 1-2:

$$CO_{gas} \rightarrow CO_{adsorbed} \quad (1)$$

$$CO_{adsorbed} + O^-_{adsorbed} \rightarrow CO_{2\,gas} + e^- \quad (2)$$

These consume chemisorbed oxygen and as consequence electrons are injected into the sensing materials. The overall effect is a change of the density of chemisorbed oxygen that is detected as an increase of sensor conductivity, equations 1 and 2. Another type of reaction is direct adsorption, which is also proposed for the gaseous species, for instance, strongly electronegative NO2 that its effect is to decrease sensor conductance, Equations 3-4:

$$NO_{2\,gas} \rightarrow NO_{2\,adsorbed} \quad (3)$$

$$e^- + NO_{2\,adsorbed} \rightarrow NO^-_{2\,adsorbed} \quad (4)$$

This phenomenon can be described as the occupation of surface states, which are much deeper in the bandgap than oxygen's, resulting in increasing in the surface potential and decreasing the overall sensor conductance, equations 3 and 4.

3.5.2 CO sensing

Carbon monoxide (CO) has long been known to have dramatic physiological effects on organisms ranging from bacteria to humans. Under ambient conditions, CO is a colourless and odorless gas long associated with incomplete combustion and best known for its toxicity. Vivid descriptions of deaths attributed to "fuel gas" leaks were common in the 19th century, since CO comprised 5 to 40% of this fuel [251]. CO is a globally increasing atmospheric pollutant (150 ppb) largely generated by the burning of fuels and biomass, with apparently minor contributions from numerous biological systems [252]. In humans, exposure to urban CO levels (100 ppm) and tobacco smoke may result in a variety of symptoms that are easily mistaken for viral illnesses [253], while acute toxicity occurs at higher exposure, The lethal dose of carbon monoxide depends on concentration and duration of exposure (Table 4) [254].

CO concentration ppm	Signs and Symptoms
35 ppm (0.0035%)	Headache and dizziness within six to eight hours of constant exposure
100 ppm (0.01%)	Slight headache in two to three hours
200 ppm (0.02%)	Slight headache within two to three hours; loss of judgment
400 ppm (0.04%)	Frontal headache within one to two hours
800 ppm (0.08%)	Dizziness, nausea, and convulsions within 45 min; insensible within 2 hours
1,600 ppm (0.16%)	Headache, tachycardia, dizziness, and nausea within 20 min; death in less than 2 hours
3,200 ppm (0.32%)	Headache, dizziness and nausea in five to ten minutes. Death within 30 minutes.
6,400 ppm (0.64%)	Headache and dizziness in one to two minutes. Convulsions, respiratory arrest, and death in less than 20 minutes.
12,800 ppm (1.28%)	Unconsciousness after 2-3 breathes. Death in less than three minutes.

Table 4. The lethal dose of carbon monoxide depends on concentration and duration of exposure.

From above information, it is obvious that in terms of health and safety, detecting CO level is critically important either in industrial field or other urban areas. A variety of different CO detector gas sensors have been fabricated using MO compound as sensing materials. J. X. Wang et al. successfully fabricated *C*-axis vertically aligned ZnO nanorod arrays were synthesized on a ZnO thin film through a simple hydrothermal route [67]. The nanorods have a diameter of 30–100 nm and a length of about several hundred nanometers. Results revealed that the gas sensor fabricated from ZnO nanorod arrays showed a high sensitivity to H_2 from room temperature to a maximum sensitivity at 250°C and a detection limit of 20 ppm, Figure 50. In addition, the ZnO gas sensor also exhibited excellent responses to NH_3 and CO exposure, Figure 51.

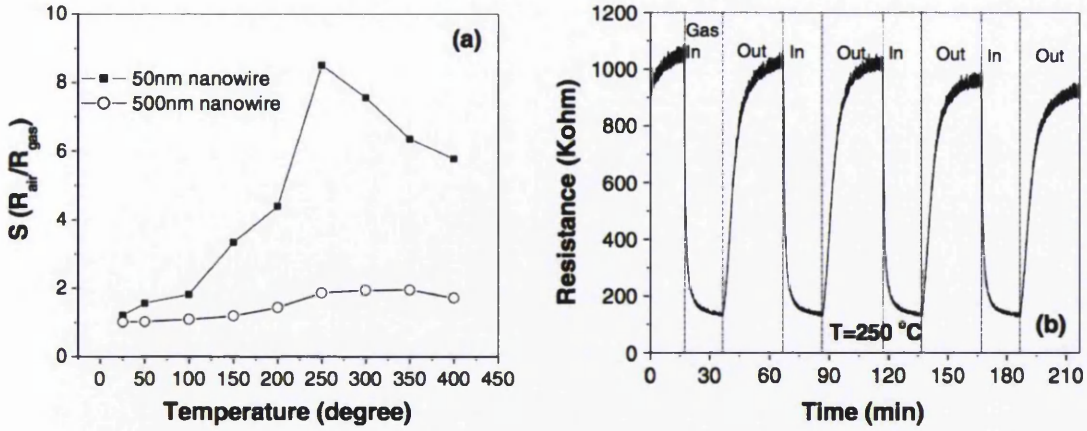

Figure 50. (a) Sensitivity *S* versus operating temperature of the ZnO nanorod with diameter less than 100 nm (solid square) and 500 nm (open circle) when exposing to 200 ppm H_2 in dry air. (b) Typical response curves of the ZnO nanorods to 200 ppm H_2 in dry air at the optimal operated temperature 250°C.

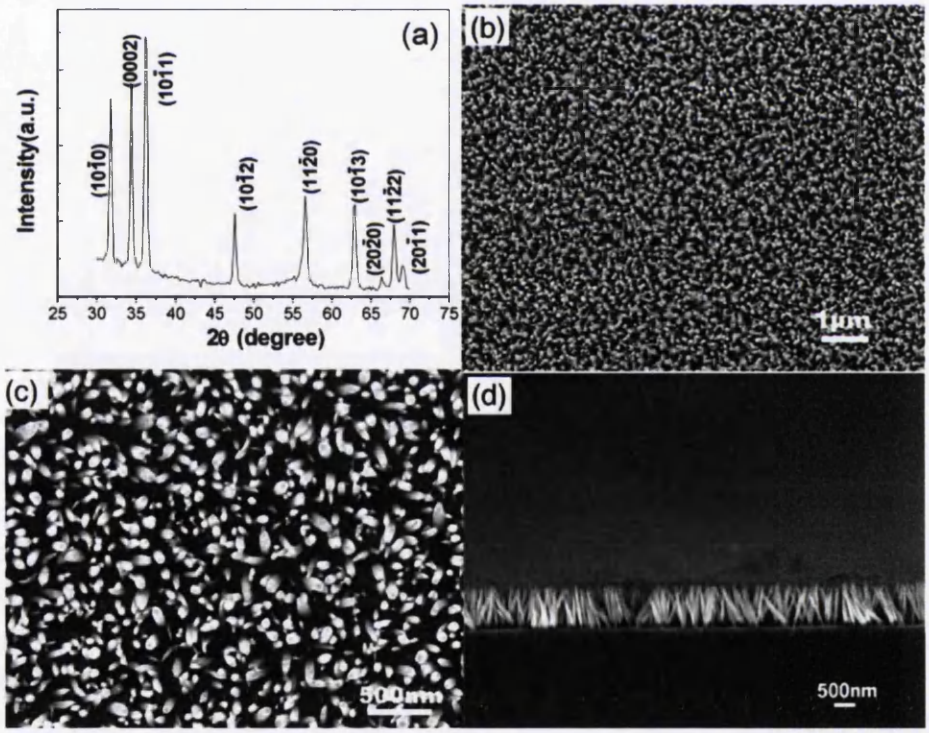

Figure 51. (a) XRD pattern of ZnO nanorod arrays. (b), (c) Typical SEM image of ZnO nanorod arrays. (d) SEM image of the cross section of the ZnO nanorod arrays.

J.F. Chang et al. successfully deposited an Al-doped ZnO films onto SiO_2/Si substrates by rf magnetron sputtering system to fabricate a CO gas sensor. The dependence of the thin film thickness on CO gas sensing properties was

investigated, where the film thickness was varied by controlling the deposition time. The CO gas sensing properties were determined by in situ measurement for surface resistance of the thin film as a function of film thickness, different atmosphere, and operation temperature. The results revealed that the films were flat and smooth with (0001) preferred orientation. The grain size was increased as the film thickness was increased during deposition Figure 52. Also results showed that, the CO gas sensing properties were relative to the structural characteristics [255].

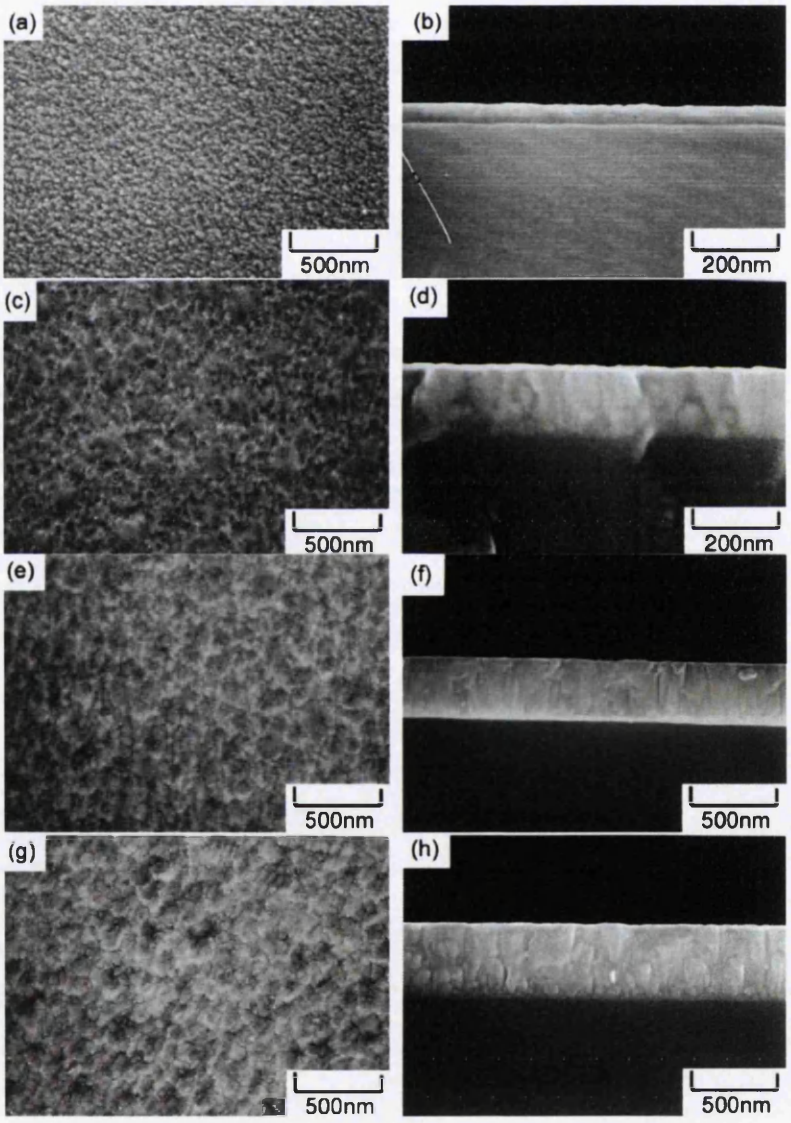

Figure 52. SEM morphology of surface and cross-section for the as-deposited AZO films with various thickness: (a, b) 65 nm, (c, d) 188.5 nm, (e, f) 280 nm and (g, h) 390 nm.

Also results showed that the grain sizes were enhanced as the film thickness was increased, which resulted in decrease in the total surface area and as a result a low sensing sensitivity. In addition, the sensitivity of the gas sensor also increased as the concentration of CO gas was increased. They showed that although the sensitivity was increased as decreasing the film thickness, the sensitivity as well as the response time was improved by increasing the operation temperature. The maximum sensitivity of 61.6% in this study was obtained for the 65 nm film at the operation temperature of 400°C [255], Figures 53-54.

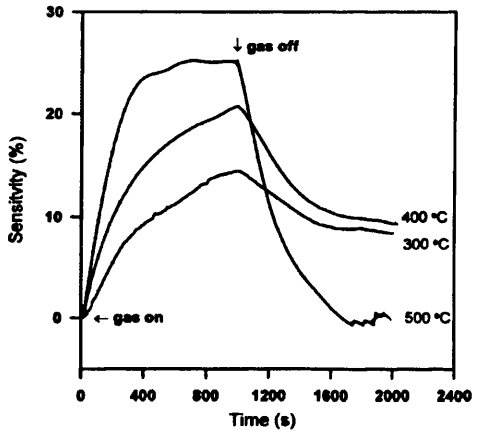

Figure 53. Effect of operation temperature in the sensitivity for as-deposited 390 nm AZO film under 1000 ppm CO atmosphere.

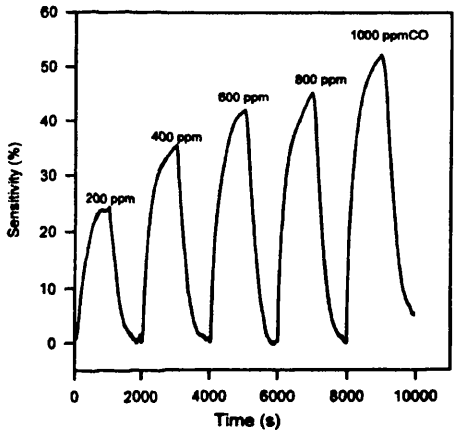

Figure 54. The effect of operation time and various CO concentration on the sensitivity of as-deposited 65 nm AZO films at 300 8C.

3.6 Summary

In this chapter the most employed techniques for ZnO nanostructure growth have been presented. In addition, the most relevant papers to this work have been reviewed including different growth techniques to synthesis ZnO nanostructure such as VPD, VCD and hydrothermal approaches focusing on nanobelts and nanosheets. Also some examples of different methods to fabricate metal oxide gas sensing and their sensitivity to CO have been revised. The main points are summarized below:

- It is possible to synthesize highly crystalline and high aspect ratio ZnO nanowires using different techniques such as PVD or CVD; however, very high synthesis temperatures and vacuum requirements limit large scaling of the substrate and, consequently, device integration, so these are expensive and time consumable routes.
- The key point is that the hydrothermal methods, in contrast, can produce ZnO nanostructures such as nanowires, nanobelts etc. at very low temperatures and atmospheric pressure over large areas and more importantly, crystal growth is possible on a wide range of different types of substrate. Due to versatility and simplicity, many researchers have investigated the hydrothermal growth techniques of ZnO nanostructures.
- But a noticeable disadvantage of using hydrothermal synthesis is the time required for the synthesis of ZnO nanostructures ranging from several hours to days.
- Microwave-assisted hydrothermal growth is an efficient modified hydrothermal route to rapid producing of nanostructures. The key point in this technique is that the reaction time is reduced to couple of seconds to minutes. But it still has some disadvantages such as using aqueous system is inevitable and the volume of the reactant solution is limited to microwave penetration in the sample.
- Synthesis of ZnO nanostructure has previously been successfully performed via different techniques. Although some of these techniques such as PVD are very efficient, the processes are very complicated, expensive and more importantly, most of time they are not exactly

reproducible. In addition, it is not possible to grow crystals on variety of substrate due to high temperature condition.

- Hydrothermal techniques may work as efficient alternative methods to PVD or CVD. Hydrothermal growth routes are simple, low cost, low temperature and also they are possible on more variety of substrates.
- Synthesis of LBZA nanostructures such as belts and sheets is simply possible through low temperature hydrothermal techniques. The as-grown particles are capable to be transformed to corresponding ZnO nanostructure via simple pyrolytic decomposition. While they can keep their shape in most cases. The obtained nanostructures have very unique and especial structure compromised of nanocrystalline nanoparticles.
- Generally, hydrothermal techniques are low cost but time consumable. The key point is that the microwave-assisted hydrothermal technique is an alternative and rapid route to produce LBZA or ZnO nanostructure just in couple of seconds to a few minutes. This happens because of fast increase in solution temperature while H_2O molecules are absorbing electromagnetic waves.
- As the measuring of the level of CO is critically important, lots of works have been done on this field focusing on fabricating more sensitive, faster and cheaper sensors.

4 EXPERIMENTAL TECHNIQUES

4.1 X-ray Diffraction (XRD)

When an X-ray beam passes a crystalline substrate, an interaction occurs between the X-ray and crystalline atoms, resulting a diffraction pattern. A.W. Hull (in 1919) published a paper about new methods of chemical analysis in which he pointed out that ".... during interaction between X-ray and crystalline structure, every crystalline substance gives a pattern; the same substance always gives the same pattern [256]; and in a mixture of substances each produces its pattern independently of the others". As about 95% of all solid materials can be described as crystalline and also the X-ray diffraction pattern of a pure matter is like a fingerprint of the substance, therefore, the powder diffraction technique is known as one of the most suitable techniques for characterization and identification of polycrystalline phases. The most important use of powder diffraction is to identify components in a sample by a search/match procedure, in addition, to quantify components, which means the areas under the peak are related to the amount of each phase present in the sample.

If an X-ray beam incident is assumed as a pair of parallel planes P1 and P2, which are separated by an interplanar spacing d (Figure 55), So the two parallel incident rays 1 and 2 make an angle (Theta) with these planes. In this case, a reflected beam of maximum intensity will result if the waves represented by 1' and 2' are in phase. The difference in path length between 1 to 1' and 2 to 2' must then be an integral number of wavelengths (λ).

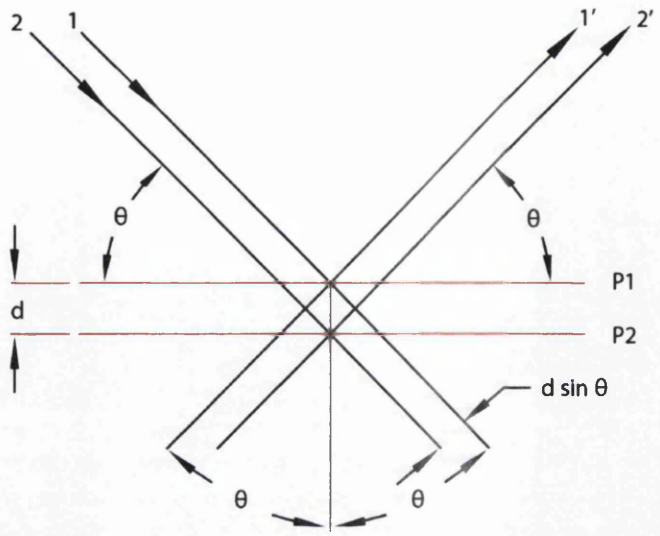

Figure 55. For parallel planes of atoms, with a space d between them, constructive interference only occurs when Bragg's law is satisfied. Each plane of atoms produces a diffraction peak at a specific angle.

W. L. Bragg explained this relationship mathematically by modeling the crystal as a set of discrete parallel planes separated by a constant parameter *d*. It was suggested that the incident X-ray beams would create a peak if their reflections off the various planes interfered constructively. So the interference will be constructive when the phase shift is a multiple of 2π. Bragg's law can define this phenomenon (Equation 5).

$$n\lambda = 2d \sin\theta \qquad (5)$$

In terms of incident and reflected (or diffracted) rays, each has an angle θ with a fixed crystal plane. Reflection rays occur from planes set at angle θ with respect to the incident beam and generate reflected beams at an angle 2θ from the incident beams. The possible *d* spacing is expressed by the shape of the unit cell. As a result, the unit cell dimensions determine the possible 2θ values where there are reflections. However, the intensity of the reflections is defined by the distribution of the electrons in the unit cell. As the highest electron density is found around the atoms in the lattice, therefore, the intensities depend on what kind of atoms are in the lattice and where in the unit cell they are located.

Consequently, planes passing through areas with high electron density will reflect strongly, while planes with low electron density will show weak intensities.

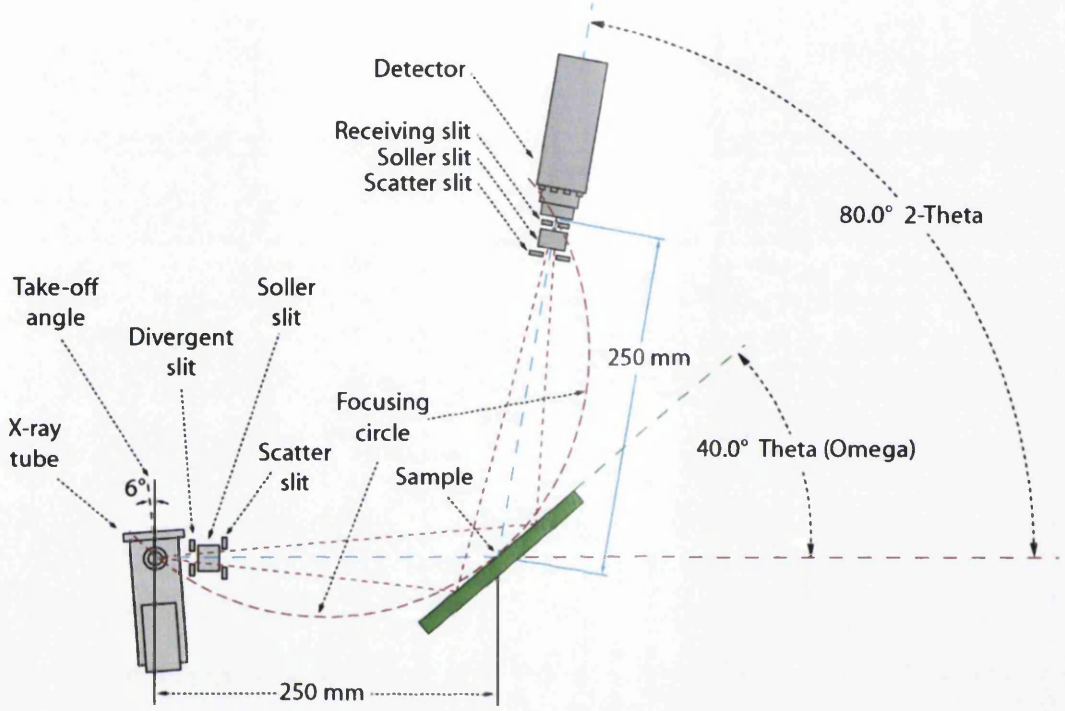

Figure 56. Illustrates schematic of θ: 2θ goniometer

Figure 56 illustrates schematic of θ: 2θ goniometer. The goniometer is generally referred to the mechanical assembly that makes up the sample holder, detector arm and associated gearing. The distance from the X-ray focal spot to the sample is the same as from the sample to the detector. If we drive the sample holder and the detector in a 1:2 relationship, the reflected (diffracted) beam will stay focused on the circle of constant radius. The detector moves on this circle.
In a θ: 2θ goniometer, the X-ray tube is stationary, the sample then moves by the angle θ and the detector moves by the angle 2θ at the same time. In contrast, in a θ: θ goniometer (Figure 57), the sample is stationary in the horizontal position, the X-ray tube and the detector both move over the angular range θ at the same time. In a θ: 2θ goniometer at high values of θ small or loosely packed samples may have a tendency to fall off the sample holder.

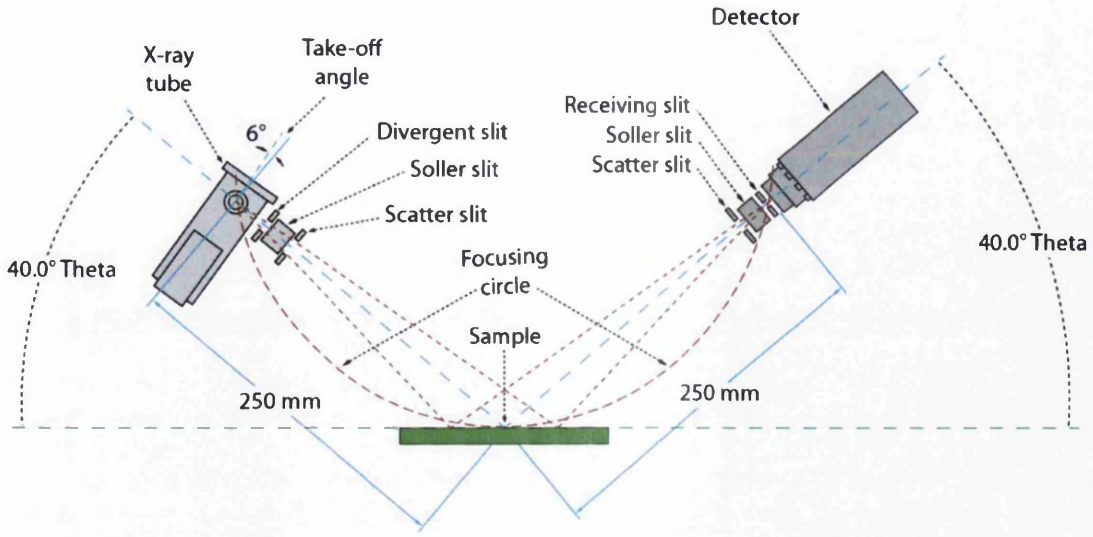

Figure 57. Illustrates schematic of θ: θ goniometer

The most important applications of XRD are identification, polymer crystallinity, residual stress and texture analysis. Identification includes search/match analysis, determinations of unit cell parameters of new materials and also investigation of high/low temperature phases and solid solutions. Basically, it is the most common use of powder (polycrystalline) diffraction is chemical analysis. A polymer can be described as a material, which is partly crystalline and partly amorphous. As the amorphous component gives a very broad peak (halo) and the crystallinity part gives sharp narrow diffraction peaks in XRD diffractogram, so measuring the ratio between these intensities can be used to calculate the amount of crystallinity in the material. Stress is defined as force per unit area. In some materials stress can be remain after an external force that caused the stress, has been removed. This is known as residual stress. Positive value of stress indicates tensile (expansion) stress while negative values are referred as a compressive state and the deformation per unit length is called strain. A residual stress can be induced via any thermal, chemical or mechanical process. Fundamentals of stress analysis using an X-ray diffraction is based on measuring angular lattice strain distributions, which includes choosing a reflection at high 2θ and measure the change in the d spacing with different orientations of the sample. And then through Hooke's law the stress can be calculated from the strain distribution.

4.2 Scanning Electron Microscopy (SEM)

An Electron Microscope (EM) instrument is made up of three main parts, the electron column, the electronic console and the computer system. Except the computer unit, all other components of an EM are usually housed in one unit. The electron column generates an adjustable electron beam with different energies; in this case (Hitachi S4800) the accelerating voltage ranges from 500v to 30Kv. In addition, the electron column components condense and focus the electron beam on specimen using condensers, reflection coils and objective lens. But scanning electron microscope is a kind of EM, which is able to scan the sample by electron beam. A computer program controls all scanning components and the imaging process including the scanning, scan speed and also visualizing and saving the image. The electronic console consists of the control knobs and switches that allow for instrument adjustments such as filament current, accelerating voltage, focus, magnification, brightness and contrast [257].

In a SEM, incident electron beam interacts with atoms from surface and produces a range of different signals through which detectors can detect information about the composition, electrical conductivity and more importantly clear image of the topography of the sample surface and dimensions of the particles. After bombarding the sample with electrons, different detectable signals will be emitted back from the sample including secondary electrons, back-scattered electrons (BSE) and also characteristic X-ray. For each type of these beams SEM employs different detectors. Back-scattered electrons can be described as a beam of electrons, which are reflected back from the surface via elastic scattering. Atomic number of the sample atoms is of importance for BSE intensity. So BSE analysis can reveal some valuable information about the distribution of different elements within the specimen. With this technique, heavier atomic number results in brighter area on SEM image.

In another hand, electron beam can cause removing an electron from inner shell of an atom. Filling this hole by an electron from higher energy shell results in

emitting characteristic X-ray. Data from such X-rays allows for measuring and quantifying the composition and abundance of respective elements in the sample.

The diagram in Figure 58 illustrates the major components of an SEM. These components are part of the primary operational systems such as vacuum, beam generation, beam manipulation, beam interaction, detection, and computer system including signal processing, displaying and recording. These systems function together to determine the results and qualities of a micrograph such as magnification, resolution, depth of field, contrast, and brightness [257].

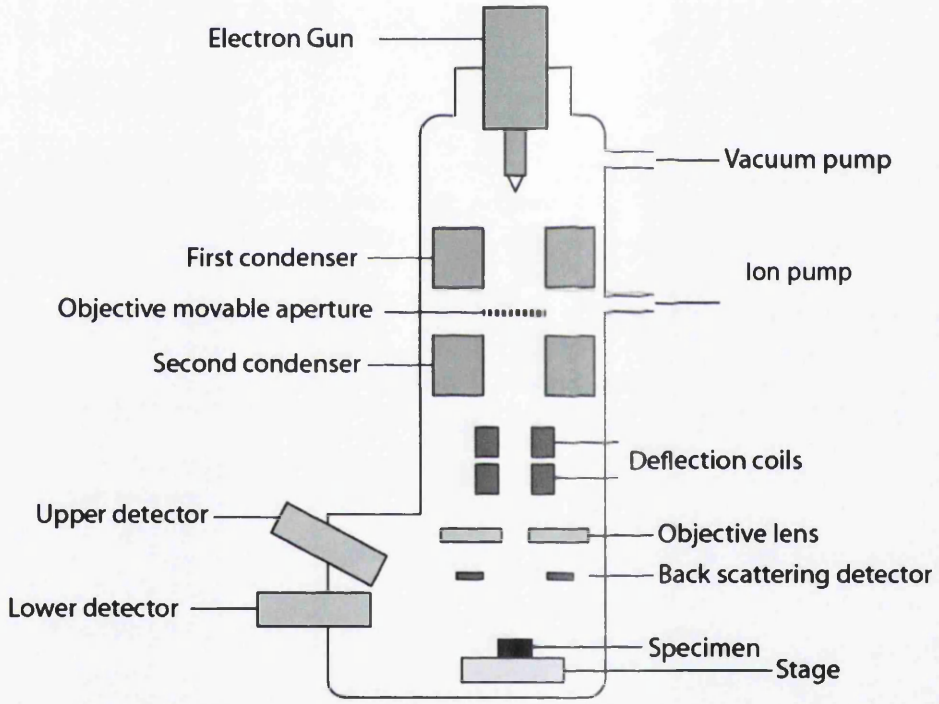

Figure 58. illustrates the major components of an SEM

A brief description of each system follows:

Basically, a SEM works in high vacuum condition; electrons behave like light only when they are manipulated in vacuum. As electrons will quickly disperse or scatter due to collisions with other atoms and molecules, consequently, the whole column from gun to sample, detectors and the camera is evacuated. The

highest vacuum achieved is of the order of a ten millionth of a millimeter of mercury, which is about 1.3×10^{-5} mbar. Different vacuum pumps are used to obtain and maintain these levels; in this case ion pumps and rotary pumps are employed.

Electron beam generator, which is generally called electron gun, is found at the top of the microscope column as shown in Figure 58. This system generates the "illuminating" beam of electrons known as the primary (1o) electron beam.

Electron beam manipulator system consists of electromagnetic lenses and coils located in the microscope column, and controls the size, shape, and position of the electron beam on the sample surface.

Detection system can consist of several different detectors, each sensitive to particular energy/particle emissions that occur on the sample such as lower and upper detectors and back scattered electrons detector.

Signal processing is provided through an electronic system that amplifies and processes the signals generated by the detectors and allows additional electronic manipulations of the image.

Display and recording system allows visualization of an electronic signal using a cathode ray tube and permits recording of the results using digital photographic procedure provided by a computer system and particular software.

4.3 Scanning probe microscopy (SPM)

As the name suggests, the heart of an SPM is a probe that is scanned over the sample surface to build up some form of image. The type of image you get depends on the interaction that is measured by the probe, Figure 59. Images can be produced that reflect many different properties of the sample. The sample height information (topography), usually forms one aspect of the image, but images can also be collected that show other properties, including mechanical, electrostatic, optical, or magnetic information about the sample surface [257].

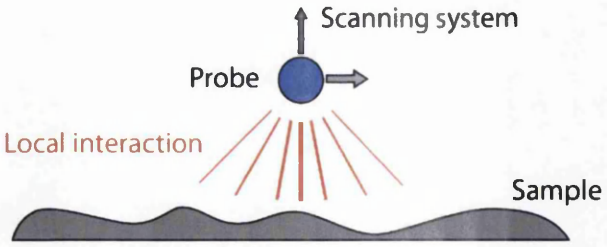

Figure 59 shows schematic interactions between the sample and probe. Scanning probe microscopy (SPM) is a probe, which is scanned over the sample surface to build up some form of image. The image type is depended on the interaction that is measured by the probe.

Different probes and measurement systems are used for some of the different properties that can be measured, but one requirement is that the interaction between the probe and the sample is localized in some way. The measured signal must be dominated by some small region of the sample close to the tip, so that an image of the sample can be formed as the tip is scanned over the surface. This implies that the interaction must have strong distance dependence, so that only the nearest parts of the sample contribute to the interaction felt by the tip. The range of the interaction will be one factor in the final resolution of the instrument. When the interaction has very strong distance dependence, such as the electron tunneling current used in scanning tunneling microscopy (STM), the resolution can be good enough to "see" individual atoms. Since the measured signal should be dominated by the small region of probe and sample that are closest together, the actual probe does not need to be an isolated point, Figure 60.

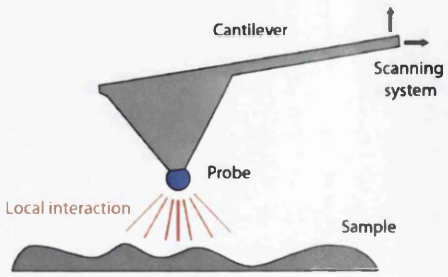

Figure 60 shows schematic of cantilever, probe and interactions between the sample and probe.

The idea of a probe measuring a local interaction and building up an image is relatively straightforward, but the actual implementation of a system with a resolution in this range is technically challenging. Many factors came together in the development of scanning probe microscopy, including the development of piezoelectric materials that made it possible to reproducibly position and scan components with a sub-nanometer precision.

4.3.1 Atomic force microscope (AFM)

AFM is one of the scanning probe microscopes families, and is widely used in nanoscale characterization (surface study at nanoscale) and biological applications. AFM uses a flexible cantilever as a type of spring to measure the force between the tip and the sample. The basic idea of an AFM is that the local attractive or repulsive force between the tip and the sample is converted into a bending, or deflection, of the cantilever. The cantilever is attached to some form of rigid substrate that can be held fixed, and depending whether the interaction at the tip is attractive or repulsive, the cantilever will deflect towards or away from the surface [258].

This cantilever deflection must be detected in some way and converted into an electrical signal to produce the images. The detection system that has become the standard method for AFM uses a laser beam that is reflected from the back of the cantilever onto a detector. The *optical lever* principle is used, which means that a small change in the bending angle of the cantilever is converted to a measurably large deflection in the position of the reflected spot as shown in Figure 61, 62.

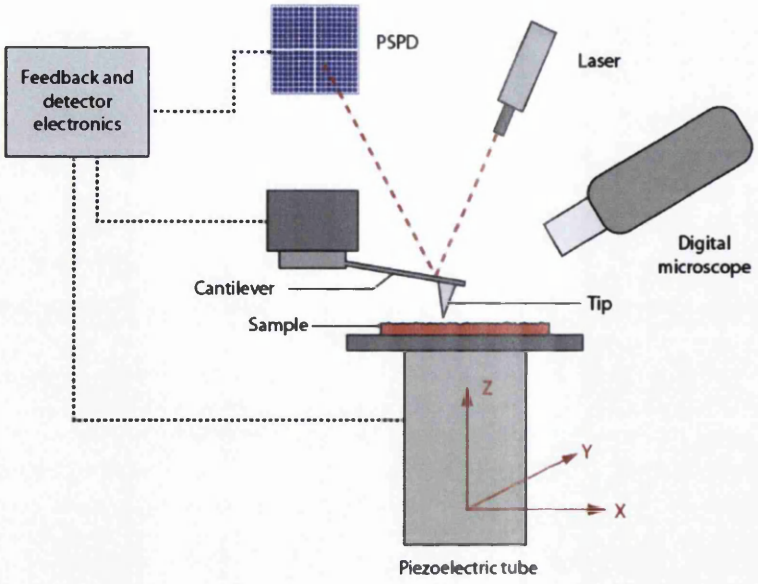

Figure 61. Schematic of typical AFM and its different components

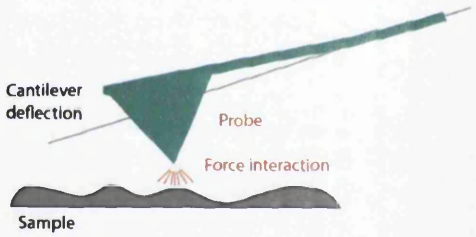

Figure 62 shows deflection of the cantilever

The position of the laser spot is measured by comparing the signals from different sections of the detector. Most AFMs use a photodiode that is made of four quadrants, so that the laser spot position can be calculated in two directions, by comparing the signals. The vertical deflection (measuring the interaction force) can be calculated by comparing the amount of signal from the "top" and "bottom" halves of the detector. The lateral twisting of the cantilever can also be calculated by comparing the "left" and "right" halves of the detector, Figure 63. The force contrast gives 3-dimensional topography information, as well as the possibility to access other information such as the mechanical properties or adhesion.

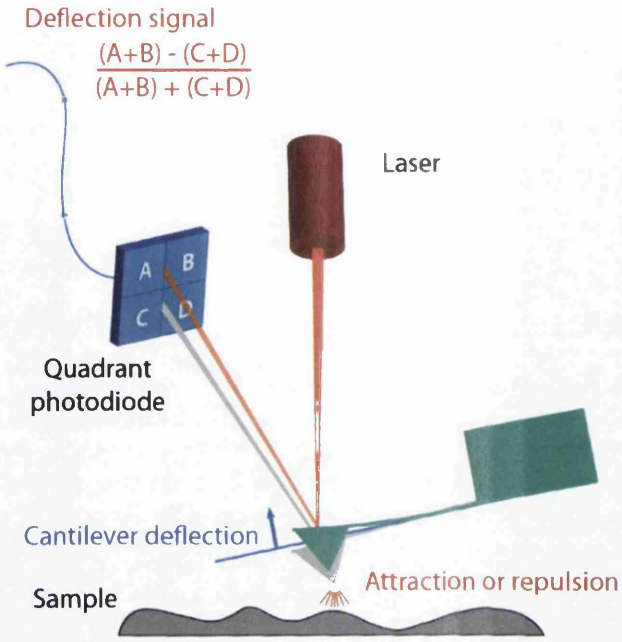

Figure 63. Illustrates that how different positions of the laser spot are used to generate surface topography

AFM is particularly suited for biological applications, because the samples can be imaged in physiological conditions. There is no need for staining or coating, and no requirement that the sample should conduct electrons. Therefore high-resolution imaging is possible in physiological buffer or medium, and over a range of temperatures. Living cells can be imaged, as well as single molecules such as proteins or DNA.

AFM makes computer generated 3D topography information from sample surface; also it is capable to provide more information such as the mechanical properties or adhesion. Basically, there are three primary imaging modes in AFM, Table 5.

AFM mode	probe-surface separation (nm)
Contact AFM	< 0.5
Intermittent contact (tapping mode AFM)	0.5-2
Non-contact AFM	0.1-10

Table 5. Illustrates different AFM modes and corresponding probe-surface separation

4.3.1.1 Contact mode

The detection system measures the cantilever response as the tip is moved over the surface by the scanning system. In most AFM systems there is also a feedback loop, which adjusts the position of the cantilever above the surface as it is scanned, to take account of the changes in surface height. A value of the cantilever deflection, for example, is selected and then the feedback system adjusts the height of the cantilever base to keep this deflection constant as the tip moves over the surface. This is known as contact mode imaging, Figure 64.

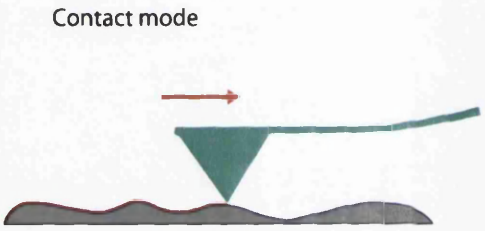

Figure 64. Schematic of the tip position in contact mode

There are other ways of operating the system, however, using dynamic modes where the cantilever vibrates, and this oscillation of the cantilever is measured rather than the static deflection of the tip. There are different ways to excite the oscillations - the cantilever substrate can be shaken directly, or a magnetic field can be used to drive the cantilever itself if it is coated with a ferromagnetic layer. In aqueous conditions, the most common technique is to drive the cantilever acoustically through the liquid. However, in all these cases, the measurement of the cantilever oscillation and control systems are the same, and the cantilever is usually driven close to resonance. In these dynamic modes, set point amplitude is chosen, and the height adjusted to match this amplitude through the feedback system. In addition to the height and error signal information from this constant amplitude mode, the phase between the drive signal and the cantilever can also be measured. There are several different dynamic modes, depending on how much of the oscillation cycle the tip actually makes contact with the surface.

4.3.1.2 Intermittent contact mode (tapping mode)

This mode is widely used, and can give a combination of the benefits of the other modes. The cantilever oscillates and the tip makes repulsive contact with the surface of the sample at the lowest point of the oscillation. The lateral forces can be much lower than contact mode, since the proportion of the time where the tip and sample are in contact is quite low. However, there may be a higher normal force between the tip and sample when they are in contact, Figure 65.

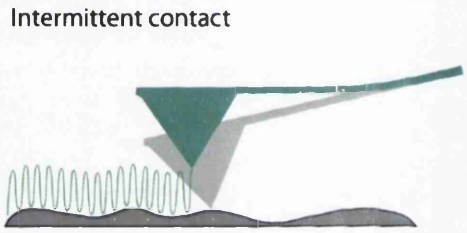

Figure 65. Illustrates the tip position and movement over the sample surface.

4.3.1.3 Non-contact mode

In this mode the cantilever oscillates close to the sample surface, but without making contact with the surface. This mode is not so widely used, since the attractive force means that there is a possibility of the tip jumping into contact with the surface, Figure 66. The capillary force makes this particularly difficult to control in ambient conditions. Very stiff cantilevers are needed so that the attraction does not overcome the spring constant of the cantilever, but the lack of contact with the sample means that this mode should cause the least disruption.

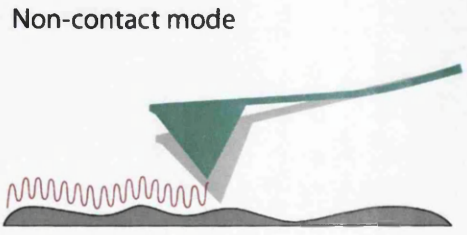

Figure 66. Illustrates the tip position and movement over the sample surface.

4.3.1.4 Force modulation mode

Another mode is possible, where the tip does not leave the surface at all during the oscillation cycle. This is something like a dynamic form of contact mode, and is usually called force modulation mode, Figure 67.

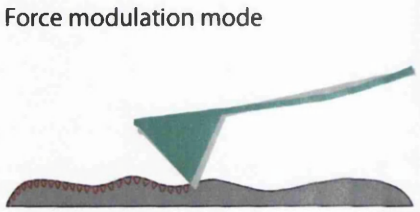

Figure 67. Illustrates the tip position and movement over the sample surface.

4.3.2 Cantilevers and spring constants

Different imaging modes tend to use cantilevers with different properties. In contact mode, the deflection of the cantilever is controlled as the tip is scanned over the surface. A softer cantilever means that a lower force can be used to give the same deflection. Often lower forces give better imaging, so the softest cantilevers are generally used for contact mode imaging, Figure 68. Many cantilevers are available with spring constants (k) below 0.5 N/m. Stiffer cantilevers are usually used for intermittent contact mode, particularly in air.

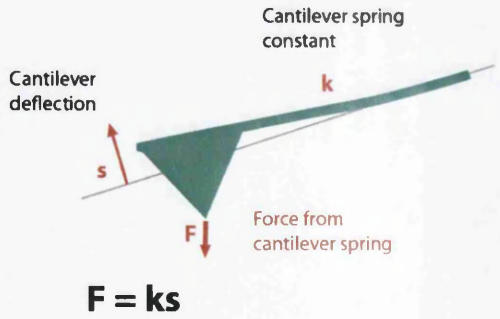

Figure 68. Different imaging modes tend to use cantilevers with different properties

These generally have a resonant frequency of 200 - 400 kHz, and spring constants of more than 10 N/m. These stiffer cantilevers give more stable

imaging in air, since the cantilever is able to break free of the capillary forces when the tip touches the sample. As there can be very low average deflection values during careful imaging, the stiffer cantilevers do not damage the surface. For intermittent contact mode in liquid, the capillary force is not a problem, and softer cantilevers are often used. "Contact mode" cantilevers are often used for intermittent contact mode in liquid conditions. The resonant frequencies are much lower, and the damping of the liquid around the cantilever has a strong effect on the resonance. The spring constant of a cantilever can be estimated from its geometry and the properties of the material it is made from. The spring constant depends very strongly on the thickness of the cantilever, however, and this can be difficult to measure accurately. If a calibrated reference cantilever is available, then the cantilevers can be pushed against one another to compare the deflection of one cantilever by the other, and hence measure the spring constant of the unknown cantilever. For soft cantilevers, another option is to measure the thermal noise and calculate the spring constant. This is an attractive option, since the cantilever is not damaged by the measurement, and no extra equipment is required.

4.4 Applications of different AFM imaging modes

4.4.1 Nanoscale surface characterization

The highest resolution images are usually employed to image single molecules immobilized on a surface such as glass or mica. It is also possible to study crystals and nanostructures or even protein sub-structure and organization, particularly in 2-dimensional protein crystals. This can also be successful with membrane proteins, in conditions that would not allow 3-dimensional crystallization for standard structural investigations. Long nanostructures or molecules such as nanobelts, nanowires can be imaged and investigated to determine their thickness and 3D structures, also biological samples such as DNA or glycoproteins can be studied to measure intrinsic properties such as the persistence length, or interactions with bound proteins. The samples do not

need coating or staining and can be imaged in air or liquid. In addition, they can be studied in action, for example enzymes such as collagenase or amylase digesting their substrate [259].

4.5 X-ray photoelectron spectroscopy (XPS)

The XPS method is employed to investigate the chemistry at the surface of a specimen (about 10 nm) [260]. Figure 69 illustrates the basic mechanism behind the XPS technique in which photons of a specific energy are used to excite the electronic states of atoms below the surface of the sample. The hemispherical analyzer (HSA) provides energy filtering, before the detector records the intensity of defined energy electrons ejected from the surface of the sample. Since core level electrons in solid-state atoms are quantized, the resulting energy spectra exhibit resonance peaks characteristic of the electronic structure for atoms at the sample surface. Although, depends on the energy of the X-ray, it may penetrate deep into the sample, the escape depth of the ejected electrons is limited. The ejected electrons from depths greater than 10nm (for energies around 1400 eV) have a low probability of leaving the surface without experiencing an energy loss event. As a consequence, these electrons contribute to the background signal rather than well-defined primary photoelectric peaks.

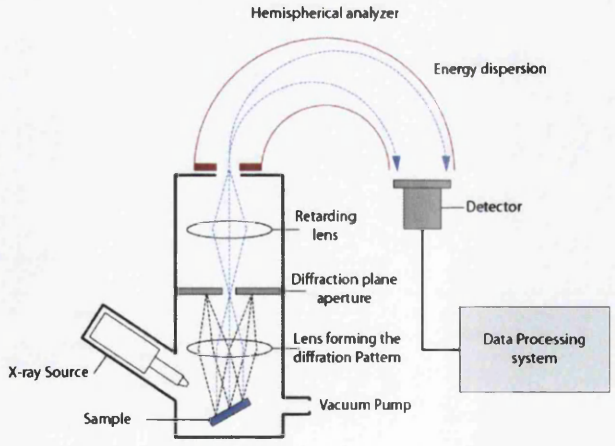

Figure 69. Illustrates the basic mechanism behind the XPS technique in which photons of a specific energy are used to excite the electronic states of atoms below the surface of the sample

Fundamentally, the energies of the photoelectric lines are well defined in terms of the binding energy of the electronic states of atoms. In addition, the chemical environment of the atoms at the surface resulting in well-defined energy shifts to the peak energies. While in conducting samples for which the detected electron energies can be referenced to the Fermi energy of the spectrometer, an absolute energy scale can be established, thus aiding the identification of species.

In contrast, identification of the species for non-conductive samples is more complicated due to difficulties of energy calibration. Electrons leaving the sample surface cause a potential difference to exist between the specimen and the spectrometer resulting in retarding field acting on the electrons escaping the surface. So a correction system is employed to reduce error in identification of chemical species. This charge compensation designed to replace the electrons emitted from the sample to reduce the influence of the sample charging in insulating materials, but without correction system, consequence can be peaks shifted in energy by as much as 150 eV. However, identification of chemical state based on peak positions requires careful analysis, Figure 70.

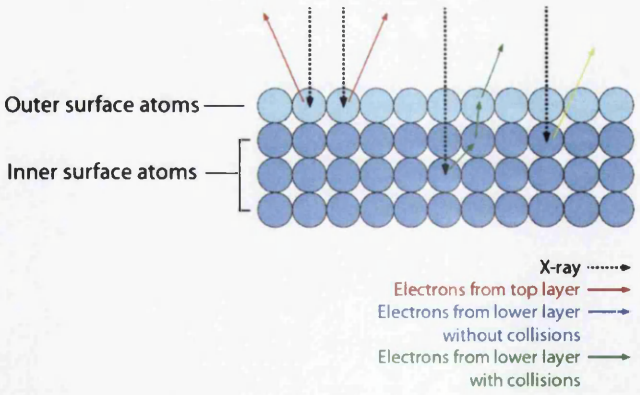

Figure 70. Illustrates different possible pathways for excited electrons of the sample surface

In a typical XPS experiment, the surface is scanned before and after a series of surface treatments such as heating at increasing temperatures, ion bombardment or incremental metal deposition. Plotting the variation of the

binding energy of the elements present at the surface as a function of surface treatments is a standard data analysis technique. This gives information about the chemical and electronic changes induced by the surface treatments

Fermi shifts indicate surface electronic changes. The "signature" of a Fermi shift is that all core levels from all the elements present at the surface shift by the same amount.

Chemical shift indicates chemical reactions are taking places. Only the binding energy of elements, which are involved in the reaction, will change. The core level peak shape is also likely to become broader as more chemical states are present. Basically, elements can be bonded to each other and other elements in different ways such as covalent bonding, ionic bonding etc. As a result, electrons in the constituent atoms of a molecule or crystal are distributed differently. Consequently, the energy levels will change to some extent and the energy, which needs to be supplied to remove an electron, is altered. Thus the precise value of the binding energy measured by XPS will depend on the chemical environment of the electron. Changes in binding energy from the value expected for a simple pure element are called Chemical Shifts. So the presence of chemical bonding (and hence, neighbouring atoms) will cause binding energy shifts. It could be used to obtain information of a chemical nature (such as atomic oxidation state) from the sample surface. Therefore, XPS is also defined as Electron Spectroscopy for Chemical Analysis (ESCA). The binding energy shifts range from 0.1 to 10eV.

Since the number of the electrons recorded for a given transition can be considered as the number of atoms at the surface, so potentially XPS is a quantitative technique. From chemical shifts in XPS data, valuable information about surface of the sample can be obtained. Changing the angle of the sample with respect to the axis of the analyzer resulting in changing the sampling depth for a given transition and the composition varies with depth, consequently, different data is obtained at different angles. The chemical shift reflects the influence of the chemical bonds with neighboring atoms. The chemical shift in the X-ray spectra is caused by changes in the electron binding energies. The more specific reason is about the electro-negativity effect in the presence of

another atom. For example, in the C-O bond, due to the electro-negativity of oxygen, C 2p electron in valence level will be attracted by atom O, and C 1s electron in core level will tend to be attracted by carbon nucleus so that the binding energy of C 1s electron will shift to higher binding energy. Therefore we shall here consider different ways of calculating the electron binding energy of an atom or a molecule, methods that can also be used to evaluate chemical shifts.

4.6 Photoluminescence (PL)

Photoluminescence (PL) is the spontaneous emission of light from a material where an intensive light such as laser beam is used for optical excitation [261]. In a PL instrument the excitation energy and intensity of the light are adjustable in order to investigate different regions of the sample and also to adjust the excitation concentrations in the sample. PL investigations can be used to characterize a variety of material parameters. PL spectroscopy provides electrical (as opposed to mechanical) characterization, and it is a selective and extremely sensitive probe of discrete electronic states. Features of the emission spectrum can be used to identify surface, interface, and impurity levels and to gauge alloy disorder and interface roughness. The intensity of the PL signal provides information on the quality of surfaces and interfaces. Under pulsed excitation, the transient PL intensity yields the lifetime of non-equilibrium interface and bulk states. Variation of the PL intensity under an applied bias can be used to map the electric field at the surface of a sample. In addition, thermally activated processes cause changes in PL intensity with temperature. PL is simple, versatile, and nondestructive. The instrumentation that is required for ordinary PL work is modest: an optical source and an optical power meter or spectrophotometer. A typical PL set up is shown in Figure 71. Also Figure 72 shows the PL set up used in this work. Because the measurement does not rely on electrical excitation or detection, sample preparation is minimal. This feature makes PL particularly attractive for material systems having poor conductivity or undeveloped contact/junction technology. Measuring the continuous wave PL intensity and spectrum is quick and straightforward. On the other hand,

investigating transient PL is more challenging, especially if recombination processes are fast. Instrumentation for time-resolved detection, such as single photon counting, can be expensive and complex. Even so, PL is one of the only techniques available for studying fast transient behavior in materials.

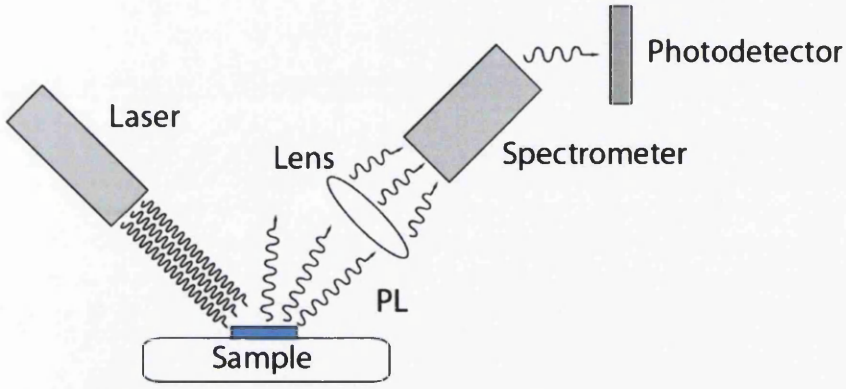

Figure 71. Typical experimental set up for PL measurements

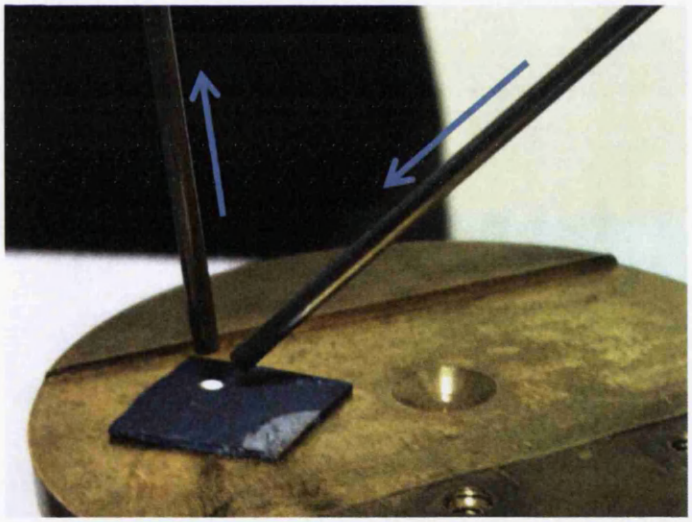

Figure 72: photograph of the PL set up used in this work. The probe on the right carries the laser light and the photoluminescence signal is gathered by the left probe and carried to the spectrometer.

The fundamental limitation of PL analysis is its reliance on radiative events. Materials with poor radiative efficiency, such as low-quality indirect bandgap semiconductors, are difficult to study via ordinary PL. There is a similar

scenario for identification of impurity and defect states depends on their optical activity. Although PL is a very sensitive probe of radiative levels, one must rely on secondary evidence to study states that couple weakly with light.

Figure 72 shows a close up picture of the set up used in the work with a ZnO nanowire array as the sample under investigation. The excitation light is produced by a HeCd laser at 325nm with a power of 8mW. The light is carried by optical fibres through a 325nm band pass filter (10nm width) to clean up the light and delivered to the sample. The photoluminescence is collected by another optical fibre, through a 340nm long pass filter to cut off any reflected laser light, and carried to an USB Ocean optics spectrometer.

4.7 Microwave-assisted crystal growth

4.7.1 History

Like many great products in history, the microwave oven is also a product of past technologies. In 1940s during World War II, scientists invented the magnetron, which is a tube capable to produce electromagnetic waves. In World War II, Magnetrons were used in radar technology in order to spot enemy's warplanes on their way. Several years later, it was Accidently discovered that microwaves also cook food by Dr. Percy Spencer. It was during a radar-related research project around 1946 that, he noticed something very unusual. During testing a new type of magnetron, he discovered that the candy bar in his pocket had melted [262]. In 1947, the first microwave oven in the world was built. It was almost 1.8 m tall, weighed 340 kg and cost about $5,000 each. It consumed 3 kilowatts, about three times as much as today's microwave ovens, and it needed a water-cooling system. During past decades, several scientists and companies worked on developing the microwave ovens, but in the 1960s, Litton bought Studebaker's Franklin Manufacturing assets, which had been manufacturing magnetrons and building and selling microwave ovens. Finally, Litton then successfully developed a new configuration of the microwave, the short, wide shape that is now common. In addition, the magnetron feed was also unique. In

1970s, the microwave oven became a more commonly owned kitchen appliance than the dishwasher, for instance, reaching nearly 60%, or about 52 million only in U.S.A. Microwave can increase the temperature of the food or target materials through a process called dielectric heating (also known as electronic heating, high-frequency heating, radio frequency (RF) heating and diathermy) in which a non-ionizing high-frequency alternating electric field (or radio wave or microwave electromagnetic radiation) heats a dielectric material resulting in rotating polarized molecules such as water and fats and consequently, molecules align themselves with the alternating electric field of the microwaves. Molecules alternate at the same frequency of the microwave, which is about 2.45 GHz in the case of kitchen microwave ovens. This molecular movement is the mean reason of temperature rising at high frequencies, however, at lower frequencies in conductive fluids, other mechanisms such as ion-drag are more important in generating thermal energy. The frequency used in commercial microwave (2.45 GHz) is more efficient on water compared to other organic and inorganic materials within the foods. Water molecules start alternating and absorbing the microwave energy, so temperature of the object increases rapidly but it hardly goes higher than 100°C (water boiling point). So microwave heats it by its own internal water content. In this study, for microwave-based experiments, water was used as a solvent so all reactions between the chemicals and crystal growths are in aqueous system (microwave-assisted hydrothermal), which will be explained in experimental chapter.

4.7.2 Theoretical aspects

Microwave energy absorbed per unit volume P_{abs} by a material depends on dielectric and magnetic properties of this material, in addition to electric and magnetic field strength as described by the following equation [263]:

$$P_{abs} = 2\pi f\left(\varepsilon_0 \varepsilon''_{eff} E^2_{rms} + \mu'' H^2_{rms}\right) \qquad (6)$$

where f is the operating frequency of microwave radiation, ε_0 is the dielectric permittivity of free space, ε'' is the effective relative dielectric loss factor, E_{rms} is root mean square of the internal electric
field, μ'' is magnetic loss factor, and H_{rms} is root mean square of the internal magnetic field.

In the case of non-magnetic materials, Equation (6) becomes for dielectric materials as follows [264]:

$$P_{abs} = 2\pi f \varepsilon_0 \varepsilon''_{eff} E^2_{rms} = 2\pi f \varepsilon_0 \varepsilon'_r \tan\delta E^2_{rms} \qquad (7)$$

where the relative dielectric constant (ε'_r) and the loss tangent (tan δ) are the two most commonly used and measured parameters that illustrate the behavior of a dielectric material under the effect of a microwave irradiation [265].

In the case of dielectric material (solid or liquid) and assuming negligible diffusion and heat losses, the majority of the absorbed microwave power per unit volume is converted into thermal energy within the dielectric material, as shown in the following equation

$$\frac{\Delta T}{\Delta t} = \frac{P_{abs}}{\rho C_p} = \frac{2\pi f \varepsilon_0 \varepsilon''_{eff} E^2_{rms}}{\rho C_p} = \frac{2\pi f \varepsilon_0 \varepsilon'_r \tan\delta E^2_{rms}}{\rho C_p} \qquad (8)$$

where ρ is the density, C_p is the specific heat capacity, ΔT is the temperature rise or the rate of heating and t is the time.
According to Debye and Stokes' theorem, the relaxation time (τ) of dipole rotation (a spherical or nearly spherical rotating dipole with radius r) is given by the following equation [266,267]:

$$\tau = \frac{4\pi\eta r^3}{kT} \qquad (9)$$

where η is the viscosity of the medium, k is Boltzmann's constant, and T is the temperature. Relaxation data for pure water play an important role in the study of the dielectric properties of aqueous solutions [268].

According to the information that we have gathered, the main controlling factors of forming zinc acetate and ZnO nanosheets are the concentration of surfactant SDS and hexamethylenetetramine. As in this study there is no surfactant, therefore, in the deionized-water system, different basicity was provided by hexamethylenetetramine decomposed with different concentration. The chemical equation is listed as follows:

$$C_6H_{12}N_4 + 10H_2O \rightarrow 4NH_3.H_2O + 6HCOH \quad (10)$$

In this system Zn^{2+} source for Equation (12) could be provided as follows:

$$2\,Zn(NO_3)_2.6H_2O \xrightarrow{Hydrolytic\ decomposition} 2Zn^{2+} + 4OH^- + 4H^+ + 2H_2O \quad (11)$$

The overall reaction in the system can be expressed by the following equation:

$$Zn^{2+} + C_6H_{12}N_4 \rightarrow Zn^{2+} - aminocomplex \rightarrow Zn(OH)_2 \rightarrow ZnO \quad (12)$$

Another possible chemical reactions throughout all stages of the microwave-assisted fast growth of the LBZA crystals can be described as follows:

$$2Zn(NO_3)_2.6H_2O \rightarrow 2Zn(OH)_2 + 4H^+ + 4NO_3^- + 2H_2O \quad (13)$$

Equation 13 shows the hydrolysis of zinc nitrate hexahydrate and possible chemical compounds and ions. H. Tada [269,270] suggested that in an acidic media, protonated ammonia can be produced undergoes hydrolytic decomposition from protonated hexamine. Equation 13 can provide both an acidic media and protons to make protonated hexamine so it can be described as follows:

$$\left[(CH_2)_6N_4 + 4H^+\right] + 6H_2O \rightarrow 6CH_2O + 4NH_4^+ \quad (14)$$

Our pH measurements before and after reactions revealed that the pH of the mixture was 6.3 and 6.2 respectively.

$$4Zn(CH_3COO)_2 + H_2O \xrightarrow{\text{microwave (MW) irradiation}} Zn_4O(CH_3COO)_6 + 2(CH_3COOH) \quad (15)$$

Zn^{2+} could be provided through equation (12) and may react with acetic acid obtained in Equation (15) to produce more zinc acetate and back to the left side of the Equation (15) as a source of zinc acetate to synthesize more nanosheets under microwave irradiation and can be described as follows:

$$2(CH_3COOH) + Zn^{2+} + 2OH^- \rightarrow Zn(CH_3COO)_2 + 2H_2O \quad (16)$$

In the case of microwaving more than 120s (the results revealed that 120s±20 is optimized microwaving time), SEM imaging showed that LBZA NSs started changing morphology to hexagonal structures. And in the case of continuing microwave irradiation, after 180s the product included only a white precipitation of micron-sized zinc oxide hexagonal crystals 101 and 102. It might be either due to microwave irradiation or over heating caused by microwave irradiation. The possible reactions can be described as follows:

$$Zn(OH)_2 + H_2O \xrightarrow{(MW)irradiation} Zn^{2+} + 2OH^- + 2H_2O \quad (17)$$

$$Zn(OH)_2 + 2OH^- \longleftrightarrow Zn(OH)_4^{2-} \quad (18)$$

$$OH^- + OH^- \longrightarrow O^{2-} + H_2O \quad (19)$$

$$Zn(OH)_2 + 2H_2O \xrightarrow{(MW)irradiation} Zn^{2+} + 2OH^- + 2H_2O \quad (20)$$

$$\xrightarrow{(MW)irradiation} Zn(OH)_4^{2-} + 2H^+$$

$$Zn(OH)_4^{2-} + Zn(OH)_4^{2-} \xrightarrow{(MW)heating} Zn_2O(OH)_6^{4-} + H_2O \quad (21)$$

$$Zn(OH)_6^{4-} + Zn(OH)_4^{2-} \xrightarrow{(MW)heating} Zn_3O_2(OH)_8^{6-} + H_2O$$

$$\xrightarrow{(MW)heating} Zn_xO_y(OH)_z^{(z+2y-2x)-} + H_2O \quad (22)$$

$$Zn^{2+} + O^{2-} \xrightarrow{(MW)irradiation} ZnO \quad (23)$$

In the ZnO crystal structure, each Zn^{2+} cation is surrounded by four O^{2-} anions, and according to Equations (20) and (21), the particle size of the cluster $Zn_xO_y(OH)_z^{(z+2y-2x)-}$ must reach a certain value z to form the initial ZnO crystal nucleus [271].

4.8 Gas sensing apparatus

In this study, DC conductometric gas sensors have fabricated in-house to investigate the sensitivity of as-grown ZnO nanoparticles including nanocrystalline ZnO nanosheets and nanobelts. Each sensor consists of an alumina substrate (about 5x6 mm) that on its topside platinum interdigitated electrodes are printed, while a platinum heater is printed on another side to control the experiment temperature as shown in Figure 73.

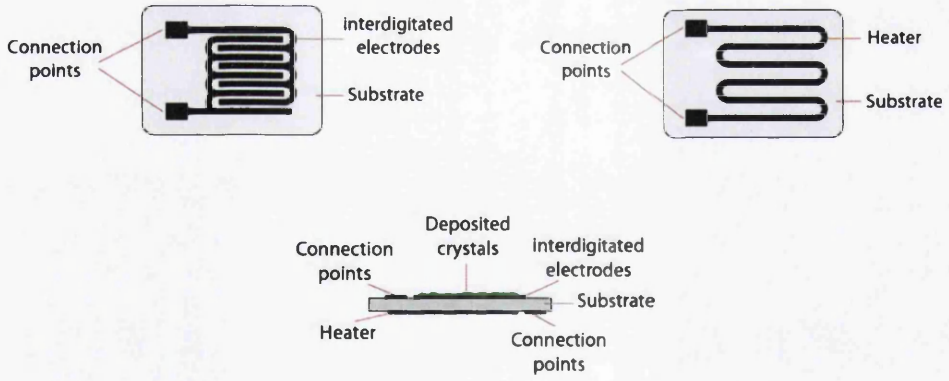

Figure 73. Illustrates a schematic of as-fabricated gas sensor, top-left: interdigitated electrodes, top-right: heater and the bottom: side view of sensor

The gas sensing apparatus (Figure 74), developed in-house, consisted of an array of four mass flow controllers (MFCs), a vacuum chamber, sensor holder, and a Keithley 2000 multimeter connected to a PC for data acquisition. Two of the MFCs were used to produce dry air from zero grades O_2 and N_2, while another MFC regulated a pre-mixed flow of 1000ppm of CO in N_2. Controlling of

the CO concentration in the test chamber was possible by adjusting the CO flow rate and the synthetic airflow rate to the desired ratio. The last MFC was used for a compensatory flow of N_2 while the sensor was not being exposed to the CO/N_2 mixture. This ensures the total flow remained constant throughout the experiments and, more importantly, that the oxygen concentration within the test chamber remained unchanged; thus, any change in the sensor's resistance was solely due to the presence/absence of CO. Care was taken when designing the apparatus to avoid pressure build up in the gas lines, which could greatly affect both the speed and magnitude of the sensor's response to CO. The response is defined as the ratio of the resistance in air and the resistance in the presence of CO.

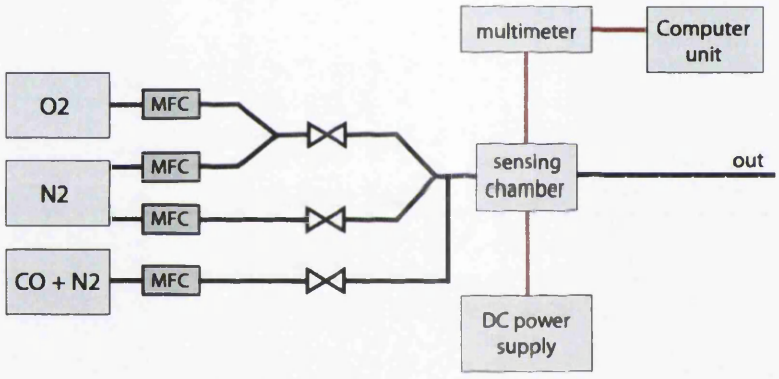

Figure 74. Illustrates the gas sensing apparatus consists of an array of four mass flow controllers (MFCs), a vacuum chamber (sensing chamber), a DC power supply to provide and control the sensor substrate temperature and connected to a computer unit multimeter for data acquisition. Two of the MFCs were used to produce dry air from zero grades O_2 and N_2, while another MFC regulated a pre-mixed flow of 1000ppm of CO in N_2. Controlling of the CO concentration in the test chamber was possible by adjusting the CO flow rate and the synthetic airflow rate to the desired ratio. The last MFC was used for a compensatory flow of N_2 while the sensor was not being exposed to the CO/N_2 mixture.

5 RESULTS AND DISCUSSION

As it is mentioned before, most of the techniques used to grow ZnO nanoparticles, such as using furnace and autoclave, are energy and time consuming. In addition, not only the majority of them include several organic or inorganic compounds but also they have remarkably complicated process. So hydrothermal techniques may provide a significant alternative route to produce nanostructures at lower temperature, lower cost, less complicated and, possibly, in some cases faster, for instance microwave-assisted technique.

In this chapter, an improved recipe for the synthesis of LBZA nanobelts and their complete characterization is presented in section 5.1, followed by an investigation into the influence of pH and temperature. Next, their thermal decomposition into ZnO is investigated in section 5.2

Section 5.3 and 5.4 describe a rapid, novel microwave assisted synthesis for LBZA nanosheets and their pyrolytic transformation in to nanocrystalline ZnO

Finally section 5.5 shows the results of the gas sensing tests performed using sensors fabricated from both the nanosheets and nanobelts.

5.1 LBZA Nanobelts

5.1.1 Experimental procedure

13.17 g of zinc acetate dihydrate (Sigma-Aldrich) was added to 600ml of deionized water (room temperature about 20°C). Solution was stirred using magnetic stirrer to achieve clear homogeneous mixture. Then solution was divided into smaller beakers (it is not necessary but it may make easier handling and transferring the samples) and sealed using aluminum foil. Beakers were transferred to dry oven adjusted at 65°C (in this research a fan-assisted dry oven has been used to provide uniform air convection and uniform distribution of heat within the oven). After 20 hours, a jelly-like-phase (Figure 75) was appeared including a high yield of LBZA nanobelts, shown in Figure 77. Depending on different use purposes, as-grown nanobelts were stored in their

original solution or washed with deionized water and turn to white circle shaped thin papers using vacuum filtration system, as shown in Figure 75. Figure 76 illustrates schematic diagram of vacuum filtration system.

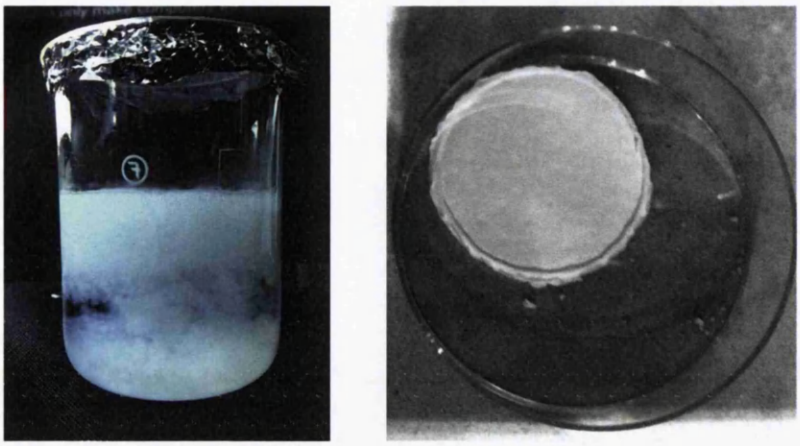

Figure 75. (left) Shows jelly-like-phase grown nanobelts after 20 hours at 65°C, (right) shows white paper shaped nanobelts after vacuum filtration

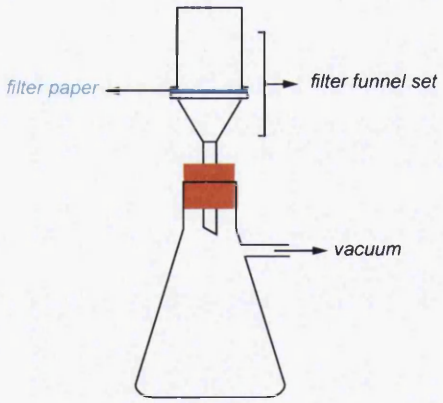

Figure 76 . Schematic diagram of vacuum filtration system

5.1.2 SEM imaging

Figure75(a) shows a low magnification SEM image of the dried jelly-like phase, which has made a thick network of LBZA NBs grown at 65°C. The sample prepared by immersing a clean silicon substrate into the jelly-like phase followed by drying at 65°C in a pre-heated dry oven, as a result, dispersed nanobelts on silicon wafer made a thick white membrane. The thickness of the

membrane is reasonably controllable by increasing or decreasing the deposited jelly-like LBZA NBs or in the case of making a really thick layer with repeating the process of immersing and drying as many times as needed. So the coverage could be in nano or micro scale.

As it can be seen in Figure 77(a) the NBs show typical ribbon-like morphology with widths ranging from 200 nanometres to couple of micrometres and lengths of up to 250 μm. The NBs width along their length appears uniform with sharp and smooth edges. This uniformity could be one the advantages of them, because the shape and the size of nanoparticles have significant influence on the electrical and optical properties, so steady properties can make them more trustable and a good candidate for a specific purposes such as using in micro or nano devices. The high magnification SEM image of Figure 77(b) shows two types of typical morphology, NBs with uniform flat top surface and NBs made up of two distinct thick layers, but each of these layers has also a uniform flat top surface. The different shapes could be a consequence of the layered growth mechanism. Arrows point towards fine steps at the edge of the flat NB, showing evidence of lamellar growth. The surface of the NBs appears reasonably smooth and free of defects.

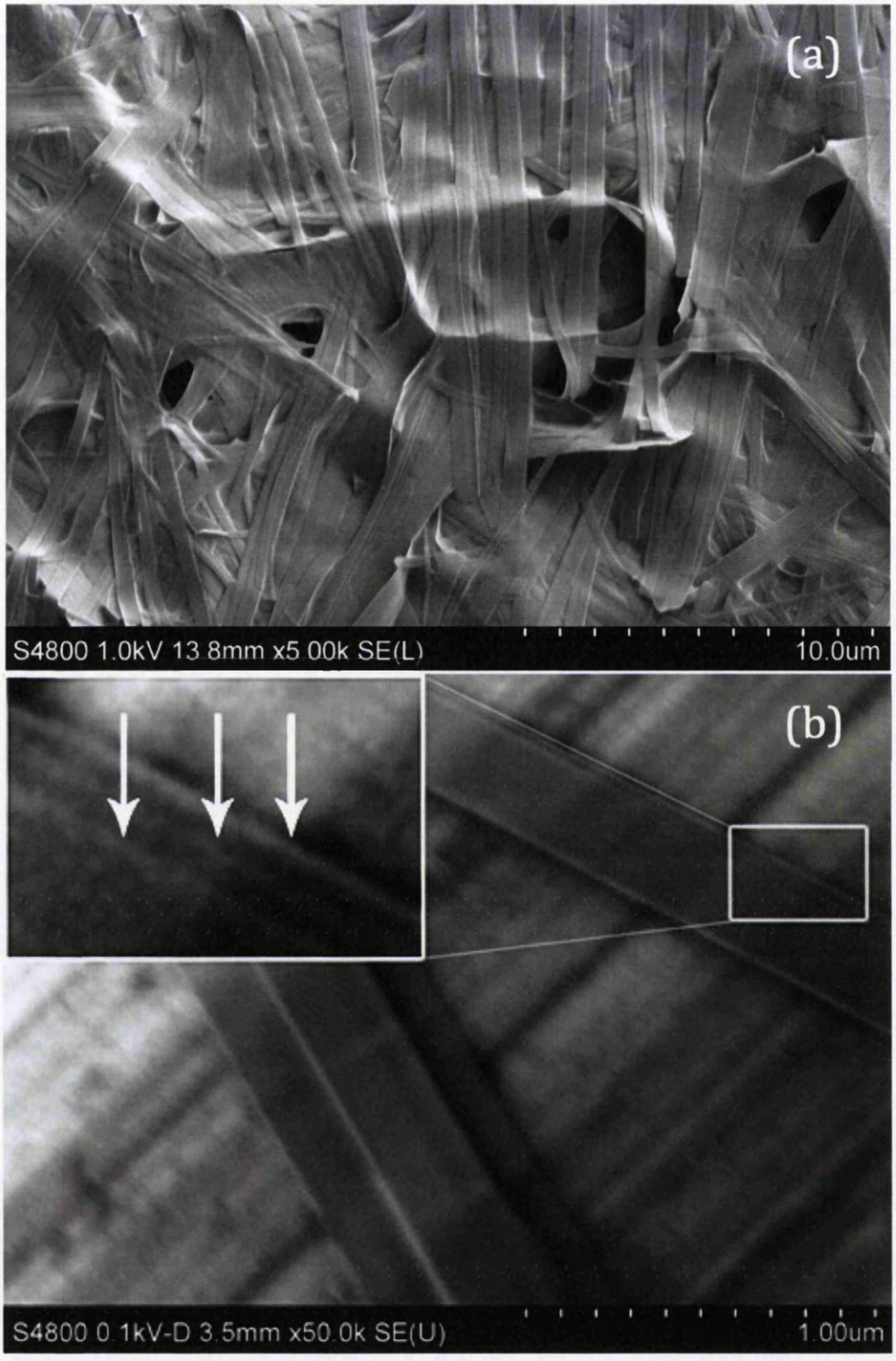

Figure 77. Shows the SEM images of LBZA NBs after drying at 65°C. (a) Thick membrane showing the range of widths and lengths, and (b) isolated NBs showing the layered structure. The arrows in (b) point to steps at the edge of the NB, confirming the layered morphology of the NB.

5.1.3 AFM imaging

A droplet of diluted suspension of LBZA NBs was put on a clean silicon wafer. After drying at 65°C, the samples were imaged using AFM tapping mode. Figure 78(a) and Figure 79(a) are the AFM imaging of the as-grown NBs. Figure 78 shows several NBs of various widths and distinctive longitudinal terraces clearly apparent on the top of some NBs, which confirms the results from SEM. Figure 79(a) is a close up image of a double layered NB, similar in morphology to the SEM image of Figure 77(b). In Figure 79(b), cross sectional line profile of LBZA NB confirms that the height of each of the two layers is about 20nm. The flat NBs displayed in Figure 78(b) have a height of 22 and 24nm, as shown in their cross sectional line profile. AFM measurements revealed that the height of the LBZA NBs ranges from 10 to 50nm but most of them range from 20 to 25nm. To the best of our knowledge the height of LBZA NBs has not been systematically measured before, although Cui et al. reported an approximate thickness of 50nm from side view SEM images [238]. Also it is in good agreement with X. Y. Kong et al [272] who used the side viewing technique of the NBs using SEM imaging and reported that the NBs have a uniform shape and their average thickness is about 15 nm. They also reported the nanorings, which are initiated by folding nanobelts into a loop with overlapped ends due to long-range electrostatic interaction among the polar charges and the thickness of the NBs composing the nanorings is measured to be about 10 nm [272].

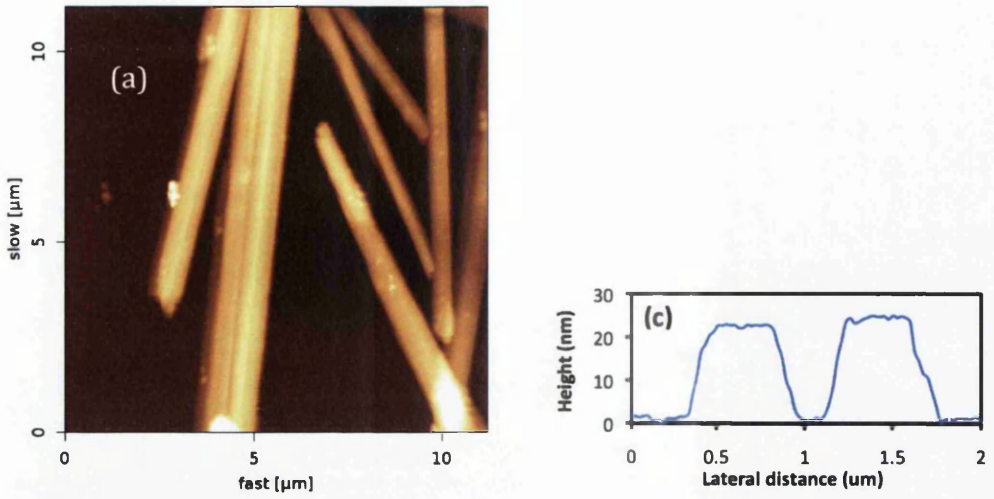

Figure 78. AFM tapping mode image of LBZA nanobelts, height profiles taken across the dashed arrows.

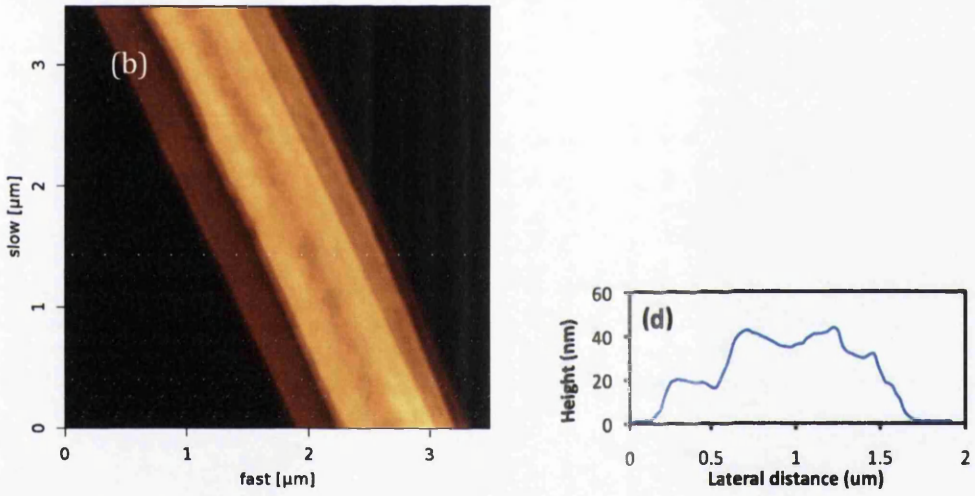

Figure 79. AFM tapping mode image of as-grown LBZA NBs, showing the characteristic layered structure, height profiles taken across the dashed arrows.

5.1.4 XRD results

The LBZA crystal structure has been previously reported to be similar to that of $Zn_5(OH)_8(NO_3)_2{\cdot}2H_2O$ [273,274]. Three-fifths of Zn^{+2} ions are octahedrally surrounded by six OH^{-1} groups and the rest of them are located above and below the empty octahedral and form tetrahedra composed of three OH groups and one water molecule. The resulting structural unit is a complex layer of $[Zn_5(OH)_8(H_2O)_2]^{2+}$, which has a positive charge. Acetate anions are intercalated between the layers. The overall crystal structure can be indexed in the hexagonal system according to XRD data [275]. Figure 80 shows low angle XRD

diffractogram of the as-grown LBZA nanobelts, illustrating that the NBs are crystalline with the characteristic main zinc acetate 001 peak at 6.67°, corresponding to an interplanar spacing within a single layer of 1.32nm, which is confirming their composition as $Zn_5(OH)_8(CH_3COO)_2.2H_2O$ [238,273] also all the diffraction patterns agree with that of LBZA [274,275]. The peaks at 13.35° and 20.07° are assigned to the 002 and 003 reflections and correspond to interplanar distances of 0.66 nm and 0.44nm, respectively. The peaks labeled $001^{(b)}$ and $002^{(b)}$ at 4.48° and 8.90° are assigned to the first and second order reflections corresponding to an interplanar distance of 1.97nm for the first order reflection. The second group of reflections was also reported by H. Zhang et al. [276] and Q. Cui et al. [238]. Our diffractogram also shows weaker peaks at 14.56° and 21.87°, which may be attributed to the second and third order of a third group of reflections. The first order peak for this reflection would then be at 7.28°, corresponding to an interplanar spacing within a single layer of 1.21nm, but would be masked by the main $001^{(a)}$ peak at 6.67°. The two peaks at 14.56° and 21.87° could also be discerned on the diffractogram published by H. Zhang et al. [276], however they did not appear as intense and were not discussed.

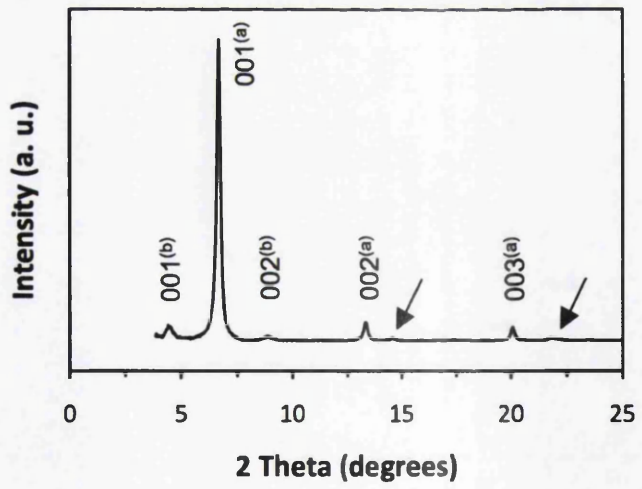

Figure 80. Low angle XRD diffractogram of the as-grown LBZA nanobelts showing characteristic zinc acetate peaks corresponding to interplanar spacing of 1.32nm and 1.97nm for the $001^{(a)}$ and $001^{(b)}$ reflections, respectively. The arrows at 14.56° and 21.87° point to weaker peaks, suggesting a third interplanar spacing at 1.21nm

5.1.5 Influence of Zinc Acetate concentration

The optimized pH in order to obtain a high yield of LBZA nanoparticles has been previously reported about 7.2 or 8.2 [238,272,276]. These groups increased the pH using different organic and inorganic compounds such as hexamethylenetetramine (HMTA), ammonia or sodium/potassium hydroxide, but, as it is described in method and materials, the mixture was simply prepared by dissolving only zinc acetate dihydrate in deionized water. For this reason, in constant concentration (in this case 0.1 M) the pH of the mixture will be reasonably constant. In addition, adding such an organic or inorganic compounds to increase the pH was not found to be necessary in this study, as a pH of 6.4-6.5 yielded large quantities of NBs. With every other parameter kept constant, we investigated the role pH played in the formation and quantity of the final product; the results revealed that pH less than 6 (zinc acetate dihydrate concentration of 0.25 M or more) resulted in no LBZA NBs (assessed either visually or with SEM imaging). In contrast, a pH higher than 8 resulted in mostly ZnO nanoparticles, including micron sized hexagonal crystals, Figure 81. It is in contrast to Zhang et al who reported that the optimum pH of 8.2 [276] but in good agreement with Cui et al [238] results in which optimum pH was found about 7.2. They also reported similar white ZnO precipitates at higher pH.

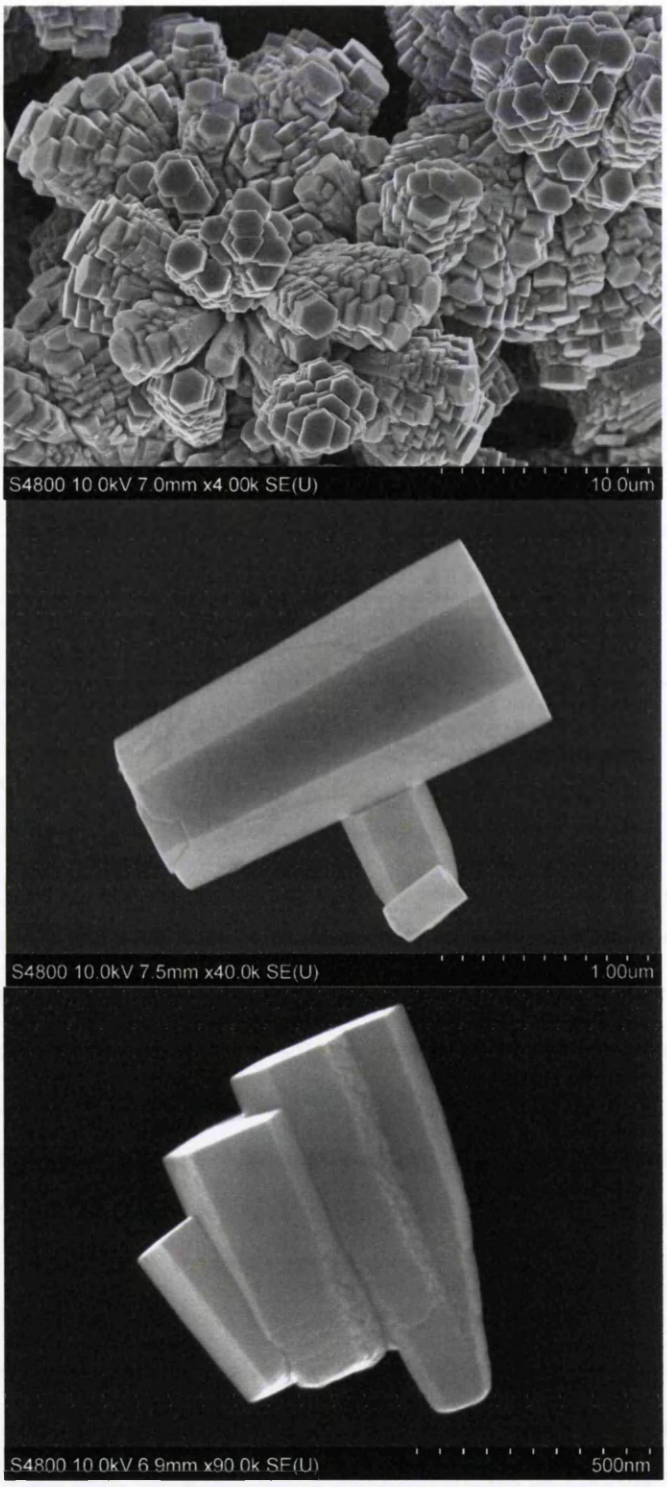

Figure 81. Shows SEM images of grown products after adding ammonium hydroxide to the zinc acetate solution to raise the pH to 8. All other growth parameters were unchanged. After heating at 65°C for 22 hours, no NBs had grown and the result included only micron-sized hexagonal crystals.

In terms of the solubility of a salt in water, it is well known that, if the cations have a different hydrolysis degree as that of anions in water, the pH of such salt aqueous solution could be either higher or lower from neutral pH. It is also known that the pH value of a solution is the primary factor determining the stable hydrolytic state of a metal ion aqua complex. Therefore, it is expected that the chemistry and morphology of the zinc compounds formed in the zinc acetate solution, including LBZA and ZnO micro/ nanocrystals, strongly depend on the pH of the solution. In order to further study of the mechanism of the reaction process, the pH value of the precursor (zinc acetate solution) was measured as a function of zinc acetate concentration; results are shown in Figure 82. The results clearly show that the pH of the zinc acetate aqueous solutions gradually reduces with increasing zinc acetate concentration. Therefore, concentration dependent pH reduction can suggest that the Zn^{2+} ions hydrolyze more than $CH3CHOO^-$ ions in water. In theory, the soluble ions should be charged metal ion Zn^{2+} or hydroxo complexes $Zn(OH)^-$ under acidic conditions. The uncharged hydroxo complexes $Zn(OH)_2$ occurs under neutral and moderately basic pH conditions. However, negatively charged $Zn(OH)_3^-$ and $Zn(OH)_4^{2-}$ hydroxo complexes will form at alkaline conditions. The results clearly indicate that when the concentration of $Zn(CH3CHOO)_2$ solutions is less than 0.2 M, and consequently, the corresponding pH is in a range of 6.0–7.0, then the hydroxo complexes $Zn(OH)^-$ is the major form for zinc compounds in the zinc acetate solutions. As a result, according to the pH between 6.0 – 7.0 and the hydroxo complexes $Zn(OH)^-$ ratio, the basic zinc salts are presented in the precipitate. In addition, Figure 80 reveals that, in different concentrations of $Zn(CH3CHOO)_2$ higher than 0.25 M, the total pH of the solution is about 6 or less and in such condition, there is another chemical equilibrium in which the Zn^{2+} ions are the most dominant ions in the solution. So as a consequence, it is obviously expected that, no precipitate could be observed in the concentrations of zinc acetates more than 0.25 M due to the low pH condition. In contrast, in the concentrations less than 0.02 M the pH of the solution is higher than 6.8, and results showed that pure ZnO nano or submicron particles could be obtained.

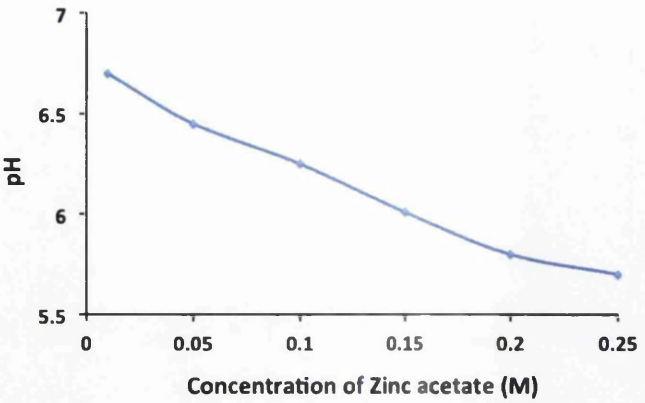

Figure 82. pH changes as a function of zinc acetate concentration (M)

Both equations (24 and 25) can be considered as a growth mechanism, which are suggested according to our findings in this research. Presence of CH_3COOH in right side of this equation may explain decrease in pH value after finishing the growth reaction and also may explain why there is no more growth after reaching equilibrium. Increasing pH can shift the equilibrium position to the left side and vice versa.

$$4Zn(CH_3COO)_2 + H2O \rightarrow Zn_4O(CH_3COO)_6 + 2(CH_3COOH) \quad (24)$$

$$5Zn(CH_3COO)_2{\cdot}2H_2O + n\ H_2O \rightarrow Zn_5(OH)_8(CH3COO)_2{\cdot}2H_2O + CH_3COOH + n\ H_2O \quad (25)$$

These equations are in good agreement with the suggested equation by E. Hosono et al. [116]. The results revealed that, at temperatures less than 45°C, no NBs had grown, it seems that to start the reaction, a temperature over 45°C is necessary otherwise chemical equilibrium is shifting to dissolving rather than formation of LBZA crystals (left shifting). Because the hydrolytic reaction is an endothermic reaction, the hydrolytic equilibrium moved to the favorable direction for hydrolysis with increasing temperature, so that Zn^{2+} cations combine more easily with OH- to form LBZA or ZnO. Also SEM imaging confirmed that after 22 hours no NBs had grown. In contrast, increasing the temperature to 60-65°C resulting in significant changes in the growth mechanism, so the equilibrium position has been shifted to the right (Equation 1 and 2).

pH measurements after 20-22 hours (the time which is required for growing) showed that the pH was around 6.5, which can be explained by presence of CH3COOH in the right side of the Equation 1 and 2. Whereas increasing the growth temperature to higher than 80-85°C resulted in precipitation of micron sized hexagonal ZnO crystals in a variety of sizes. Figure 83 shows SEM imaging of growing LBZA NBs at temperature about 80-85°C. It also shows that a range of micron sized hexagonal crystals has been grown. The optimum NB growth temperature for our parameters was found to be 65°C.

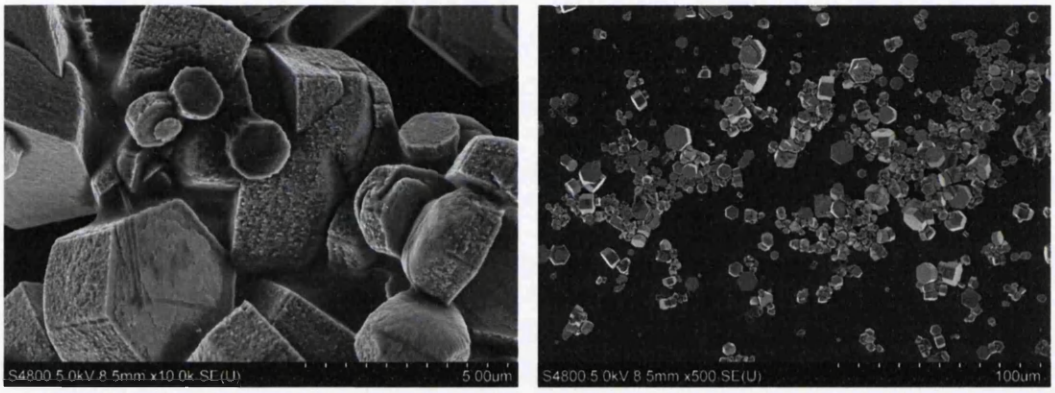

Figure 83. SEM imaging of as-grown LBZA NBs at temperature about 80-85°C and it shows that a range of micron sized hexagonal crystals

5.2 Thermal decomposition into ZnO nanobelts

Pyrolytic transformation of the LBZA nanoproducts such as nanobelts and nanosheets to the corresponding ZnO nanoparticles has previously studied in which heating the LBZA NBs resulted in the formation of polycrystalline ZnO via thermal decomposition [123,238,276,277]. As it is explained, LBZA in aqueous system was produced via hydrothermal system using zinc acetate dihydrate in deionized water. It is suggested that, during LBZA transformation to ZnO, Equation 26 may explain the OH^- groups gradually replaced the acetate groups coordinated to the matrix zinc cation, and the acetate groups were released completely. Finally, the $Zn(OH)_2$ and ZnO were formed at high temperature. The conversion process from $Zn(CH_3COO)_2$ to ZnO with release of acetate anions can be described as:

$$Zn(CH_3COO)_2.2H_2O \rightarrow Zn_5(OH)_8(CH3COO)_{2\ (LBZA)} \rightarrow Zn(OH)_2 \rightarrow ZnO \quad (26)$$

It is in good agreement with the experiment performed by Y. Wang et al in which they investigated pyrolytic decomposition of different LBZA nanoparticles and their corresponding products. They suggested that zinc acetate in hydrothermal system makes the bilayered basic zinc acetate (BLBZA) and annealing them resulting in transformation of BLBZA to LBZA to $Zn(OH)_2$ and then to ZnO [274].

5.2.1 XRD and SEM results

In this study, LBZA NBs were annealed at different temperatures 110-1000°C in air using a furnace for 10 minutes in each temperature. The pyrolytic transformation is confirmed by the XRD data of Figure 84, which shows the changes in the diffraction spectra when annealing temperature increases. Annealing at 110°C did not change the crystal structure significantly but after the 210°C, the XRD measurements showed distinct Wurtzite ZnO peaks (JCPDS # 01-079-2205). This is in good agreement with Cui et al. who reported a transition to ZnO after annealing in air at 150°C. However, annealing at higher temperature generally increased the intensity of the Wurtzite ZnO peaks and decreased their FWHM (Full width at half maximum), indicating an increase in crystallite size with temperature which is in good agreement with Wurtzite structured ZnO [116].

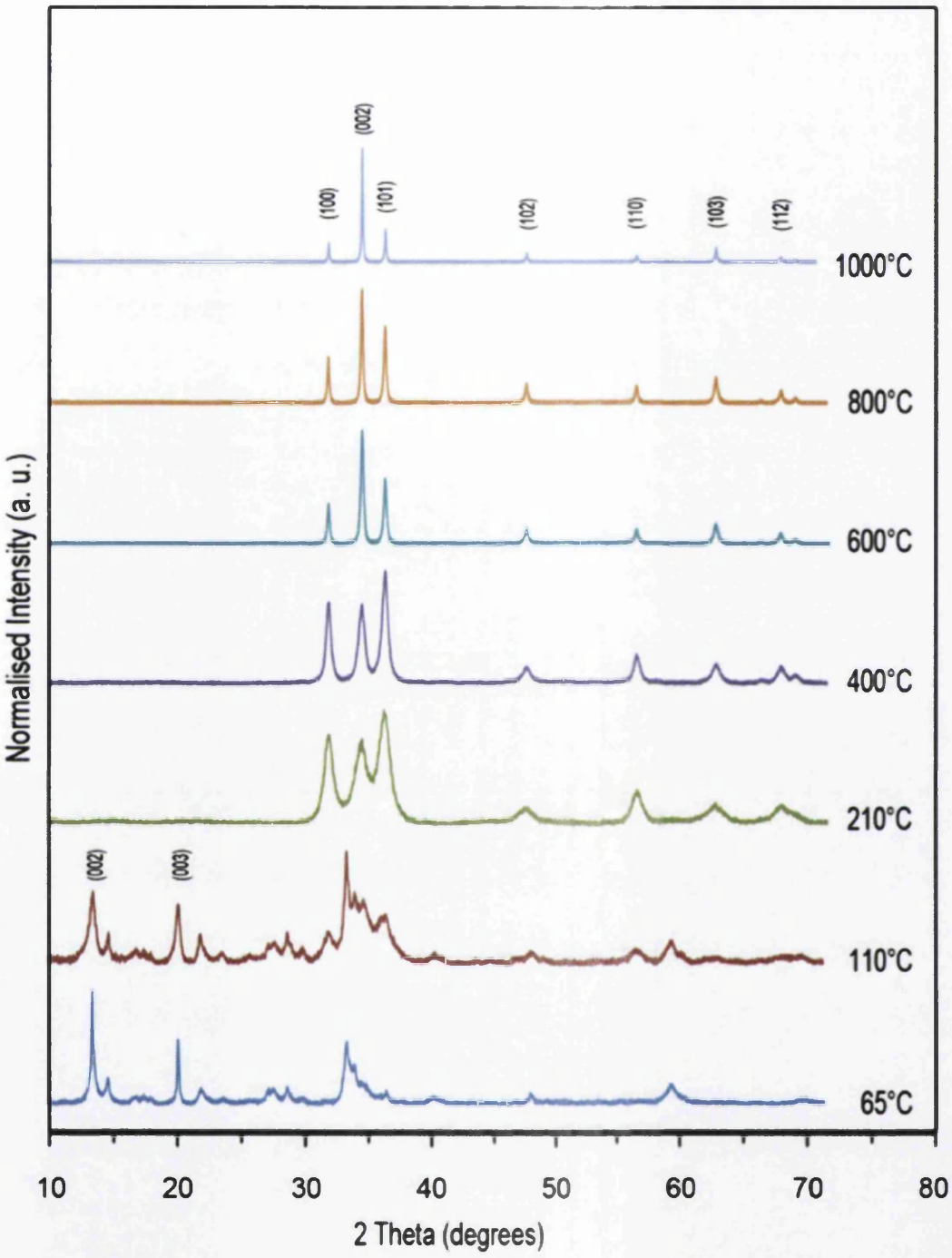

Figure 84. XRD measurements of as-grown LBZA NBs (65°C), and after annealing at increasing temperatures from 110 to 1000°C

SEM images of corresponding NBs after annealing the as-synthesized LBZA NBs at increasing temperatures from 110°C to 1000°C are shown in Figure 85, as it can be seen, increasing the temperature resulting in increasing the grain sizes

within NBs. SEM size analysis was performed for temperatures from 210°C to 1000°C and revealed that, the size of the particles in ZnO nanocrystalline NBs is temperature dependent. Table 6 shows the results from SEM size analyzing and XRD data. SEM shows that the average particle size for NBs annealed at 210°C is 9.25 nm (standard deviation 2.8 nm) while XRD calculations show it is about 9.18 nm (standard deviation 0.058 nm), which is in really good agreement. There is a same scenario for other temperatures (Table 6).

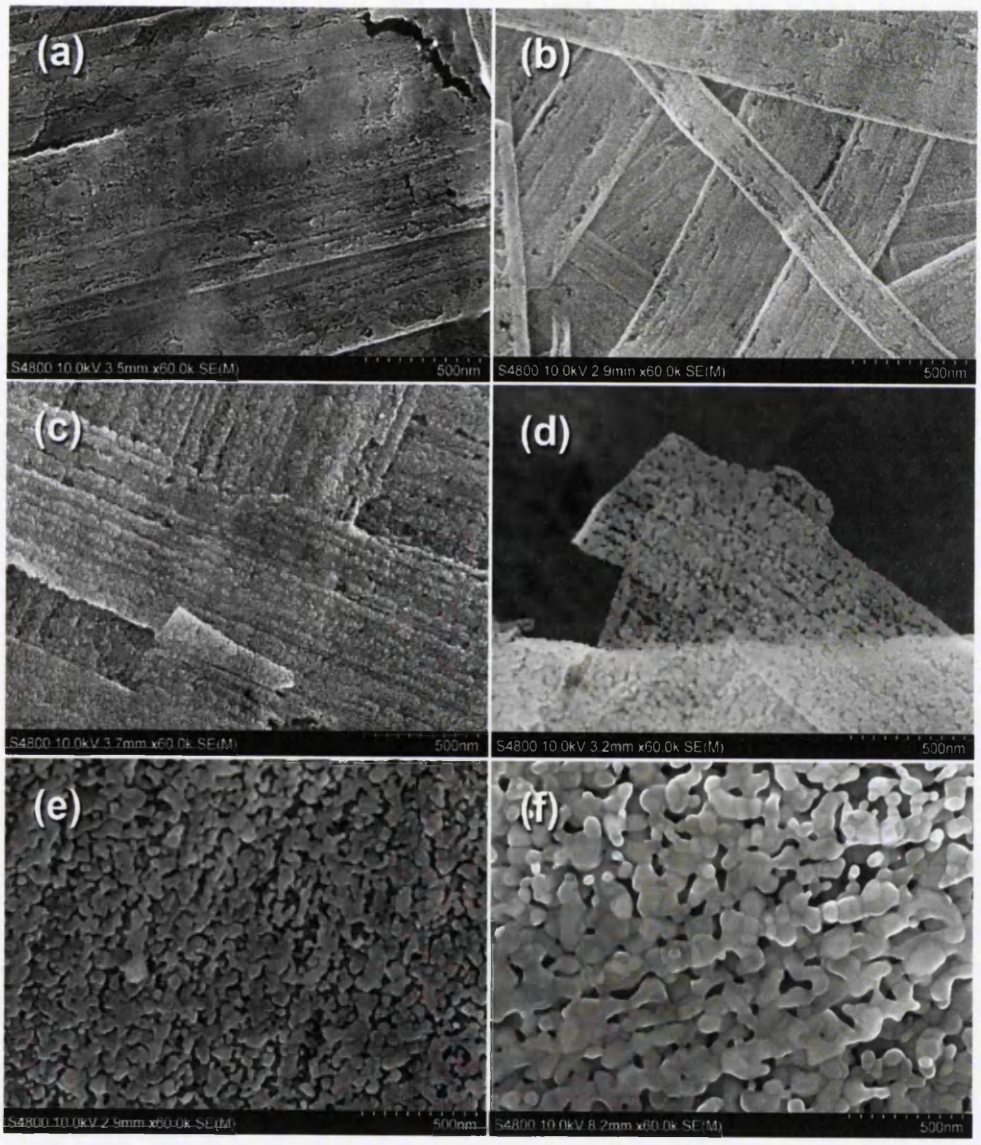

Figure 85. SEM images of ZnO polycrystalline NBs annealed at (a) 110°C, (b) 210°C, (c) 400°C, (d) 600°C, (e) 800°C and (f) 1000°C at 60k magnification.

Temperature °C	XRD grain size (nm)	XRD standard deviation (nm)	SEM particle size (nm)	SEM standard deviation (nm)
210	9.18	0.058	9.25	2.8
400	18.6	0.09	14.3	5.9
600	42.4	0.18	30.7	20.4
800	53.9	0.29	55.2	32.5
1000	95.2	0.56	89.6	41

Table 6. Average size of ZnO grains/particles, extracted from XRD/SEM measurements, as a function of temperature

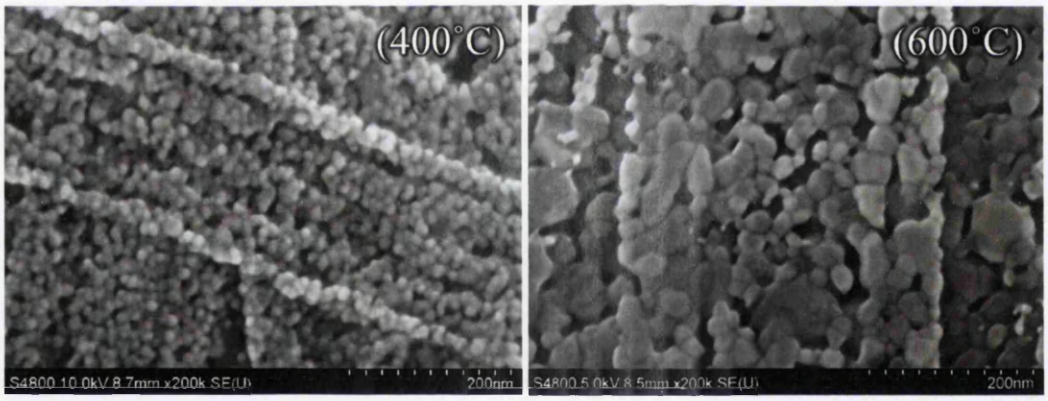

Figure 86. High magnification SEM imaging of the annealed NBs at 400°C (left) and 600°C (right), after annealing at 210°C, the surface morphology of the NBs clearly shows a polycrystalline nature with interconnected nanoparticles arranged in a chain-like pattern along the long axis, and about 600°C sintering of the crystallite appears

To investigate the 3D model of the ZnO nanocrystalline nanobelts, AFM tapping mode were used, Figures 87, 88, 90-92. AFM analyses showed some NBs have more than one layer, but each layer has the average thickness of 20 nm (ranges from 10 to 50 nm).

Furthermore, After annealing at 110°C the morphology and surface of the NBs appears to be altered, with the emergence of clear lines along the long axis of the NB and the introduction of structural damage, there is a kind of self-

assembly in aligning the ZnO nanoparticles inside of the each NB through which after annealing at any of different temperatures, as it can be seen in, Figures 85-88, 90-92 a chain-like pattern appeared. These are apparent on both SEM and AFM images and therefore are not a result of SEM electron beam damage. They may be caused by the removal of water from the LBZA compound. Thermogravimetry measurements [52,116] have shown a 6% weight loss for LBZA at a temperature of 100°C, attributed to the loss of intercalated water, which could explain the partial break-up of the structure observed in our experiments. Although with increasing the temperature, there is an increasing in the particle size, the chain-like pattern is significantly dominant. After annealing at 210°C, the surface morphology of the NBs clearly shows a polycrystalline nature (Figure 85), with interconnected nanoparticles arranged in a chain-like pattern along the long axis, Figure 84 shows high magnification SEM imaging of the annealed NBs at 400°C (left) and 600°C (right). This structure could facilitate electron transport along the ZnO NBs and help possibly lower the resistance of devices fabricated from the NBs, while retaining the high surface to volume ratio of the nanoscale particles. Such performance would be particularly beneficial for gas sensing devices and dye sensitized solar cells. In the section on gas sensing will expand on that last point. Sintering of the crystallite also appears to have taken place after the 600°C anneal. After annealing at 800°C and 1000°C the sintering process intensifies. Yet the overall ribbon shape of the structures remains even after the 1000°C anneal (Figure 85), similar to results reported by Cui et al. [238]. However, the unidirectional arrangement of the nanoparticle chains is lost after annealing at 800°C, due to the intensifying of the sintering process. The thickness of the NBs was not affected by the annealing process and remained within the 10 to 50 nm range, as confirmed by AFM images and their cross section (Figures 87-91).

5.2.2 AFM results

AFM images of LBZA NBs taken after annealing at 110°C and 1000°C are shown in Figures 87-92. After the 110°C anneal the morphology and surface of the NBs appears to be altered, with the emergence of clear lines along the long axis of the NB and the introduction of structural damage. These are apparent on both SEM and AFM images and therefore are not a result of beam damage. They may be caused by the removal of water from the LBZA compound. Thermogravimetry measurements [116] have shown a 6% weight loss for LBZA at a temperature of 100°C, attributed to the loss of intercalated water, which could explain the partial break-up of the structure observed in our experiments. After annealing at 200°C and 400 °C, the surface morphology of the NBs clearly shows a poly-crystalline nature, with interconnected nanoparticles arranged in a chain-like pattern along the long axis (Figures 88-92). This structure could facilitate electron transport along the ZnO NBs and help lower the resistance of devices fabricated from the NBs, while retaining the high surface to volume ratio of the nanoscale particles. Such performance would be particularly beneficial for gas sensing devices and dye sensitized solar cells. The crystallite size increases after each subsequent anneal, as suggested by the XRD data. Sintering of the crystallite also appears to have taken place after the 600°C anneal. After annealing at 800°C and 1000°C the sintering process intensifies. Yet the overall ribbon shape of the structures remains even after the 1000°C anneal, similar to results reported by Cui et al [238]. However, the unidirectional arrangement of the nanoparticle chains is lost after annealing at 800 °C, because of the sintering process. The thickness of the NBs was not affected by the annealing process and remained within the 10 to 50 nm range (Line profiles shown in Figures 87-92).

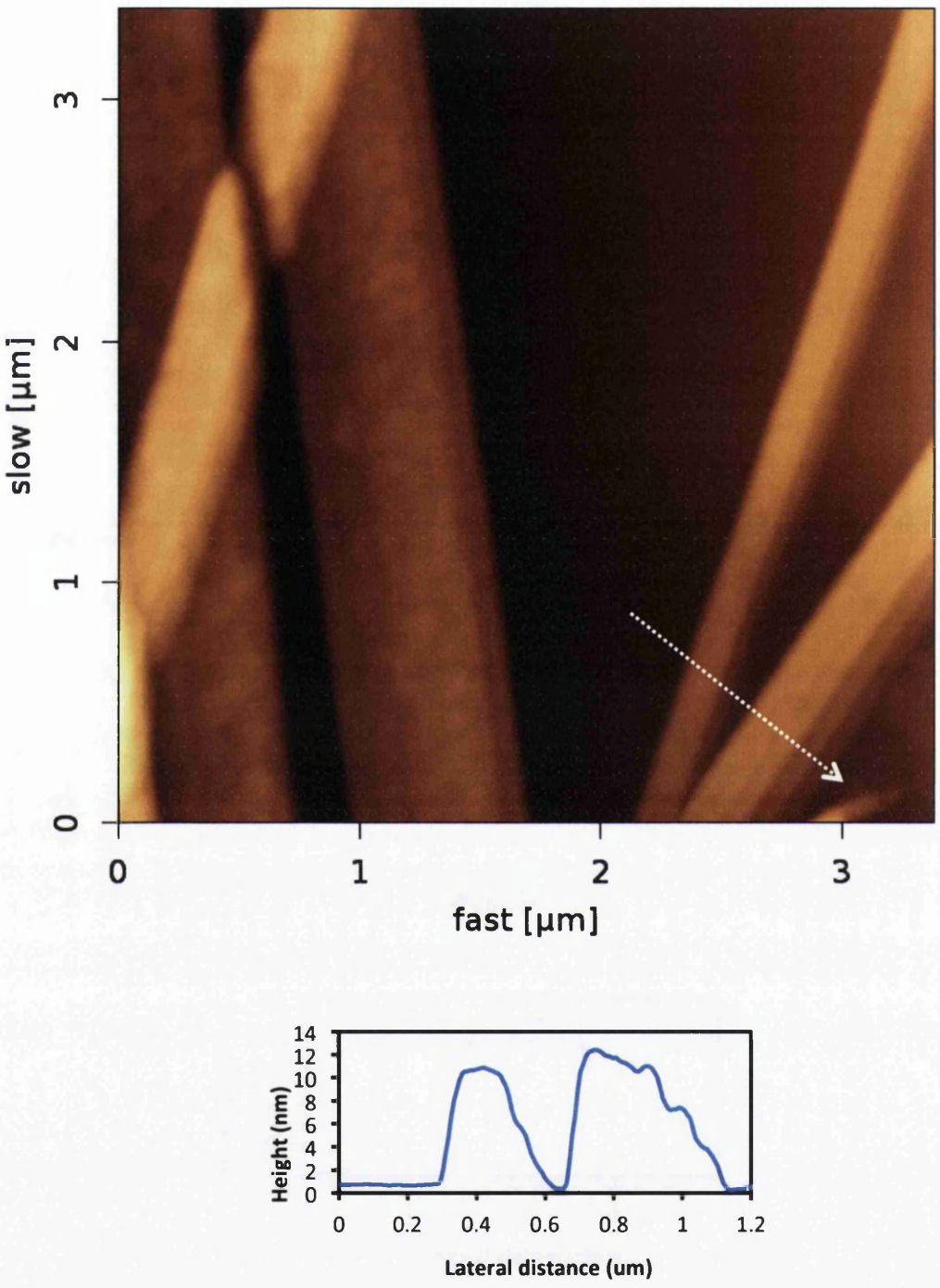

Figure 87. AFM image and corresponding line profile of as grown LBZA NBs annealed at 110°C, changing in morphology clearly can be seen from AFM and line profile along the long axis.

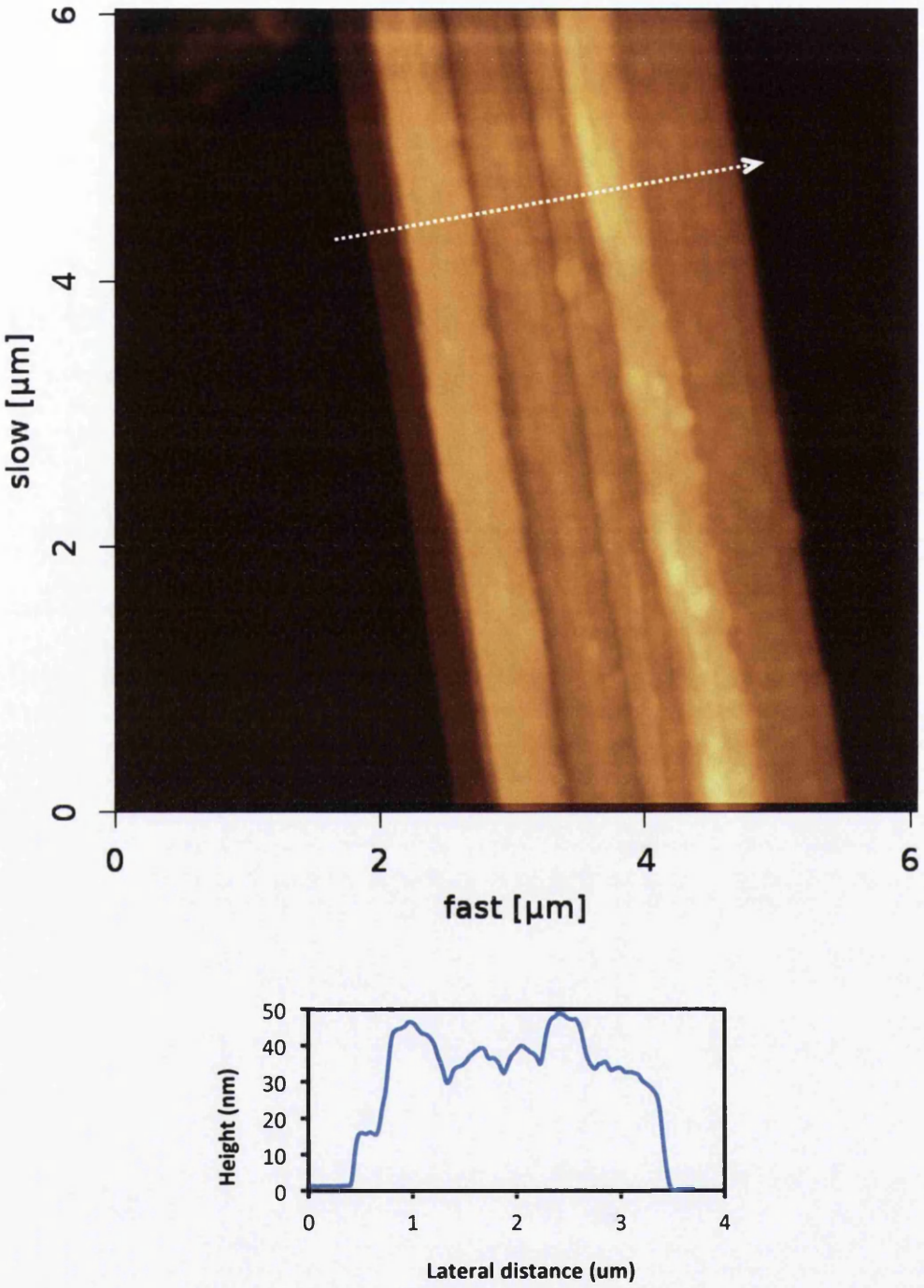

Figure 88 AFM image and corresponding line profile of as grown LBZA NBs annealed at 200°C, in this image, start of formation of the chain-pattern along the long axis is more significant

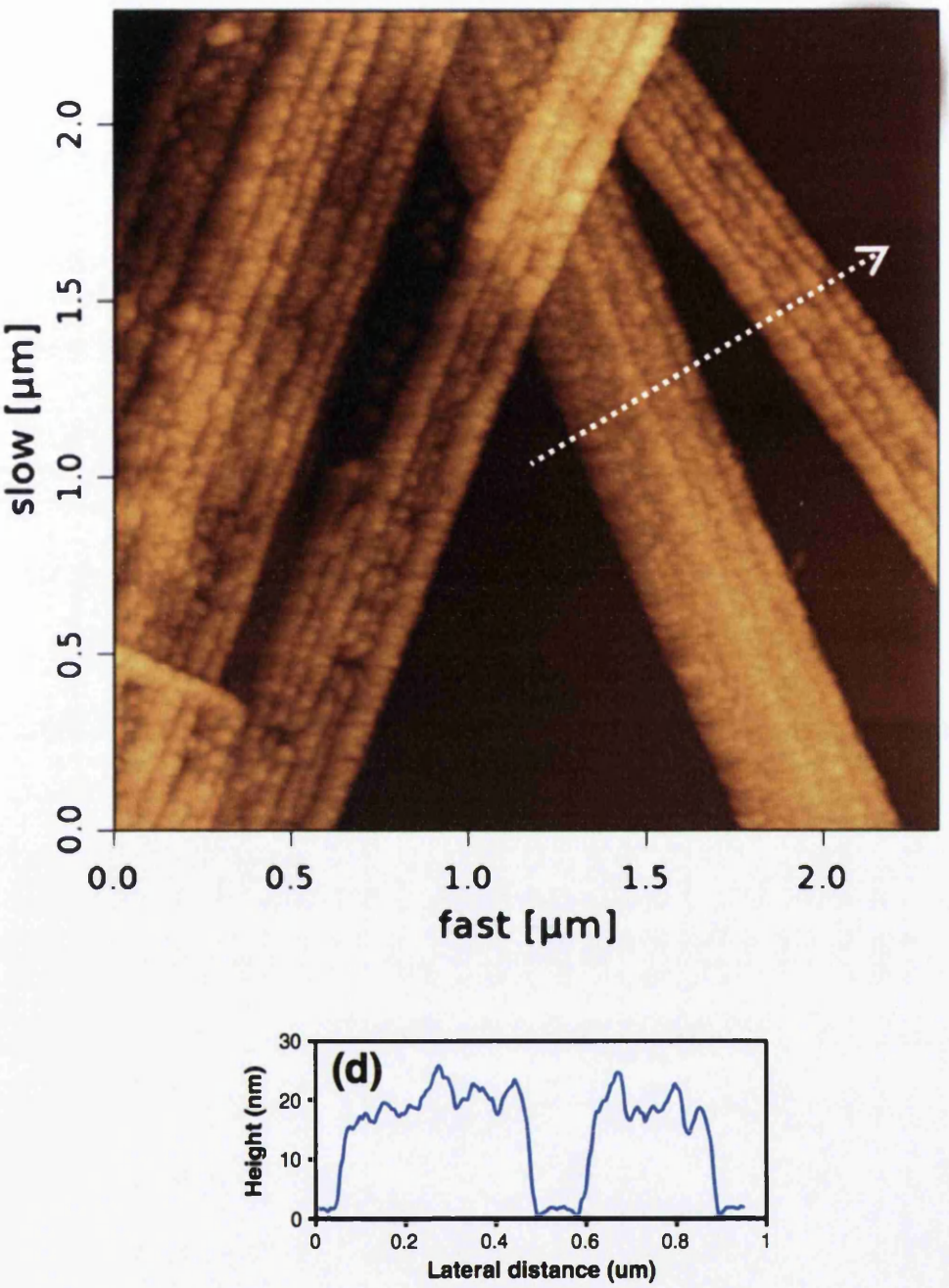

Figure 89 AFM image and corresponding line profile of as grown LBZA NBs annealed at 400°C, in this image, start of formation of the chain-pattern along the long axis is more significant

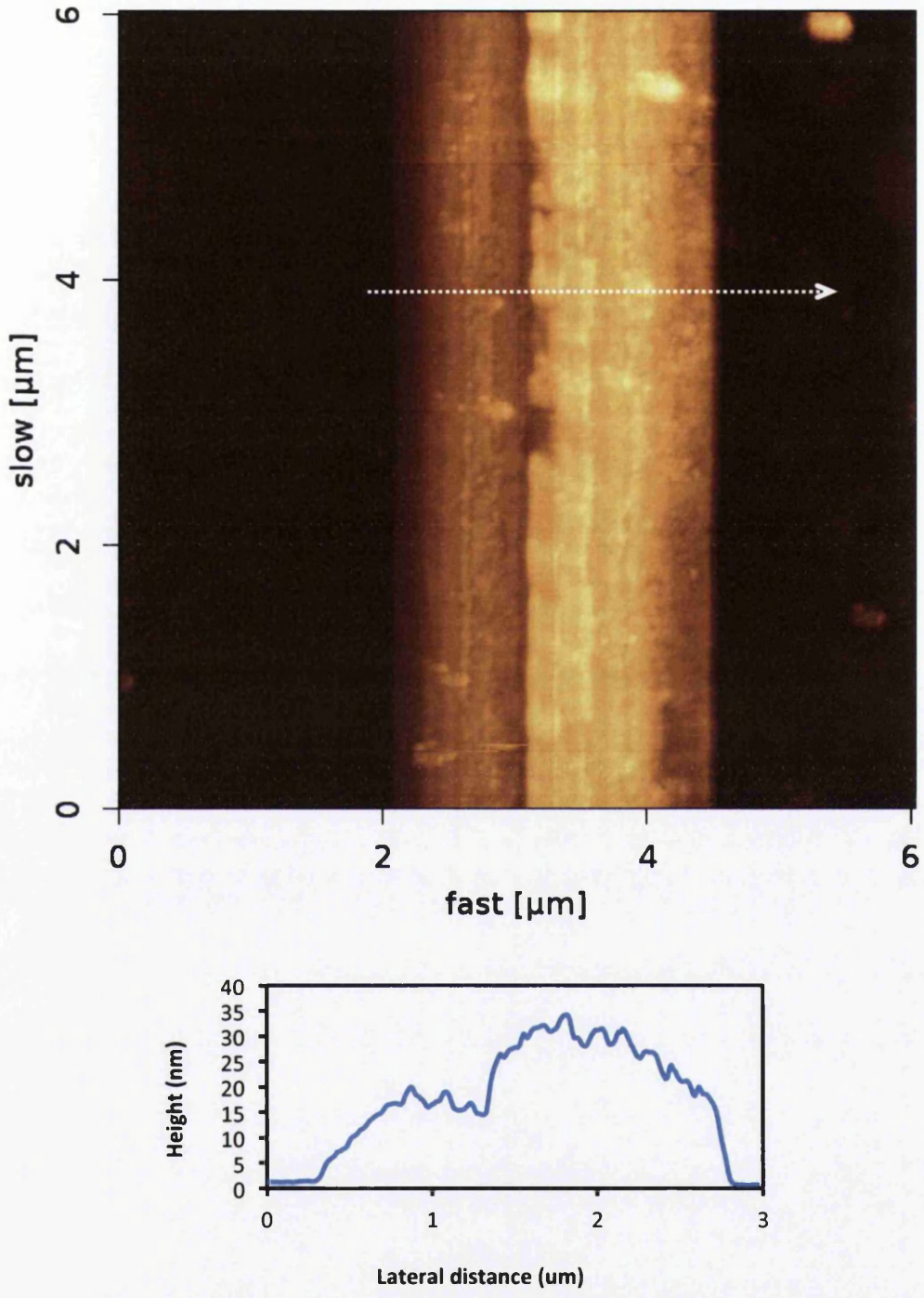

Figure 90 AFM image and corresponding line profile of as grown LBZA NBs annealed at 600°C

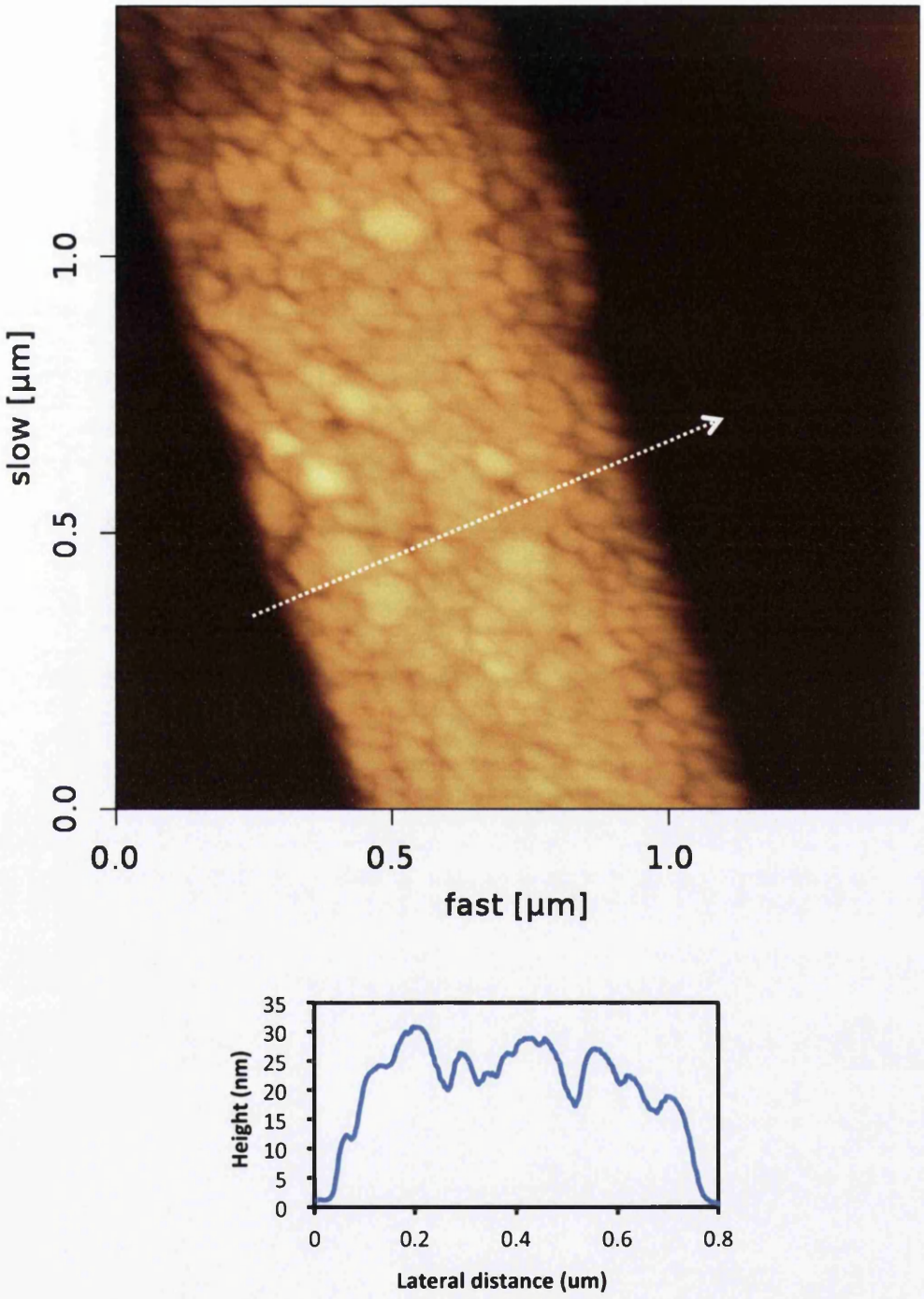

Figure 91 AFM image and corresponding line profile of as grown LBZA NBs annealed at 800°C, sintering of the crystallite is more dominant to chain-pattern.

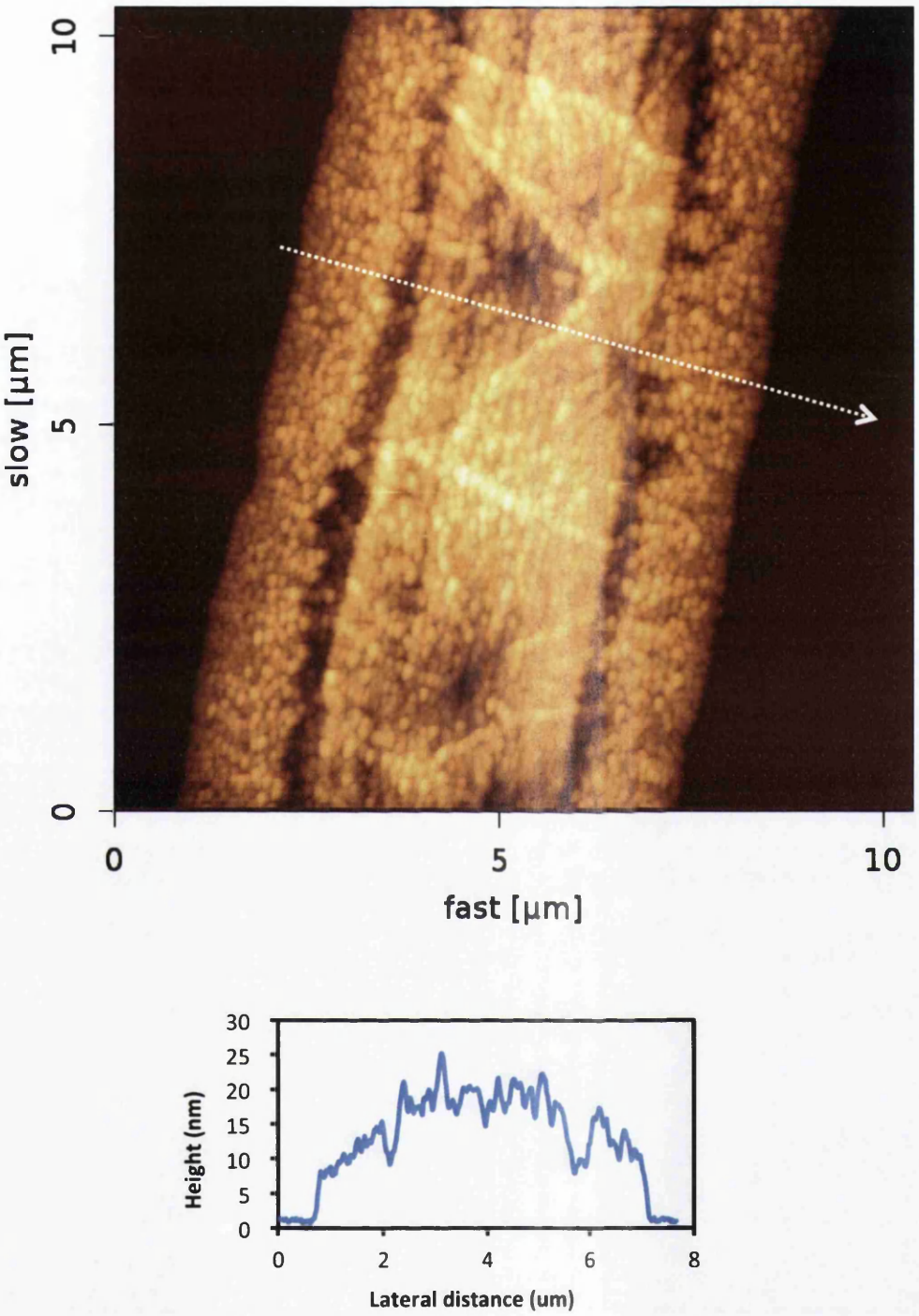

Figure 92 AFM image and corresponding line profile of as grown LBZA NBs annealed at 1000°C

5.2.3 XPS and PL results

XPS measurements were used to compare the composition of annealed ZnO NBs with LBZA NBs and confirming the XRD data to show transformation from LBZA to ZnO. In addition, XPS data was also obtained from a commercial ZnO powder as a control. Figure 93 shows the O1s core level scans of the as-grown LBZA NBs and the ZnO NBs produced by annealing at 400°C in air for 10 minutes. The top graph in this Figure shows the data obtained from the commercial ZnO powder, the control scan of commercial ZnO powder is virtually identical to that of the ZnO NBs, indicating complete transformation to ZnO. The ZnO NBs spectrum could be fitted with O-Zn, OH and H_2O components in good agreement with published data for ZnO [278]. The Zn2p to O1s ratio measured from the ZnO NBs is almost double that of the LBZA material, which is consistent with the stoichiometry of the compounds. The LBZA O1s core level was fitted with a Zn-OH component and a Zn-O component, using the same energy offset between the two as for the ZnO NBs (1.4eV). The FWHM of the components used to fit the LBZA NBs are much larger than those of the ZnO NBs, possibly because of charging effects broadening the peak. This could explain why no separate H_2O component was observed as the energy separation between OH and H_2O might be too small to be resolved. The charging of the insulating LBZA sample resulted in a 5.9 eV difference for the binding energy of the C 1s core level between LBZA and ZnO. Therefore, in order to compensate for charging, the LBZA NB spectrum for O1s was normalized to the C 1s energy and shifted 5.9 eV to lower binding energy. The Zn 2p core level peak shape was similar for both samples, possibly because the energy offset between Zn-O and Zn-OH is below the resolution of the instrument. Figure 93 clearly shows the chemical transition from LBZA to ZnO, with the LBZA scan dominated by O-H bonding, which decreases after annealing, while the O-Zn bond increases.

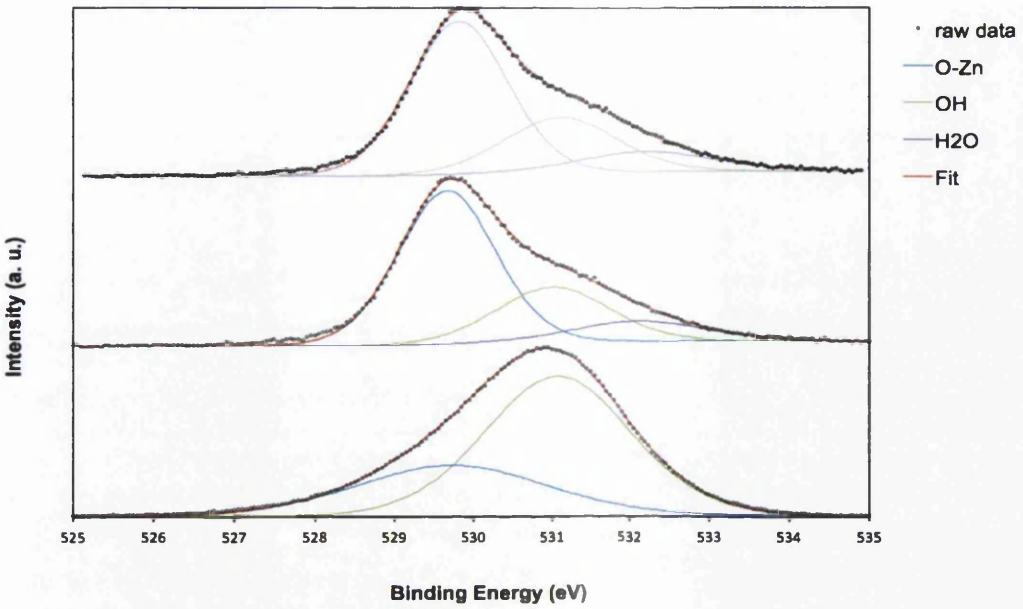

Figure 93. O1s core level XPS spectra of commercial ZnO powder (top), after annealing at 400°C (middle) and as-grown LBZA NBs (bottom). The fitted components are shown as solid red lines.

The photoluminescence properties of the ZnO nanocrystalline belts fabricated by annealing the LBZA nanobelts in air at 400°C, 600°C, 800°C and 1000°C in shown on Figure 94. The spectra show the exciton peak at about 376nm and the broad visible emission band typical of ZnO nanostructures. The ratio of the intensity of the exciton band and the visible band is often used as a measure of the defect density for ZnO nanostructures, with a large visible band indicative of a high concentration of defect. From Figure 94 it is apparent that the 400°C nanobelts have the lowest defect density while increasing the temperature to 600°C dramatically increase the intensity of the visible band compared to the exciton, indicating a large increase in defect density. Annealing at 800°C reduces the defect density slightly and the 1000°C step reduces it further. Annealing at 1000°C also significantly shifts the visible emission from the red-orange part of the spectrum to the green, showing that the nature of the radiative defect recombination has changed. Overall the PL analysis proves that the ZnO nanocrystalline belts have optical properties comparable to previously published single crystal nanostructures such as nanowires or nanorods.

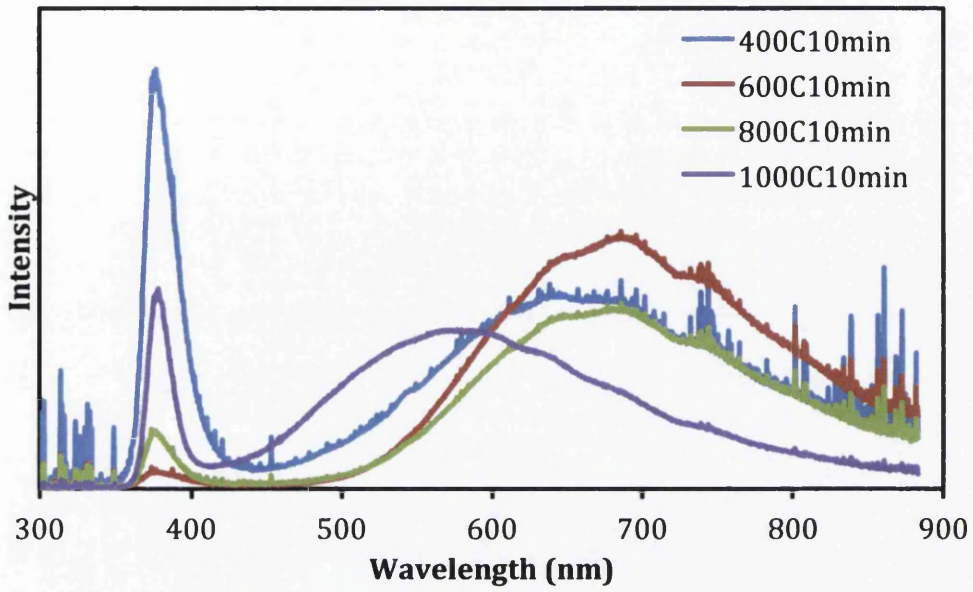

Figure 94. PL measurement of the ZnO nanobelts obtained after annealing the LBZA nanobelts at at 400°C, 600°C, 800°C, and 1000°C.

5.3 LBZA nanosheets

The results presented in the previous section show that the thermal decomposition of LBZA provide an easy and low cost method for the fabrication of ZnO nanocrystalline structures with good optical properties and high surface to volume ratio. The only drawback to the technique is the relatively long synthesis time of 20h. In this section an alternative method for fabricating LBZA nanostructures following a similar approach but using a microwave oven in the much faster time of 2mins is presented. First, the experimental procedure is detailed then the characterization of the LBZA products is presented using AFM, SEM and XRD, followed by an investigation of the role of the concentration of the different chemical precursors. Finally the thermal decomposition into ZnO is investigated using SEM, XRD and PL.

5.3.1 Experimental details

To produce LBZA NSs a simple two-step procedure was employed, making the chemical mixture in deionized water and microwaving to grow crystals. 13.17 g

of zinc acetate dihydrate (Sigma-Aldrich) was dissolved in 600ml of deionized water (0.1 M) using magnetic stirrer for about 5 minutes to obtain a clear homogenous solution. Temperature of the deionized water is of importance, it is must be under 20°C. And then 1.78 g zinc nitrate hexahydrate was added to the solution (0.02 M) stirring about 5 minutes to achieve homogenous mixture and finally 0.84 g of hexamethylenetetramine (HMTA) was added to the mixture (0.02 M). After 5 minutes more mixing using magnetic stirrer, as-prepared mixture was divided into 10 smaller beakers (150ml glass beakers), 60ml in each. Each beaker then was put in a commercial microwave exactly in the middle of the microwave turntable, for 120s at maximum power (800W according to the factory information). After microwaving sample was put in the safe place to be cool at room temperature, Figure 95.

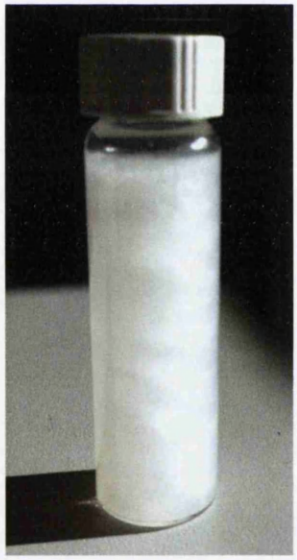

Figure 95. As-grown LBZA NSs stored after cooling at room temperature

5.3.2 Characterisation

To investigate the morphology and 3D structure of the LBZA nanosheets, AFM tapping mode was used. Figure 96 shows the AFM tapping mode of as-synthesized LBZA sheets. AFM clearly shows the layered structure of the

nanosheets; also cross section across the arrow can confirm layered structure. As it can be seen, each layer has a thickness about 20 nm.

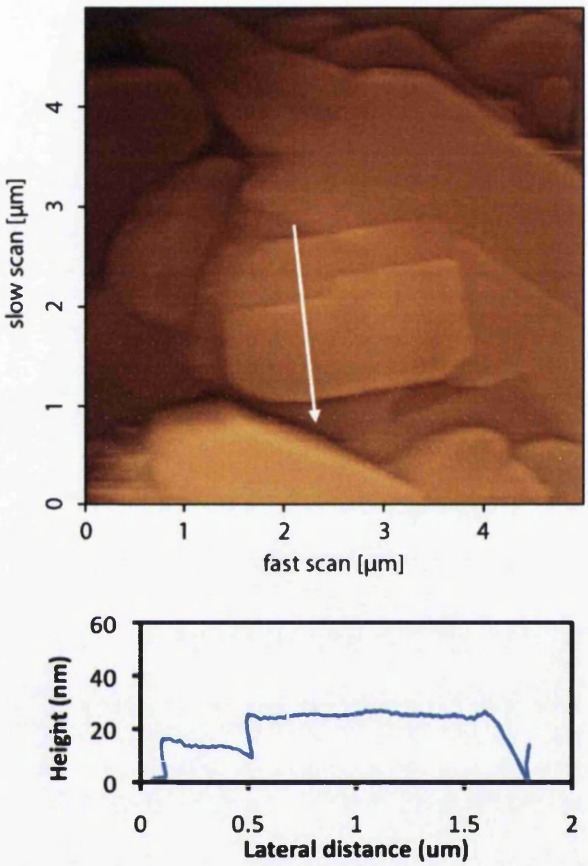

Figure 96. AFM tapping mode image of as-grown LBZA NSs, showing the characteristic layered structure, also height profile taken across the arrows, confirming the layered structure, each layer has a thickness about 20 nm.

The XRD diffractogram of as-synthesized LBZA NSs is presented in Figure 97 and shows that LBZA NSs structure is crystalline with the characteristic main zinc acetate 001 peak at 6.67°, corresponding to an interplanar spacing within a single layer of 1.32nm and confirming their composition as $Zn_5(OH)_8(CH_3COO)_2.2H_2O$. The peaks at 13.35° and 20.07° are assigned to the 002 and 003 reflections and correspond to interplanar distances of 0.66nm and 0.44nm, respectively. The diffractogram also shows weaker peaks at 14.56° and 21.87°, which we have attributed to the second and third order of another group of reflections, corresponding to an interplanar spacing within a single

layer of 1.21nm [123]. In addition, there are clear Wurtzite ZnO peaks (JCPDS # 01-079-2205) between 30-40° on the NS diffractogram (100, 002, 101). As it is previously explained in section " influence of the concentration of the chemicals", this could be caused by the presence of hexagonal ZnO microcrystals which are also formed with the NSs. However the concentration of the ZnO microcrystals is estimated to be less than 1%. Also, there is another possibility for existence of zinc oxide peaks. It is reported in previous literatures that there is a potential for transforming from zinc acetate to zinc oxide via pyrolytic decomposition at temperatures above 100°C to 150°C [116]. On the other hand, as it is previously explained, in microwave assisted technique, glass beakers can absorb microwave irradiations and reach to higher temperature over 100°C. Consequently, as-grown LBZA, which are very close to the glass surface might be converted to ZnO. As a result, the ZnO peaks are more likely to be caused by both either partial decomposition of the LBZA or microscale hexagonal ZnO crystals.

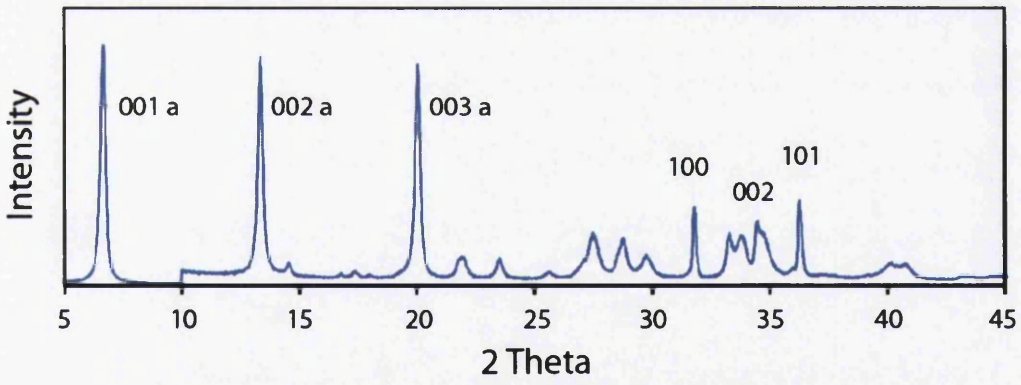

Figure 97. XRD diffractogram of as-synthesized LBZA NSs. The region between 10° and 45°has been magnified 15 times. LBZA NSs structure is crystalline with the characteristic main zinc acetate 001 peak at 6.67°. Also there are main ZnO peaks between 30-40°

Similar to NBs, XPS was employed to investigate the composition of LBZA NSs and annealed ZnO NSs. In addition, commercial ZnO powder was used as a control. Figure 98 shows the O1s core level results of the as-grown LBZA NSs (top) and annealed ZnO NSs at 400 °C in air for 10 min (middle) and commercial ZnO powder (bottom). Very similar to NBs, the ZnO NSs spectrum could be

fitted with O–Zn, OH and H_2O components in good agreement with published data for ZnO[279]. The result from XPS scan of commercial ZnO powder was almost identical to that of the ZnO NSs. The Zn2p to O1s ratio obtained from the ZnO NSs was about double compared to as-synthesis LBZA material. Because of the limitation in the instrument resolution, and the amount of the energy offset between Zn–O and Zn–OH, which was below this resolution, the Zn 2p core level peak shape was similar for both samples. The results in Figure 98 confirm the chemical transition from LBZA to ZnO, with the LBZA scan dominated by O–H bonding, which decreases after annealing, while the O–Zn bond increases.

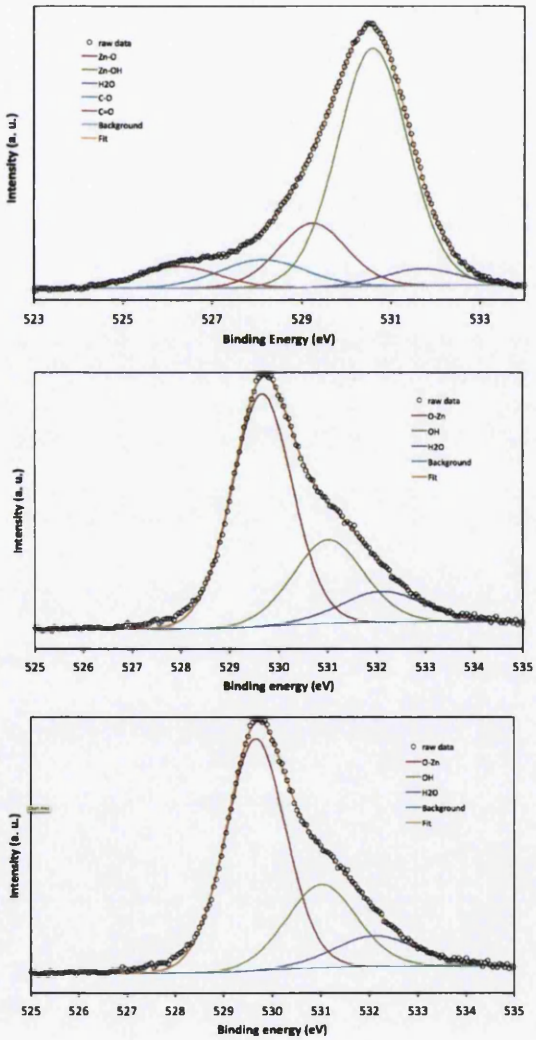

Figure 98. O1s core level XPS spectra of as-grown LBZA NSs (top), after annealing at 400°C (middle) and commercial ZnO powder (bottom). The fitted components are shown as solid orange lines.

5.3.3 The influence of the zinc acetate dihydrate concentration

Figure 96 shows the influence of the different concentrations of the zinc acetate. The results from Figure 99 (a-b) reveal that in low concentration of zinc acetate (0.01 M) after 2 min microwaving at maximum power (800 W) there are no sheets and the final product is only a range of different sizes of hollow-ended hexagonal prism crystals. They have width ranging from 500nm to 1.5 μm and length from 1 to 2.5 μm. The lateral surfaces of the crystals are not smooth.

In the higher concentration of zinc acetate (0.05 M), after 2 min microwaving at 800 w the result is completely different. Figure 99 (c) shows a SEM image of the as-grown rectangular NSs, with lateral dimensions ranging from 200nm to 5um. A small concentration of ZnO hexagonal microscale crystals is also present, as shown by the arrow. They might be a consequence of the parallel reaction between zinc nitrate hexahydrate and HMTA used in this recipe for the NSs growth. As it is explained in pyrolytic decomposition of LBZA (Equation 26)

$$Zn(CH_3COO)_2.2H_2O \rightarrow Zn_5(OH)_8(CH3COO)_{2\ (LBZA)} \rightarrow Zn(OH)_2 \rightarrow ZnO \qquad (26)$$

There is a possible alternative route for existence of the zinc oxide crystals at higher temperature from zinc acetate complex through a process in which a zinc acetate complex such as $Zn(CH_3COO)_2$ releases the acetate anions and can be converted to ZnO crystal. Although it seems that the temperature of the mixture during microwaving is always about or under 100°C (boiling point of the DI water) and is not enough to activate this hydrothermal alternative route, the glass beakers have higher temperature due to localized thermal runaways phenomenon, it is happened in such materials with low thermal conductivity, which also have dielectric constants increasing with temperature. An example is glass, which can exhibit thermal runaway during microwaving to the point of melting. Thermal runaway refers to a situation where an increase in temperature changes the conditions in a way that causes a further increase in temperature, often leading to a destructive result. It is a kind of uncontrolled

positive feedback. Therefore existence of microscale ZnO crystals might be a consequence of the higher temperature (above 100°C) in an area very close to the inner glass surface. So in this case, zinc acetate complexes are potentially able to provide zinc hydroxide compounds in aqueous system, which can play precursor role for another reaction to produce zinc oxide crystals in higher sufficient temperature [280]. Therefore, in the area on or very near to the glass beaker surface, possibly, temperature is more than 100°C even for a short time and it may explain the existence of ZnO hexagonal crystals. In addition, visual observations revealed that the boiling process always starts from the area by the glass beakers and it is in good agreement with the thermal runaway theory. ZnO hexagonal crystals or any other possible shapes of crystals except nanosheets, the target product, are named unwanted crystals due to the aim of this research and it is estimated that, the average number of them is less than 2 %. The estimation has done visually by counting the sheets and unwanted crystals from SEM images.

In the next step, zinc acetate concentration was increased to double (0.1 M). After 2 min microwaving in the exactly same conditions, quantitative measurement and SEM investigations revealed that, firstly, the product is increased and there is a high yield nanosheets crystal. Secondly, the percentage of the unwanted crystals dramatically decreased to less than 0.1 per cent, which is significantly lower compared to the 0.05 M concentration of the zinc acetate. It can be explained by assuming that there is an improvement in the ratio between the chemicals concentrations. Additionally, SEM images of Figure 99 (e-f) look more rectangular and more uniform compared to the lower concentration (0.5 M), which are preferably rounded corners with carved edges rather than sharp corners and smooth and straight edges. In the next step of this experiment, zinc acetate concentration increased to double amount (0.2 M).

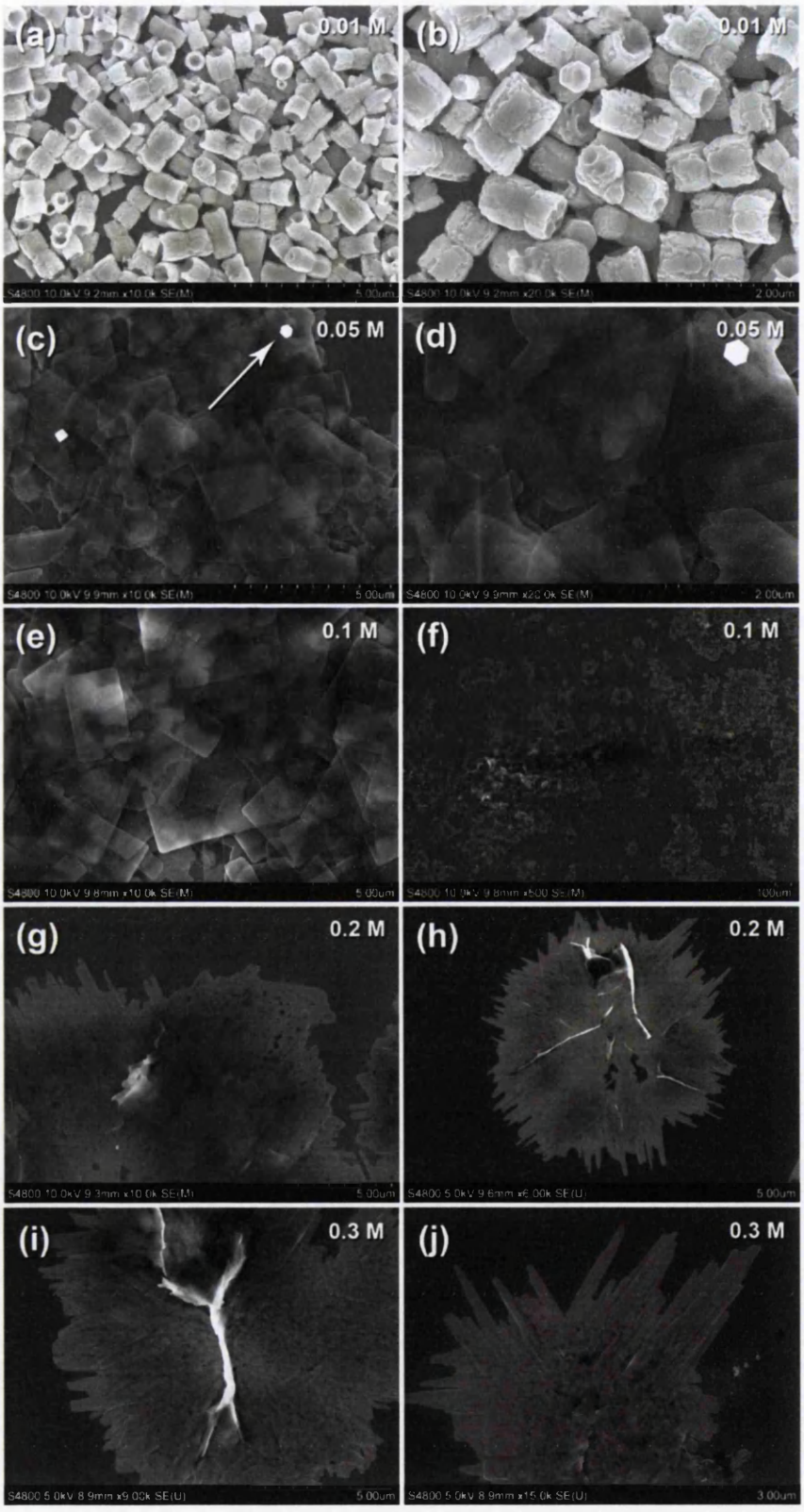

Figure 99. SEM images of different concentration of zinc acetate and its influence on the morphology and quantity of the product

In terms of increasing the zinc acetate concentration, it is expected that the pH of the mixture decrease, in fact, concentration dependent pH reduction can suggest that the Zn^{2+} ions hydrolyze more than $CH3CHOO^-$ ions in water. In theory, the soluble ions should charge metal ion Zn^{2+} or hydroxo complexes $Zn(OH)^-$ under acidic conditions. The uncharged hydroxo complexes $Zn(OH)_2$ occurs under neutral and moderately basic pH conditions. However, negatively charged $Zn(OH)_3^-$ and $Zn(OH)_4^{2-}$ hydroxo complexes form at alkaline conditions. Therefore, in such conditions that the concentration of $Zn(CH_3CHOO)_2$ solution is less than 0.2 M, and as a result, the equivalent pH of the zinc acetate solution is in a range of 6.0–7.0, then the hydroxo complexes $Zn(OH)^-$ is the dominant expected form for zinc compounds in the solution. So, according to the pH between 6.0 – 7.0 and the hydroxo complexes $Zn(OH)^-$ ratio, the basic zinc salts are presented in the precipitate. In any concentrations of zinc acetate higher than 0.25 M, the total pH of the solution is about 6 or less and in this case, there is another chemical equilibrium in which the Zn^{2+} ions are the most dominant ions in the solution. So as a consequence, it is obviously expected that, no precipitate could be observed at the concentration of zinc acetates more than 0.25 M because of the low pH condition. In contrast, in zinc acetate concentrations less than 0.02 M the pH of the solution is higher than 6.8, so pure ZnO nano or submicron particles could be obtained. This explanation can clearly describe what happen in zinc acetate solutions with different concentrations but the problem is, in this experiment, there are two more chemicals, which are able to change the pH of the zinc acetate solutions. pH measurements from different concentrations of the zinc acetate in an equimolar concentration of zinc nitrate hexahydrate and HMTA revealed that the resulting pH is higher compared to the same concentration of zinc acetate without presence of zinc nitrate hexahydrate and HMTA. The results are shown in Figure 100.

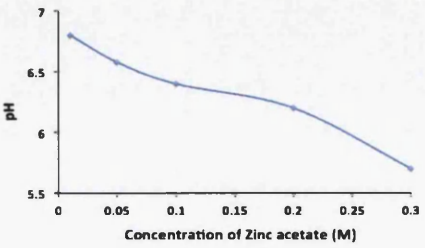

Figure 100 . pH changes as a function of zinc acetate concentration (M)

The differences between the pH of the mixture and the expected pH of zinc acetate solutions may explain why LBZA crystals can be obtained in zinc acetate concentrations higher than 0.2M. Figure 99 (g, h) and (I, j) show the SEM results from zinc acetate concentrations of 0.2 and 0.3 M respectively. As it can be seen, increasing the concentration of zinc acetate resulting in formation of the LBZA nanoparticles, but in this case it seems that there is different lateral dimensions ratio and nanosheets have been changed to particles more likely to the belts. More interestingly, our observations revealed that there are no crystals in the mixture after microwaving while zinc acetate concentration increases to 0.5 or more. So it can be concluded that increasing zinc acetate concentration can either reduce the unwanted hexagonal crystals or increase the quantity of the product, but there is a limitation, and the ratio of zinc acetate concentration to other chemicals must be about 50 to have an optimized result, a high yield LBZA nanosheets suspension and low concentration of unwanted crystals.

5.3.4 The influence of zinc nitrate concentration

To investigate the effects of changing the zinc nitrate concentration on the target nanoproduct, a series of experiments were run in which except the zinc nitrate concentration, all other factors and conditions were kept constant. In first step, 0.01 M zinc nitrate was added into 0.1 M zinc acetate and 0.02 M HMTA in deionized water. After 2 min microwaving at maximum power (800 W), a high yield nanosheets suspension was obtained, the results are shown in Figure 101. Figure 101 (a) shows a high magnification SEM image of the as-synthesized LBZA nanosheets. Arrow indicates a microscale ZnO hexagonal crystal representing unwanted crystals in final product. Quantity measurements of SEM images revealed that the percentage of unwanted crystals is less than 1 per cent. They might be either a consequence of unoptimized concentration ratio between zinc acetate, zinc nitrate hexahydrate and HMTA used for the NSs growth or over heating the mixture vary near to the glass beaker surface, as microwave heating can cause localized thermal runaways in some materials with low thermal conductivity, which also have dielectric constants that

increase with temperature. An example is glass, which can exhibit thermal runaway in a microwave to the point of melting. It is a kind of uncontrolled positive feedback. So, as it is explained in section "the influence of zinc acetate concentration", glass beakers are used in all our experiments. Therefore existence of microscale ZnO crystals might be a consequence of the higher temperature (above 100°C) in an area very close to the inner glass surface. So in this case, there is a possibility for zinc acetate complex to change into the zinc hydroxide and at the end into the zinc oxide [281].

In terms of the use of microwave irradiation there is a common misconception, which is microwave ovens work "from the inside out", it means from the center of the entire mass of the object outwards. This idea arises from heating behavior seen if an absorbent layer of water lies beneath a less absorbent dryer layer at the surface of an object; in this case, the deposition of heat inside the object can exceed that on its surface. In most cases, however, with non-uniform structured or reasonably homogenous items, microwaves are absorbed in the outer layers of the object in a same way similar to other deeper parts. Depending on water content, the depth of initial heat deposition may be several centimeters or more with microwave ovens, so in our experiments it is expected to have a uniform heating pattern in glass beakers due to their size and capacity, which is 100 ml with diameter about 6 cm. But using glass beakers that naturally have low thermal conductivity and also dielectric constants it is expected to have an area with higher temperature close to the glass surface. Further investigation on inner surface of the glass beakers revealed that, always, there is a very thin deposited layer of zinc oxide crystals. SEM imaging (Figure 102) confirms the existence of the crystals. Figure 102 (a, b) shows SEM images of the beaker side after 2 min microwaving, Figure 102 (c, d) shows SEM images of the beaker bottom. Images clearly show that there are hexagonal crystals deposited on the glass surfaces.

In next step, zinc nitrate concentration was doubled (0.02 M). Increasing the zinc nitrate concentration had some affects on the shape and quantity of the product. Figure 101 (c) is high magnification SEM image of LBZA nanosheets after 2 min in same conditions as pervious experiment except the zinc nitrate

concentration. The first point that it can be recognized is the shape and the morphology of the sheets. The most of them lost their rectangular shape and their sharp corners. Although lateral dimensions ranges from 200 nm to 5 μm, the small sheets look more likely circle instead of rectangular duo to loosing their sharp corners. The quantity has not changed and measurements revealed that there is reasonably the same amount of the product compared to the pervious concentration. But, from SEM images, it is estimated that the percentage of the unwanted hexagonal crystals have significantly increased to about 3 per cent.

The zinc nitrate concentration was doubled again and increased to 0.04 M. SEM images in Figure 101 (e, f) show the influence of increasing the concentration. The first notable point is, the number of the unwanted decreased dramatically and measurements revealed that their concentration is less than 0.5 per cent. Decreasing the number of unwanted hexagonal crystals is considered best from the optimization point of view, but in this concentration, as it can be seen in Figure 101 (e), the shape of the nanosheets completely changed and some of them start to make thicker structures. In addition, measurements revealed that the quantity of the product slightly decreased. So disadvantages of this concentration are more significant compared to the advantages. The concentration of zinc nitrate was increased to 0.1 M. After 2 min microwaving, SEM images were taken from the products, results are in Figure 101 (g, h). SEM images revealed that, interestingly, there is no hexagonal crystal (using visual technique by counting the different crystals from SEM images) and quantity measurements showed that there is reasonably same amount of the product, but morphology of the nanosheets has changed. Obviously, this shape cannot be considered as an advantage in this research. Therefore, although increasing the hexagonal crystals (unwanted crystals) decreased and consequently the product purity is improved, the quantity is same and the shape of the crystals shows no improvement. Last step was to increase the zinc nitrate concentration to 0.2 M, SEM results are in Figure 101 (I, j). Firstly, the same as pervious concentration (0.1 M), there is no hexagonal crystal, in addition, the morphology of the grown nanocrystals have dramatically changed, rectangular crystals are

changed to surfing board-shaped with two tapered-end. Also as a control, in another experiment, we used 0% zinc nitrate, after 2 min microwaving there was no crystal at all, and result was a clear solution. So, it might be concluded that, existence of zinc nitrate is inevitable but increasing its concentration has potential to change the shape and quantity of the product (0.1 M of zinc acetate dihydrate and 0.02 M of HMTA).

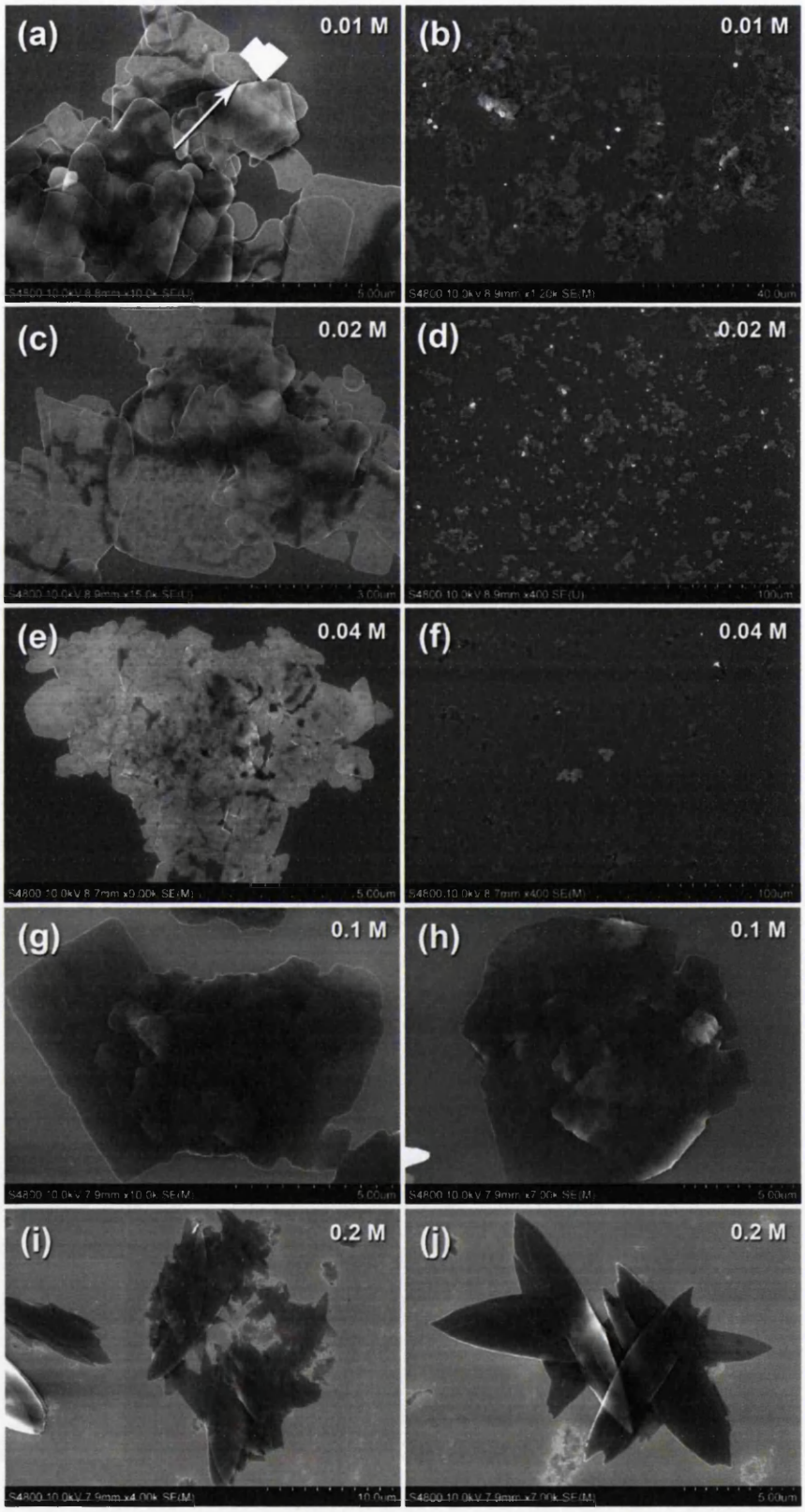

Figure 101. SEM images of different concentration of zinc nitrate and its influence on the morphology and quantity of the product

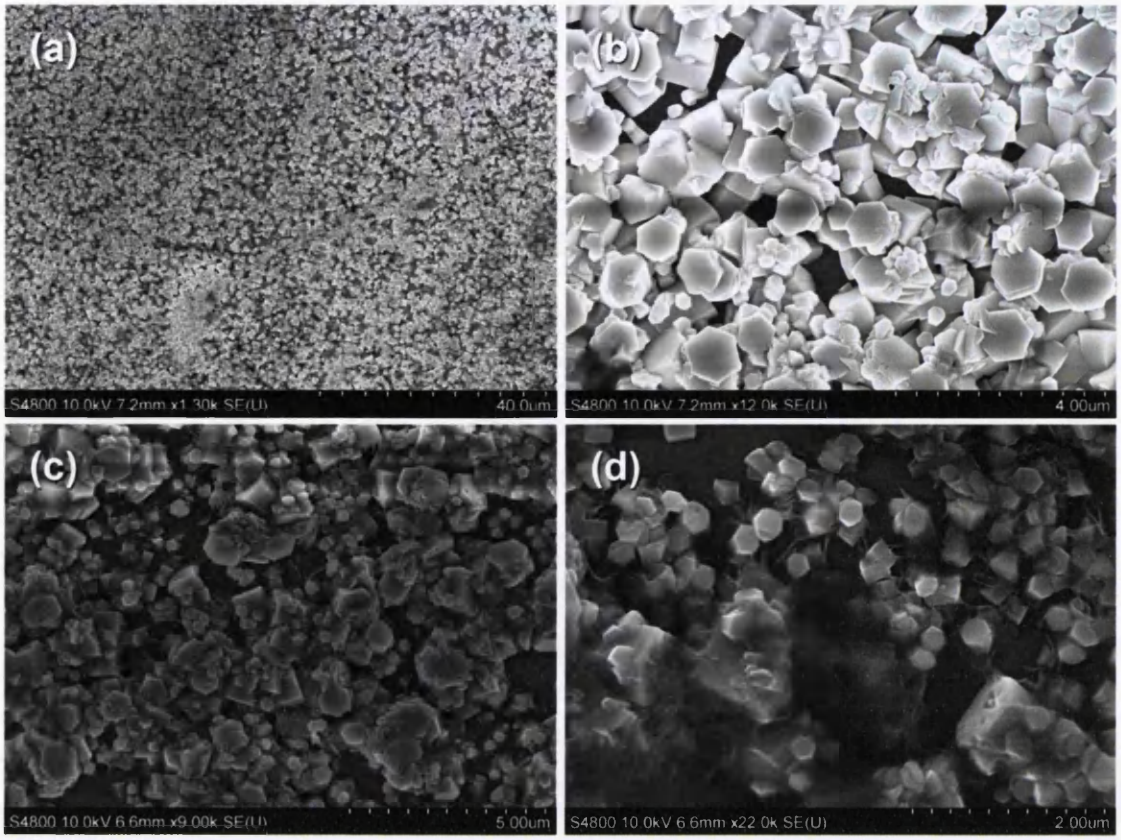

Figure 102. SEM images of the inner surface of the beaker after 2 min microwaving, (a, b) side wall and (c, d) bottom of the beaker.

5.3.5 The influence of HMTA concentration

To investigate the influence of HMTA concentration, a same series of experiments were run in which all factors and conditions were kept constant while HMTA concentration was variable. 0.01 M of HMTA has been used for the first step. After 2 min microwaving, the result is a high yield LBZA nanosheets, but existence of hexagonal ZnO crystals is of importance, results are in Figure 103(a, b). SEM measurements revealed that the percentage of the unwanted crystals is less than 2 per cent. However, the shape and morphology of the sheets are satisfactory and most of them have reasonably rectangular shape with identified corners. Increasing the HMTA concentration to 0.02 M resulting in an increase of the quantity of the product. In addition, the percentage of rectangular nanosheets has increased. Also a significant decrease in the percentage of the unwanted hexagonal ZnO crystals is of importance and

measurements revealed that it is less than 0.5 per cent; results are shown in Figure 103 (c, d). In the next step, HMTA concentration was increased to 0.04 M, after 2 min microwaving at 800 W, SEM images revealed that there is no significant difference compared to pervious concentration (0.02 M), results are shown in Figure 103 (e-f). However, SEM measurements showed that the sheets have same lateral dimensions as pervious sheets from different experiments range from 200 nm to 5 μm, while the number of unwanted crystals slightly increased to less than 1 per cent, but the most important change has happened to the morphology of the crystals, corners started to be rounded in some cases.

The HMTA concentration changed again and increased to 0.1 M. After 2 min microwaving at 800 W, SEM was used to investigate the changes under influence of HMTA, the results are shown in Figure 103(g, h).

SEM measurements revealed that, nothing has changed remarkably, while the number of the rounded-corners sheets has increased, also the percentage of the unwanted crystals increased slightly. Another point is that the sheets have reasonably the same size; also very similar quantity of sheets has been obtained.

The last HMTA concentration was 0.2 M, microwaving for 2 min at 800 W resulting in a high yield sheets product, however, there are more rounded-corner sheets, and the percentage of the unwanted crystals slightly increased, results are shown in Figure 103 (I, j). According to the results, it can be suggested that, increasing the HMTA concentration causes a defined pattern, increasing the HMTA concentration resulting increasing the quantity of the product but it also causes a deformity in the shape of the rectangular nanosheets. In addition, in higher concentration of HMTA, the number of the unwanted crystals has raised. So, as the purity (maximum sheets and minimum unwanted crystals) of the product and uniformity in the morphology of as-synthesized nanocrystals are of importance of this research, it is found that the best HMTA concentration to obtain a high yield NBZA nanosheets and minimum concentration of the unwanted hexagonal ZnO crystals is 0.02 M.

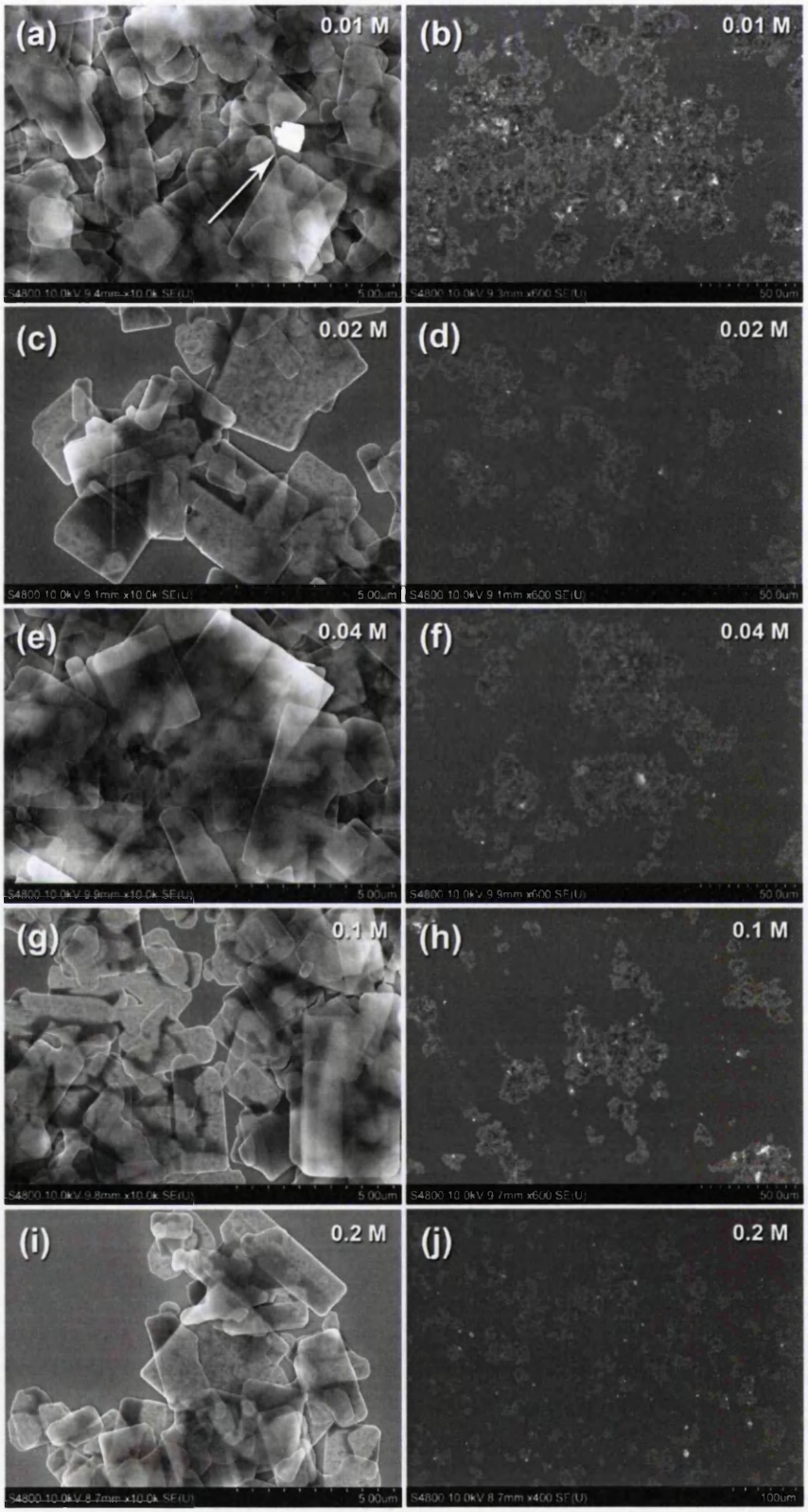

Figure 103. SEM images of different concentration of HMTA and its influence on the morphology and quantity of the product

5.3.6 Influence of microwaving time

SEM imaging was employed to investigate the Influence of microwaving time on the optimized recipe (0.1 M zinc acetate dihydrate, and equimolar concentration of zinc nitrate hexahydrate and HMTA, 0.02M). Our finding revealed that the optimized microwaving time was 120s ±20. After 120s to 140s, SEM imaging showed that LBZA NSs started changing morphology to hexagonal structures. And in the case of continuing microwave irradiation, after 180s the product included only a white precipitation of micron-sized zinc oxide hexagonal crystals (Figures 104, 105). It might be either due to microwave irradiation or over heating caused by microwave irradiation, as it is explained in details in 4.8.2.

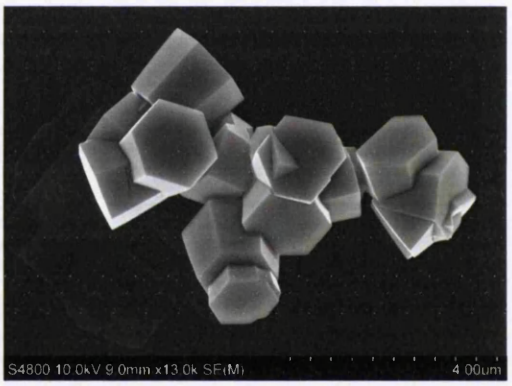

Figure 104. SEM shows the product after 150s microwaving. Coexistence of sheets and hexagonal structres.

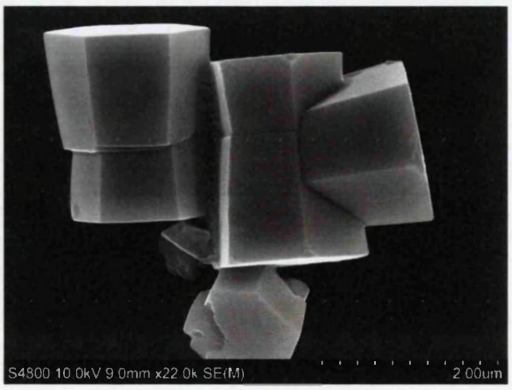

Figure 105. SEM shows the product after 180s microwaving, transforming LBZA nanostructures to hexagonal nanoparticles

5.4 ZnO nanocrystalline nanosheets

Pyrolytic decomposition of Layered basic zinc salts (LBZs) is well known method to convert zinc acetate compound nanoparticles to corresponding ZnO nanoproducts. The suggested conversion process of zinc acetate compounds to ZnO with release of acetate anions is described in Equation 3. So to obtain ZnO nanosheets from LBZA NSs, prepared samples have simply annealed at different temperatures (200°C to 1000°C) for 10 min in each temperature in air using a tube furnace. Figures 106 and 108 show the results.

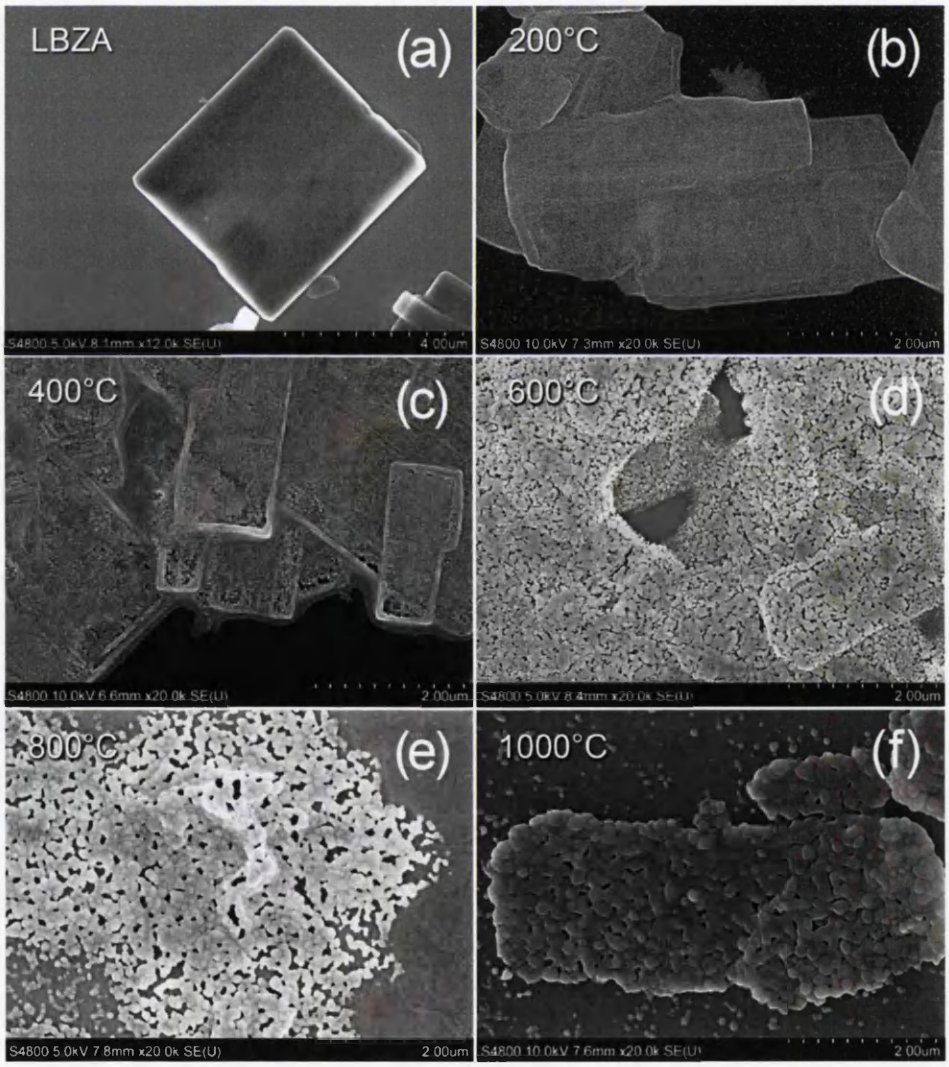

Figure 106. SEM images of annealed LBZA NSs at different temperatures except (a) which shows original LBZA NSs. All images have the same magnification and are spread on silicon wafer.

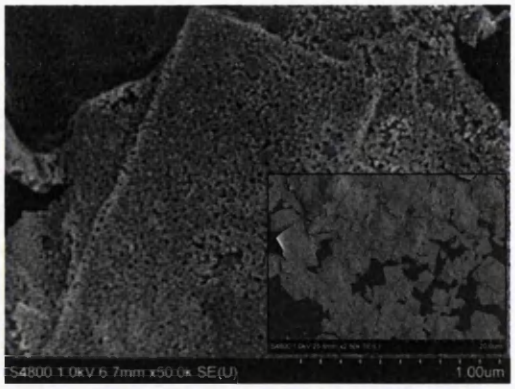

Figure 107. SEM images of LBZA nanosheets annealed at 400C, inset is low magnification SEM of the sheets

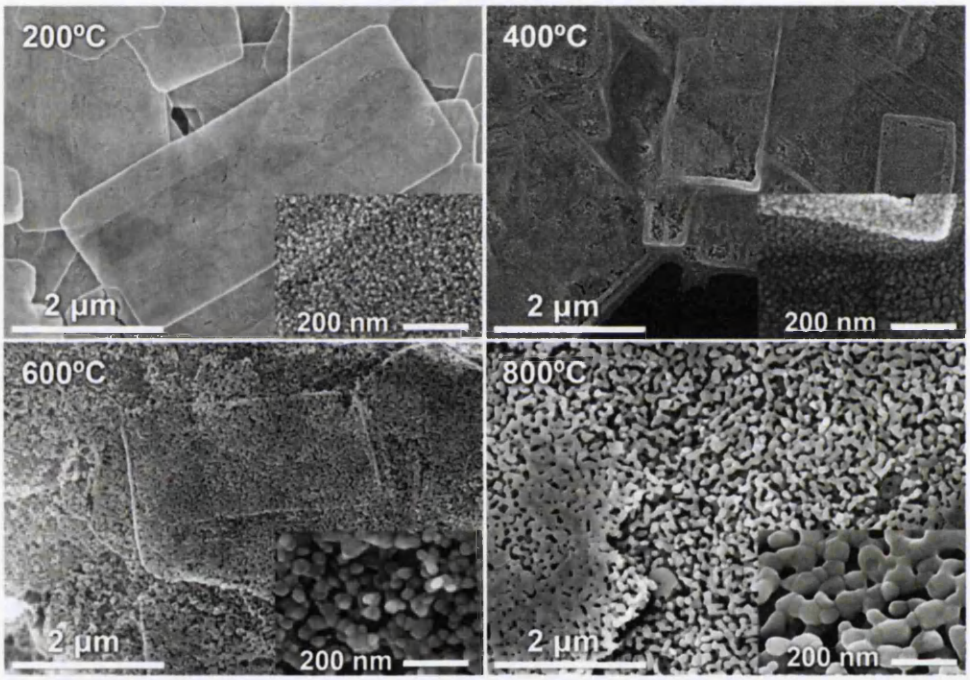

Figure 108. SEM images from annealed LBZA NSs at 200°C, 400°C, 600°C and 800°C. Scale bar 2 um. Insets: detail of the nanocrystals, scale bar 200nm.

SEM measurements reveal that LBZA NSs have reasonably kept their shape after annealing even at 1000°C. In addition, it shows nanocrystalline structure within the nanosheets (Figure 108). Another important point is the size of the nanocrystals. SEM size measurement was used to determine the average size of the nanocrystals annealed at different temperatures. Table 7 shows the results. The results reveal that increasing the temperature resulting in an increase in the size of the nanocrystals. Figure 109 shows high magnification SEM images of LBZA NSs annealed at 400°C (a) and 600°C (b) and confirms the difference

between the size of the nanocrystalline structure of the sheets annealed at different temperature for 10 min.

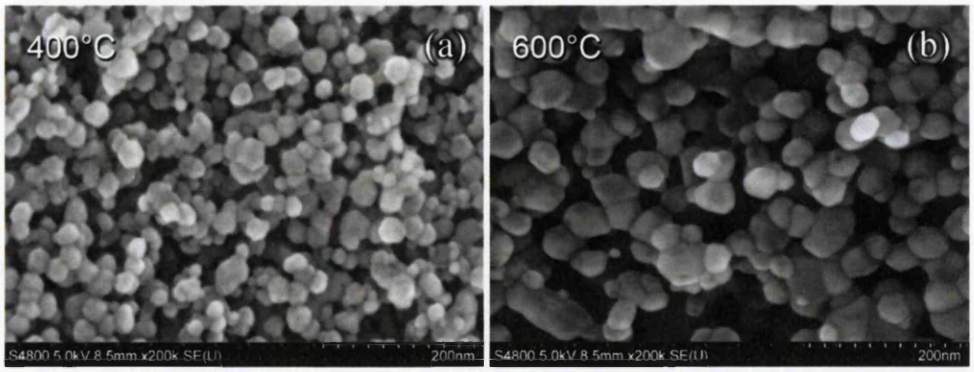

Figure 109. High magnification SEM images of LBZA NSs at different temperature, (a) 400°C, (b) 600°C

Temperature (°C)	200°C	400°C	600°C	800°C	1000°C
Average Size (nm)	15.8	23.1	37.4	70.3	104
Standard Deviation (nm)	3.2	9.34	14.66	22.6	38.5
Standard Deviation %	20.25	40.43	39.2	32.14	37.01

Table 7. SEM size measurement of LBZA NSs annealed at different temperatures and their standard deviation and percentage of the standard deviation

Figure 110 shows the XRD diffractogram of pyrolytic decomposition of the as-synthesized LBZA nanosheets and annealed nanosheets at different temperatures (200°C to 1000°C). As it can be seen, XRD results of LBZA clearly illustrate that LBZA structures are crystalline with the characteristic main zinc acetate 001 peak at 6.67°, also in LBZA diffractogram, there are clear Wurtzite ZnO peaks (between 30° to 40°, which are representative for 100, 002 and 101 peaks). Existence of the zinc oxide peaks was previously explained and could be caused by either partial decomposition of LBZA nanostructures due to over heating the LBZA nanosheets, which were very close to the inner surface of the glass beaker or possibly caused by existence microscale hexagonal ZnO crystals (unwanted crystals), which are also grown at higher temperature generated by microwave absorbance ability of glass beakers compared to the mixture. At temperature higher than 200°C, Wurtzite ZnO peaks are more significant and

can confirm that a part of the LBZA has transformed into the ZnO while main zinc acetate 001 peak at 6.67° still exists. It is in good agreement with Q. Cui et al. [43] and E. S. Jang et al. [44] experiments, they suggested that pyrolytic decomposition of LBZA starts at 100°C to 150°C but ZnO has been completely formed at 250°C to 300°C respectively. Figure 110 also shows that increasing the annealing temperature resulting in sharper and narrower peaks, which means there is an increase in nanocrystalline particle size. It confirms SEM size measurement results and may suggest a temperature size dependent pattern for pyrolytic decomposition.

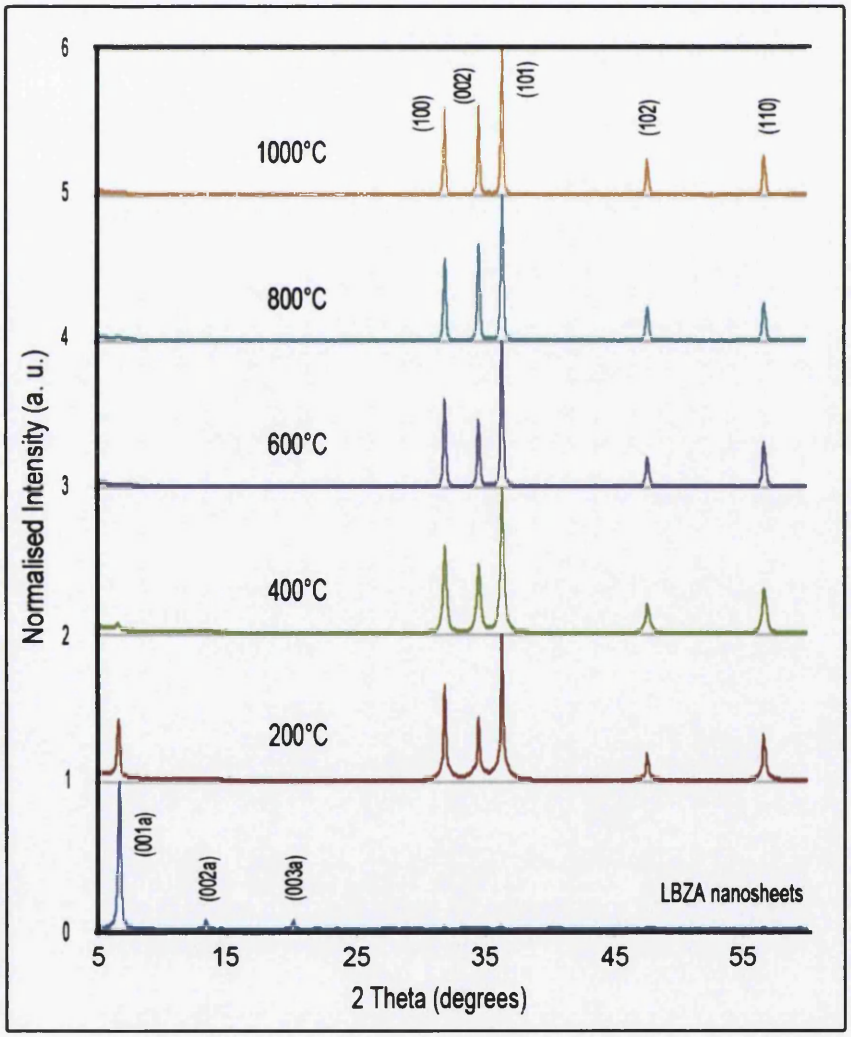

Figure 110. XRD results of pyrolytic decomposition of the LBZA nanosheets at different temperatures. LBZA structures are crystalline with the characteristic main zinc acetate 001 peak at 6.67°, also at temperature higher than 200°C, there are clear Wurtzite ZnO peaks

Figure 111 shows the PL spectra of ZnO NSs produced by annealing LBZA NSs in air at various temperatures. The spectra show the narrow near band edge (NBE) peak at 380nm and the broad visible band typical of ZnO, associated with deep level emission (DLE). The DLE band is centered around 550nm (yellow) for the NSs produced at 400°C, similar to many reported PL results for hydrothermally grown ZnO nanostructures. However, after annealing at 600°C the band broadens and at 800°C, the orange contribution of the visible band becomes more intense. Annealing at 1000°C resulted in a predominantly green visible band. Additionally, the NBE to DLE band ratio is significantly higher at 400°C than at higher temperatures, which indicates a decrease in crystal quality at annealing temperatures higher than 400°C. This is very similar to the results obtained from the nanobelts presented in the previous section. The visible band has been attributed to various ZnO lattice defects, but its origin is still debated. The green contribution is conventionally attributed to oxygen vacancies, despite convincing evidence pointing to surface defects for nanostructures [282,283].

Y. Zhang et al have written extensively about the origin of the DLE band [284]. They report that oxygen interstitials (yellow), zinc interstitials (orange-red), excess oxygen (orange-red), impurities, dislocations, grain boundaries and surface OH groups (yellow) have also been put forward as possible causes. Figure 111 clearly shows several individual components, corresponding to different radiative transitions, which vary in intensity with the annealing temperature. This material system could therefore help shed light on the origin of the visible band.

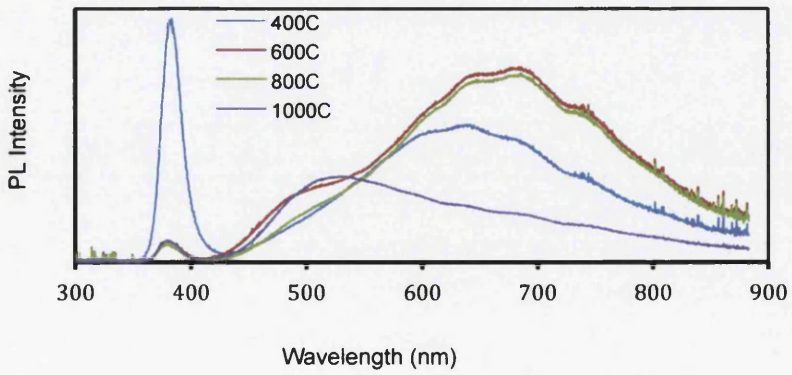

Figure 111. (a) PL spectra of ZnO NSs produced via annealing of LBZA NSs in air at 400°, 600°, 800° and 1000°C, (b) repeated experiment.

5.5 Gas Sensing

The resistive gas sensing potential of the polycrystalline ZnO NBs and NSs was tested by measuring the change in resistance of a network of nanocrystals annealed at 400°C as a function of CO concentration. As explained in section "Metal oxide gas sensing mechanism", when semiconducting sensing materials, are being exposed to the air, oxygen species are absorbed to the surface, causing reduction in conductivity of the sensor. CO sensing with metal oxide semiconductors is based on electron exchanges between the CO molecules and the oxygen species ion adsorbed on the surface (O_2^-, O^-, O^{2-}) [285]. Equation 25 shows possible reaction between CO and O^{2-}:

$$2CO + O^{2-} \rightarrow 2CO_2 + 2e^- \qquad (27)$$

Therefore it increases the amount of conduction electrons and consequently, the overall conductivity for n-type semiconductors. In terms of polycrystalline sensing films, these reactions also control the height of the potential barrier between adjacent particles and therefore electron transport, leading to higher sensitivity. In the absence of reducing gas, the oxygen ions create a depletion region and lead to a high potential barrier, which is lowered when CO molecules react with the oxygen [286,287]. The response was defined as the ratio of the resistance in air and the resistance in the presence of CO.

5.5.1 Experimental details

Our in-house gas sensing apparatus was previously described in details in section 4.8. Figure 112 shows SEM images of the gas sensing apparatus covered by LBZA NSs annealed at 400°C. Figure 112 (a) is low magnification SEM image of sensing material spread over interdigitated electrodes and shows reasonably uniform coverage. Figure 112 (b) confirms that the NSs keep their shape and their structures reasonably constant even after annealing, also shows how NSs overlie each other and make a brilliant connection over the sensing site, uniformity in thickness of the sensing material may play significant role in

calibration and repeatability of fabrication of the sensor. Figure 112 (c) is a high magnification SEM and shows nanocrystalline structure with interconnected nanoparticles within the sheets, resulting in a significant increase in surface area to volume ratio. Figure 113 shows SEM images from exactly the same sensor substrate as used to fabricate ZnO NSs gas sensor but it is covered by LBZA NBs annealed at 400°C. Figure 113 (a) clearly illustrates that not only NBs are able to keep their morphology and structures constant after annealing, but duo to their longer length compered to NSs also can make a brilliant network with an abundant connection points. It may increase their potential to conduct electrons. Figure 113 (b) is a high magnification SEM and confirms polycrystalline ZnO nanoparticles structure within the NBs, SEM size measurement shows that the average size of nanoparticles is about 14.3 ± 5.9 nm). More importantly, after annealing the LBZA NBs, a kind of self-assembly chain-like pattern in aligning the ZnO nanoparticles inside each NB appears (as it is shown previously in Figures 85, 86). This phenomenon may provide better electrons conduction duo to nanowire-shaped nanocrystalline pattern within the NBs, along side with excellent network making and connection between NBs, it may introduce them as a great candidate for sensing, solar cells or any other application with similar needs such as uniform coverage, excellent network making and high surface area to volume ratio.

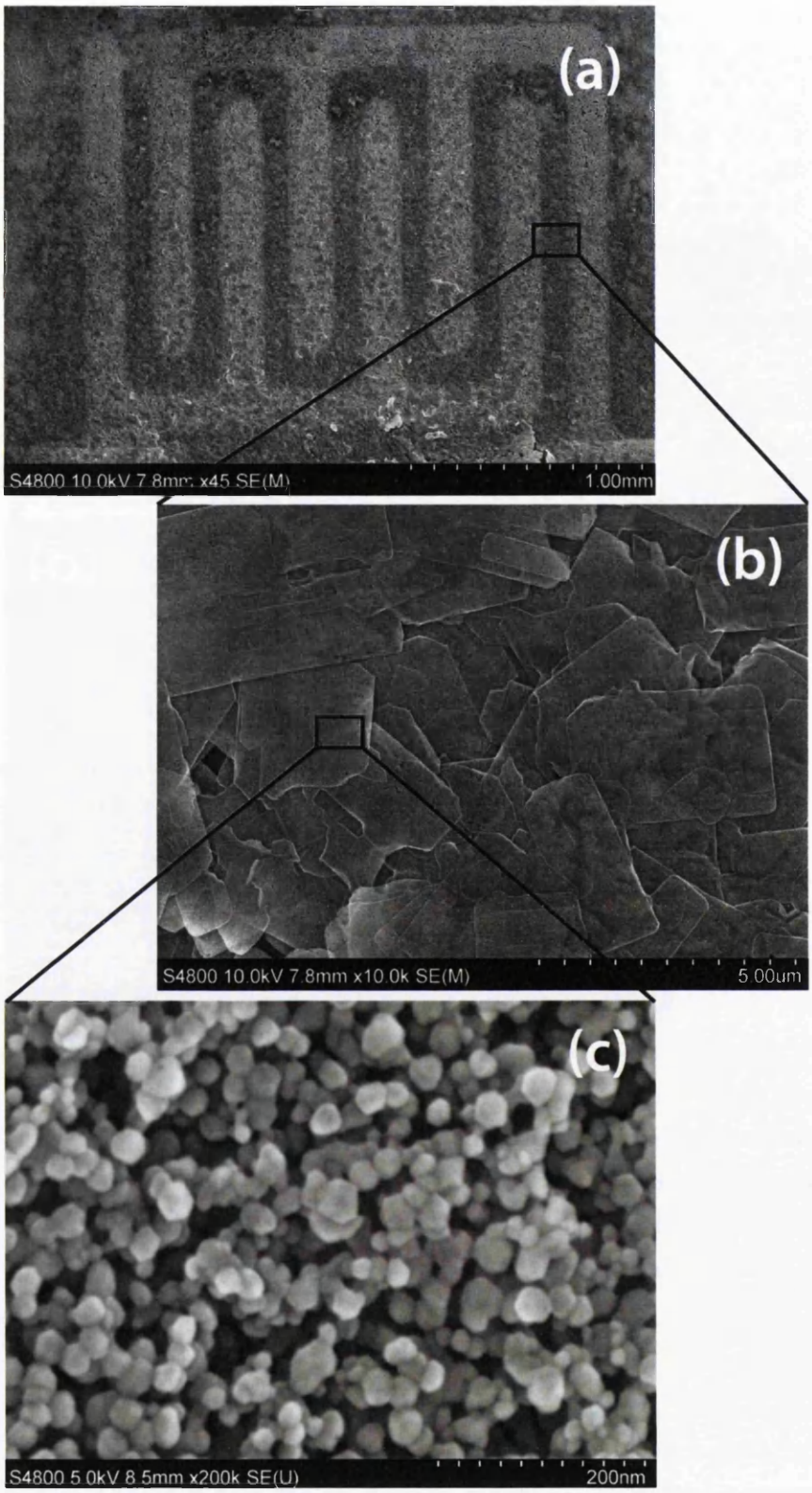

Figure 112: SEM imaging of the gas sensing device surface covered by LBZA nanosheets annealed at 400°C, (a) 45x shows interdigitated electrodes and reasonably uniform coverage of the sensing are by a thin layer of annealed LBZA nanosheets, (b) 10000x confirms that the nanosheets keep their shape and their structures reasonably constant even after annealing and (c) 200000x magnification shows nanocrystalline structure with interconnected nanoparticles within the sheets (high surface area to volume ratio).

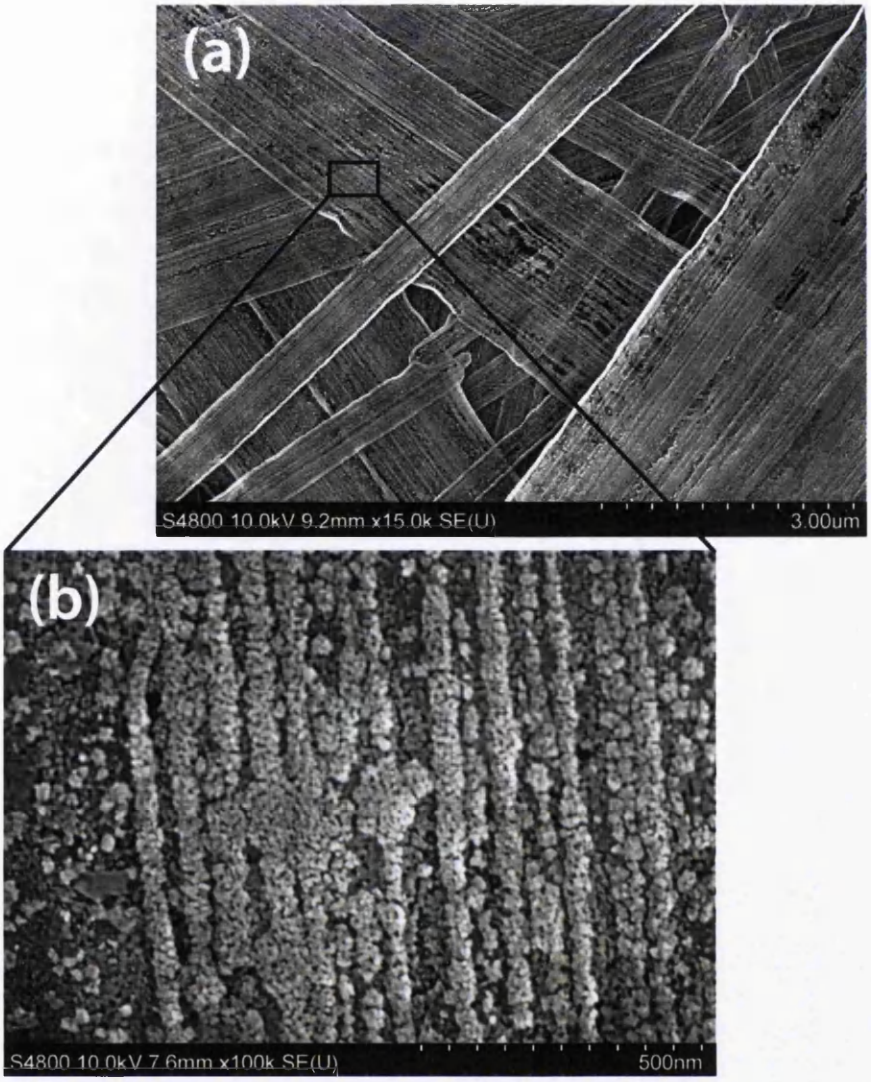

Figure 113: SEM imaging of the gas sensing device surface covered by LBZA nanobelts annealed at 400°C, (a) 15000x shows that the nanobelts can make a network system also it confirms that they keep their shape and their structure reasonably constant even after annealing and (b) 100000x magnification shows a polycrystalline nature with interconnected nanoparticles arranged in a chain-like pattern along the long axis and may work as wires to conduct electrons.

5.5.2 Results and discussion

Figure 114(a) shows the changes in resistance to decreasing concentrations of CO at 400°C for ZnO NBs. Measurements shows a stable and reproducible behavior for the sensor as well as a relatively low resistance of 83 kΩ at 400 °C,

compared to published data for nanocrystalline ZnO, where the resistance of the sensors is in the MΩ range [67,288,289]. It could be possibly due to particular unique chain-like structure pattern, which is providing enhanced conduction along the long axis of the NBs and enables them to conduct electrons much easier, further more it might be a consequence of excellent overlapping and network making with numerous contact points between ZnO nanoparticles. The response as a function of CO concentration is shown on Figure 114(b) and increases linearly from 1.04 for 12.5 ppm to 1.62 for 200 ppm. These values are in good agreement with published work [288] and could be considerably improved by optimizing the deposition process and thickness of the sensing film. In sensing experiments performed by Comini et al. they showed that the sensitivity of devices fabricated with single crystal SnO2 NBs depends greatly on film thickness, which can also affect the optimum temperature [290], it is in good agreement with Q. Kuang et al.[291]. The linear behavior of the response shape has been reported before [292] and is consistent with low gas concentrations. The linear fit has a correlation coefficient of 0.99 and a p value of less than 0.01. Sensing investigations on response to 200 ppm CO as a function of sensor temperature revealed that the highest response to 200 ppm of CO (1.63) occurred at 400°C. Figure 114(c) shows the variation of the response to 200 ppm of CO at different temperatures, peaking at 400 °C. This is in good agreement with previously published results for ZnO sensing. Ryu et al. reported an optimum operating temperature of 350 °C for CO [289] while Bai et al. also reported an optimum temperature of 400 °C for NO2 detection with their ZnO nanorod sensors [293]. Xu et al., who investigated the response of ZnO to various organic compounds [294], found that the highest sensitivity ranged from 370 °C to 420 °C, depending on the fabrication method. The response in Figure 114(c) was extracted from the resistance plot in Figure 114(a) using the resistance before CO exposure and the resistance at equilibrium during the CO exposure. The discontinuities between the end of an exposure and the start of the next are caused by time gaps of no more than 4 min.

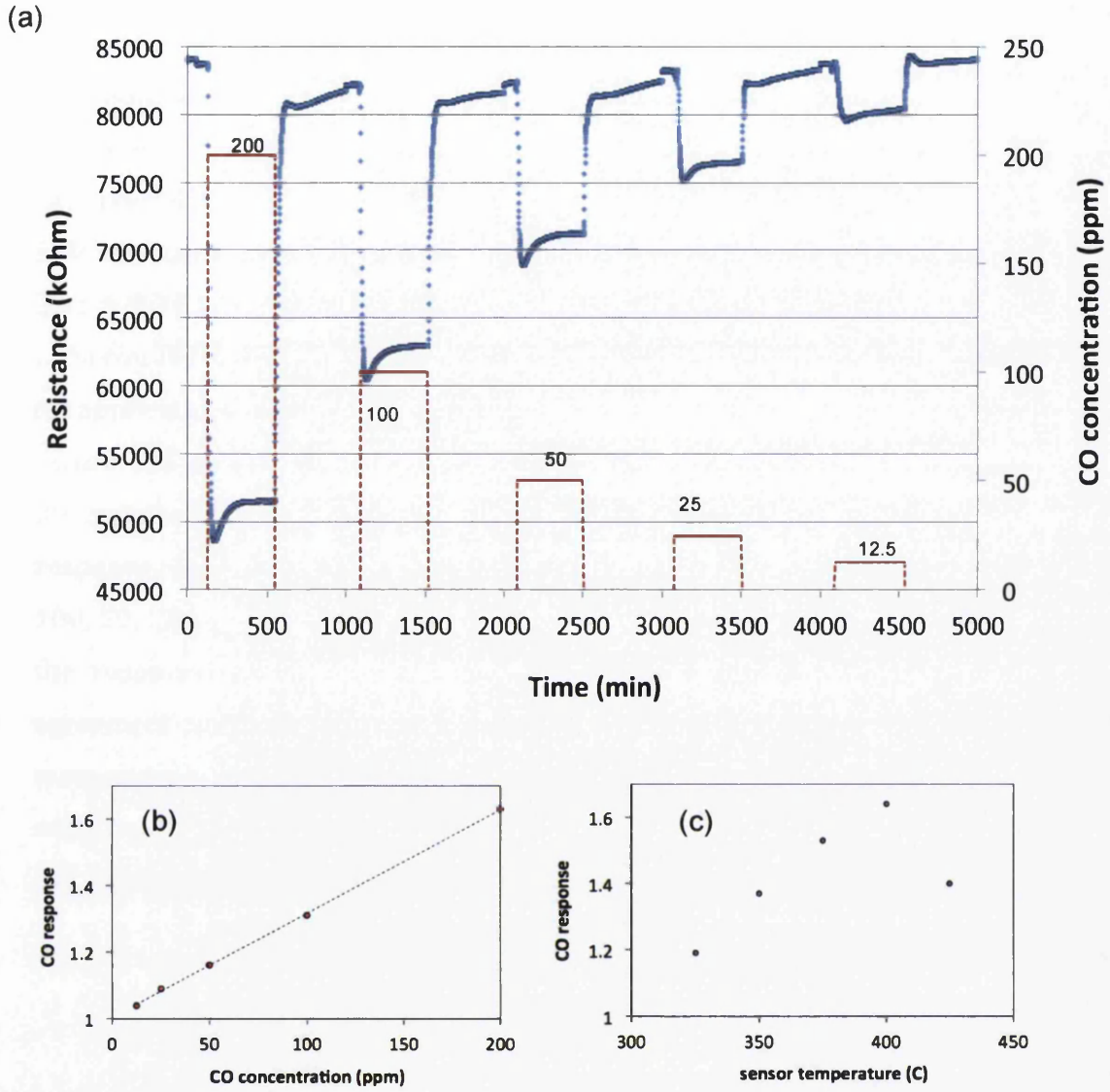

Figure 114. Response to CO of a mat of ZnO NBs produced by annealing at 400 °C. (a) Variation of the resistance in the presence of various CO concentrations at 400 °C. (b) Sensor response as a function of CO concentration at 400 °C. The linear fit has a correlation coefficient of 0.99 and a p value of less than 0.01. (c) Response to 200 ppm CO as a function of sensor temperature. The response was extracted from the resistance plot in (a) using the resistance before CO exposure and the resistance at equilibrium during the CO exposure. The discontinuities between the end of an exposure and the start of the next are caused by time gaps of no more than 4 min.

The same sensor substrate was used to fabricate a resistive gas sensor using LBZA NSs. Drop casting technique was used to make a thin film of nanocrystals, after drying in room temperature it was transferred into the tube furnace to anneal at 400°C for 10 min. Figure 112(a) shows SEM imaging after annealing, it confirms reasonably uniform dispersion of nanocrystals. Figure 112(b) is higher

magnification SEM and shows NSs kept their shape considerably constant after annealing and also shows the overlapping of the sheets, which may improve electrons conduction. Figure 112(c) is very high magnification to show nanocrystalline structure with interconnected nanoparticles within the sheets, SEM measurements revealed that the average size of the nanoparticles is about 23.1 ± 9.34 nm, not only this structure provides high surface area to volume ratio condition, but it can also increase the electron conduction which is suitable for applications with particular needs.

Figure 115 shows the effect of CO exposures of decreasing concentrations on the resistance of as-fabricated thin film of ZnO NSs. The graph shows that the response, defined as R(air)/R(CO), was 1.65, 1.48, 1.32, 1.22 and 1.13 at 200, 100, 50, 25 and 12.5ppm of CO, respectively. It also shows a linear behavior of the response pattern, which has been reported before [292] and is in good agreement with low gas concentrations. Sensing investigations at different temperature revealed that the highest response to 200 ppm of CO (1.65) occurred at 325°C, Figure 116 demonstrates the reproducibility and stability of the sensing and emphasises the potential of the material for this application.

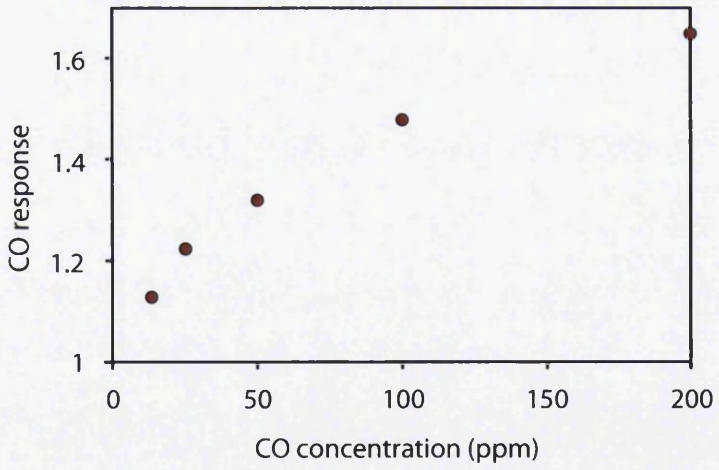

Figure 115 shows the effect of the different concentrations of CO exposed to the as-fabricated gas sensor on the resistance of ZnO NSs film. The graph shows that the response, defined as R(air)/R(CO).

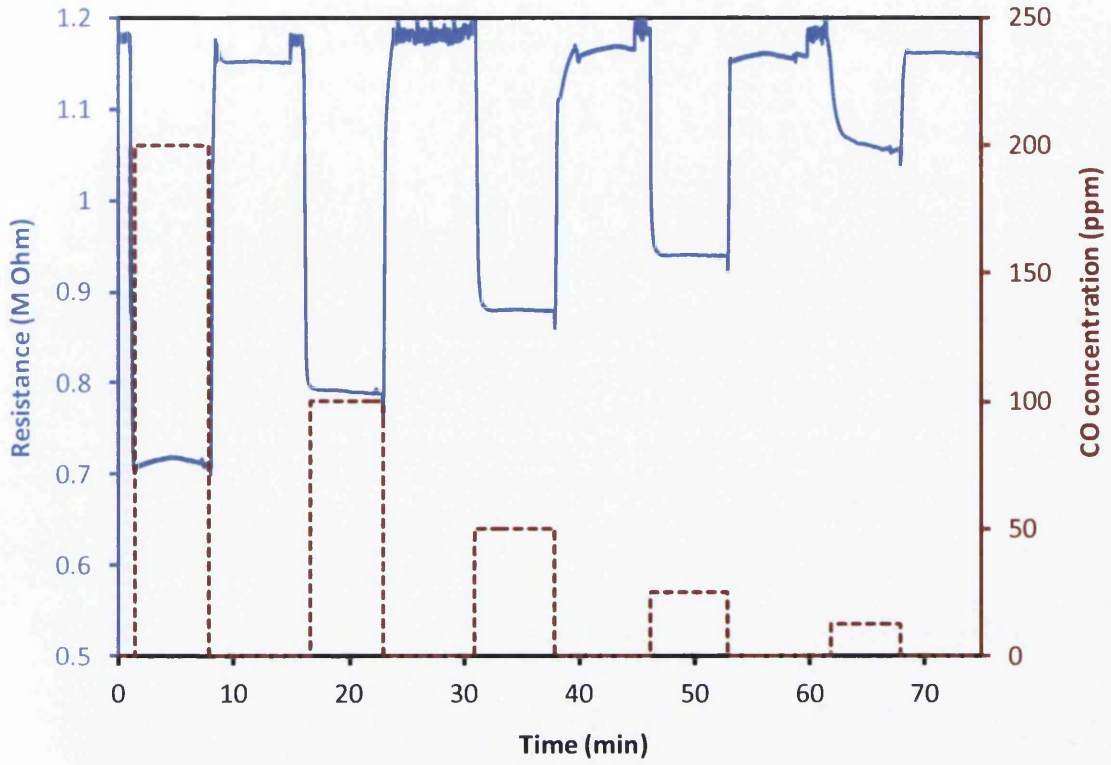

Figure 116: The resistance versus time curve (blue solid line) of a film of ZnO NSs at 325°C, as various CO concentrations are mixed with the flowing dry air of the test chamber. The decreasing CO concentrations, from 200ppm to 12.5ppm are shown by the dashed red line. The inset shows the response of the sensing film as a function of CO concentration.

Figure 117 is normalised of Figure 114(a) and Figure116, and shows a comparison between our two novel nanomaterials, LBZA NBs and LBZA NSs annealed at 400 °C. As it can be seen resistance of the sheets are in the MΩ range, which is in good agreement with published literatures where the resistance of the nanocrystalline ZnO sensors are in the MΩ range [67,288,289]. In contrast, resistance of the NBs' sensor is in kΩ range, it could be explained by possessing very particular chain-like structure along the long axis of NBs through which electrons conduction might be easier. Despite having lower resistance, NSs had better respond to changes of CO concentrations especially in lower concentrations. It could be possibly due to coating techniques we used for NBs and NSs in this research. As it mentioned before drop casting technique was used to fabricate NSs sensor but because of the nature of the belts and their tendency to make 3D network structure in DI water, drop casting was unsuccessful and resulted in an ununiformed coverage on sensor substrate.

Therefore, deep coating technique was used to make a uniform thin film. Although deep coating was found more efficient, achieving uniform coverage was not possible. It could be imaginable that with optimizing and developing the coating system, the performance of the NBs gas sensing could improve as it is in good agreement with previous research done by Comini et al., it revealed the influence of the thickness of the film on sensitivity of the sensor [290]. Although XRD and SEM data showed a smaller particle size for the NBs at 400°C, possibly due to a higher defect concentration in the LBZA crystal, the sensor covered with LBZA NSs works at lower temperature and shows better response to CO concentration changes. It is more significant at lower concentration of CO.

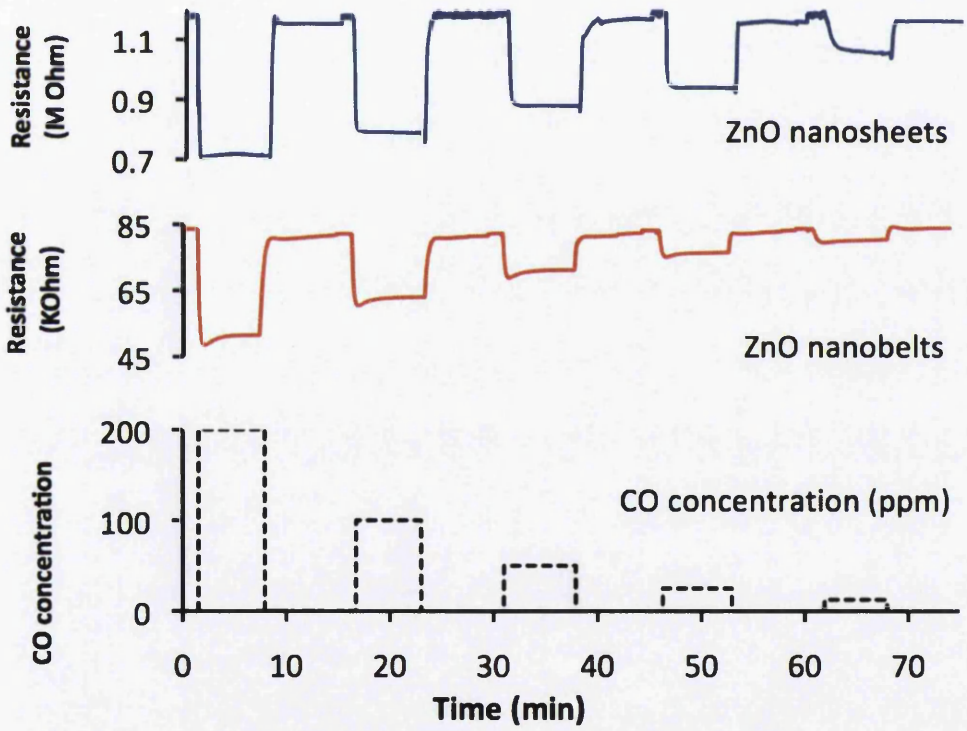

Figure 117. Changes in resistance to decreasing concentrations of CO at 400°C for ZnO NBs and at 350°C for ZnO NSs. CO concentration was decreased from 200ppm to 12.5ppm.

6 Conclusion

Herein, we have systematically developed and introduced a very simple and very low cost technique to generate mass production of pure ZnO nanocrystalline NBs from precursor LBZA (not a mixture of nanowires and nanobelts). Synthesizing via hydrolysis of zinc acetate in aqueous solution without adding any basic materials or surfactants makes this novel method more beneficial. In addition, we are introducing a novel rapid microwave-assisted hydrothermal technique to produce LBZA NSs and pyrolytic decomposition to pure ZnO nanocrystalline. Finally through home-designed gas sensing apparatus, sensitivity and gas sensing behavior of as-grown nanostructures to CO have been investigated.

The LBZA NBs were grown at 65°C for 20 hours whilst the NSs were grown in 2 minutes in a commercial microwave oven. The NBs have widths ranging from 200 nm to several micrometers and lengths in the several hundred of micrometers range. The thickness of the LBZA NBs ranges from 10nm to 50nm with morphologies typical of lamellar growth. NSs have a similar thickness with lateral dimensions ranging from 200x200 nm to, in some cases, more than 5x5 μm. Thermal decomposition into ZnO starts during annealing in air about 200°C and becomes complete after 400°C resulting in producing ZnO NBs and NSs consisting of nanocrystalline nanoparticles within them. XRD and SEM data showed a smaller particle size for the NBs at 400°C, possibly due to a higher defect concentration in the LBZA crystal. PL shows evidence of better crystallinity for the ZnO NSs than for the NBs following pyrolytic decomposition at 400°C. Annealing at 600°C results in an increase of the nanoparticle size and sintering was observed for the NBs. While generally sintering effect occurs at the temperatures over 600°C for NSs. Gas sensing investigations on sensitivity to CO showed that the NSs had a lower optimized sensing temperature (325°C) compared to the NBs for the same response at 200ppm of CO, which was about 400°C. Also results showed better sensitivity at lower concentration. As it is mentioned before (5.1.3.), either high magnification SEM imaging (Figures 85-86) or AFM imaging (Figures 89-91) showed a polycrystalline nature with

interconnected nanoparticles arranged in a chain-like pattern along the NBs long axis and may work as wires to conduct electrons. It was expected better conductivity for NBs compared to NSs. But it can be explained by PL results that better crystalline quality and less defects for NSs. These results demonstrate that as-developed hydrothermal technique to produce NBs has a great potential to be used as a nanostructures mass production route due to being simple, very low-cost, very low temperature, high yield and more importantly reproducible. But similar to any other technique it has some disadvantages including; growth procedure must be done within aqueous system and also to transform LBZA to ZnO nanostructure, thermal decomposition is inevitable, which occurs at temperature about 400°C, consequently fabrication of the NBs is not possible on substrates which can not tolerate this temperature. There is same scenario for NSs synthesized by microwave-assisted hydrothermal technique. The key point in this research is: the results demonstrate that novel rapid microwave-assisted growth of LBZA crystals not only leads to higher quality ZnO nanomaterials than conventional hydrothermal growth but could also lead to a fast and very low cost method for the mass production of nanocrystals and consequently of high sensitivity sensors.

References

1. Singh, M., Manikandan, S. & Kumaraguru, A. K. Nanoparticles: A new technology with wide applications. *Res. J. Nanosci. Nanotechnol* 1, 1–11 (2011).

2. Bhushan, B. Nanotribology and nanomechanics of MEMS/NEMS and BioMEMS/BioNEMS materials and devices. *Microelectronic Engineering* 84, 387–412 (2007).

3. Sakamoto, J. H. *et al.* Enabling individualized therapy through nanotechnology. *Pharmacological Research* 62, 57–89 (2010).

4. Singh, R. & Tawaniya, J. R EVIEW ON N ANOTECHNOLOGY WITH. 3, 1–8 (2013).

5. Prashant, Y. R., Nirangan, C. A., Shripal, M. C. & Krishna, M. S. Nanotechnology: Needs and Applications. *International Journal of Pharmaceutical Sciences Review & Research* 20, (2013).

6. Albrecht, M. A., Evans, C. W. & Raston, C. L. Green chemistry and the health implications of nanoparticles. *Green Chemistry* 8, 417–432 (2006).

7. Adlakha-Hutcheon, G. *et al.* in *Nanomaterials: Risks and Benefits* 195–207 (Springer, 2009).

8. Jena, M., Mishra, S., Jena, S. & Mishra, S. S. IJBCP International Journal of Basic & Clinical Pharmacology. *International Journal* 2, 353 (2013).

9. Zhang, L. & Webster, T. J. Nanotechnology and nanomaterials: promises for improved tissue regeneration. *Nano Today* 4, 66–80 (2009).

10. Cimalla, V., Pezoldt, J. & Ambacher, O. Group III nitride and SiC based MEMS and NEMS: materials properties, technology and applications. *Journal of Physics D: Applied Physics* 40, 6386 (2007).

11. Wang, Z. L. Nanostructures of zinc oxide. *Materials today* 7, 26–33 (2004).

12. Micronews. *MEMS market Forecast 2011-2017 in value.* at <MEMS market will continue to see steady, sustainable double-digit growth for the next six years>

13. Lyshevski, S. E. NANO- AND MICROELECTROMECHANICAL. (2001).

14. BCC Research. "Nanotechnology in Medical Applications: The Global Market."*Global Information Inc.* (2012).

15. Enterprise and Industry, E. C. the global market for nanomaterials. *Enterprise and Industry magazine* (2013). at <http://ec.europa.eu/enterprise/magazine/index_en.htm>

16. Commission, E. *Nanomaterials: Case by case safety approach for breakthrough technology.*

17. Roco, M. C. The long view of nanotechnology development: the National Nanotechnology Initiative at 10 years. *Journal of Nanoparticle Research* 13, 427–445 (2011).

18. Kuno, M. Introductory nanoscience: Physical and chemical concepts. *MRS Bulletin* 37, 169–170 (2012).

19. Trivedi, N. & Ashcroft, N. W. Quantum size effects in transport properties of metallic films. *Phys. Rev. B* 38, 12298–12309 (1988).

20. V. E. Borisenko. Physics, Chemistry andApplication of Nanostructures.

21. Reed, M. A. & Member, S. Molecular-Scale Electronics. 87, (1999).

22. Hersam, M. C. Silicon-based molecular nanotechnology. 11, 70–76 (2000).

23. Belomoin, G. *et al.* Observation of a magic discrete family of ultrabright Si nanoparticles. *Applied Physics Letters* 80, 841 (2002).

24. Scriba, M. R., Arendse, C., Härting, M. & Britton, D. T. Hot-wire synthesis of Si nanoparticles. *Thin Solid Films* 516, 844–846 (2008).

25. Körmer, R., Jank, M. P. M., Ryssel, H., Schmid, H.-J. & Peukert, W. Aerosol synthesis of silicon nanoparticles with narrow size distribution—Part 1: Experimental investigations. *Journal of Aerosol Science* 41, 998–1007 (2010).

26. Hoshino, A. *et al.* Physicochemical Properties and Cellular Toxicity of Nanocrystal Quantum Dots Depend on Their Surface Modification. *Nano Letters* 4, 2163–2169 (2004).

27. Ni, Z., Ying, P., Luo, Y. & Li, Z. Preparation and Characterization of Amorphous Silicon Oxide Nanowires. *Journal of China University of Mining and Technology* 17, 587–589 (2007).

28. Demami, F., Ni, L., Rogel, R., Salaun, a. C. & Pichon, L. Silicon nanowires synthesis for chemical sensor applications. *Procedia Engineering* 5, 351–354 (2010).

29. Morishita, T., Spencer, M. J. S., Russo, S. P., Snook, I. K. & Mikami, M. Surface reconstruction of ultrathin silicon nanosheets. *Chemical Physics Letters* 506, 221–225 (2011).

30. Gao, F., Yang, W., Fan, Y. & An, L. Mass production of very thin single-crystal silicon nitride nanobelts. *Journal of Solid State Chemistry* 181, 211–215 (2008).

31. Canham, L. T. Silicon quantum wire array fabrication by electrochemical and chemical dissolution of wafers. *Applied Physics Letters* 57, 1046 (1990).

32. Bley, R. A., Kauzlarich, S. M., Fendler, J. H. & Dekany, I. Nanoparticles in Solids and Solutions. *Nanoparticles in Solids and Solutions* (1996).

33. Ziegler, K. J., Doty, R. C., Johnston, K. P. & Korgel, B. A. Synthesis of organic monolayer-stabilized copper nanocrystals in supercritical water. *Journal of the American Chemical Society* 123, 7797–7803 (2001).

34. Ashcroft, N. W. & Mermin, N. D. Solid State. *Physics (New York: Holt, Rinehart and Winston) Appendix C* (1976).

35. Scavetta, E. *et al.* Nanoporous Ge coated by Au nanoparticles for electrochemical application. *Electrochemistry Communications* 30, 83–86 (2013).

36. Oku, T. *et al.* Formation and photoluminescence of Ge and Si nanoparticles encapsulated in oxide layers. *Materials Science and Engineering: B* 74, 242–247 (2000).

37. Renard, C. *et al.* Size effect on Ge nanowires growth kinetics by the vapor–liquid–solid mechanism. *Thin Solid Films* 520, 3314–3318 (2012).

38. Morgunov, R. B. *et al.* Electron spin resonance in Ge nanowires doped with Mn. *Journal of Magnetism and Magnetic Materials* 310, e824–e826 (2007).

39. Wan, L. & Gao, T. Structural, electronic properties and stability of Ag-doped GaAs nanowires: First-principles study. *Physica E: Low-dimensional Systems and Nanostructures* 54, 301–307 (2013).

40. Mi, Z. & Bianucci, P. When self-organized In(Ga)As/GaAs quantum dot heterostructures roll up: Emerging devices and applications. *Current Opinion in Solid State and Materials Science* 16, 52–58 (2012).

41. Cho, S. *et al.* Metalorganic vapor phase epitaxy growth and properties of GaAs/AlGaAs and InGaAs/GaAs quantum well structures on (111)A GaAs substrates. *Microelectronics Journal* 30, 455–459 (1999).

42. Jangir, R. *et al.* Synthesis and characterization of β-Ga2O3 nanostructures grown on GaAs substrates. *Applied Surface Science* 257, 9323–9328 (2011).

43. Chao, J.-J., Shiu, S.-C. & Lin, C.-F. GaAs nanowire/poly(3,4-ethylenedioxythiophene):poly(styrenesulfonate) hybrid solar cells with incorporating electron blocking poly(3-hexylthiophene) layer. *Solar Energy Materials and Solar Cells* 105, 40–45 (2012).

44. Pradhan, D., Kumar, M., Ando, Y. & Leung, K. T. Fabrication of ZnO nanospikes and nanopillars on ITO glass by templateless seed-layer-free electrodeposition and their field-emission properties. *ACS Applied Materials & Interfaces* 1, 789–796 (2009).

45. A. Tarat, R. Majithia, R. A. Brown, M. W. Penny, K. E. Meissner, and T. G. G. M. Nanocrystalline ZnO obtained from pyrolytic decomposition of layered basic zinc acetate: comparison between conventional and microwave oven growth. *IEEE* 701–705 (2012).

46. Goyal, A. & Kachhwaha, S. ZnO thin films preparation by spray pyrolysis and electrical characterization. *Materials Letters* 68, 354–356 (2012).

47. WangWang *et al.* Piezoelectric Field Effect Transistor and Nanoforce Sensor Based on a Single ZnO Nanowire. *Nano Letters* 6, 2768–2772 (2006).

48. Znaidi, L., Soler Illia, G., Benyahia, S., Sanchez, C. & Kanaev, A. V. Oriented ZnO thin films synthesis by sol--gel process for laser application. *Thin Solid Films* 428, 257–262 (2003).

49. Steve Dunn, Joe Briscoe, Mark Stewart, Paul M. Weaver, M. G. C. Nanostructured zinc oxide piezoelectric energy generators based on semiconductor P-N junctions. *microtechnologies conferance* (2013).

50. Park, J.-S. *et al.* Flexible full color organic light-emitting diode display on polyimide plastic substrate driven by amorphous indium gallium zinc oxide thin-film transistors. *Applied Physics Letters* 95, 13503 (2009).

51. Fortunato, E. M. C. *et al.* Fully Transparent ZnO Thin-Film Transistor Produced at Room Temperature. *Advanced Materials* 17, 590–594 (2005).

52. Tarat, A., Majithia, R., Brown, R. a., Penny, M. W. & Meissner, K. E. Synthesis of nanocrystalline ZnO nanobelts via pyrolytic decomposition of zinc acetate nanobelts and their gas sensing behavior. *Surface Science* 606, 715–721 (2012).

53. Fortunato, E. *et al.* Recent advances in ZnO transparent thin film transistors. *Thin Solid Films* 487, 205–211 (2005).

54. Karpina, V. a. *et al.* Zinc oxide - analogue of GaN with new perspective possibilities. *Crystal Research and Technology* 39, 980–992 (2004).

55. Pauporté, T., Lupan, O., Viana, B. & le Bahers, T. ZnO nanowire-based light-emitting diodes with tunable emission from near-UV to blue. in *SPIE OPTO* 86410L–86410L (2013).

56. Ralib, A. A. M. & Nordin, A. N. Comparative analysis of zinc oxide and aluminium doped ZnO for GHz CMOS MEMS surface acoustic wave resonator. in *Design, Test, Integration and Packaging of MEMS/MOEMS (DTIP), 2013 Symposium on* 1–6 (2013).

57. Peng, W. *et al.* Performance Improvement of ZnO Nanowire based Surface Acoustic Wave Ultraviolet Detector via Poly (3, 4-ethylenedioxythiophene) Surface Coating. *Sensors and Actuators A: Physical* (2013).

58. Lee, K.-H. *et al.* All-Solution-Processed Transparent Thin Film Transistor and Its Application to Liquid Crystals Driving. *Advanced Materials* (2013).

59. Qian, X., Wang, T. & Yan, D. Transparent organic thin-film transistors based on high quality polycrystalline rubrene film as active layers. *Organic Electronics* (2013).

60. Caruso, F. Nanoengineering of Particle Surfaces. *Advanced Materials* 13, 11–22 (2001).

61. Choy, J.-H. *et al.* Soft Solution Route to Directionally Grown ZnO Nanorod Arrays on Si Wafer; Room-Temperature Ultraviolet Laser. *Advanced Materials* 15, 1911–1914 (2003).

62. Jang, E.-S. *et al.* Quantum confinement effect in ZnO/ MgZnO multishell nanorod heterostructures. *Applied physics letters* 88, 23102 (2006).

63. Tsukazaki, A. *et al.* Repeated temperature modulation epitaxy for p-type doping and light-emitting diode based on ZnO. *Nature Materials* 4, 42–46 (2004).

64. Hwang, D.-K. *et al.* p-ZnO/n-GaN heterostructure ZnO light-emitting diodes. *Applied Physics Letters* 86, 222101 (2005).

65. Tsukazaki, A. *et al.* Blue Light-Emitting Diode Based on ZnO. *Japanese Journal of Applied Physics* 44, L643–L645 (2005).

66. Jang, E. S., Won, J.-H., Hwang, S.-J. & Choy, J.-H. Fine tuning of the face orientation of ZnO crystals to optimize their photocatalytic activity. *Advanced Materials* 18, 3309–3312 (2006).

67. Wang, J. X. *et al.* Hydrothermally grown oriented ZnO nanorod arrays for gas sensing applications. *Nanotechnology* 17, 4995–4998 (2006).

68. Liu, J. *et al.* Novel porous single-crystalline ZnO nanosheets fabricated by annealing ZnS (en) 0.5 (en= ethylenediamine) precursor. Application in a gas sensor for indoor air contaminant detection. *Nanotechnology* 20, 125501 (2009).

69. Keis, K., Magnusson, E., Lindström, H., Lindquist, S.-E. & Hagfeldt, A. A 5% efficient photoelectrochemical solar cell based on nanostructured ZnO electrodes. *Solar energy materials and solar cells* 73, 51–58 (2002).

70. Keis, K. *et al.* Nanostructured ZnO electrodes for dye-sensitized solar cell applications. *Journal of Photochemistry and photobiology A: Chemistry* 148, 57–64 (2002).

71. Lu, Y., Emanetoglu, N. W. & Chen, Y. ZnO piezoelectric devices. *Zinc Oxide Bulk, Thin Films and Nanostructures: Processing, Properties, and Applications* 443 (2011).

72. Emanetoglu, N. W., Gorla, C., Liu, Y., Liang, S. & Lu, Y. Epitaxial ZnO piezoelectric thin ® lms for saw ® lters. 2, 3–8 (1999).

73. Vayssieres, L. Growth of arrayed nanorods and nanowires of ZnO from aqueous solutions. *Advanced Materials* 15, 464–466 (2003).

74. Nasi, L. *et al.* Mesoporous single-crystal ZnO nanobelts: supported preparation and patterning. *Nanoscale* 5, 1060–1066 (2013).

75. Shi, Y. *et al.* Ultrarapid Sonochemical Synthesis of ZnO Hierarchical Structures: From Fundamental Research to High E ffi ciencies up to 6.42% for Quasi-Solid Dye-Sensitized Solar Cells. (2013).

76. Wang, Z. L. Zinc oxide nanostructures: growth, properties and applications. *Journal of Physics: Condensed Matter* 16, R829–R858 (2004).

77. Gao, P.-X., Ding, Y. & Wang, Z. L. Electronic transport in superlattice-structured ZnO Nanohelix. *Nano letters* 9, 137–43 (2009).

78. Gao, T. & Wang, T. H. Synthesis and properties of multipod-shaped ZnO nanorods for gas-sensor applications. *Applied Physics A* 80, 1451–1454 (2005).

79. Hang Leung, Y. *et al.* Synthesis and properties of ZnO multipod structures. *Journal of crystal growth* 274, 430–437 (2005).

80. Lu, F., Cai, W. & Zhang, Y. ZnO hierarchical micro/nanoarchitectures: solvothermal synthesis and structurally enhanced photocatalytic performance. *Advanced Functional Materials* 18, 1047–1056 (2008).

81. Hu, J. Q. & Bando, Y. Growth and optical properties of single-crystal tubular ZnO whiskers. *Applied Physics Letters* 82, 1401–1403 (2003).

82. Gao, P. X. & Wang, Z. L. Mesoporous polyhedral cages and shells formed by textured self-assembly of ZnO nanocrystals. *Journal of the American Chemical Society* 125, 11299–305 (2003).

83. Wang, Z., Qian, X., Yin, J. & Zhu, Z. Tube-like ZnO Arrays by a Simple Chemical Solution Route. 3441–3448 (2004).

84. Zhou, J., Xu, N. S. & Wang, Z. L. Dissolving Behavior and Stability of ZnO Wires in Biofluids: A Study on Biodegradability and Biocompatibility of ZnO Nanostructures. *Advanced Materials* 18, 2432–2435 (2006).

85. Banoee, M. *et al.* ZnO nanoparticles enhanced antibacterial activity of ciprofloxacin against Staphylococcus aureus and Escherichia coli. *Journal of Biomedical Materials Research Part B: Applied Biomaterials* 93, 557–561 (2010).

86. Singer, A., Serfaty, V. & others. Cement-retained implant-supported fixed partial dentures: a 6-month to 3-year follow-up. *The International journal of oral & maxillofacial implants* 11, 645–649 (1995).

87. Saunders, W. P. & Saunders, E. M. Coronal leakage as a cause of failure in root-canal therapy: a review. *Dental Traumatology* 10, 105–108 (1994).

88. Gomes, B. P. F. A. *et al.* Antimicrobial action of intracanal medicaments on the external root surface. *Journal of Dentistry* 37, 76–81 (2009).

89. Going, R. E. & Massler, M. Influence of cavity liners under amalgam restorations on penetration by radioactive isotopes. *The Journal of Prosthetic Dentistry* 11, 298–312 (1961).

90. Rasmussen, J. W., Martinez, E., Louka, P. & Wingett, D. G. Zinc oxide nanoparticles for selective destruction of tumor cells and potential for drug delivery applications. *Expert opinion on drug delivery* 7, 1063–1077 (2010).

91. Chen, S. J. *et al.* Structural and Optical Properties of Uniform ZnO Nanosheets. *Advanced Materials* 17, 586–590 (2005).

92. Li, J., Fan, H. & Jia, X. Multilayered ZnO nanosheets with 3D porous architectures: synthesis and gas sensing application. *The Journal of Physical Chemistry C* 114, 14684–14691 (2010).

93. Huang, Y., Duan, X., Wei, Q. & Lieber, C. M. Directed assembly of one-dimensional nanostructures into functional networks. *Science* 291, 630–633 (2001).

94. Moon, H., Nam, C., Kim, C. & Kim, B. Synthesis and photoluminescence of zinc sulfide nanowires by simple thermal chemical vapor deposition. *Materials Research Bulletin* 41, 2013–2017 (2006).

95. Park, W. Il, Kim, D. H., Jung, S.-W. & Yi, G.-C. Metalorganic vapor-phase epitaxial growth of vertically well-aligned ZnO nanorods. *Applied Physics Letters* 80, 4232 (2002).

96. Choi, K.-S., Lichtenegger, H. C., Stucky, G. D. & McFarland, E. W. Electrochemical synthesis of nanostructured ZnO films utilizing self-assembly of surfactant molecules at solid-liquid interfaces. *Journal of the American Chemical Society* 124, 12402–3 (2002).

97. Fan, Z. & Lu, J. G. Zinc oxide nanostructures: synthesis and properties. *Journal of nanoscience and nanotechnology* 5, 1561–73 (2005).

98. Jang, E.-S., Won, J.-H., Kim, Y.-W., Cheng, Z. & Choy, J.-H. Synthesis of porous and nonporous ZnO nanobelt, multipod, and hierarchical nanostructure from Zn-HDS. *Journal of Solid State Chemistry* 183, 1835–1840 (2010).

99. Hu, H., Huang, X., Deng, C., Chen, X. & Qian, Y. Hydrothermal synthesis of ZnO nanowires and nanobelts on a large scale. *Materials Chemistry and Physics* 106, 58–62 (2007).

100. Tasker, P. W. The stability of ionic crystal surfaces. *Journal of Physics C: Solid State Physics* 12, 4977 (1979).

101. Dulub, O., Boatner, L. A. & Diebold, U. STM study of the geometric and electronic structure of ZnO (0001)-Zn,(0001)-O,(1010), and (1120) surfaces. *Surface Science* 519, 201–217 (2002).

102. Meyer, B. & Marx, D. Density-functional study of the structure and stability of ZnO surfaces. *Physical Review B* 67, 35403 (2003).

103. Gutiérrez Sosa, A., Evans, T. M., Parker, S. C., Campbell, C. T. & Thornton, G. Orientation of benzene and phenoxy on the polar ZnO (0001)-Zn surface. *The Journal of Physical Chemistry B* 105, 3783–3785 (2001).

104. Dulub, O., Diebold, U. & Kresse, G. Novel stabilization mechanism on polar surfaces: ZnO (0001)-Zn. *Physical review letters* 90, 16102 (2003).

105. Wander, A. & Harrison, N. M. The stability of polar oxide surfaces: The interaction of HO with ZnO (0001) and ZnO (0001). *The Journal of chemical physics* 115, 2312 (2001).

106. Staemmler, V. *et al.* Stabilization of polar ZnO surfaces: Validating microscopic models by using CO as a probe molecule. *Physical review letters* 90, 106102 (2003).

107. Ma, Y., Du, G., Yin, J., Yang, T. & Zhang, Y. Structural and optoelectrical properties of ZnO thin films deposited on GaAs substrate by metal-organic chemical vapour deposition (MOCVD). *Semiconductor science and technology* 20, 1198 (2005).

108. Look, D. C. *et al.* Characterization of homoepitaxial p-type ZnO grown by molecular beam epitaxy. *Applied Physics Letters* 81, 1830 (2002).

109. Morkoç, H. & Özgür, Ü. General properties of ZnO. *Zinc Oxide: Fundamentals, Materials and Device Technology* 1–76 (2009).

110. Dong, X. *et al.* Pressure-induced structural transition of ZnO nanocrystals studied with molecular dynamics. *Computational Materials Science* 65, 450–455 (2012).

111. Dai, Z. R., Pan, Z. W. & Wang, Z. L. Ultra-long single crystalline nanoribbons of tin oxide. *Solid State Communications* 118, 351–354 (2001).

112. Chang, P.-C. *et al.* High-performance ZnO nanowire field effect transistors. *Applied physics letters* 89, 133113 (2006).

113. Qin, Y., Wang, X. & Wang, Z. L. Microfibre--nanowire hybrid structure for energy scavenging. *Nature* 451, 809–813 (2008).

114. Unalan, H. E. *et al.* Photoelectrochemical cell using dye sensitized zinc oxide nanowires grown on carbon fibers. *Applied Physics Letters* 93, 133116 (2008).

115. Tang, L., Ding, X., Zhao, X., Wang, Z. & Zhou, B. Preparation of zinc oxide particles by using layered basic zinc acetate as a precursor. *Journal of Alloys and Compounds* (2012).

116. Hosono, E., Fujihara, S., Kimura, T. & Imai, H. Growth of layered basic zinc acetate in methanolic solutions and its pyrolytic transformation into porous zinc oxide films. *Journal of colloid and interface science* 272, 391–398 (2004).

117. Reeber, R. R. & Wang, K. Thermal expansion and lattice parameters of group IV semiconductors. *Materials chemistry and physics* 46, 259–264 (1996).

118. Lee, J., Easteal, A. J., Pal, U. & Bhattacharyya, D. Evolution of ZnO nanostructures in sol--gel synthesis. *Current Applied Physics* 9, 792–796 (2009).

119. Riaz, M., Song, J., Nur, O., Wang, Z. L. & Willander, M. Study of the Piezoelectric Power Generation of ZnO Nanowire Arrays Grown by Different Methods. *Advanced Functional Materials* 21, 628–633 (2011).

120. Fan, Z., Wang, D., Chang, P.-C., Tseng, W.-Y. & Lu, J. G. ZnO nanowire field-effect transistor and oxygen sensing property. *Applied Physics Letters* 85, 5923 (2004).

121. Wan, Q. *et al.* Fabrication and ethanol sensing characteristics of ZnO nanowire gas sensors. *Applied Physics Letters* 84, 3654–3656 (2004).

122. Yakimova, R. *et al.* Novel material concepts of transducers for chemical and biosensors. *Biosensors and Bioelectronics* 22, 2780–2785 (2007).

123. Song, R.-Q., Xu, A.-W., Deng, B., Li, Q. & Chen, G.-Y. From layered basic zinc acetate nanobelts to hierarchical zinc oxide nanostructures and porous zinc oxide nanobelts. *Advanced Functional Materials* 17, 296–306 (2007).

124. Yuan, C. Z. *et al.* Hierarchically structured carbon-based composites: Design, synthesis and their application in electrochemical capacitors. *Nanoscale* 3, 529–545 (2011).

125. Neumark, G. F., Kuskovsky, I. L., Jiang, H. *Zinc Oxide Fundamentals, Materials and Device Technology*. (WILEY-VCH Verlag GmbH & Co. KGaA, Weinheim, 2009).

126. Pamplin, B. & Feigelson, R. S. Spray pyrolysis of CuInSe2 and related ternary semiconducting compounds. *Thin Solid Films* 60, 141–146 (1979).

127. Mattox, D. M. *Handbook of physical vapor deposition (PVD) processing.* (Access Online via Elsevier, 2010).

128. York, N. *HANDBOOK OF THIN-FILM DEPOSITION PROCESSES AND TECHNIQUES.*

129. Schubert, U. S., Hofmeier, H. & Newkome, G. R. *Synthesis of Inorganic Materials The Chemistry of Nanomaterials Synthetic Metal-Containing Polymers One-Dimensional Metals Polymeric Materials in Organic Synthesis and Catalysis.*

130. Xu, W. Z. *et al.* ZnO light-emitting diode grown by plasma-assisted metal organic chemical vapor deposition. *Applied Physics Letters* 88, 173506 (2006).

131. Laudise, R. A. & Ballman, A. A. HYDROTHERMAL SYNTHESIS OF ZINC OXIDE AND ZINC SULFIDE1. *The Journal of Physical Chemistry* 64, 688–691 (1960).

132. Yu, J. & Yu, X. Hydrothermal synthesis and photocatalytic activity of zinc oxide hollow spheres. *Environmental science & technology* 42, 4902–4907 (2008).

133. Li, M. *et al.* Electrochemical Deposition of Conductive Superhydrophobic Zinc Oxide Thin Films. 9954–9957 (2009).

134. Zheng, M. J., Zhang, L. D., Li, G. H. & Shen, W. Z. Fabrication and optical properties of large-scale uniform zinc oxide nanowire arrays by one-step electrochemical deposition technique. *Chemical Physics Letters* 363, 123–128 (2002).

135. Manabe, Y. & Mitsuyu, T. Zinc oxide thin films prepared by the electron-cyclotron-resonance plasma sputtering method. *Japanese journal of applied physics* 29, 334–339 (1990).

136. Wagner, R. S. & Ellis, W. C. Vapor-liquid-solid mechanism of single crystal growth. *Applied Physics Letters* 4, 89–90 (1964).

137. George, a., Kumari, P., Soin, N., Roy, S. S. & McLaughlin, J. a. Microstructure and field emission characteristics of ZnO nanoneedles grown by physical vapor deposition. *Materials Chemistry and Physics* 123, 634–638 (2010).

138. Cao, B. *et al.* Different ZnO nanostructures fabricated by a seed-layer assisted electrochemical route and their photoluminescence and field emission properties. *The Journal of Physical Chemistry C* 111, 2470–2476 (2007).

139. Cao, B. *et al.* A template-free electrochemical deposition route to ZnO nanoneedle arrays and their optical and field emission properties. *Nanotechnology* 16, 2567–2574 (2005).

140. Jun, Y., Choi, J. & Cheon, J. Shape control of semiconductor and metal oxide nanocrystals through nonhydrolytic colloidal routes. *Angewandte Chemie International Edition* 45, 3414–3439 (2006).

141. Leprince-wang, Y., Wang, G. Y., Zhang, X. Z. & Yu, D. P. Study on the microstructure and growth mechanism of electrochemical deposited ZnO nanowires. 287, 89–93 (2006).

142. Zhang, Z. *et al.* Phase transition induced vertical alignment of ultrathin gallium phosphide nanowire arrays on silicon by chemical beam epitaxy. *RSC Advances* 2, 8631 (2012).

143. Hui, J., Lin, Y., Feng, Y. & Jun, T. High-density arrays of low-defect-concentration zinc oxide nanowire grown on transparent conducting oxide glass substrate by chemical vapor deposition. *Acta Materialia* 57, 1813–1820 (2009).

144. Kou, H., Jia, L. & Wang, C. Electrochemical deposition of flower-like ZnO nanoparticles on a silver-modified carbon nanotube / polyimide membrane to improve its photoelectric activity and photocatalytic performance. *Carbon* 50, 3522–3529 (2012).

145. Psaras, P. A. & Langford, H. D. *Advancing materials research.* (National Academies Press, 1987).

146. Somiya, S. *Advanced technical ceramics.* (Access Online via Elsevier, 1989).

147. Yan, C., Xue, D. & Zou, L. A solution-phase approach to the chemical synthesis of ZnO nanostructures via a low-temperature route. *Journal of Alloys and Compounds* 453, 87–92 (2008).

148. Liu, B. & Zeng, H. C. Hydrothermal Synthesis of ZnO Nanorods in the Diameter Regime of 50 nm. *Journal of the American Chemical Society* 125, 4430–4431 (2003).

149. Yang, A. & Cui, Z. ZnO layer and tubular structures synthesized by a simple chemical solution route. *Materials Letters* 60, 2403–2405 (2006).

150. Ndifor-Angwafor, N. G. & Riley, D. J. Synthesis of ZnO nanorod/nanotube arrays formed by hydrothermal growth at a constant zinc ion concentration. *physica status solidi (a)* 205, 2351–2354 (2008).

151. Zhu, Y. F. & Shen, W. Z. Synthesis of ZnO compound nanostructures via a chemical route for photovoltaic applications. *Applied Surface Science* 256, 7472–7477 (2010).

152. Hu, X., Masuda, Y., Ohji, T., Saito, N. & Kato, K. Low-Temperature Fabrication of Bunch-Shaped ZnO Nanowires Using a Sodium Hydroxide Aqueous Solution. *Journal of Nanoscience and Nanotechnology* 11, 10935–10939 (2011).

153. Zhou, H., Fang, G., Liu, N. & Zhao, X. Ultraviolet photodetectors based on ZnO nanorods-seed layer effect and metal oxide modifying layer effect. *Nanoscale research letters* 6, 147 (2011).

154. Kärber, E. *et al.* Photoluminescence of spray pyrolysis deposited ZnO nanorods. *Nanoscale research letters* 6, 1–7 (2011).

155. Van Quy, N., Minh, V. A., Van Luan, N., Hung, V. N. & Van Hieu, N. Gas sensing properties at room temperature of a quartz crystal microbalance coated with ZnO nanorods. *Sensors and Actuators B: Chemical* 153, 188–193 (2011).

156. Warule, S. S., Chaudhari, N. S., Ambekar, J. D., Kale, B. B. & More, M. A. Hierarchical nanostructured ZnO with nanorods engendered to nanopencils and pin-cushion cactus with its field emission study. *ACS Applied Materials & Interfaces* 3, 3454–3462 (2011).

157. Mou, J., Zhang, W., Fan, J., Deng, H. & Chen, W. Facile synthesis of ZnO nanobullets/nanoflakes and their applications to dye-sensitized solar cells. *Journal of Alloys and Compounds* 509, 961–965 (2011).

158. Lupan, O. *et al.* Well-aligned arrays of vertically oriented ZnO nanowires electrodeposited on ITO-coated glass and their integration in dye sensitized solar cells. *Journal of Photochemistry and Photobiology A: Chemistry* 211, 65–73 (2010).

159. Saravana Kumar, R., Sathyamoorthy, R., Matheswaran, P., Sudhagar, P. & Kang, Y. S. Growth of novel ZnO nanostructures by soft chemical routes. *Journal of Alloys and Compounds* 506, 351–355 (2010).

160. Gurav, K. V, Patil, U. M., Pawar, S. M., Kim, J. H. & Lokhande, C. D. Controlled crystallite orientation in ZnO nanorods prepared by chemical bath deposition: Effect of H2O2 *Journal of Alloys and Compounds* 509, 7723–7728 (2011).

161. Dhawale, D. S. & Lokhande, C. D. Chemical route to synthesis of mesoporous ZnO thin films and their liquefied petroleum gas sensor performance. *Journal of Alloys and Compounds* 509, 10092–10097 (2011).

162. Gurav, K. V *et al.* Morphology evolution of ZnO thin films from aqueous solutions and their application to liquefied petroleum gas (LPG) sensor. *Journal of Alloys and Compounds* 525, 1–7 (2012).

163. Jiang, P., Zhou, J.-J., Fang, H.-F., Wang, C.-Y. & Xie, S.-S. ZnO nanowhisker clusters formed on Zn microspheres by wet chemical route. *Materials Letters* 60, 2516–2521 (2006).

164. Zhang, H. *et al.* A novel low-temperature chemical solution route for straight and dendrite-like ZnO nanostructures. *Materials Science and Engineering: B* 141, 76–81 (2007).

165. Yue, S., Lu, J. & Zhang, J. Controlled growth of well-aligned hierarchical ZnO arrays by a wet chemical method. *Materials Letters* 63, 2149–2152 (2009).

166. S.C. Singh, D.P. Singh, J. Singh, P.K. Dubey, R. S. T. and O. N. S. Metal Oxide Nanostructures; Synthesis, Characterizations and Applicat.

167. Huang, J. *et al.* Large-scale synthesis of flowerlike ZnO nanostructure by a simple chemical solution route and its gas-sensing property. *Sensors and Actuators B: Chemical* 146, 206–212 (2010).

168. Liu, Z., Liu, C., Ya, J. & Lei, E. Controlled synthesis of ZnO and TiO2 nanotubes by chemical method and their application in dye-sensitized solar cells. *Renewable Energy* 36, 1177–1181 (2011).

169. Xie, J., Li, P., Wang, Y. & Wei, Y. Synthesis of needle-and flower-like ZnO microstructures by a simple aqueous solution route. *Journal of Physics and Chemistry of Solids* 70, 112–116 (2009).

170. Xie, J., Li, Y., Zhao, W., Bian, L. & Wei, Y. Simple fabrication and photocatalytic activity of ZnO particles with different morphologies. *Powder Technology* 207, 140–144 (2011).

171. Pradhan, D., Kumar, M., Ando, Y. & Leung, K. T. Fabrication of ZnO nanospikes and nanopillars on ITO glass by templateless seed-layer-free electrodeposition and their field-emission properties. *ACS applied materials & interfaces* 1, 789–96 (2009).

172. Zhang, L., Yin, L., Wang, C., Lun, N. & Qi, Y. Sol- Gel Growth of Hexagonal Faceted ZnO Prism Quantum Dots with Polar Surfaces for Enhanced Photocatalytic Activity. *ACS applied materials & interfaces* 2, 1769–1773 (2010).

173. Gao, K. *et al.* Correlation between structure and photoluminescence of< i> c</i>-axis oriented nanocrystalline ZnO films and evolution of photo-generated excitons. *Solar Energy Materials and Solar Cells* 96, 117–123 (2012).

174. Chiu, W.-H. *et al.* Efficient electron transport in tetrapod-like ZnO metal-free dye-sensitized solar cells. *Energy & Environmental Science* 2, 694 (2009).

175. Al-Hardan, N. H., Abdullah, M. J. & Aziz, A. A. Sensing mechanism of hydrogen gas sensor based on RF-sputtered ZnO thin films. *International journal of hydrogen energy* 35, 4428–4434 (2010).

176. Chiu, W. S. *et al.* Synthesis of two-dimensional ZnO nanopellets by pyrolysis of zinc oleate. *Chemical Engineering Journal* 142, 337–343 (2008).

177. Zhu, Y. F. *et al.* Controllable synthesis of hierarchical ZnO nanostructures via a chemical route. *Physica E: Low-dimensional Systems and Nanostructures* 42, 2460–2465 (2010).

178. Qi, Q. *et al.* Selective acetone sensor based on dumbbell-like ZnO with rapid response and recovery. *Sensors and Actuators B: Chemical* 134, 166–170 (2008).

179. Law, M., Greene, L. E., Johnson, J. C., Saykally, R. & Yang, P. Nanowire dye-sensitized solar cells. *Nature materials* 4, 455–9 (2005).

180. Wang, Y., Iqbal, Z. & Mitra, S. Rapidly functionalized, water-dispersed carbon nanotubes at high concentration. *Journal of the American Chemical Society* 128, 95–99 (2006).

181. Ko, C.-J., Lin, Y.-K. & Chen, F.-C. Microwave annealing of polymer photovoltaic devices. *Advanced Materials* 19, 3520–3523 (2007).

182. Fang, X., Bando, Y., Gautam, U. K., Ye, C. & Golberg, D. Inorganic semiconductor nanostructures and their field-emission applications. *Journal of Materials Chemistry* 18, 509 (2008).

183. Zhai, T., Fang, X., Li, L., Bando, Y. & Golberg, D. One-dimensional CdS nanostructures: synthesis, properties, and applications. *Nanoscale* 2, 168–187 (2010).

184. Fang, X. *et al.* ZnO and ZnS nanostructures: ultraviolet-light emitters, lasers, and sensors. *Critical Reviews in Solid State and Materials Sciences* 34, 190–223 (2009).

185. Kuchibhatla, S. V. N. T., Karakoti, A. S., Bera, D. & Seal, S. One dimensional nanostructured materials. *Progress in materials science* 52, 699–913 (2007).

186. Xia, Y. *et al.* One-dimensional nanostructures: synthesis, characterization, and applications. *Advanced materials* 15, 353–389 (2003).

187. Raghavan, U. Optical Properties of ZnS Nanoparticles and Effect of Doping with d Block Elements (Transition Elements). 98–119 (2011).
at <http://dspace.vpmthane.org:8080/jspui/bitstream/123456789/2918/6/Chapter-5.pdf>

188. Yeh, C.-Y., Lu, Z. W., Froyen, S. & Zunger, A. Zinc-blende--wurtzite polytypism in semiconductors. *Physical review B* 46, 10086 (1992).

189. Ludi, B. & Niederberger, M. Zinc oxide nanoparticles: chemical mechanisms and classical and non-classical crystallization. *Dalton Trans.* (2013).

190. Schmidt-Mende, L. & MacManus-Driscoll, J. L. ZnO--nanostructures, defects, and devices. *Materials today* 10, 40–48 (2007).

191. Tran, T. K. *et al.* Photoluminescence properties of ZnS epilayers. *Journal of applied physics* 81, 2803–2809 (1997).

192. Manna, L., Milliron, D. J., Meisel, A., Scher, E. C. & Alivisatos, A. P. Controlled growth of tetrapod-branched inorganic nanocrystals. *Nature materials* 2, 382–385 (2003).

193. Yin, Y. & Alivisatos, A. P. Colloidal nanocrystal synthesis and the organic--inorganic interface. *Nature* 437, 664–670 (2004).

194. Xu, C. X. & Sun, X. W. Multipod zinc oxide nanowhiskers. *Journal of crystal growth* 277, 330–334 (2005).

195. Yao, B. D., Chan, Y. F. & Wang, N. Formation of ZnO nanostructures by a simple way of thermal evaporation. *Applied Physics Letters* 81, 757–759 (2002).

196. Lee, S. Y. Controllability of Structural, Optical and Electrical Properties of Ga doped ZnO Nanowires Synthesized by Physical Vapor Deposition. *TRANSACTIONS ON ELECTRICAL AND ELECTRONIC MATERIALS* 14, 148–151 (2013).

197. Silva, L. J. *et al.* ZnO electrodeposition onto gold from recordable compact discs and its use as photocatalyst under solar irradiation. *Brazilian Journal of Chemical Engineering* 30, 155–158 (2013).

198. Lee, G.-H. Effect of the O_2/N_2 ratio on the morphology of ZnO nanostructures grown by a thermal evaporation technique. *Ceramics International* (2013).

199. Zhou, M., Gao, X., Hu, Y., Chen, J. & Hu, X. Uniform hamburger-like mesoporous carbon-incorporated ZnO nanoarchitectures: One-pot solvothermal synthesis, high adsorption and visible-light photocatalytic decolorization of dyes. *Applied Catalysis B: Environmental* (2013).

200. Promnimit, S., Baruah, S., Lamdu, U. & Dutta, J. Hydrothermal Growth of ZnO Hexagonal Nanocrystals: Effect of Growth Conditions. *Journal of Nano Research* 21, 57–63 (2013).

201. Bando, K., Sawabe, T., Asaka, K. & Masumoto, Y. Room-temperature excitonic lasing from ZnO single nanobelts. *Journal of luminescence* 108, 385–388 (2004).

202. Z.W. Pan, Z.R. Dai, Z. L. W. Nanobelts of semiconducting oxides. *Science* 291, (2001).

203. Alemán, B., Fernández, P. & Piqueras, J. Indium-zinc-oxide nanobelts with superlattice structure. *Applied Physics Letters* 95, 013111 (2009).

204. Chen, Y. F. *et al.* TEM investigations on ZnO nanobelts synthesized via a vapor phase growth. *Micron (Oxford, England : 1993)* 35, 481–7 (2004).

205. Chen, Y. X. & Guo, S. W. Twinning-induced ZnO bicrystalline nanobelts. *Materials Letters* 61, 5275–5277 (2007).

206. Choopun, S. *et al.* Single-crystalline ZnO nanobelts by RF sputtering. *Journal of Crystal growth* 282, 365–369 (2005).

207. Lee, G.-H. & Song, J.-H. Catalyst-free synthesis of novel brush-shaped ZnO particles by a simple oxidation in air. *Applied Surface Science* 256, 2837–2840 (2010).

208. Lee, G.-H. & Kim, M.-S. Synthesis of ZnO crystals with tubular structure by the oxidation of Al-Zn-Au mixture. *Journal of the Ceramic Society of Japan* 117, 878–880 (2009).

209. Liu, L. *et al.* Controlled synthesis of ZnO with adjustable morphologies from nanosheets to microspheres. *Colloids and Surfaces A: Physicochemical and Engineering Aspects* 348, 124–129 (2009).

210. Al-Gaashani, R., Radiman, S., Tabet, N. & Daud, A. R. Effect of microwave power on the morphology and optical property of zinc oxide nano-structures prepared via a microwave-assisted aqueous solution method. *Materials Chemistry and Physics* 125, 846–852 (2011).

211. Kou, H. *et al.* Electrochemical synthesis of ZnO nanoflowers and nanosheets on porous Si as photoelectric materials. *Applied Surface Science* 257, 4643–4649 (2011).

212. Xing, L.-L. & Xue, X.-Y. Electrochemistry-assisted self-assembly of oriented zinc oxide and long-chain alkyl amine surfactant multilamellar nanostructures. *Solid State Sciences* 12, 1593–1598 (2010).

213. Qiu, J., Guo, M. & Wang, X. Electrodeposition of hierarchical ZnO nanorod-nanosheet structures and their applications in dye-sensitized solar cells. *ACS Applied Materials & Interfaces* 3, 2358–2367 (2011).

214. Luo, X., Xu, L., Xu, B. & Li, F. Electrodeposition of zinc oxide/tetrasulfonated copper phthalocyanine hybrid thin film for dye-sensitized solar cell application. *Applied Surface Science* 257, 6908–6911 (2011).

215. Xie, C. *et al.* Fabrication and formaldehyde gas-sensing property of ZnO--MnO_2; coplanar gas sensor arrays. *Sensors and Actuators B: Chemical* 145, 457–463 (2010).

216. Huang, J. *et al.* Fabrication and gas-sensing properties of hierarchically porous ZnO architectures. *Sensors and Actuators B: Chemical* 155, 126–133 (2011).

217. Kakiuchi, K., Saito, M. & Fujihara, S. Fabrication of ZnO films consisting of densely accumulated mesoporous nanosheets and their dye-sensitized solar cell performance. *Thin Solid Films* 516, 2026–2030 (2008).

218. Lei, A. *et al.* Facile synthesis and enhanced photocatalytic activity of hierarchical porous ZnO microspheres. *Materials Letters* 66, 72–75 (2012).

219. Newman, S. P. & Jones, W. Comparative study of some layered hydroxide salts containing exchangeable interlayer anions. *Journal of Solid State Chemistry* 148, 26–40 (1999).

220. Aisawa, S. *et al.* Intercalation of amino acids and oligopeptides into Zn--Al layered double hydroxide by coprecipitation reaction. *Journal of Physics and Chemistry of Solids* 67, 920–925 (2006).

221. Ma, R. *et al.* Synthesis and exfoliation of Co2+-Fe3+ layered double hydroxides: An innovative topochemical approach. *Journal of the American Chemical Society* 129, 5257–5263 (2007).

222. Silva, C. G., Bouizi, Y., Fornés, V. & García, H. Layered double hydroxides as highly efficient photocatalysts for visible light oxygen generation from water. *Journal of the American Chemical Society* 131, 13833–13839 (2009).

223. Del Arco, M., Gutiérrez, S., Martín, C., Rives, V. & Rocha, J. Synthesis and characterization of layered double hydroxides (LDH) intercalated with non-steroidal anti-inflammatory drugs (NSAID). *Journal of Solid State Chemistry* 177, 3954–3962 (2004).

224. Arizaga, G. G. C., Satyanarayana, K. G. & Wypych, F. Layered hydroxide salts: synthesis, properties and potential applications. *Solid State Ionics* 178, 1143–1162 (2007).

225. Rodeghiero, E. D., Chisaki, J. & Giannelis, E. P. In situ microstructural control of Ni/Al2O3 and Ni/NiAl2O4 composites from layered double hydroxides. *Chemistry of materials* 9, 478–484 (1997).

226. Hosono, E., Fujihara, S., Honma, I. & Zhou, H. Fabrication of morphology and crystal structure controlled nanorod and nanosheet cobalt hydroxide based on the difference of oxygen-solubility between water and methanol, and conversion into Co3O4. *Journal of Materials Chemistry* 15, 1938 (2005).

227. Petrov, K., Lyubchova, A. & Markov, L. Synthesis and thermal decomposition of magnesium hydroxide nitrates. *Polyhedron* 8, 1061–1067 (1989).

228. Haile, S. M., Johnson, D. W., Wiseman, G. H. & Bowen, H. K. Aqueous precipitation of spherical zinc oxide powders for varistor applications. *Journal of the American Ceramic Society* 72, 2004–2008 (1989).

229. Zhang, Q., Dandeneau, C. S., Zhou, X. & Cao, G. ZnO Nanostructures for Dye-Sensitized Solar Cells. *Advanced Materials* 21, 4087–4108 (2009).

230. Wang, Z. L. & Song, J. Piezoelectric nanogenerators based on zinc oxide nanowire arrays. *Science (New York, N.Y.)* 312, 242–6 (2006).

231. Morioka, H., Tagaya, H., Kadokawa, J.-I. & Chiba, K. Studies on layered basic zinc acetate. *Journal of materials science letters* 18, 995–998 (1999).

232. Biswick, T., Jones, W., Pacu\la, A., Serwicka, E. & Podobinski, J. Evidence for the formation of anhydrous zinc acetate and acetic anhydride during the thermal degradation of zinc hydroxy acetate, Zn5(OH)8(CH2). *Solid State Sciences* 11, 330–335 (2009).

233. Biswick, T., Jones, W., Pacu\la, A., Serwicka, E. & Podobinski, J. The role of anhydrous zinc nitrate in the thermal decomposition of the zinc hydroxy nitrates Zn 5(OH)8(NO3) 2.2H2O. *Journal of Solid State Chemistry* 180, 1171–1179 (2007).

234. Audebrand, N., Auffrédic, J.-P. & Louër, D. X-ray diffraction study of the early stages of the growth of nanoscale zinc oxide crystallites obtained from thermal decomposition of four precursors. General concepts on precursor-dependent microstructural properties. *Chemistry of materials* 10, 2450–2461 (1998).

235. Zhang, W. & Yanagisawa, K. Hydrothermal synthesis of zinc hydroxide chloride sheets and their conversion to ZnO. *Chemistry of materials* 19, 2329–2334 (2007).

236. Arii, T. & Kishi, A. The effect of humidity on thermal process of zinc acetate. *Thermochimica acta* 400, 175–185 (2003).

237. Kozawa, T., Onda, A., Yanagisawa, K., Kishi, A. & Masuda, Y. Effect of water vapor on the thermal decomposition process of zinc hydroxide chloride and crystal growth of zinc oxide. *Journal of Solid State Chemistry* 184, 589–596 (2011).

238. Cui, Q., Yu, K., Zhang, N. & Zhu, Z. Porous ZnO nanobelts evolved from layered basic zinc acetate nanobelts. *Applied Surface Science* 254, 3517–3521 (2008).

239. Hou, Q., Zhu, L., Chen, H., Liu, H. & Li, W. Highly regular and ultra-thin porous ZnO nanosheets: An indirect electrodeposition method using acetate-containing precursor and their application in quantum dots-sensitized solar cells. *Electrochimica Acta* 94, 72–79 (2013).

240. Comini, E. Metal oxide nano-crystals for gas sensing. *Analytica chimica acta* 568, 28–40 (2006).

241. Yamazoe, N. New approaches for improving semiconductor gas sensors. *Sensors and Actuators B: Chemical* 5, 7–19 (1991).

242. Bonini, N. *et al.* Doping of a nanostructured titania thick film: structural and electrical investigations. *Sensors and Actuators B: Chemical* 68, 274–280 (2000).

243. Comini, E. *et al.* Production and characterization of titanium and iron oxide nano-sized thin films. *Journal of Materials Research* 16, 1559–1564 (2001).

244. Pan, Z. W., Dai, Z. R. & Wang, Z. L. Nanobelts of Semiconducting Oxides. 291, 2000–2002 (2001).

245. Comini, E., Faglia, G., Sberveglieri, G., Pan, Z. & Wang, Z. L. Stable and highly sensitive gas sensors based on semiconducting oxide nanobelts. *Applied Physics Letters* 81, 1869 (2002).

246. Kolmakov, a., Zhang, Y., Cheng, G. & Moskovits, M. Detection of CO and O2 Using Tin Oxide Nanowire Sensors. *Advanced Materials* 15, 997–1000 (2003).

247. Hu, J. Q., Bando, Y., Liu, Q. L. & Golberg, D. Laser-Ablation Growth and Optical Properties of Wide and Long Single-Crystal SnO2 Ribbons. *Advanced Functional Materials* 13, 493–496 (2003).

248. Chen, Y. *et al.* Bulk-quantity synthesis and self-catalytic VLS growth of SnO2 nanowires by lower-temperature evaporation. *Chemical Physics Letters* 369, 16–20 (2003).

249. Dang, H. Y., Wang, J. & Fan, S. S. The synthesis of metal oxide nanowires by directly heating metal samples in appropriate oxygen atmospheres. *Nanotechnology* 14, 738 (2003).

250. Faglia, G., Baratto, C., Sberveglieri, G., Zha, M. & Zappettini, a. Adsorption effects of NO2 at ppm level on visible photoluminescence response of SnO2 nanobelts. *Applied Physics Letters* 86, 011923 (2005).

251. Mason, W. P. FATAL POISONING BY CARBON MONOXIDE. *Journal of the American Chemical Society* 10, 176–178 (1888).

252. Conrad, R. & Conrad, R. Soil microorganisms as controllers of Soil Microorganisms as Controllers of Atmospheric Trace Gases (H 2 , CO , CH 4 , OCS , N 2 O , and NO). 60, (1996).

253. Thauer, R. K., Fuchs, G., Käufer, B. & Schnitker, U. Carbon-monoxide oxidation in cell-free extracts of Clostridium pasteurianum. *European journal of biochemistry / FEBS* 45, 343–9 (1974).

254. Goldstein, M. Carbon Monoxide Poisoning. *Journal of emergency nursing: JEN : official publication of the Emergency Department Nurses Association* 34, 538–542 (2008).

255. Chang, J. F., Kuo, H. H., Leu, I. C. & Hon, M. H. The effects of thickness and operation temperature on ZnO:Al thin film CO gas sensor. *Sensors and Actuators B: Chemical* 84, 258–264 (2002).

256. Hull, A. W. A new method of chemical analysis. *Journal of the American Chemical Society* 41, 1168–1175 (1919).

257. Williams, D. B. & Carter, C. B. *The Transmission Electron Microscope.* (Springer, 1996).

258. Binnig, G., Quate, C. F. & Gerber, C. Atomic force microscope. *Physical review letters* 56, 930 (1986).

259. Magonov, S. N. & Whangbo, M.-H. *Surface analysis with STM and AFM: experimental and theoretical aspects of image analysis.* (Wiley. com, 2008).

260. Moulder, J. F., Chastain, J. & King, R. C. *Handbook of X-ray photoelectron spectroscopy: a reference book of standard spectra for identification and interpretation of XPS data.* (Physical Electronics Eden Prairie, MN, 1995).

261. Das, A. K. Effect of Mg diffusion on bilayer photoluminescence spectra of Mg0. 29Zn0. 710/ZnO interface at different annealing temperatures. *arXiv preprint arXiv:1302.4246* (2013).

262. Osepchuk, J. M. A history of microwave heating applications. *Microwave Theory and Techniques, IEEE Transactions on* 32, 1200–1224 (1984).

263. Metaxas, A. C. & and Meredith, R. J. Industrial microwave heating. (1983).

264. Dinčov, D. D., Parrott, K. A. & Pericleous, K. A. Heat and mass transfer in two-phase porous materials under intensive microwave heating. *Journal of Food Engineering* 65, 403–412 (2004).

265. Sutton, W. H. Microwave processing of ceramics-an overview. in *MRS Proceedings* 269, (1992).

266. Sahraoui, N., Vian, M. A., Bornard, I., Boutekedjiret, C. & Chemat, F. Improved microwave steam distillation apparatus for isolation of essential oils: Comparison with conventional steam distillation. *Journal of Chromatography A* 1210, 229–233 (2008).

267. Bernard, T., Perineau, F., Delmas, M. & Gaset, A. Extraction of Essential Oils. Part III. Two-Stage Production of the Oil of Lavandula angustifolia Mill. *Journal of Essential Oil Research* 1, 261–267 (1989).

268. Loupy, A. Microwaves in organic synthesis. *Weinheim: Wiley-VCH, 2002De la Hoz A, Diaz-Ortiz A, Moreno A. Chem. Soc. Rev* 34, 164–178 (2005).

269. Tada, H. (1960) J. Am. Chem. Soc. 82:255. *journal of american chemistry* 82, 255 (1960).

270. Sugunan, A., Warad, H. C., Boman, M. & Dutta, J. Zinc oxide nanowires in chemical bath on seeded substrates: role of hexamine. *Journal of Sol-Gel Science and Technology* 39, 49–56 (2006).

271. Byrappa, K. & Yoshimura, M. *Handbook of hydrothermal technology*. (Access Online via Elsevier, 2001).

272. Kong, X. Y., Ding, Y., Yang, R. & Wang, Z. L. Single-crystal nanorings formed by epitaxial self-coiling of polar nanobelts. *Science* 303, 1348–1351 (2004).

273. Kasai, A. & Fujihara, S. Layered single-metal hydroxide/ethylene glycol as a new class of hybrid material. *Inorganic chemistry* 45, 415–418 (2006).

274. Wang, Y., Li, Y., Zhou, Z., Zu, X. & Deng, Y. Evolution of the zinc compound nanostructures in zinc acetate single-source solution. *Journal of Nanoparticle Research* 13, 5193–5202 (2011).

275. Zhang, H., Chen, B., Gilbert, B. & Banfield, J. F. Kinetically controlled formation of a novel nanoparticulate ZnS with mixed cubic and hexagonal stacking. *Journal of Materials Chemistry* 16, 249–254 (2006).

276. Schlur, L., Carton, A., Lévêque, P., Guillon, D. & Pourroy, G. Optimization of a New ZnO Nanorods Hydrothermal Synthesis Method for Solid State Dye Sensitized Solar Cells Applications. *The Journal of Physical Chemistry C* 117, 2993–3001 (2013).

277. Moezzi, A., McDonagh, A., Dowd, A. & Cortie, M. Zinc Hydroxyacetate and Its Transformation to Nanocrystalline Zinc Oxide. *Inorganic chemistry* 52, 95–102 (2012).

278. Zheng, Y. *et al.* Ag/ZnO heterostructure nanocrystals: synthesis, characterization, and photocatalysis. *Inorganic chemistry* 46, 6980–6986 (2007).

279. Van Quy, N., Minh, V. A., Van Luan, N., Hung, V. N. & Van Hieu, N. Gas sensing properties at room temperature of a quartz crystal microbalance coated with ZnO nanorods. *Sensors and Actuators B: Chemical* 153, 188–193 (2011).

280. Ye, F., Peng, Y., Chen, G.-Y., Deng, B. & Xu, A.-W. Facile solution synthesis and characterization of ZnO mesocrystals and ultralong nanowires from layered basic zinc salt precursor. *The Journal of Physical Chemistry C* 113, 10407–10415 (2009).

281. Bogdal, D. & Prociak, A. *Microwave-enhanced polymer chemistry and technology*. (Wiley. com, 2008).

282. Djurišić, a. B. *et al.* Photoluminescence and Electron Paramagnetic Resonance of ZnO Tetrapod Structures. *Advanced Functional Materials* 14, 856–864 (2004).

283. Djurišić, a B. *et al.* Defect emissions in ZnO nanostructures. *Nanotechnology* 18, 095702 (2007).

284. Zhang, Y., Zhu, F., Zhang, J. & Xia, L. Converting layered zinc acetate nanobelts to one-dimensional structured ZnO nanoparticle aggregates and their photocatalytic activity. *Nanoscale Research Letters* 3, 201–204 (2008).

285. Kohl, D. The role of noble-metals in the chemistry of solid-state gas sensors. *Sensors and Actuators B: Chemical* 1, 152–156 (1990).

286. Moseley P T. Solid state gas sensors. *Measurement Science & Technology* 8, 223–237 (1997).

287. Yoon, D. Microstructure and CO gas sensing properties of porous ZnO produced by starch addition. *Sensors and Actuators B: Chemical* 45, 251–257 (1997).

288. Jiaqiang, X., Yuping, C., Daoyong, C. & Jianian, S. Hydrothermal synthesis and gas sensing characters of ZnO nanorods. *Sensors and Actuators B: Chemical* 113, 526–531 (2006).

289. Ryu, H.-W. *et al.* ZnO sol--gel derived porous film for CO gas sensing. *Sensors and Actuators B: Chemical* 96, 717–722 (2003).

290. Comini, E. *et al.* Tin oxide nanobelts electrical and sensing properties. *Sensors and Actuators B: Chemical* 111-112, 2–6 (2005).

291. Kuang, Q. *et al.* Enhancing the Photon- and Gas-Sensing Properties of a Single SnO 2 Nanowire Based Nanodevice by Nanoparticle Surface Functionalization. 11539–11544 (2008).

292. Gupta, S. K., Joshi, A. & Kaur, M. Development of gas sensors using ZnO nanostructures. *Journal of Chemical Sciences* 122, 57–62 (2010).

293. Bai, S. *et al.* Synthesis of ZnO nanorods and its application in NO2 sensors. *Sensors and Actuators B: Chemical* 153, 110–116 (2011).

294. Xu, J. *et al.* Selective detection of HCHO gas using mixed oxides of ZnO/ZnSnO3; *Sensors and Actuators B: Chemical* 120, 694–699 (2007).

List of abbreviations

AFM	Atomic Force Microscope
APCVD	Atmospheric Pressure Chemical Vapour Deposition
BSE	Back-Scattered Electrons
BZN	Basic Zinc Nitrate
CAGR	Compound Annual Growth Rate
CBE	Chemical Beam Epitaxy
CNS	Central Nervous System
CVI	Chemical Vapour Infiltration
DI	Deionized Water
DMO	Direct Melt Oxidation
DMO	Direct Melt Oxidation
EDXD	Energy-Dispersive X-ray Diffraction
HAS	Hemispherical Analyzer
HMTA	Hexamethylenetetramine
HRXRD	High-Resolution X-ray Diffraction
HWCVD	Hot Wire Chemical Vapour Deposition
ITO	Indium Tin Oxide
LBZA	Layered Basic Zinc Acetate
LBZA Ss	Layered Basic Zinc Acetate Salts
LCVD	Laser Chemical Vapour Deposition

LED	Light Emitting Diode
LPCVD	Low-Pressure Chemical Vapour Deposition
MEMS	Micro-electromechanical systems
MFC	Mass Flow Controller
MHS	Metal Hydroxide Salts
MOCVD	Metal Organic Chemical Vapour Deposition
MOGSs	Metal Oxide Gas Sensors
NEMS	Nano-electromechanical systems
P3HT	poly(3-hexylthiophene)
PACVD	Plasma-Assisted Chemical Vapour Deposition
PECVD	Plasma-Enhanced Chemical Vapour Deposition
PEDOT:PSS	poly(3,4-ethylenedioxythiophene): poly (styrenesulfonate)
PET	poly(ethylene terephthalate)
PL	Photoluminescence
PVD	Photochemical Vapour Deposition
RF	Radio Frequency
SAW	Surface Acoustic Wave
sccm	Standard cubic centimeters per minute
SCTG	Sample-Controlled Thermogravimetry
SEM	Scanning Electron Microscopy
SMO	Semiconductor Metal Oxide
SPM	Scanning Probe Microscopy

TECD	Templated Electrochemical Deposition
TG-MS	Thermogravimetry Mass Spectrometry
TSPcCu	Tetrasulfonated Copper Phthalocyanine
TTFT	Transparent Thin-Film Transistors
VLS	Vapour Liquid Solid
VTP	Vapour Transport Process
XPS	X-ray Photoelectron Spectroscopy
XRD	X-ray Diffraction
XRD–DSC	X-ray Diffractometry and Differential Scanning Calorimetry
ZAHH	Zinc Acetate Hydroxide Hydrate
ZHSs	Zinc Hydroxide Salts
Zn-HDS	Zn based hydroxide double salts

Publications

1. **Nanocrystalline ZnO obtained from pyrolytic decomposition of layered basic zinc acetate: comparison between conventional and microwave oven growth, IEEE, 2012, p 701-705**

A. Tarat, R. Majithia, R. A. Brown, M. W. Penny, K. E. Meissner, and T. G. G. Maffeis1

2. **Synthesis of nanocrystalline ZnO nanobelts via pyrolytic decomposition of zinc acetate nanobelts and their gas sensing behaviour, Surface Science, 2012, p 715-721.**

A. Tarat, R. Majithia, R. A. Brown, M. W. Penny, K. E. Meissner, and T. G. G. Maffeis1

3. **Microwave-assisted synthesis of layered basic zinc acetate nanosheets and their thermal decomposition into nanocrystalline ZnO, Springer, 2014**

A. Tarat, C.J. Nettle, D.T.J. Bryant, D. R. Jones, M.W. Penny, R.A. Brown, R. Majitha, K.E. Meissner, and T.G.G. Maffeis

4. **The viability of U-2 OS cells on Zinc Oxide nanowires observed via MTS assay in vitro, IEEE, 2012**

Richard A. Brown, Chris J. Barnett, Afshin Tarat, Dan R. Jones, Lewis W. Francis, Steven Conlan and Thierry G. G. Maffeis

5. **The effect of metal layers on the morphology and optical properties of hydrothermally grown zinc oxide nanowires, Journal of Materials, Springer, 2013**

Richard A. Brown, Jon E. Evans, Afshin Tarat, Daniel R. Jones, Nathan A. Smith, Chris J. Barnett, and Thierry G. G. Maffeis

6. **Investigation into the initial growth parameters of hydrothermally grown zinc oxide nanowires, IEEE, 2013**

Chris J. Barnett, Richard A. Brown, Daniel R. Jones, Afshin Tarat, Richard J. Cobley and Thierry G.G. Maffeis.